ISSN 2423-9992

# JAEA R&D Review 2016-17

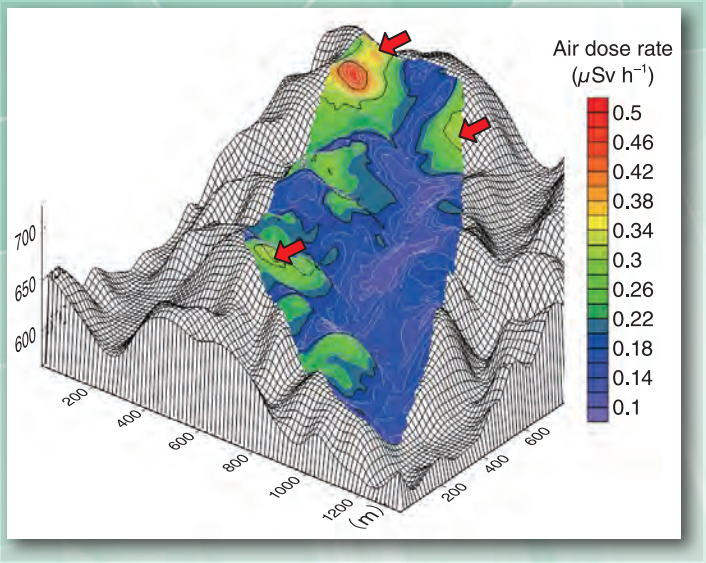


A Contour Map of the Air Dose Rate of a Mountainous Forest Catchment (Topic 1-12)

Appearance of the Extreme Environment Single Crystal Neutron Diffractometer “SENJU” (Topic 5-4)

# *Message from the President*

児玉敏雄

*President Toshio KODAMA*

We sincerely thank you for your understanding and continued support of our research and development (R&D) activities. This publication has been issued annually since the foundation of the Japan Atomic Energy Agency (JAEA), with the intention of informing you of the agency's day-to-day accomplishments.

JAEA is the sole comprehensive R&D institute dedicated to nuclear energy in Japan, and our mission is to contribute to the welfare and prosperity of human society through nuclear science and technology. In accordance with our 3rd medium- and long-term goals set in April 2015, we are working on R&D. JAEA aims to contribute to nuclear science and technology through active cooperation with industries and universities, with maximizing our R&D achievements with a focus on the following our priority fields. In particular, JAEA has focused on issues such as the response to the accident at the Fukushima Daiichi Nuclear Power Station operated by the Tokyo Electric Power Company Holdings, Inc., the research for safety improvement in the field of nuclear energy, R&D toward the establishment of nuclear fuel cycle technology such as fast reactors and reprocessing, and the development of technology for the treatment and disposal of radioactive waste. In addition, to support these R&D and create new technologies, we have implemented nuclear science research and human resources development.

This publication introduces representative results achieved through JAEA's R&D activities. A part of quantum beam science research and nuclear fusion research development were taken over to the National Institutes for Quantum and Radiological Science and Technology established in April 2016. The research results in these fields achieved before the transfer and integration, are posted in this issue.

We are pleased that you will gain further understanding of JAEA's accomplishments through this publication, and we expect your continued encouragement and guidance in our R&D activities.

# 5 Quantum Beam Science Research



# 6 HTGR Hydrogen and Heat Application Research

# 9 Nuclear Fusion Research and Development



# 10 Computational Science and E-Systems Research



# 11 Development of Science & Technology for Nuclear Nonproliferation

# About This Publication and the Outline of the Organization of JAEA

This publication introduces our latest research and development (R&D) results in each field. Each chapter presents the activities of one R&D Sector. The various R&D Sectors perform their activities through R&D centers or institutes. Depending on the R&D activities, some of these centers or institutes comprise only one site, whereas others comprise two or more sites. The R&D centers and institutes are located throughout Japan, as shown on the map below. The following brief introduction outlines the research undertaken by each R&D Sector at various R&D centers and institutes.

1. **The Sector of Fukushima Research and Development** is engaged in R&D, aimed at recovery from the accident at the Fukushima Daiichi Nuclear Power Station of Tokyo Electric Power Company Holdings, Inc. (TEPCO). To contribute to the realization of a secure environment for residents, the Fukushima Environmental Safety Center has been conducting environmental radiation monitoring and R&D for monitoring radioactive cesium behavior in the environment and for developing decontamination and volume reduction technologies. The Collaborative Laboratories for Advanced Decommissioning Science (CLADS) has been conducting R&D ranging from basic research to applied studies, such as understanding of the properties of fuel debris, analysis of the situation inside the reactors, and processing and disposal of radioactive waste, in line with the "Mid-and-Long-Term Roadmap towards the Decommissioning of the TEPCO's Fukushima Daiichi Nuclear Power Station Units 1-4". Moreover, the Fukushima Research Infrastructural Creation Center has two indispensable bases for R&D facilities, promoting the decommissioning of the TEPCO's Fukushima Daiichi Nuclear Power Station. One of those, "Naraha Remote Technology Development Center" has started operations. Another one, "Okuma Analysis and Research Center" has been preparing for start.
2. **The Nuclear Safety Research Center, Sector of Nuclear Safety Research and Emergency Preparedness,** is in charge of safety research that supports the national nuclear safety bodies that regulate nuclear power plants, nuclear fuel cycle facilities, and radioactive waste-disposal facilities. This work is being conducted at the Nuclear Science Research Institute.
3. **The Advanced Science Research Center, Sector of Nuclear Science Research,** explores yet-undiscovered disciplines and studies advanced atomic energy sciences via the Nuclear Science Research Institute to develop new theories and investigate novel phenomena, materials, and technologies. In particular, six research themes have been organized under the two divisions "advanced actinides science" and "advanced nuclear materials science".
4. **The Nuclear Science and Engineering Center, Sector of Nuclear Science Research,** is engaged in key and basic research on various fundamental technologies that support nuclear power use. These efforts are being conducted mainly at the Nuclear Science Research Institute and the Oarai Research and Development Center.
5. **The Quantum Beam Science Center, Sector of Nuclear Science Research,** is engaged in research using neutrons at the Nuclear Science Research Institute and Japan Proton Accelerator Research Complex (J-PARC). Work using electron beams, gamma rays, and ion beams is being conducted at the Takasaki Advanced Radiation Research Institute. Research using lasers and synchrotron radiation is being performed at the Kansai Photon Science Institute. A part of quantum beam science research was taken over to the National Institutes for Quantum and Radiological Science and Technology (QST) established in April 2016, and the Quantum Beam Science Center was reorganized into the Materials Sciences Research Center.

## Japan Atomic Energy Agency -Outline of Organization-

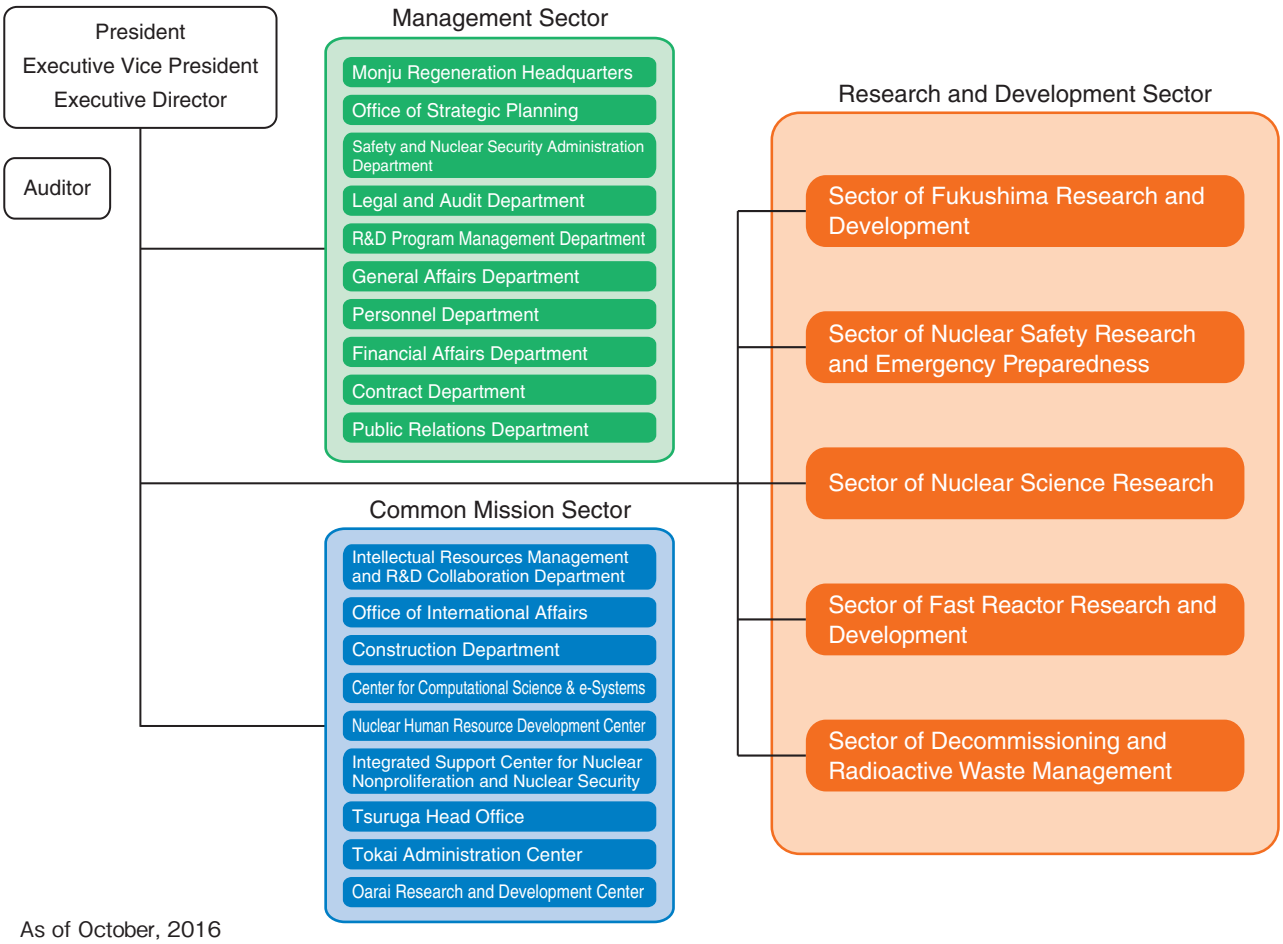


As of October, 2016

6. **The HTGR Hydrogen and Heat Application Research Center, Sector of Nuclear Science Research,** conducts R&D on technologies for high-temperature gas-cooled reactors (HTGRs) and thermochemical hydrogen production at the Oarai Research and Development Center.
7. **The Sector of Fast Reactor Research and Development** is conducting R&D toward the establishment of fast reactor (FR) cycles to address long-term energy security and global environmental issues. In Tsuruga, staff at the Prototype Fast Breeder Reactor Monju and the Monju Project Management and Engineering Center are conducting R&D on "MONJU". R&D activities are also aimed at enhancing the safety of the FR system at the Oarai Research and Development Center and at manufacturing plutonium fuel and reprocessing spent FBR fuel at the Nuclear Fuel Cycle Engineering Laboratories.
8. **The Sector of Decommissioning and Radioactive Waste Management** develops technologies for the safe and rational decommissioning of nuclear power facilities as well as measures for processing and disposing of radioactive waste in their R&D centers or institutes. This sector also conducts multidisciplinary R&D aimed at improving the reliability of geological isolation of high-level radioactive waste in Japan. A particular focus involves establishing techniques for investigating the deep geological environment through R&D at the Tono Geoscience Center and the Horonobe Underground Research Center. At the Nuclear Fuel Cycle Engineering Laboratories, the focus is on improving the technologies for disposal facility design and safety assessment. Additionally, ongoing work is focused on the development of a next-generation knowledge management system based on the above R&D activities. Furthermore, the development of nuclear fuel cycle technology for LWRs is in progress at the Nuclear Fuel Cycle Engineering Laboratories.
9. **The Sector of Fusion Research and Development** is performing fusion R&D as a domestic agency of the International Thermonuclear Experimental Reactor (ITER) project and as an implementing agency of the Broader Approach (BA) activities. The procurement activity of the ITER project, upgrade of JT-60 into a superconducting machine as a BA activity, fusion plasma research, and R&D on various elemental technologies are being conducted at the Naka Fusion Institute. Moreover, the International Fusion Energy Research Center project and the Engineering Validation and Engineering Design Activities of the International Fusion Material Irradiation Facility as a BA activity are mainly being performed at the Rokkasho Fusion Institute. Nuclear fusion research development was taken over to the National Institutes for Quantum and Radiological Science and Technology (QST) established in April 2016.
10. **The Center for Computational Science & e-Systems** performs research on advanced simulation technology and on basic technology in computational science, and also operates and maintains computer systems. These efforts are mainly conducted at the Nuclear Science Research Institute and the Kashiwa Office.
11. **The Integrated Support Center for Nuclear Nonproliferation and Nuclear Security** plays an active role in technology development in the field of nuclear nonproliferation and nuclear security in international organizations, such as IAEA, and each country, activities to contribute nuclear material management and peaceful uses on ensuring transparency, and policy research. And ISCN continues human capacity development support projects which contribute the capacity building in Asian countries. These efforts are carried out mainly at the Head Office and the Nuclear Science Research Institute.

## R&D Institutes/Centers of JAEA

# 1 Research and Development Related to the Accident at TEPCO's Fukushima Daiichi NPS

## Aiming to Provide Research and Development Results to Promote Environmental Recovery, Early Repatriation, and Decommissioning

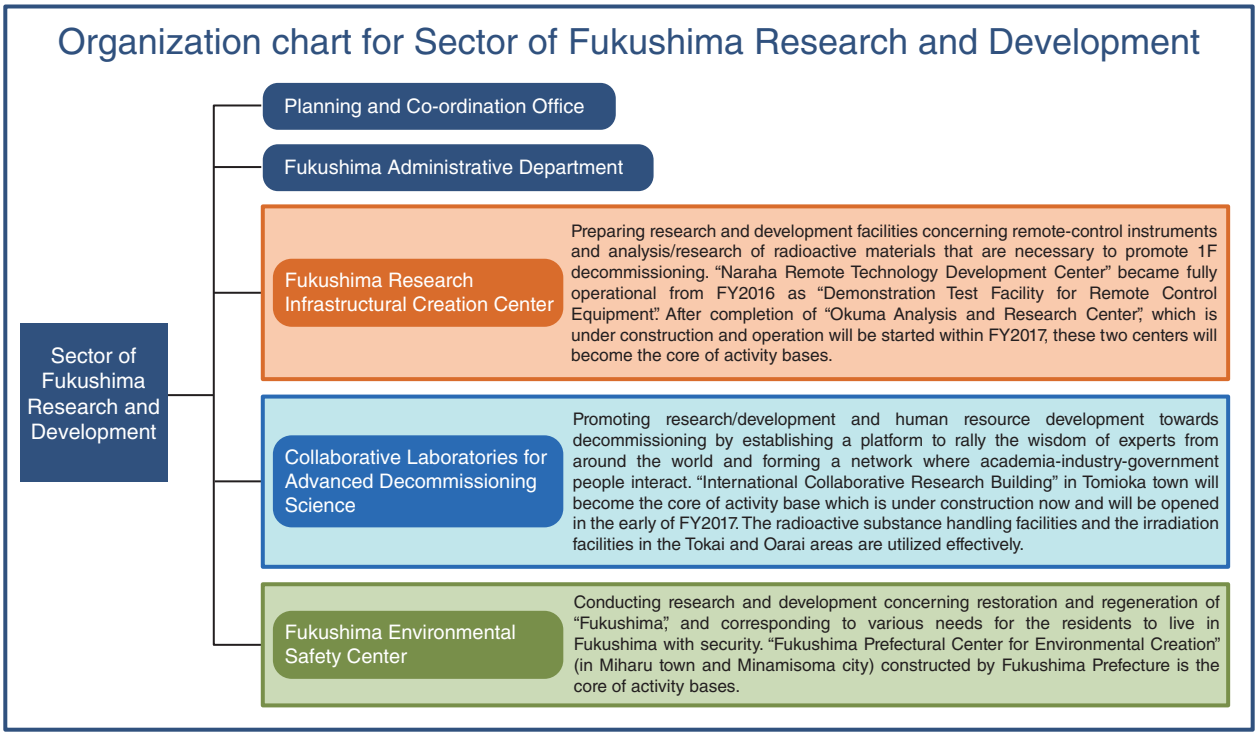


**Fig.1-1 Organization of Sector of Fukushima Research and Development (as of October 2016)**

### Core organization and activity bases for R&D related to the accident at the TEPCO's Fukushima Daiichi NPS (1F)

As a public institution created by the Basic Act on Disaster Control Measures after The Great East Japan Earthquake in March 11, 2011, we have conducted R&D related to the accident at 1F and responded to various actions such as radiation measurement. These activities have been presented in annual reports published from 2012 to 2015. In the 2015 report, we noted that we had organized a Sector of Fukushima Research and Development as a core organization related to 1F (Fig.1-1) and that activity bases were being developed. Such bases are taking shape as of 2016 (Fig.1-2).

### Development of essential R&D bases to promote the decommissioning of 1F

The Fukushima Research Infrastructural Creation Center is establishing two essential R&D bases to promote the decommissioning of 1F. These bases will assume roles in the preparation for removal of fuel debris from nuclear reactors and in the treatment and disposal of radioactive wastes generated by the decommissioning work.

The first facility for R&D is the Naraha Remote Technology Development Center in Naraha town. The Research-management Building and Mock-up Test Building were completed in September 2015 and February 2016, respectively, and the center became fully operational in FY2016. The second facility for R&D is the Okuma Analysis and Research Center in Okuma town, which is now under construction.

The Naraha Remote Technology Development Center serves primarily to promote the decommissioning of 1F based on the Mid-and-Long-Term Roadmap (Fig.1-3) formulated by the Inter-Ministerial Council for Contaminated Water and Decommissioning Issues as well as improvement of science and technology to support the decommissioning, enhancement of the safety base, and community symbiosis. To promote the decommissioning of 1F, we have developed a virtual-reality system that simulates work-area conditions in 1F; this system will be used to check work plans prior to commencing operation and to train workers and operators of remote-controlled equipment to study work plans and secure worker safety.

The Okuma Analysis and Research Center conducts analysis and research of radioactive materials generated from 1F, such as radioactive waste and debris samples obtained after the removal of fuel debris from nuclear reactors. The design of this facility proceeds based on such policies as the Technical Strategic Plan formulated by the NDF and the operation schedule outlined in the Mid-and-Long-Term Roadmap. Construction of the Administrative Building for the main facilities (which consist of the Administrative Building, Laboratory-1, and Laboratory-2) started in FY2016. This building will commence operation in FY2017.

### Establishment of a platform for rallying the wisdom of experts from around the world to promote the development of an R&D base for accelerating decommissioning work and addressing challenges

The Collaborative Laboratory for Advanced Decommissioning Science (CLADS) was established as an R&D center for decommissioning reactors in the Tokai area in April 2015. To accelerate this decommissioning research, experts must share their understanding of current requirements and anticipated future problems and R&D must be enhanced from basic to practical use. CLADS forms an interacting human resource network of universities, research institutions, and industries at home and abroad to meet the R&D challenge related to decommissioning reactors and promote human resource development by industry, academia and government. The International Collaborative

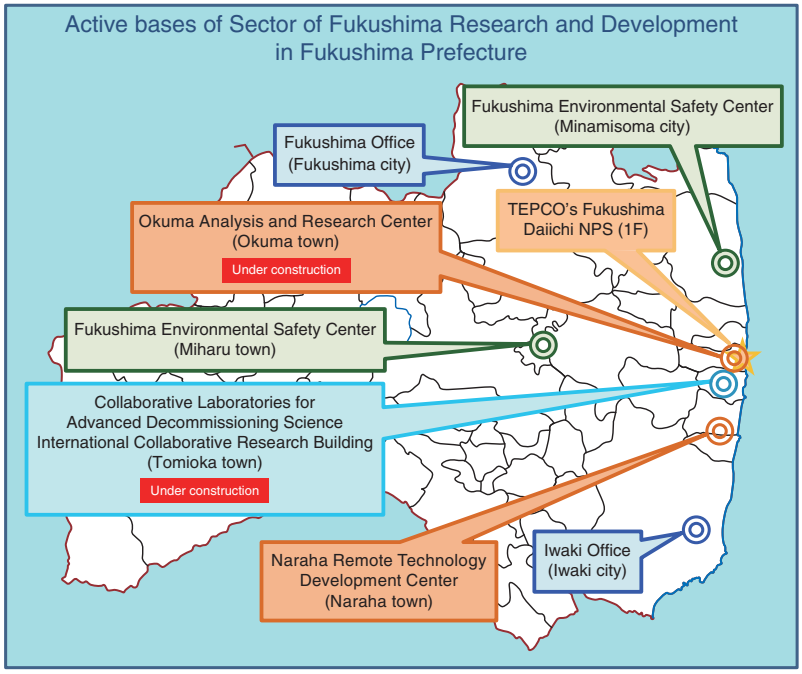


**Fig.1-2 Location of activity bases related to the Sector of Fukushima Research and Development in Fukushima Prefecture (as of October 2016)**
The Fukushima Research Infrastructural Creation Center established the Naraha Remote Technology Development Center as a base for research. The Research-management Building and Mock-up Test Building were completed in September 2015 and February 2016, respectively. Construction will soon commence on the "Administrative building" of the "Okuma Analysis and Research Center" in Okuma Town; in addition to the Administrative building, the main facilities will include two laboratories labeled "Laboratory-1" and "Laboratory-2." The Administrative building will commence operation in FY2017. The Collaborative Laboratory for Advanced Decommissioning Science (CLADS) is constructing an International Collaborative Research Building in Tomioka Town, which will be the core of R&D for reactor decommissioning after its opening in early FY2017. The Fukushima Environmental Safety Center is located at the Fukushima Prefectural Center for Environmental Creation in Miharu Town and Minamisoma City and serves as the base institute constructed by Fukushima Prefecture; it shares facilities with Fukushima Prefecture and the National Institute for Environmental Studies (NIES), and progresses with research and development in cooperation with these institutions.

Research Building (tentative name) is under construction in Tomioka town in Fukushima Prefecture as a base institute for gathering the wisdom of experts from home and abroad; it will be completed by the end of FY2016 and will be opened in the early part of FY2017.

Regarding experiment and research using actual nuclear and radioactive materials, we conduct R&D at handling and irradiation facilities in the Tokai and Oarai areas. CLADS has achieved various research results; we have devised an approach for predicting the melt progression of nuclear-fuel debris (an amorphous mixed oxide consisting of melted and hardened material from both the nuclear fuel in the reactor-pressure vessel (RPV) and the core structure) using a simulation model (Topic 1-1); and we are analyzing the concentration of each element under segregation and distribution of nuclear and core-structural material in nuclear fuel debris from outside of the RPV using laser-induced breakdown spectroscopy (Topic 1-2).

Beginning in FY2017, we will conduct collaborative research and information exchanges with universities, research institutes, and industries at home and abroad, utilizing our own facilities, with the International Collaborative Research Building (in Tomioka town) constituting a core component. In the mid- and long-term, we are also promoting research on decommissioning 1F based on policies such as the Technical Strategic Plan; this is done in accordance with the on-site requirements and in cooperation with the Fukushima Prefecture, the International Research Institute for Nuclear Decommissioning (IRID), and the NDF.

## R&D related to the decommissioning of 1F based on our knowledge and technical skill

We are Japan's sole comprehensive R&D institute in the field of nuclear energy and we have knowledge and technical skill in various subjects. Annual R&D results on the decommissioning of 1F based on such knowledge and technical skill are presented.

We have developed a cutting technique based on remote operation of a plasma jet, and confirmed this technique's utility in flooded vessels and output enhancement that enables to cut and crush thickly aggregated ceramics (such as nuclear-fuel debris) (Topic 1-3).

We have conducted simulation assessment using supercomputers to elucidate the core-melting procedure in severe accidents and developed a technique for calculating the possible melt-relocation behavior that may occur in actual accidents (Topic 1-4).

In order to clarify the mechanism of radioactive cesium (Cs) deposition onto the RPV structural material, we have determined that radioactive Cs may form chemical compounds by interaction with not only silicon but also iron in the carbon steel; our results suggest that once deposited, radioactive Cs can re-vaporize when its temperature rises (Topic 1-5).

Evaluation of the soundness of containers used to stably preserve the spent radioactive Cs removed from the contaminated water of 1F showed that adsorption vessels containing zeolite decreased the possibility of localized corrosion occurring during long-term storage (Topic 1-6).

Pyrochemical-reprocessing technologies is usually used as a reprocessing technology of the spent fuel in the reprocessing plant. We studied the applicability of this technology to a candidate treatment method for the 1F. Through this study, new (improved) chlorination method was developed. We developed a new chlorination method as a pretreatment technology. The entire quantity of uranium (U) was successfully converted into uranium tetrachloride ($UCl_4$) and separated by distillation at a lower temperature than before. We confirmed that this method is applicable for processing the nuclear-fuel debris in principle (Topic 1-7).

## Preparation of R&D-activity bases related to environmental recovery in Fukushima

To proceed with the activities outlined in the Basic Guidelines for Fukushima Reconstruction and Revitalization (Cabinet Decision, July 2012) and the Fukushima Prefecture Center for Environmental Creation Policy for Medium- and Long-term Initiatives (formulated by the Fukushima Prefectural Center for Environmental Creation's Management Strategy Conference), the Fukushima Environmental Safety Center has researched and developed technologies related to environmental recovery for the safety and security of residents. The Fukushima Environmental Safety Center is located at the Fukushima Prefectural Center for Environmental Creation (in Miharu Town and Minamisoma City) and was created by Fukushima Prefecture as a base institute. It shares its facilities with Fukushima Prefecture and the National Institute for Environmental Studies (NIES) and conducts research and development in cooperation with these bodies. In concrete terms, the Fukushima Environmental Safety Center in Miharu town serves four functions: monitoring, research, information collection/dissemination, and education/training/communication.

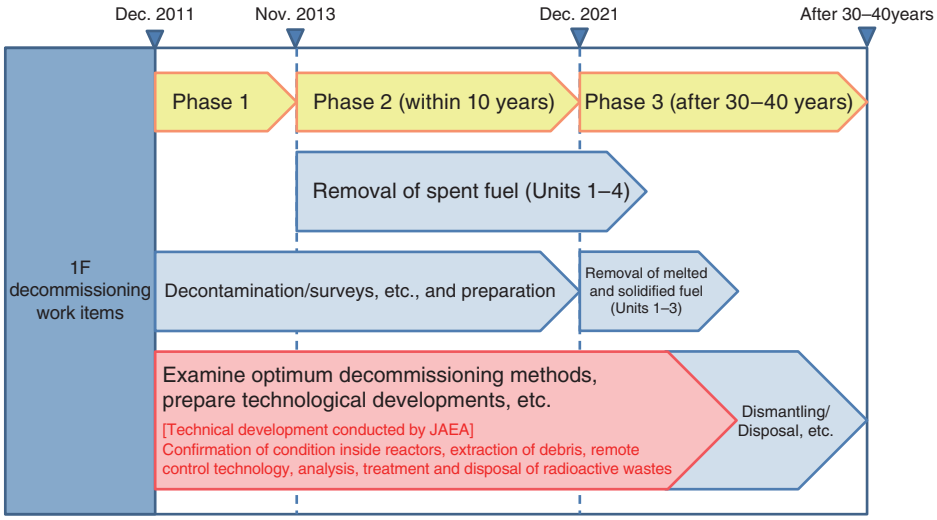


[Source] Reference to current efforts (as of March 2015) at the Fukushima Daiichi Nuclear Power Plant for reactor decommissioning and contaminated water measures–Fukushima Council Secretariat (addendum)

**Fig.1-3 Outline of the roadmap for 1F-decommissioning work**
We conduct R&D with a view to secure and train human resources based on policies such as the Technical Strategic Plan formulated by the Nuclear Damage Compensation and Decommissioning Facilitation Corporation (NDF) and adopt a medium- to long-term perspective according to on-site requirements. By providing technical support to the decommissioning site, we will contribute to achieving highly safe and efficient early decommissioning while enhancing the safety of nuclear energy.

We conduct R&D on radiation-measurement technology, the migration behavior of radioactive Cs in the environment in watershed areas from forests to rivers (i.e., environmental dynamics), and rational soil-removal methods and reuse strategies for the removed contaminated soil. The Fukushima Environmental Safety Center in Minamisoma city serves the function of monitoring the vicinities of nuclear power plants. We perform research and safety monitoring in cooperation with the Beach Local Agriculture Reproduction Research Center and the Nuclear Emergency Response Operations Facility (Offsite Center), and develop advanced radiation-measurement technologies at this facility.

The Fukushima Environmental Safety Center assumes a core role in studying environmental recovery. Other sectors and bases also conduct ambitious research in this field. Our full results in this field are described below.

## Contributing to the safety of residents through research on environmental recovery

We promote technology for visualizing the distribution of radioactive Cs using unmanned helicopters over a widespread area that includes forests. We also support the development of a visible and highly accurate radiation-dose map that cancels out the influence of the surroundings (Topic 1-8). For the purpose of investigating the necessary calibration condition of detectors for accurate measurement of the doses in the environment, the influence of the incident direction of radiation in the dose-rate measurement was analyzed using the particle and heavy-ion transport-code system (PHITS) (Topic 1-9). It was clarified that radioactive Cs in the Fukushima environment was mostly distributed up to 5 cm from the surface of the ground. We evaluated the relationship between the distribution of radioactive Cs and the air dose rate (Topic 1-10).

The radioactive Cs concentration in the stems of deciduous broad-leafed trees was measured to understand how Cs was distributed in the forest (Topic 1-11). Since this distribution is required to restart the forestry industry, we conducted detailed air-dose-rate measurements in a mountainous catchment contaminated by radioactive Cs from 1F to characterize the spatial variation of deposition in a mountainous forest with complex landforms and investigate the difference in deposition due to landform and altitude (Topic 1-12).

We conducted research to determine the migration mechanism of radioactive Cs to reduce burden of management of the removed soil by decontamination and investigate rational soil-removal methods and reuse strategies utilizing the results of the research. Since the establishment of a stable management method for the enormous amount of contaminated soil waste accumulated by stripping the topsoil for decontamination and the development of a method for reducing the waste volume are strongly desired, we promote both an experimental approach (Topic 1-13) and a scientific-calculation approach (Topic 1-14) to determining the adsorption/desorption mechanism of radioactive Cs to clay minerals.

To suppress the migration of radioactive Cs from forests to the life zones, polyelectrolytes (which are polymers having electric charges) and clay minerals are used and the migration of the radioactive Cs is controlled with these minerals through natural sources such as rainfall and rainwater runoff (Topic 1-15). The treatment method, that after once remove the surface soil contaminated by the accident of the 1F, the removed soil was disposed in the same place and covered with clean soil, can guard against direct radiation exposure. This method also showed that radiation Cs did not moved and amount of radiation reduced. These results showed that this method is effective for preventing groundwater pollution (Topic 1-16).

Since the analytical method for radioactive strontium-90 ($^{90}$Sr) is more complicated and time-intensive than that for radioactive Cs ($^{134}$Cs and $^{137}$Cs), an effective analytical method is required. To this end, we developed a wet-digestion system, an automatic chemical-separation system, and an automatic ion-exchange system to automate analytical work for isolating radioactive Sr. We automated analysis of incinerated agricultural, farm, and marine products (Topic 1-17).

The R&D bases of the Sector of Fukushima Research and Development gather the wisdom of experts from home and abroad and are primarily intended to promote environmental recovery, resident repatriation and the decommissioning of reactors by enhancing science and technology, and strengthening safety infrastructures and regional relationships. By conducting R&D and delivering results from Fukushima, we aim to promote the use of facilities and to establish an attractive international research base. By so doing, we hope to contribute to the revitalization of regional industry.

# 1–1 Evaluation of the Temperature Range of Melted Debris in the Reactor at the Nuclear Accident
## — The Influences of Pu and Zr upon the Melting Temperatures of (U, Pu, Zr)$O_2$ —

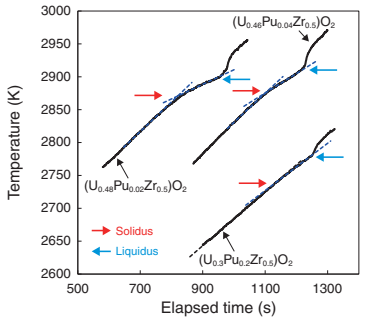


**Fig.1-4 Typical heating temperature curves of specimens of $(U_{0.5-y}\ Pu_y\ Zr_{0.5})O_2$**
The rate of temperature increase became low between the starting and ending points of the melting of the specimen. These points are determined as solidus and liquidus temperatures.

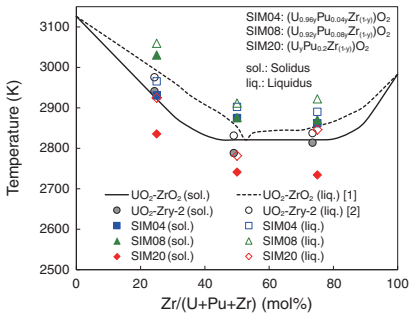


**Fig.1-5 Solidus and liquidus temperatures of sim-debris as functions of Zr-content**
In specimens containing similar Pu-contents, the melting temperatures of specimens with Zr contents approximately in the range from 50 to 75mol% seemed to be lower than those of other compositions.

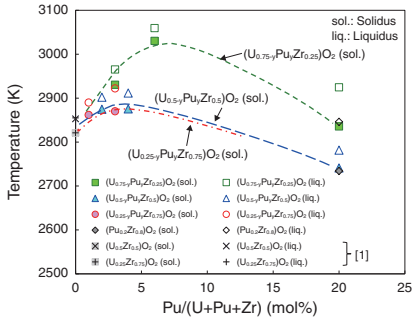


**Fig.1-6 Solidus and liquidus temperatures of sim-debris as functions of Pu-content**
The solidus and liquidus temperatures of (U, Pu, Zr)$O_2$ had a local-maximum value in the Pu-content range from 0 to 20mol%.

[1] Lambertson, W. A., Mueller, M. H., J. Amer. Cer. Soc., vol.36, issue 11, 1953, p.365-368.
[2] Kato, M. et al., Mater. Res. Soc. Symp. Proc., vol.1444, 2012.

As a part of the decommissioning plan for the reactors damaged at the TEPCO's Fukushima Daiichi NPS (which was the site of a severe accident), some strategies for removing debris from the reactors and storing it are being discussed. In these considerations, predicting the melt progression during the accident based on theoretical evidence and evaluating the current state of the debris based on its thermal and mechanical characteristics are necessary. The influences of Pu upon these characteristics are important for the prediction because subassemblies of uranium-plutonium mixed oxide (MOX) fuel were loaded into Unit 3 of the plant. Melting temperature is an important thermal characteristic for melt-progression analysis. In addition, it is important for predicting debris states because the central part of the debris is expected to have been in a molten state for a long time owing to its decay heat.

In this study, nine specimens of (U, Pu, Zr)$O_2$ with different chemical compositions were prepared as simulated corium debris (sim-debris). The melting temperatures of the specimens were measured by the thermal-arrest technique described as follows. The specimen was encapsulated in a tungsten capsule in vacuum. This capsule was heated at a constant rate by a high-frequency induction furnace. The temperature of the specimens were measured with a two-color pyrometer sighted on a black-body hole at the bottom of the tungsten capsule. Fig.1-4 shows typical heating-temperature curves of specimens.

The solidus and liquidus temperatures of all specimens are shown in Fig.1-5 as functions of the Zr-content. Examining specimens containing similar Pu-contents in Fig.1-5, the melting temperatures of those containing between approximately 50mol% and 75mol% of Zr seemed to be lower than those with other compositions. From this, it was found that Zr had a similar influence on the melting temperatures of both (U, Pu, Zr)$O_2$ and (U, Zr)$O_2$.

The solidus and liquidus temperatures are shown in Fig.1-6 as functions of Pu-content. The temperatures of (U, Pu, Zr)$O_2$ were higher than those of (U, Zr)$O_2$ at the same Zr-content when the Pu-content was less than approximately 10mol%. In contrast, these temperatures were lower than those of (U, Zr)$O_2$ when Pu-content was 20mol%. From these results, it was found that the solidus and liquidus temperatures of (U, Pu, Zr)$O_2$ had a local maximum value in the Pu-content range between 0 to 20mol%. The results obtained in this study are expected to contribute to the prediction of reactor-core situations and severe-accident analysis.

This topic includes a part of the results obtained under the research program entrusted to the International Research Institute for Nuclear Decommissioning (IRID) by the Agency for Natural Resources and Energy, Ministry of Economy, Trade and Industry of Japan (METI).

**Reference**

Morimoto, K. et al., The Influences of Pu and Zr on the Melting Temperatures of the $UO_2$–$PuO_2$–$ZrO_2$ Pseudo-Ternary System, Journal of Nuclear Science and Technology, vol.52, issue 10, 2015, p.1247-1252.

# 1–2 Laser Remote Analysis of Nuclear Fuel Debris

## — Evaluation of Uranium Spectra by Laser Induced Breakdown Spectroscopy (LIBS) —

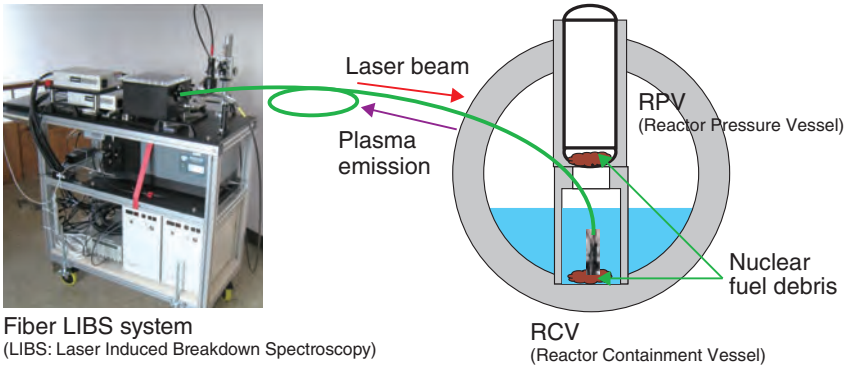


**Fig.1-7 Image of the fiber LIBS system**
The laser and spectrometer are set up in the low-radiation environment outside of a RCV. The laser beam is delivered to the nuclear-fuel debris through radiation-resistant optical fiber and focused onto the debris by the focusing probe. The plasma emission from the debris is sent back to the spectrometer through the same fiber and measured as spectra.

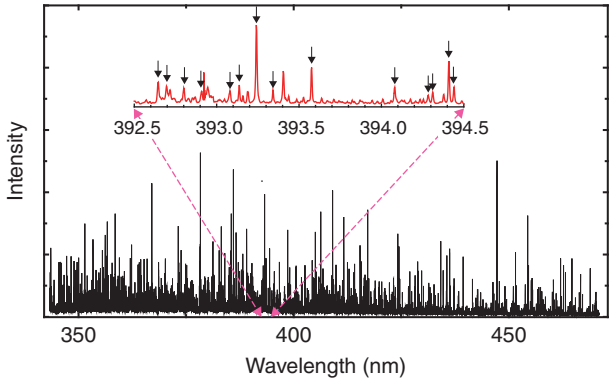


**Fig.1-8 U spectrum measured by the LIBS**
The black line shows the U spectra in the wavelength range of 350–470 nm and the red show those in the range of 392.5–394.5 nm. The analyzed and the assigned U-emission lines are shown with arrows.

To safely retrieve, process, and dispose of the nuclear-fuel debris from the accident at the TEPCO's Fukushima Daiichi NPS, it is very important to know state of the debris itself. One piece of information is the elementary composition of the debris. However, in an extremely high radiation environment, the nuclear reactor containment vessel (RCV) cannot be approached, electronic equipment cannot be employed, and the debris cannot be analyzed *in situ*.

Therefore, we are developing a fiber LIBS system (Fig.1-7). This system, which uses a laser and spectrometer, is set up in a low-radiation environment. The laser beam delivered through the fiber is focused onto the surface of the debris in the reactor vessel by a focusing probe. The plasma emission generated by laser irradiation is collected into the same optical fiber, delivered to the spectrometer, and measured as spectra. These spectra are analyzed and information concerning the elementary composition of the debris is evaluated. In this fashion, the radiation exposure to workers and electronic equipment is avoided.

Fuel debris is mainly composed of nuclear fuel (uranium (U) and plutonium (Pu)), actinides, fission products, and cladding tubes (zirconium (Zr)). Concrete (calcium), stainless steel (iron, nickel, and chrome) in the structural materials, and the like may also be included in debris. To distinguish nuclear fuel materials, such as U, from the other elements, detailed spectral data for these materials must be collected.

For this reason, using the LIBS, the U spectrum in the 350–470 nm region (Fig.1-8) was measured and the relative spectral intensities and absolute wavelengths were calibrated. For elemental composition analysis of these results, the 247 atomic lines and 294 ion lines of U were assigned and selected as useful.

To contribute to safe retrieval, processing, and disposal of nuclear-fuel debris, it is necessary to compile reliable spectral databases of U, Pu, Zr, and the other elements of the core-structure materials and the like.

The present study contains part of the result of the "Development of laser remote analysis for next generation nuclear fuel and applied study by MOX sample" project entrusted to the JAEA by the Ministry of Education, Culture, Sports, Science and Technology of Japan (MEXT).

**Reference**

Akaoka, K. et al., Measurement of Uranium Spectrum using Laser Induced Breakdown Spectroscopy –High Resolution Spectroscopy (350-470 nm)–, JAEA-Research 2015-012, 2015, 48p. (in Japanese).

# 1–3 Development of a Cutting Technique for Core-Structural Materials and Fuel Debris
## — Cutting and Crushing of Core-Structural Materials and Fuel Debris with a Plasma Jet —

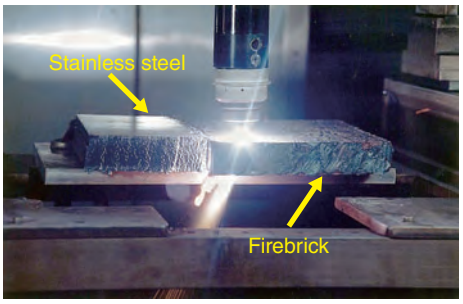


**Fig.1-9 Metal- and nonmetal-cutting with a plasma jet**
Plasma-jet cutting of stainless steel and firebrick.

**Fig.1-10 Stainless steel after cutting**
State of the stainless steel cut underwater by a plasma jet.

| Place | In the water | In the air |
|---|---|---|
| Gass flow ($cm^3/s$) | 650 | 450 |
| | 750 | |
| Stand off (mm) | 5 | 15 |
| | 10 | 20 |

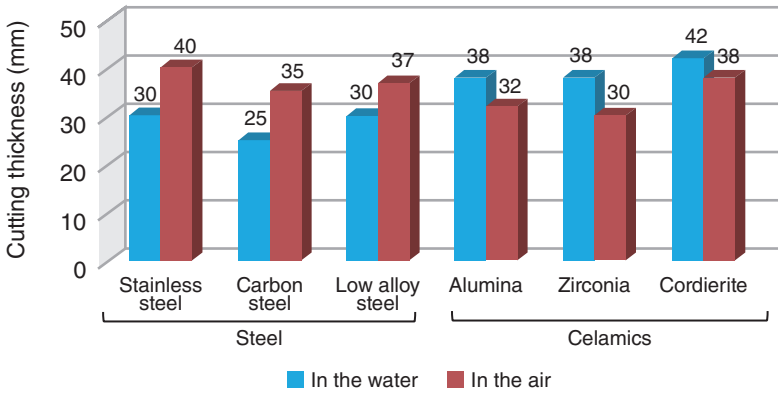


**Fig.1-11 Cutting Ability of the plasma jet**
Cutting ability of the plasma jet in water and air for steel and ceramics.

The TEPCO's Fukushima Daiichi NPS (1F) lost its core-cooling function during the Great East Japan Earthquake of 2011, leading to core meltdown. Removing the molten fuels and core internal materials for the decommissioning of 1F is necessary; however, it is assumed that the original shapes of the core's internal materials were not retained and the interior of the reactor is a very narrow space. Choosing cutting technologies appropriate to this situation is necessary for safe and certain decommissioning.

Plasma-jet cutting technology (max output current: 250 A) is being developed for the dismantling of nuclear facilities at the Oarai Research and Development Center. The plasma jet was developed to cut steel materials and concrete. It can be applied to not only metal but also conductive nonmetal. It can also crush firebricks by thermal shock (Fig.1-9). Plasma-jet cutting technology is applicable for removal of the debris. A plasma-jet torch (max output current: 600 A) was produced for this application. This torch is available for the cutting of thick core-internal materials in water. Its ability to cut debris and core internal material has been confirmed.

This technology is capable of cutting for more than 30 min underwater with use of the torch (tip diameter: 5.0 mm; restriction ratio: 3.0; output current: 600 A). It can cut steel materials 40-mm thick in air and 30-mm thick underwater, cut ceramics 38-mm thick in air and 42-mm thick underwater (Figs.1-10 and 1-11), and crush ceramics 50-mm thick underwater.

In future, we will conduct a cutting examination and a performance evaluation to confirm the jet's applicability to 1F. We will also undertake an examination of the fuel-debris-takeoff system, which combines the cutting tool with remote-control technology. These results will be used to determine decommissioning measures for 1F.

**References**

Shoji, T., Fukui, Y. et al., Development of a Cutting Technique of Core Structural Materials and Fuel Debris –Applicability Test of the Plasma Jet Cutting Technique–, JAEA-Technology 2015-035, 2016, 70p. (in Japanese).
Tezuka, M., Fukui,Y. et al., The Development of Thermal and Mechanical Cutting Technology for the Dismantlement of the Internal Core of Fukushima Daiichi NPS, Journal of Nuclear Science and Technology, vol.51, issues 7-8, 2014, p.1054-1058.

# 1–4 Elucidation of the Core-Meltdown Procedure in Severe Accidents using Supercomputers

## — Development of A Numerical Simulation Method for Evaluating the Influences of Chemical Reactions of Core Materials —

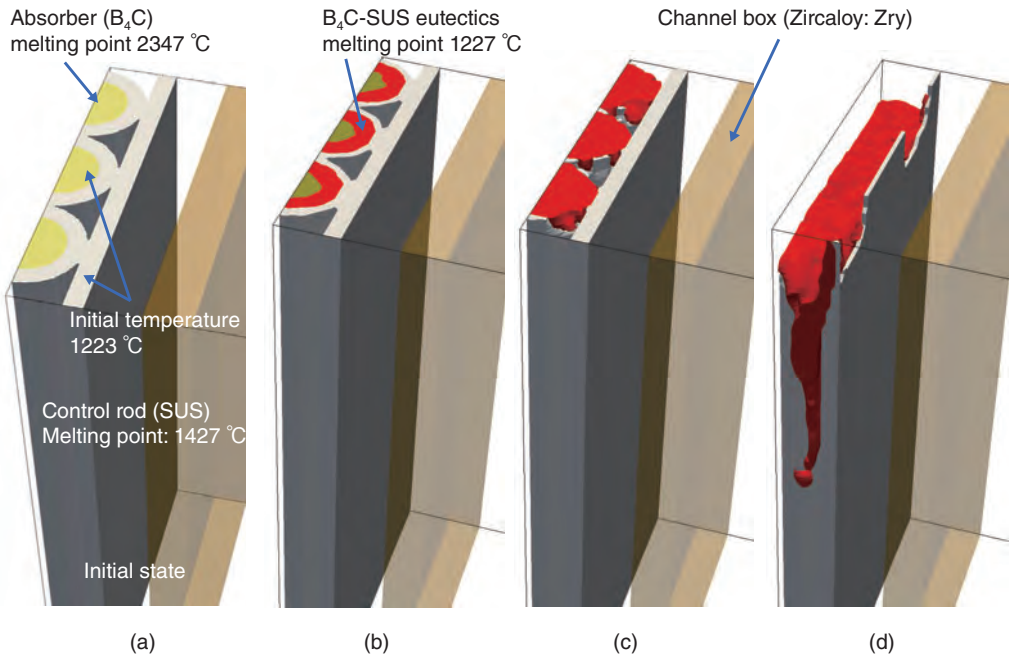


**Fig.1-12 Growth of the liquid phase (red region) induced at the interface between $B_4C$ inside the control rods (yellow region) and SUS, as well as its melt-relocation behavior**
(a) We perform calculations with the developed model using a simplified system consisting of a part of the reactor core, i.e., a control rod and a channel box. (b) When the $B_4C$ and SUS reach a given temperature, a liquid phase will be formed at the interface by the eutectic reaction. (c) The liquid phase gradually spreads with increasing temperature. (d) Eventually, the melt created by the eutectic reaction relocates downward under gravity.

In the accident at the TEPCO's Fukushima Daiichi NPS, the meltdown is believed to have occurred in the reactor pressure vessel (RPV), after which molten fuel reached the lower head. Although it is very important to understand the distribution of molten fuels distribute in the RPV in detail, this is quite difficult to measure because of high radiation levels. In this case, a numerical simulation is useful. However, existing severe-accident-simulation methods that treat meltdowns have been insufficiently validated in terms of their assumptions and numerical models. Therefore, we face the problem that information concerning the relocation paths and circumstances of the debris distribution in the RPV's lower head cannot be obtained with sufficient accuracy. Thus, to elucidate melt behavior in severe accidents, we have been developing a new simulation method, according to which the core-meltdown process and its pathway can be evaluated using supercomputers by eliminating assumptions and simplifying models.

In the reactor core during severe accidents, chemical reactions occur at the interface between the control rods (stainless steel or SUS) and the absorber (boron carbide or $B_4C$). From previous experiments, it is known that at temperatures beyond a certain threshold, materials melt. Because this threshold is much lower than the melting points of SUS and $B_4C$, our method must consider the growth of the liquid phase and its downward-relocation behavior. Since a method that accounts for the complicated liquid-phase formation has yet to be established, we develop a new liquid-phase-growth model that is suitable our numerical method.

As shown in Fig.1-12, we confirmed that the method could treat the following phenomena: 1. Liquid-phase formation at the interface between the control rod and the absorber; 2. Growth of the liquid phase; 3. Downward relocation of the liquid phase. Therefore, it is possible to calculate the melt-relocation behavior that may occur in actual accidents.

Toward the elucidation of the molten-fuel distribution in the RPV or PCV, we will check the validity of the model through comparison with experimental results and implement oxidation and radiation models. We will perform a more accurate simulation of core-melt-relocation behaviors in the near future.

**Reference**

Yamashita, S. et al., Development of Numerical Simulation Method for Melt Relocation Behavior in Nuclear Reactors: Validation of Applicability for Actual Core Support Structures, Proceedings of 24th International Conference on Nuclear Engineering (ICONE 24), Charlotte, North Carolina, USA, 2016, ICONE24-60453, 5p., in DVD-ROM.

# 1–5 Behavior of Radioactive Cesium Deposited in the Nuclear Reactor
## — Investigation of Cesium-Deposition Behavior onto Stainless Steel —

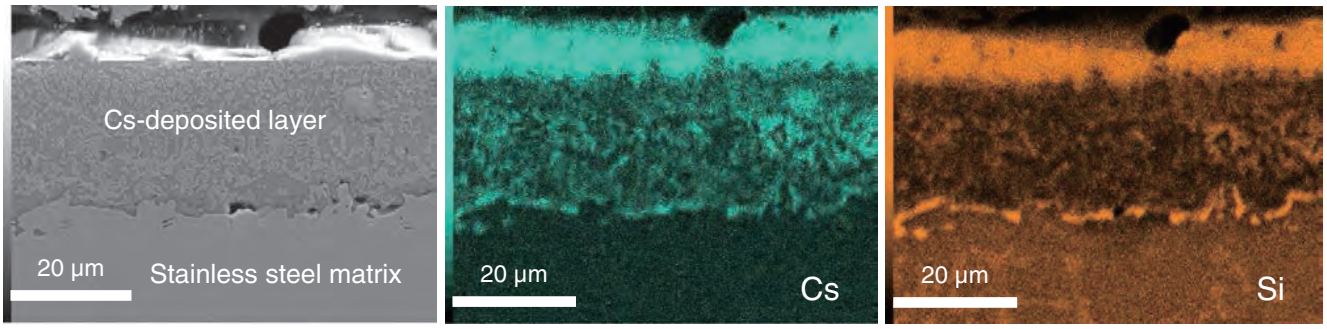


Secondary electron image | Characteristic X-ray image of Cs | Characteristic X-ray image of Si

**Fig.1-13 Microstructural cross-section of Cs deposited onto stainless steel**
The formation of a cesium silicate is suggested by cross-sectional analysis of stainless steel exposed to CsOH vapor. The congruent distributions of Cs and Si are also found in the interface region between the Cs-deposition layer and the stainless-steel matrix, which is of concern for Cs decontamination.

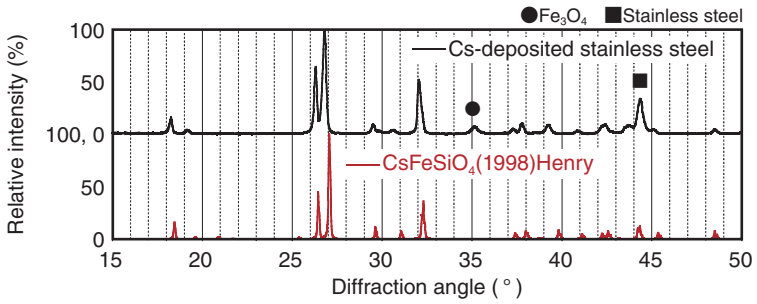


**Fig.1-14 XRD patterns of Cs-chemisorbed stainless steel and $CsFeSiO_4$**
The results of XRD pattern and elemental analysis indicate that $CsFeSiO_4$ is present in the Cs-deposition layer over stainless steel.

Radioactive cesium (Cs) is expected to be one of the main radiation sources during fuel-debris retrieval at the TEPCO's Fukushima Daiichi NPS. To manage workers' radiation doses, it is necessary to know where the Cs is deposited, how the deposited Cs can be removed, how much Cs may be included in dust generated during removal, how much Cs can be migrated to dismantled wastes, and so on. To predict these behaviors, knowledge on the deposition behavior of Cs onto structural materials is essential. However, there is little information on such behavior. Therefore, our basic study has started to clarify mechanism of Cs deposition.

Cesium hydroxide (CsOH) is predicted to be one of the main Cs chemical species released during a severe accident, and large amounts of stainless steel are used as a structural material within a nuclear-reactor pressure vessel. Therefore, we have investigated Cs deposition onto stainless steel using simulation experiments in which stainless steel samples are exposed to CsOH vapor at 800 °C and 1000 °C in an argon atmosphere that includes hydrogen and steam. The Cs-deposited samples were then examined using secondary electron microscopy/energy dispersion spectroscopy (SEM/EDS) and X-ray diffractometry (XRD) to identify Cs-reaction products.

Fig.1-13 shows that Cs is located congruently with silicon (Si), which is present as a minor component of stainless steel. Fig.1-14 indicates that the XRD pattern of the Cs-deposition surface agrees well with that of $CsFeSiO_4$. Elemental analyses by EDS also indicate that the concentrations of Si and iron (Fe) are almost the same as that of Cs. Thus, it is verified that $CsFeSiO_4$ is formed by the interaction between CsOH vapor and stainless steel. Furthermore, we found that the deposited amounts did not always increase with increasing temperature and we suggested that Cs deposits can re-vaporize under some experimental conditions.

We will continue Cs-deposition tests under varying parameters such as atmosphere. From these data, we will estimate the amount of Cs deposited onto structural materials. In addition, we will examine the dissolution property of the deposited Cs for water and the detachability, which can help us develop removal methods for the deposited Cs and take measures to protect against scattering dusts.

**Reference**

Di Lemma, F. G., Nakajima, K. et al., Surface Analyses of Cesium Hydroxide Chemisorbed onto Type 304 Stainless Steel, Nuclear Engineering and Design, vol.305, 2016, p.411-420.

# 1–6 Integrity Evaluation of a Storage Vessel Containing Spent Cesium Adsorption Material

## — Investigating the Possibility of Localized Corrosion of the Vessel Material under Irradiation —

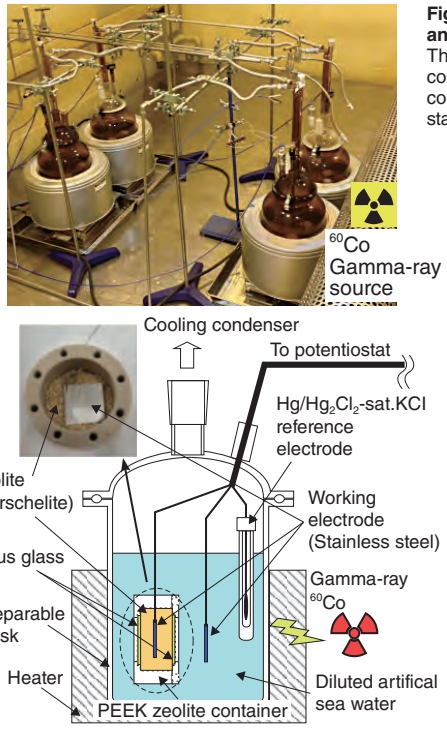


**Fig.1-15 The appearance of the test equipment in the gamma-irradiation room and a schematic of the electrochemical-testing cell**
The stainless-steel specimen was put in contact with the packed zeolite using a container of polyether ether ketone, which is highly resistant to both radiation and corrosion; the zeolite was separated from the test solution using glass filters. The stainless steel un-contacted with zeolite was used in the bulk water for comparison.

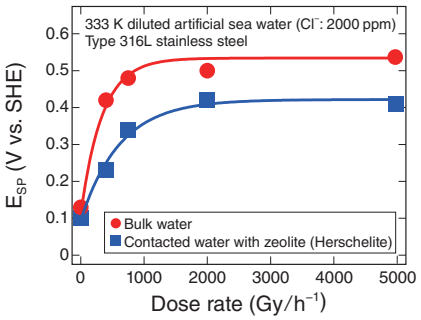


**Fig.1-16 The relationship between the dose rate and the spontaneous potential, $E_{SP}$, of type 316L stainless steel in the bulk water and the system in contact with zeolite**
The $E_{SP}$ value under irradiation, which can also be defined as the steady-state rest potential, increased with an increase in the dose rate. This tendency suggests the possibility that localized corrosion increases under irradiation, whereas this increase was suppressed by contact with zeolites.

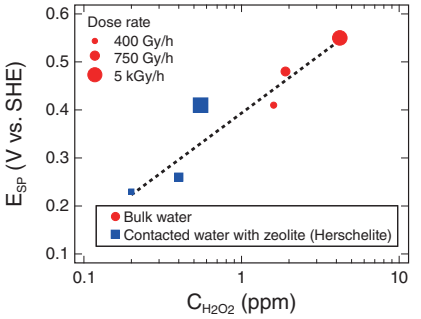


**Fig.1-17 The relationship between the spontaneous potential $E_{SP}$ of type 316L and hydrogen peroxide concentration $C_{H2O2}$ in the bulk water and the water in contact with zeolites under irradiation**
The concentration of $H_2O_2$ in the bulk water under irradiation also increased with the increase in the dose rate. This increase was suppressed in systems that were in contact with zeolites, owing to the zeolites' decomposition of $H_2O_2$. A clear relationship was observed between $E_{SP}$ and the $H_2O_2$ concentration. The contact with the zeolites caused the increase in $E_{SP}$ under irradiation to be suppressed.

A cesium (Cs)-adsorption system was installed in the TEPCO's Fukushima Daiichi NPS after it was damaged by the tsunami in 2011. This Cs-adsorption system removes radioactive Cs from the contaminated water using adsorption vessels made of KURION, which contains zeolites (Herschelite).

The spent Cs-adsorption vessels were stored in a provisional storage facility; their insides were washed with fresh water and drained to remove all seawater components. However, if the spent Cs-adsorption vessels are stored for a long period, the stainless steel in these vessels may still undergo corrosion owing to the chloride ions ($Cl^-$) present in the water remaining in the vessel. In addition, the Cl-ion concentration in the water remaining in the vessel will increase because of water evaporation owing to the increase in the temperature inside the vessel, owing to the heat generated by the decay of radioactive Cs. Furthermore, hydrogen peroxide ($H_2O_2$) may be produced in the remaining water owing to the radiation from the adsorbed Cs; this would also increase the likelihood of the stainless-steel corrosion.

In this study, we performed electrochemical tests on stainless steel in zeolite-containing diluted artificial seawater under gamma-ray irradiation. This was done to investigate the effects of gamma-ray irradiation upon the spontaneous potential, $E_{SP}$, of stainless steel in systems in contact with zeolites as well as to study the effects of coexisting zeolites on the conditions that can cause the localized corrosion of the stainless steel.

The electrochemical tests were performed at the $^{60}$Co gamma-ray-irradiation facility at the Takasaki Advanced Radiation Research Institute of the Japan Atomic Energy Agency. Fig.1-15 shows a schematic diagram of the apparatus used for the electrochemical tests. The dose rate at the location of the electrochemical test apparatus was set to 400 Gy/h, 750 Gy/h, 2000 Gy/h, or 5000 Gy/h. These values were selected because they were close to the estimated value of the dose rate (755 Gy/h) at the bottom of the spent-Cs adsorption vessel (KURION), as calculated from the maximum amount of Cs adsorbed. Furthermore, these values allowed the effects of a large absorbed-dose rate (5000 Gy/h) to be evaluated. The distance from the $^{60}$Co radiation source was adjusted to achieve these dose rates.

Fig.1-16 shows the effects of the dose rate and contact with the zeolite upon $E_{SP}$. Under gamma-ray irradiation, $E_{SP}$ increased along with increase in the dose rate; this was true both in bulk water and in the system with coexisting zeolite. The $E_{SP}$ value in the system in contact with the zeolite under irradiation was less noble than that in bulk water unconnected with zeolite. Contact with the zeolite suppressed the increase in the potential under irradiation; this decreased the possibility of localized corrosion occurring during long-term storage.

Analyses of the water samples were performed after the gamma-ray-irradiation tests in order to determine the concentrations of $H_2O_2$ and DO in bulk water and in water samples that came in contact with zeolite. The value of $E_{SP}$ changed almost linearly with the logarithm of the $H_2O_2$ concentration. It can be seen that the increase in $E_{SP}$ under irradiation was primarily dependent upon the $H_2O_2$ concentration. Furthermore, it is clear that $E_{SP}$ decreased owing to an increase in the rate of decomposition of $H_2O_2$ in the case of the systems in contact with the zeolites. Accordingly, it can be surmised that the coexistence of zeolite can suppress the increase in the potential under irradiation (Fig.1-17).

Parts of this study were performed as a union member of the International Research Institute for Nuclear Decommissioning (IRID) in accordance with the Project of Decommissioning and Contaminated Water Management in the FY2014 supplementary budget from the Agency for Natural Resources and Energy, Ministry of Economy, Trade and Industry of Japan (METI).

**Reference**

Kato, C. et al., Localized Corrosion Behavior of Stainless Steel in the Diluted Artificial Sea-Water Contacted with Zeolite under Gamma-ray Irradiation, Nippon Genshiryoku Gakkai Wabun Ronbunshi (Transactions of the Atomic Energy Society of Japan), vol.14, no.3, 2015, p.181-188 (in Japanese).

# 1–7 Toward the Recovery of Uranium from Fuel Debris
## — Development of a Chlorination Method for Slightly Soluble Components —

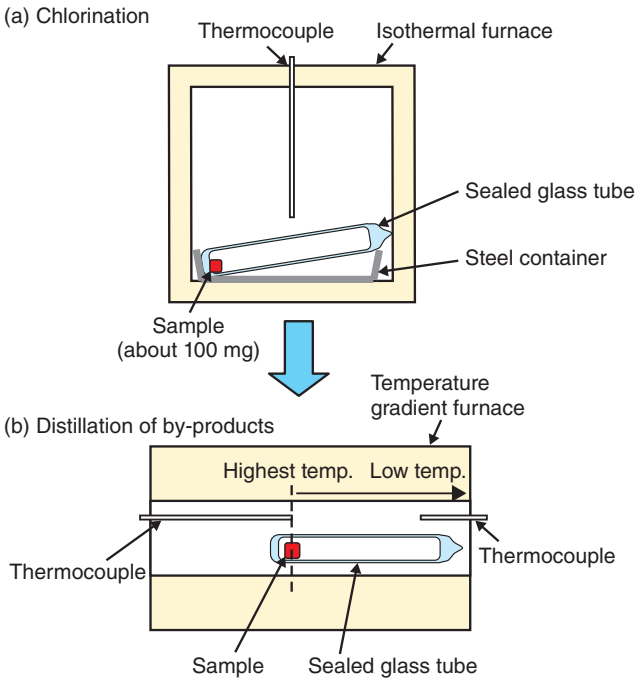


**Fig.1-18 Outline of a chlorination experiment with fuel debris from $MoCl_5$**
A mixture of $(U_{0.5}Zr_{0.5})O_2$ and $MoCl_5$ is sealed in a glass tube in vacuum. It is converted to chloride by homogeneous heating at 573–773 K and by-products are separated by distillation at 573 K under a temperature-gradient condition.

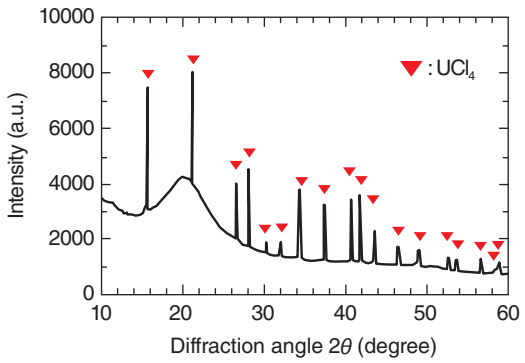


**Fig.1-19 XRD profiles of the product obtained from a reaction between $(U_{0.5}Zr_{0.5})O_2$ and $MoCl_5$**
Observed peaks were identified as tetragonal $UCl_4$ obtained by a chlorination reaction.

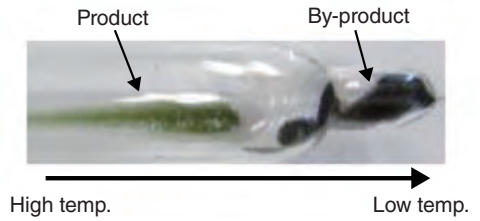


**Fig.1-20 Appearance of the product after separation of by-products**
By chlorination of $(U_{0.5}Zr_{0.5})O_2$, green $UCl_4$ was obtained as a product (left side in the figure), and $MoOCl_3$ and $ZrCl_4$ by-products were separated by distillation (right side in the figure).

As a result of the accident at the TEPCO's Fukushima Daiichi NPS, the treatment of fuel debris generated by solidification of melted fuels has been studied. One possible treatment option that has been proposed is the application of pyrochemical reprocessing technologies of spent nuclear fuels to treat fuel debris. According to the pyrochemical method, uranium and plutonium in spent fuels are separated from fission products and recovered to a cathode by electrolysis in a molten salt. A large issue with this method is the development of a pretreatment technique for converting fuel debris into chlorides.

Conventional chlorination techniques using chlorine gas over 873 K require the use of corrosion-resistant structural materials. In contrast, the chlorination technique using molybdenum pentachloride ($MoCl_5$) is expected to have advantages such as a lower reaction temperature, ease of handling the solid $MoCl_5$. By-products of this method can also be efficiently separated from chloride products by distillation.

In this study, we propose a new chlorination method of fuel debris using $MoCl_5$ and study the applicability of this method through basic experiments.

Using uranium–zirconium oxide solid solution ($(U_{0.5}Zr_{0.5})O_2$) powder and sintered pellets as simulated fuel debris, chlorination experiments with $MoCl_5$ were conducted and the reaction principle of uranium chlorination and separation of by-products by distillation (Fig.1-18) were confirmed.

Regarding the chlorination reaction, most uranium in the sample was successfully converted to uranium tetrachloride ($UCl_4$) at 573 K (for the powder) or 773 K (for the sintered particles) based on the following equation (Fig.1-19):

$$2(U_{0.5}Zr_{0.5})O_2 + 4MoCl_5 \rightarrow UCl_4 + ZrCl_4 + 4MoOCl_3$$

By-products of this reaction include $MoOCl_3$ and zirconium tetrachloride ($ZrCl_4$). These were successfully separated from $UCl_4$ by distillation at 573 K (Fig.1-20).

On the basis of these results, we proposed a new chlorination method for fuel debris using $MoCl_5$ and confirmed its applicability in principle.

These results were obtained in accordance with the project for development of the fuel debris characterization and treatment technologies as funded by the Agency for Natural Resources and Energy, Ministry of Economy, Trade and Industry of Japan (METI).

**Reference**

Sato, T. et al., Chlorination of $UO_2$ and (U, Zr)$O_2$ Solid Solution using $MoCl_5$, Journal of Nuclear Science and Technology, vol.52, issue 10, 2015, p.1253-1258.

# 1–8 Visualization of the Radioactive-Cesium Distribution using a New Compton Camera Mounted on an Unmanned Helicopter — Field Test of the Ce:$Gd_3(Al,Ga)_5O_{12}$ (GAGG) Scintillator Compton Camera —

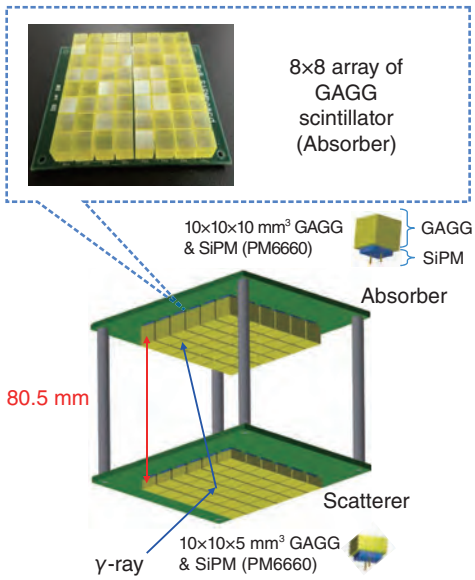


**Fig.1-21 New Compton camera using GAGG scintillators**
The new Compton camera has 2 layers of scatterers and absorbers comprising 8 × 8 arrays of GAGG scintillators and silicone photomultipliers for scintillator-signal processing. An increase in the GAGG scintillator array from 4 × 4 to 8 × 8 and expansion of the interlayer distance enhanced the detection efficiency and angular resolution, respectively.

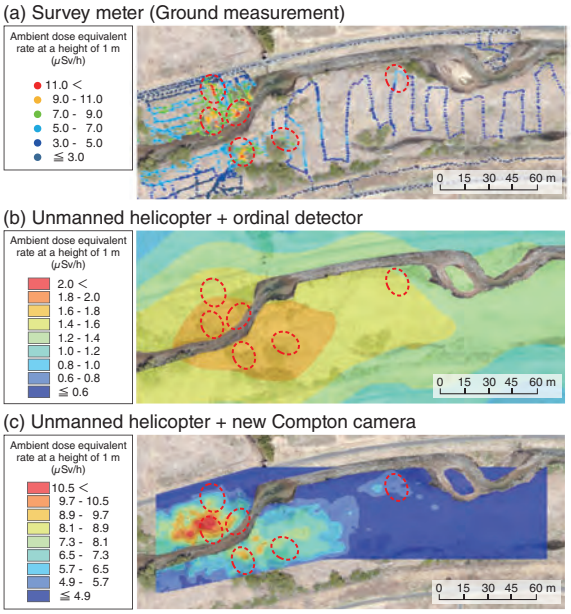


**Fig.1-22 Ambient dose-equivalent-rate map**
The ambient dose-equivalent-rate maps at a height of 1 m indicated the measured results using (a) the survey meter in the ground measurement, (b) the unmanned helicopter and the ordinal detector, and (c) the unmanned helicopter and the new Compton camera. To facilitate comparison, hot spots are indicated with red-dashed ellipses. The precise measurement performance of the new Compton camera was confirmed from the test results.

To accurately ascertain the situation of the wide area contaminated by the radioactive cesium (Cs) emitted following the accident at the TEPCO's Fukushima Daiichi NPS and to conduct efficient decontamination work, it is effective to use an unmanned helicopter to rapidly survey a wide area from the sky. However, difficulties were encountered in mounting an ordinal detector with a single scintillator in that its resolution was only approximately 80 m owing to its sensitivity to radiation from all directions.

Therefore, building upon the prototype Compton camera that was mountable on an unmanned helicopter and could measure the incidence direction of $\gamma$-rays, a new Compton camera (Fig.1-21) was developed here. This camera had four times as many detector elements as the prototype, with each comprising a Ce:$Gd_3(Al,Ga)_5O_{12}$ (GAGG) scintillator and a silicone photomultiplier. The resulting increase in the area of the cross-section owing to increase in the number of detector elements for each layer improved the sensitivity 5-fold. This enabled analysis to be conducted with sufficient statistical precision even after strict event selection for high positional resolution. Expansion of the interlayer distance made the solid angle of the 2nd layer's scintillator viewed from the 1st layer's one smaller than that of the prototype. This improved the angular resolution from 14 ° to 10 °.

In February 2015, we performed programming and hovering flights over the Ukedo riverbed in Namie, Fukushima Prefecture, during which the unmanned helicopter flew along a pre-planned comb-shaped path (50 min) and then hovered in various positions (15–20 min for each position), respectively. In the measurement, the helicopter position and measured $\gamma$-ray-event data were recorded. In the analysis, the Compton scattering angle was restricted to a small value by selecting the events with a small scattering energy, and under this condition, $\gamma$-ray events originating below the detector were selected. For the programming flight, the count-rate data obtained were converted into the ambient dose-equivalent rate. Based on the dose rate with position data, a map was produced by the interpolation method with the geographical information-system software. For the hovering flight, after selecting events whose summed scatterer and absorber energies were near the $^{137}Cs$ peak energy of 662 keV, a $\gamma$-ray image was obtained using the reconstruction software for the $\gamma$-ray-intensity distribution.

Fig.1-22(c) is the ambient dose-equivalent-rate map at a height of 1 m, as obtained from the programming flight. From this map, we confirmed that relatively small hot spots could be detected. Thus, rapid measurement of the ambient dose-equivalent-rate distribution over a wide area with a position resolution of about 10 m was realized using the new Compton camera.

The present study was sponsored by the Japan Science and Technology Agency (JST).

**Reference**

Shikaze, Y. et al., Field Test around Fukushima Daiichi Nuclear Power Plant Site using Improved Ce:$Gd_3(Al,Ga)_5O_{12}$ Scintillator Compton Camera Mounted on an Unmanned Helicopter, Journal of Nuclear Science and Technology, vol.53, issue 12, 2016, p.1907-1918.

# 1–9 Accurate Measurement and Evaluation of Environmental Dose Rates in Air
## — Dose-Rate Evaluation in the Environment using Monte Carlo Simulation —

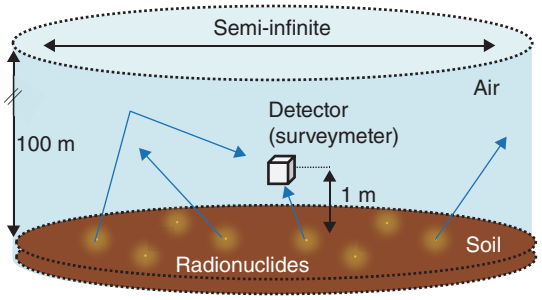


**Fig.1-23 The simulation geometry of the environment**
The transport of the γ-rays emitted from radionuclides distributed in soil was simulated using the radiation-transport-calculation code PHITS. Dose rates in air were calculated with consideration of the energies and incident directions of γ-rays entering a detector 1 m above the ground.

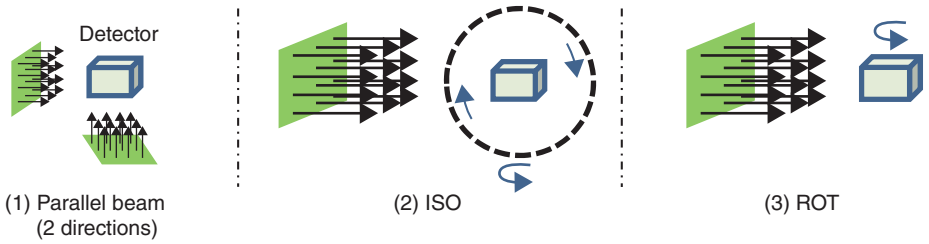


**Fig.1-24 Various irradiation conditions of γ-rays**
Various irradiation conditions are shown for a CsI(Tl) scintillation detector (13 × 13 × 20 $mm^3$), which is simulated by calculation analysis. The irradiations of the ISO and ROT were performed under the condition where the source was rotated around the detector.

**Table 1-1 Comparison of dose rates under various γ-ray-irradiation conditions**
Dose rates depend on the irradiation geometry of γ-rays. Ratios of dose rates to those in the environment (environmental dose) are also shown.

| | Environmental source | Parallel beam | | ROT | ISO |
|---|---|---|---|---|---|
| | | 13 × 13 $mm^2$ | 13 × 20 $mm^2$ | | |
| Dose rate (μSv/h) | 5.19 ± 0.09 | 6.06 ± 0.20 | 5.12 ± 0.09 | 5.35 ± 0.13 | 5.66 ± 0.13 |
| Ratio | 1.00 | 1.17 ± 0.04 | 0.98 ± 0.02 | 1.03 ± 0.03 | 1.09 ± 0.03 |

Following the TEPCO's Fukushima Daiichi NPS (1F) accident on March 11, 2011, radiation monitoring has been periodically performed to obtain environmental dose rates in air. Because scintillation-crystal-based detectors such as survey meters are usually used for ensuring safety in nuclear power plants, dose-rate calibration is performed for accurate measurement under conditions where the radiation is incident on a detector from one direction. In contrast, the radiations that were released from radionuclides such as cesium into the environment by the 1F accident and which were widely deposited in soil are incident on the detector from various directions.

Therefore, for the purpose of investigating the necessary calibration condition of detectors for accurate measurement of the doses in the environment, the influence of the incidence direction of radiation upon the dose-rate measurement was analyzed using the particle and heavy-ion transport system (PHITS). First, an environment with radionuclides existing in the soil (Ground source, Fig.1-23) was reproduced on a computer, and the dose rates 1 m above the ground's surface were calculated. The CsI(Tl)-scintillation detector of crystal size 13 × 13 × 20 mm, was selected for a car-borne survey. Second, the dose rates were calculated under the following irradiation conditions: (1) a uniform parallel-beam condition against each crystal surface (13 × 13 $mm^2$ and 13 × 20 $mm^2$); (2) the condition where a detector is irradiated isotropically from all directions (ISO); and (3) the condition where only the lateral surface of a detector is irradiated laterally (ROT) (Fig.1-24). Furthermore, all calculated results were normalized by the dose rates measured around 1F (Table 1-1 Dose rates for the Ground source).

The results of the calculated dose rates under the irradiation conditions are shown in Table 1-1. The dose rate for the parallel beam irradiation on the 13 × 13 $mm^2$ crystal surface is approximately 17% larger than that for the Ground source. Conversely, the dose rates in the ISO and ROT geometries agree with the dose rate for the Ground source to within 10%; this result indicates that the incident directions of gamma rays in the ISO and ROT geometries are similar to that for the Ground source. Moreover, the parallel-beam irradiation on the 13 × 20 $mm^2$ crystal surface agrees well with the dose rate for the Ground source. It is found from these results that a simple calibration method under unidirectional irradiation can be sufficiently accurate to obtain the dose rates in the environment.

In the future, the dependence of detector configuration on the gamma rays' incidence direction will be analyzed.

**Reference**

Tsuda, S. et al., Spectrum-Dose Conversion Operator of NaI(Tl) and CsI(Tl) Scintillation Detectors for Air Dose Rate Measurement in Contaminated Environments, Journal of Environmental Radioactivity, vol.166, part 3, 2017, p.419-426.

# 1–10 Evaluating Air-Dose Rates due to Radiocesium using a Supercomputer

## — Calculation of Air-Dose Rates from Radioactive Cesium Distributed in the Ground —

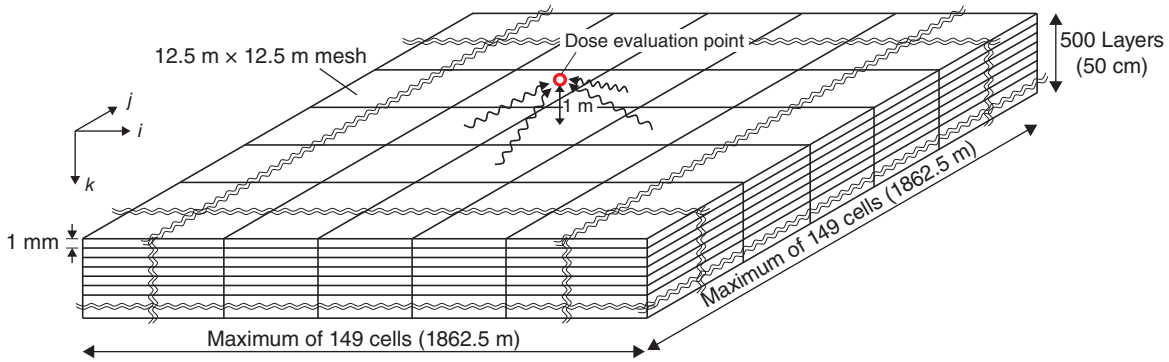


**Fig.1-25 Schematic of a tool for evaluating air-dose rates**
Different radiocesium ($^{134}$Cs and $^{137}$Cs)-activity concentrations (Bq/m$^3$) can be set for the blocks on the mesh. Conversion factors relate the activities to the air-dose rate (μSv/h) above the ground.

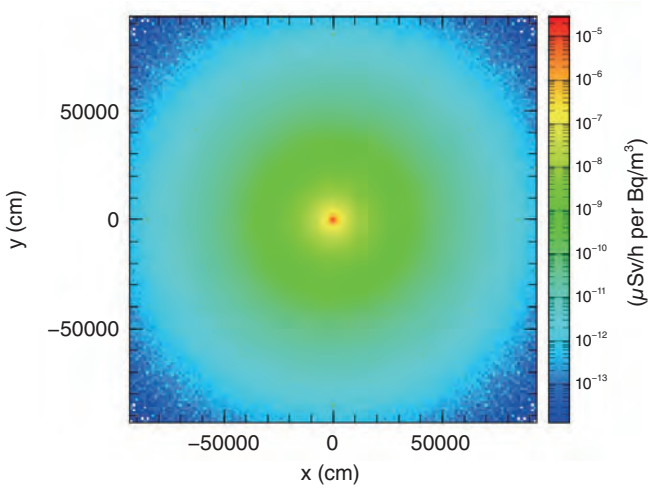


**Fig.1-26 Plot of radiocesium activity to dose-rate-conversion factors**
Relating air dose rate at the center (μSv/h) to radioactive cesium (Bq/m$^3$) within the blocks.

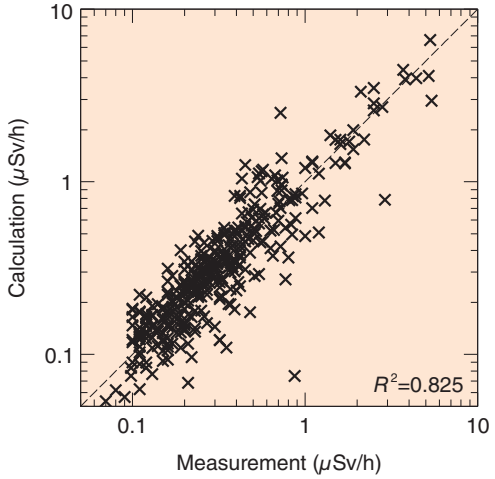


**Fig.1-27 Correlation of calculated and measured dose rates**
Comparison between calculated and measured values at about 80 sites in Fukushima Prefecture.

Massive amounts of radioactive cesium ($^{134}$Cs and $^{137}$Cs) were released during the accident at the TEPCO's Fukushima Daiichi NPS in 2011. $^{137}$Cs will remain in the environment for a long time owing to its 30-year half-life. These isotopes migrate horizontally and vertically owing to disturbances by decontamination, typhoons, penetration of rain into the ground, and so on. Understanding the relationship between the distribution of radioactive cesium and the air-dose rate in realistic situations is not easy. Therefore, we developed a tool to evaluate complex three-dimensional distributions of radioactive cesium and calculate dose rates (Fig.1-25).

Using this tool, we divide the ground up into 10 million blocks of soil. The $^{134}$Cs- and $^{137}$Cs-radioactivity amounts are given by measurements, simulations of surface-soil transport, and the like and are set individually for each block. This precise setting of the radioactive-cesium distribution enables accurate evaluation. Conversion factors for calculating the air-dose rate were evaluated by PHITS, the Monte Carlo transport-simulation code developed by JAEA. Using a supercomputer, an accurate calculation was attained over a short calculation time. An example of the conversion factors is shown in Fig.1-26, which converts from $^{137}$Cs 1 Bq/m$^3$ on the blocks' surfaces to the air-dose rate at 1 m above the surface.

We tested the tool using the soil-activity and dose-rate measurements at about 80 different locations in Fukushima Prefecture, including rice paddies, fields, and parks. It was verified that the tool gave realistic predictions for the actual dose rates (Fig.1-27).

The tool is applicable for numerous purposes, e.g., choosing the best remediation method and evaluating the change in air-dose rates before and after typhoons that move the surface soil. It is also being used to understand how dose rates in the Prefecture are influenced over time by radioactive decay and seepage deeper into soil.

**Reference**

Malins, A. et al., Evaluation of Ambient Dose Equivalent Rates Influenced by Vertical and Horizontal Distribution of Radioactive Cesium in Soil in Fukushima Prefecture, Journal of Environmental Radioactivity, vol.151, part 1, 2016, p.38-49.

# 1–11 Transfer of Radioactive Cesium in the Hardwood Forest

## — Study of Radioactive-Cesium-Transport Behavior in Trees in a Forest —

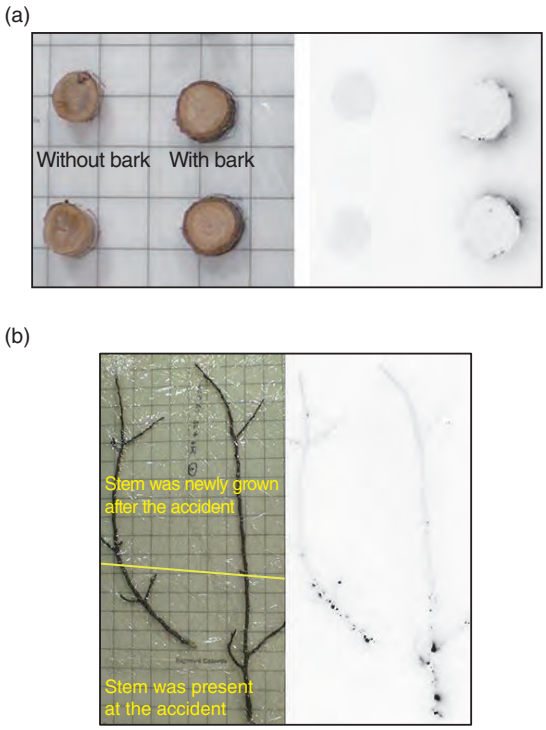


**Fig.1-28 Autoradiograph in a deciduous broad-leafed tree**
(a) Radioactive Cs was found mostly on the bark. (b) Radioactive Cs was homogeneously distributed in the stem that was newly grown since the 1F accident, whereas a heterogeneous and spotted radioactive-Cs distribution was observed in the stem that was present at the time of the accident.

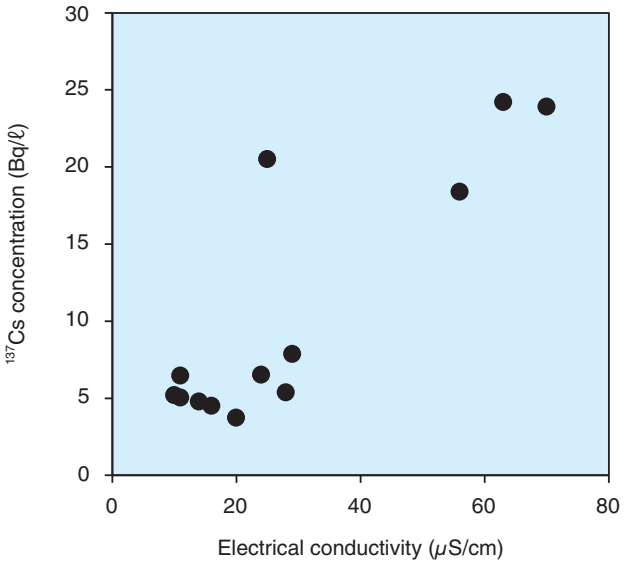


**Fig.1-29 Relationship between radioactive Cs ($^{137}$Cs) concentration and electrical conductivity in a dissolved fraction of stemflow**
A positive correlation was observed between electrical conductivity and $^{137}$Cs concentration in the dissolved fraction of the stemflow. This result suggests that major ions and radioactive Cs in the stemflow are controlled by the same elution mechanism.

Numerous radionuclides were released into the environment as a result of the accident at the TEPCO's Fukushima Daiichi NPS (1F), which occurred as a result of the Great East Japan Earthquake on March 11, 2011. Radioactive cesium (Cs) isotopes with relatively long half-lives are still present in the environment. Deciduous broad-leafed trees such as Konara oak, Mizunara oak, and Japanese chestnut are used in people's daily lives as forest products (firewood and mushroom cultivation). From the perspective of the use of forest products, it is important to understand the radioactive Cs behavior in these trees. At the time of the 1F accident, because the deciduous trees were in a dormant stage and their leaves ware falling, released radioactive Cs was caught in the branches and trunks. In cases where the radioactive Cs deposited onto the surface of a tree was transferred inside, some of the radioactive Cs was transferred to newly generated branches and leaves after the 1F accident. In contrast, the radioactive Cs on the trees' outside can be transferred by rain running down the trunk (stem flow). To elucidate the distribution of radioactive Cs and the radioactive-Cs-transfer mechanism to stemflow in deciduous broad-leafed trees, we surveyed the radioactive-Cs distribution and concentration in the stems of Chestnut trees growing in deciduous broad-leafed forest located approximateyl 35 km from 1F as well as the radioactive-Cs concentration and the characteristics of the soluble fraction (the solution that passed through a filter with a pore size of 0.45 $\mu$m) of stemflow.

On the bark surface of the chestnut trees that was presented at the time of the 1F accident, the radioactive Cs had a heterogeneous and spotty distribution. In contrast, radioactive Cs on branches newly grown after the 1F accident was uniformly distributed (Fig.1-28). The radioactive-Cs concentration in the bark was approximately 10 times that of rest of the wood. The radioactive-Cs concentration in the dissolved fraction of the stem flow was approximately $10^{-3}$ times that on the bark. Because radioactive-Cs concentration in the bark is still high and that in the soluble fraction of stem flow is low, elution of radioactive Cs from the trees to the stem flow would occur very slowly. Electrical conductivity is an index of the flowability of electricity in the solution and depends upon the abundances of ions in solution. There was a positive correlation between the radioactive-Cs concentration and the electrical conductivity of the dissolved fraction of the stem flow. This result suggests that the predominant ions (nitrogen, phosphorus, sulfur, potassium, calcium, magnesium, manganese, etc.) and radioactive Cs in the stemflow are controlled by the same elution mechanism (Fig.1-29).

We need to study the elution mechanism of radioactive Cs and other ions into the stem flow.

**Reference**

Sasaki, Y. et al., The Transfer of Radiocesium from the Bark to the Stemflow of Chestnut Trees (*Castanea Crenata*) Contaminated by Radionuclides from the Fukushima Dai-Ichi Nuclear Power Plant Accident, Journal of Environmental Radioactivity, vol.161, 2016, p.58-65.

# 1–12 Spatial Variation in Radioactive-Cesium Deposition Caused by Topographical Factors
## — Detailed Examination of the Air-Dose Rate in a Mountainous Forest Catchment —

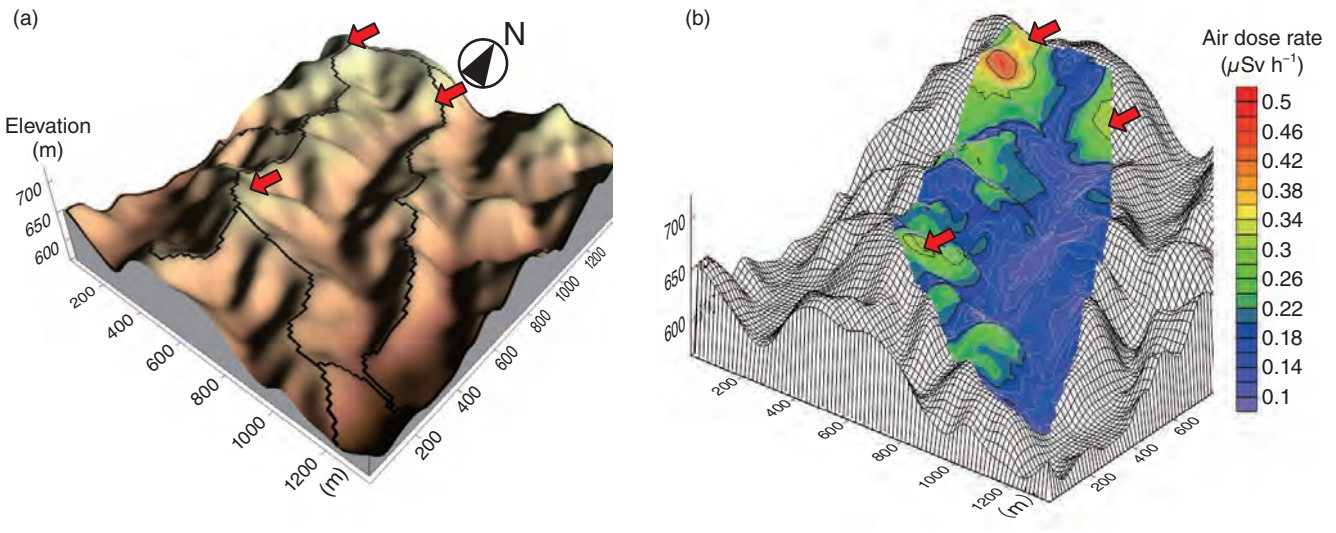


**Fig.1-30 (a) A topographical map with a bird's-eye view and (b) a three-dimensional contour map of the air-dose rate of the forest catchment**
The catchment area bounded by the lines in panel (a) was investigated. The higher and east-facing slopes are colored more lightly because the map is lit from the east. (b) The spatial pattern of the air-dose rate is similar to the lighting pattern on the topographical map, indicating that more radioactive Cs was deposited on the ridges, shown as lines in panel (a) (*e.g.*, the points indicated with red arrows), and east-facing slopes. This study showed that the spatial distribution of radioactive Cs deposition was strongly affected by topographical features.

Most of the area contaminated by the radioactive cesium (Cs) released by the TEPCO's Fukushima Daiichi NPS (1F) accident is mountainous and forested. This region had a prosperous forestry industry; thus, estimating the dose-exposure to forest workers and the contamination of forest products is critical. To do this, the spatial distribution of radioactive Cs deposition in the forest must be measured in detail; however, most mountainous areas are difficult to access for direct measurement. Although airborne monitoring has been conducted in this region, its capabilities in such complex topography remain unverified. Therefore, data must be collected to verify airborne monitoring.

We conducted air-dose-rate measurements in a mountainous catchment subject to radioactive Cs deposition from 1F (Fig.1-30(a)) to verify airborne monitoring and understand the spatial variation of radioactive Cs deposition in a mountainous forest with complex topography. To achieve this, we used KURAMA-II, a GPS-aided mobile radiation-monitoring system developed by the Kyoto University Research Reactor Institute. To perform systematic measurements, a researcher carried the KURAMA-II unit on a backpack frame while walking through the area. Using the collected data, we conducted a geostatistical analysis and generated a contour map, which revealed the effects of topography upon the spatial distribution of radioactive Cs (Fig.1-30(b)).

The results showed that the air-dose rates in the mountainous forest are highly variable spatially and topographically anisotropic. The air-dose rates increased with elevation, indicating that more radioactive Cs was deposited on ridges. The results suggest that it is important to consider topography when selecting sampling points and resolution to assess the spatial variation of dose rates. The results of the comparison with airborne monitoring imply that such monitoring provides an accurate estimation of air-dose rate averaged over thousands of meters, even in mountainous areas.

**Reference**

Atarashi-Andoh, M. et al., Catchment-Scale Distribution of Radiocesium Air Dose Rate in a Mountainous Deciduous Forest and its Relation to Topography, Journal of Environmental Radioactivity, vol.147, 2015, p.1-7.

# 1–13 Environmental Behavior of a Minute Amount of Radioactive Cesium

## — Cs-Sorption/Desorption Behavior of Clay Minerals Considering the Actual Contamination Condition in Fukushima —

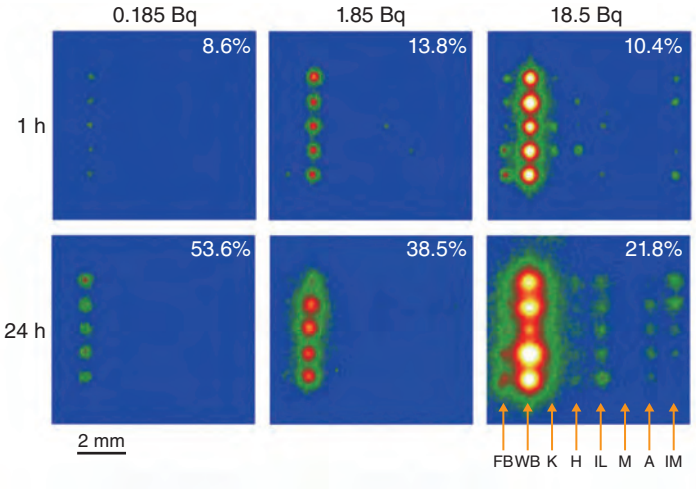


**Fig.1-31 Read-out images of IPs with particles of various minerals adsorbing $^{137}$Cs from the solutions**
The radioactivity input to the solution and reaction time are at the top and left, respectively. The figure at the top right of each image is the percentage of radioactivity adsorbed to all mineral particles, as estimated from the IP signal.

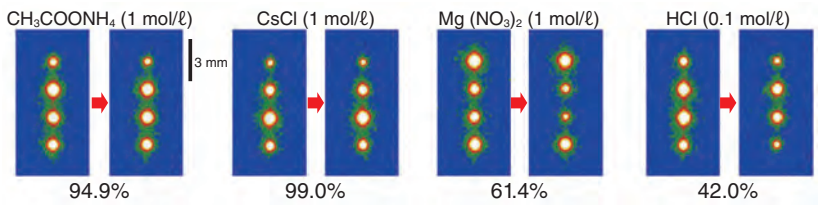


**Fig.1-32 IP read-out images to show the desorption feature of $^{137}$Cs from WB using various chemical reagents**
Left and right of the red arrow are the conditions before and after immersion, respectively. The figure at the bottom of each image represents the percentage of $^{137}$Cs remaining in the mineral particles after immersion. Reagents include ammonium acetate, cesium chloride, magnesium nitrate, and hydrochloric acid, respectively, from the left side.

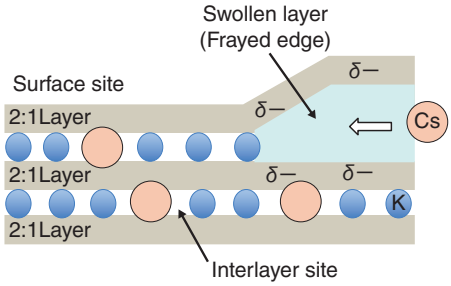


**Fig.1-33 A model of radioactive-cesium adsorption into WB**
Cs enters from a swollen layer called a frayed edge, and is strongly fixed by collapsing the layers.

After the accident at the TEPCO's Fukushima Daiichi NPS in March 2011, many radioactive materials were dispersed in the environment and huge amounts of radioactive soil waste were generated by the decontamination project to reduce air-dose rate. Most of the radioactive cesium (Cs) in the waste was fixed in clay minerals. On the basis of this result, the development of stable interim-storage and volume-reduction methods for the waste is strongly desired. Thus, Cs sorption/desorption experiments for various clay minerals, considering actual contamination conditions in Fukushima, were conducted to elucidate the sorption mechanism of Cs into the clay. This was done using $^{137}$Cs radioisotope and autoradiography using imaging plates (IPs).

In this experiment, eight clay-mineral species with five particles were arranged on an acrylic substrate; then, aqueous solutions containing low concentration of $^{137}$Cs were dropped to cover all particles on the substrates. Fig.1-31 shows the read-out images of the IPs. Under any $^{137}$Cs concentration and immersion periods, the amount $^{137}$Cs adsorbed by weathered biotite (WB) collected from Fukushima was much higher than that of other minerals. Therefore, when WB was present in the soils, Cs is considered to be selectively adsorbed onto this mineral.

Moreover, desorption experiments were conducted using the Cs-adsorbed particles of WB and various chemical reagents for elution. Consequently, the elution of $^{137}$Cs was observed only when acid sufficiently strong to dissolve clay minerals was used as an eluent (Fig.1-32). This result suggests that Cs is strongly fixed to interlayer sites of WB (Fig.1-33) and that Cs, once adsorbed on WB, hardly leaches out into the environment.

This study revealed that WB is an important material for understanding radioactive contamination in Fukushima soils. For example, the existence of WB will dominate the fixing and leaching behaviors of radioactive materials. These results are expected to lead to the suggestion of effective reduction and safe interim-storage methods for radioactive waste soils.

This study is a part of the result of contract research "Elucidation of adsorption and transition mechanism of radioactive cesium in soil particle" commissioned by the University of Tokyo.

**Reference**

Mukai, H., Yaita, T. et al., Cesium Adsorption/Desorption Behavior of Clay Minerals Considering Actual Contamination Conditions in Fukushima, Scientific Reports, vol.6, 2016, p.21543-1-21543-7.

# 1–14 Elucidating the Adsorption States of Cesium in Clay Minerals
## — Analysis via First-Principles-Based Simulations —

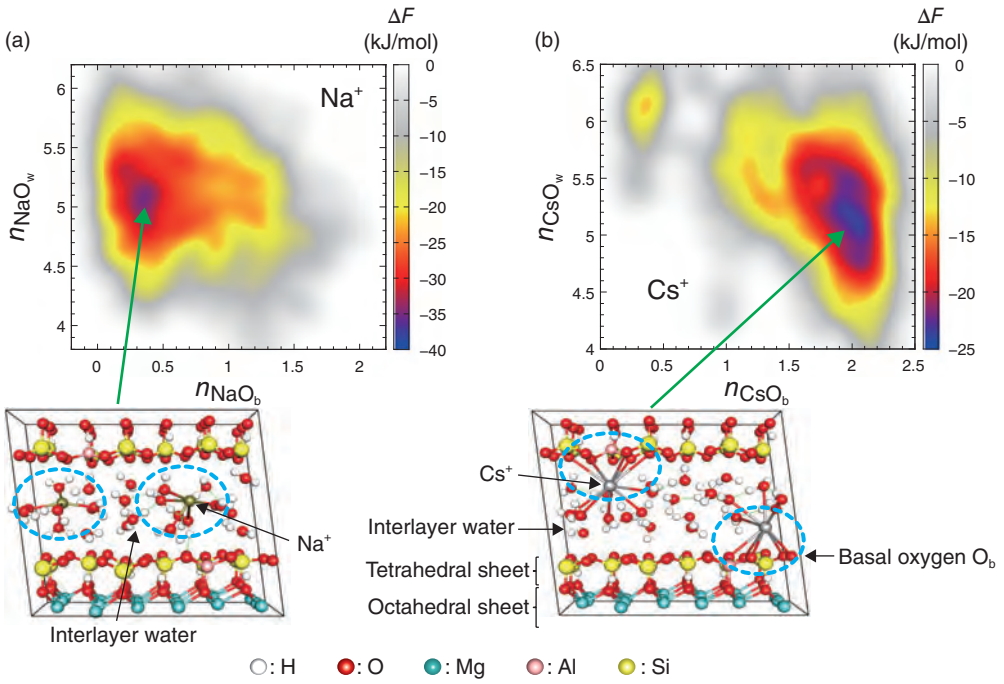


**Fig.1-34 The free-energy surface, $\Delta F$, representing the adsorption states of (a) $Na^+$ and (b) $Cs^+$ in the interlayer of 2:1-type tri-octahedral clay minerals obtained from first principles metadynamics and the adsorption structure corresponding to its minimum**
The vertical and horizontal axes in the figures show the metal (M)-water O ($O_w$) coordination number (CN), $n_{MOw}$, and the M-basal O ($O_b$) CN, $n_{MOb}$, per metal ion, respectively. These two CNs are regarded as indicators of the affinity of the metal cations for the water and clay layers, respectively.

The accident at the TEPCO's Fukushima Daiichi NPS in 2011 released a large amount of radioactive cesium (Cs) into the environment. The resultant Cs deposited onto the ground remains at its subsurface and continues to emit radioactive rays. Large-scale decontamination has been performed at Fukushima, thus reducing the radiation significantly. Thus, an emerging issue that is recognized today is as to how to treat the huge amount of accumulated waste soil.

Cs in the soil is observed to be predominantly adsorbed by weathered biotites (WBs). Hence, the waste volume can be reduced if Cs desorption is realized from them. However, an effective method for volume reduction has not been successfully developed owing to missing fundamental knowledge of Cs adsorption at an atomic scale. It is therefore necessary to elucidate the adsorption states of Cs in WBs for this purpose.

The weathering of mica clay minerals including biotite leads to the loss of some quantity of interlayer cations, which are eventually replaced with water molecules. Therefore, interlayer water is expected to play an important role in the adsorption and subsequent fixation of Cs in the WBs of Fukushima. We systematically investigated the adsorption states of alkali metal cations in 2:1-type swelling clay minerals via first-principles-based metadynamics simulations by fully utilizing supercomputers. We found that the characteristic adsorption state for light- and heavy-alkali-metal cations observed in tri-octahedral clay minerals (Fig.1-34) tends to disappear in di-octahedral ones, suggesting that particular clay minerals selectively adsorb Cs, in agreement with the experimental observations.

The present success in characterizing interlayer water and cations in clay minerals, which is difficult to achieve experimentally, enables us to promote the development of an economical, yet efficient, method for reducing the volume of waste soil.

**Reference**
Ikeda, T. et al., Characterization of Adsorbed Alkali Metal Ions in 2:1 Type Clay Minerals from First-Principles Metadynamics, The Journal of Physical Chemistry A, vol.119, issue 30, 2015, p.8369-8375.

# 1–15 New Technology for Suppressing Cesium Migration from Forests
## — Mild Regeneration of Village Forests with Polymers and Clay —

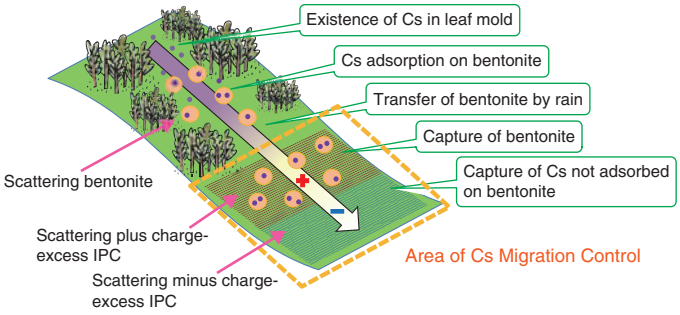


**Fig.1-35 Scheme for suppression of Cs migration**
Using interpolyelectrolyte complexes (IPCs) and bentonite (clay), the migration of Cs in sloped areas in forests is suppressed (Cs-migration-control area).

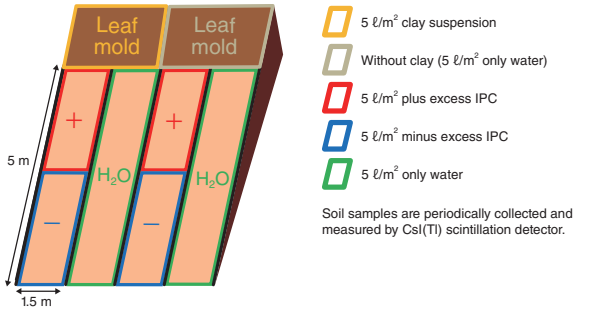


**Fig.1-36 Verification-testing procedure in Iitate-mura, Fukushima**
On the lower side of the leaf-mold zone, bentonite was either scattered or not scattered, and four alternate lanes with IPCs (plus-charge-excessive IPC and minus-charge-excessive IPC) and without IPCs are prepared.

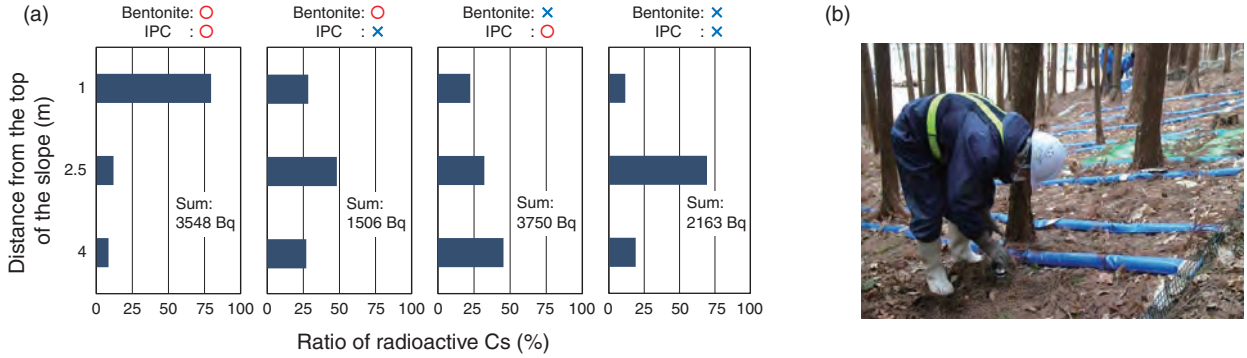


**Fig.1-37 (a) Distribution of radioactive Cs on the slope after three months and (b) Appearance of soil-core sampling on the slope**
The abundance ratios of radioactive Cs on the slope at the upper (1 m), middle (2.5 m), and lower (4 m) positions on the four lanes below the leaf-mold zone is indicated using a bar chart, showing a photo of soil-core sampling at each position.

Much of the radioactive cesium (Cs) in forests exists in leaf mold (a form of compost produced by biodegradation) between litter and soil layers. Some plants can take up the radioactive Cs existing in the leaf mold when it is released from organic substances owing to their decomposition and dissolved into soil water. In addition, on a sloped ground, the Cs is transferred to a lower zone; thus, there is the potential that living areas already decontaminated may be polluted again.

A new technology to suppress Cs migration from forests has been developed collaboratively by Ibaraki University, Kumagai gumi Co., Ltd. and its group of company, and the Japan Atomic Energy Agency. The new technology using polyelectrolytes (which are polymers with electric charges and clay minerals) to control Cs migration with the aid of natural forces such as rainfall and rainwater runoff; the polyelectrolytes are utilized as food additives etc. and clay minerals are utilized as ordinary natural products; both are non-hazardous. The new technology is expected to mildly regenerate village forests (i.e., forests near human dwellings) without destroying their ecosystems. In Iitate-mura, Fukushima, verification tests of the new technology have been performed and its effect on controlling Cs migration in sloped areas of the forests has been proven.

By scattering bentonite (the generic name of clay having montmorillonite as a main component) particles that strongly adsorb radioactive Cs existing in leaf mold, Cs can be expected to be changed from the dissolved form that is easily taken up by plants into the fixated form, which is difficult for plants to absorb; the Cs bound to organic substances, which is easily released and dissolved into soil water, is changed into Cs that is immobilized in clays and almost insoluble in water. In contrast, the bentonite particles adsorbing radioactive Cs are transferred to a lower zone as mud water by being mixed with rainwater; then, these particles can be captured by electric-charge-controlled IPCs. The IPCs formed by mixing two polyelectrolytes having charges opposite to each other are highly viscous gels and can thus catch bentonite particles together with soil particles using their strong viscosity. Plus-charge-excessive IPCs, in which the number of cationic polyelectrolytes is larger than that of anionic polyelectrolytes, can capture bentonite particles with negatively charged surfaces more effectively than can non-charged IPC. Moreover, by arranging minus-charge-excessive IPC below the plus-charge-excessive-IPC zone in a sloped area, positively charged radioactive Cs unfixed by bentonite particles can also be caught, ensuring definitive Cs-migration control (Fig.1-35). By scattering both bentonite and IPCs over a slope area, a larger amount of radioactive Cs remains on an upper position and Cs migration is reduced to less than one-fifth its original concentration (Figs.1-36 and 1-37).

The present study is a fruit developed by applying a patent method in the reference below and press-released by the Ibaraki University, the Kumagai Gumi Co., Ltd., and the JAEA, on May 10, 2016.

**Reference**

Naganawa, H. et al., Decontamination Method for Soils Polluted by Radioactive Cesium, Patent Application Publication, pub.no.JP2013-185941, 2013-09-19 (in Japanese).

# 1–16 Safety of Burial of Contaminated Soil at Public Parks

## — In situ Experiments on the Migration of Radioactive Cesium from the Buried Soil —

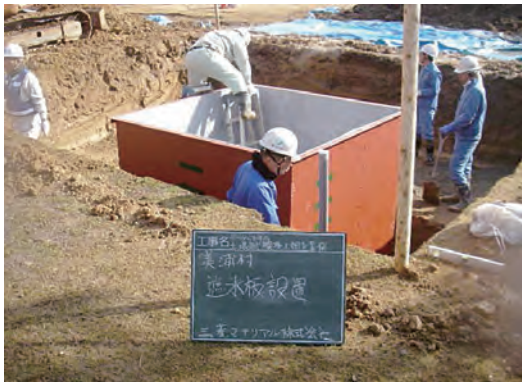

**Fig.1-38 Preparation at a site in Miho village**
A trench with an area of 6 m × 6 m was dug and equipped with a 2 m × 2 m water-impermeable steel plate. Contaminated soil stripped from the surface was buried, as shown in Fig.1-39 for migration experiments.

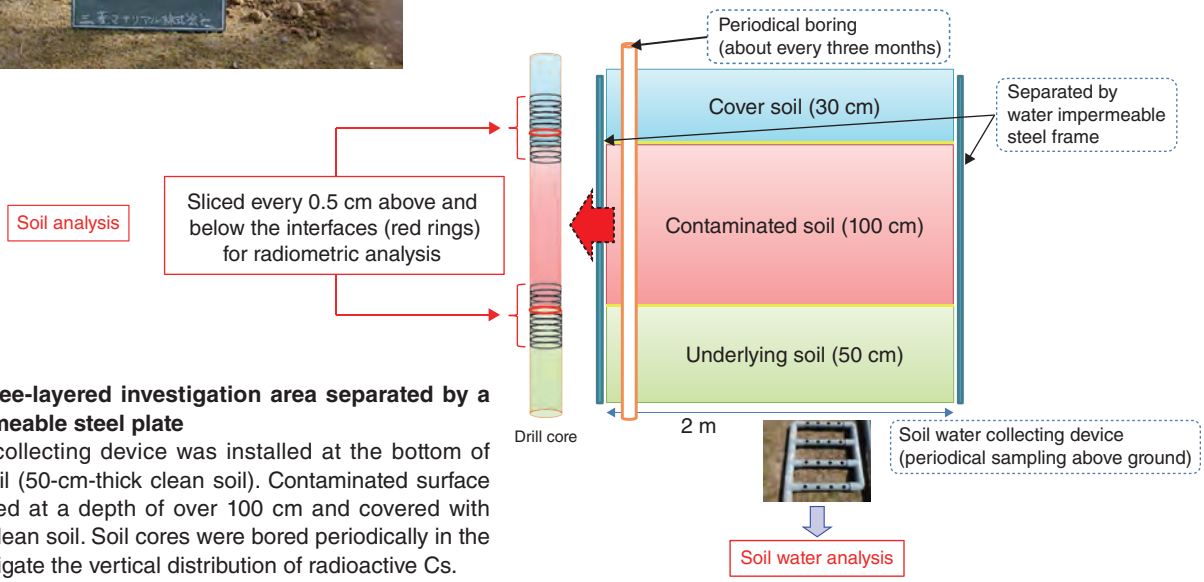


**Fig.1-39 Three-layered investigation area separated by a water-impermeable steel plate**
A soil-water-collecting device was installed at the bottom of underlying soil (50-cm-thick clean soil). Contaminated surface soil was buried at a depth of over 100 cm and covered with 30-cm-thick clean soil. Soil cores were bored periodically in the area to investigate the vertical distribution of radioactive Cs.

Previous field studies performed in China and Canada have predicted that radioactive cesium (Cs) would hardly migrate into surrounding soils and groundwater from soils contaminated by the accident at the TEPCO's Fukushima Daiichi NPS if they were to be buried and covered with clean local soils. This study verifies the prediction by performing *in situ* migration experiments over a year in a public park in Miho Village, Ibaraki Prefecture and in two public parks in Misato City, Saitama Prefecture.

Contaminated surface soils (to a depth of 3 cm) were gathered and buried in a 1–1.3-m-deep trench (Fig.1-38) and sprinkled with water to accelerate the radioactive Cs migration. In order to let the water flow through the contaminated soil, a 2 m × 2 m area in the burial site was separated as an investigation area by a water-impermeable steel frame. 3200–3900 mm of water was sprinkled, which is equivalent to 8–10 years of natural infiltration. Vertical borings were performed every three months to analyze the radioactive Cs distribution in the soil cores, as shown in Fig.1-39. The concentration of Cs-137 ($^{137}$Cs) is 1000–3000 Bq/kg in the contaminated soil and less than 40 Bq/kg in the cover and underlying soils. The water that flowed through the contaminated soil was analyzed after sampling by a soil-water-collecting device that had been installed at the bottom of the underlying soil. Migration of radioactive Cs was not observed from these analyses.

Laboratory column and sorption experiments using the soil samples revealed that the radioactive Cs hardly leaches out of the soil and even if does, it will be adsorbed on surrounding soils and barely migrate through the soil layer (at a rate as slow as one 7000th of the groundwater-flow rate). Although the experiments were terminated after a year, simulation of $^{137}$Cs migration for 100 years by an advection–diffusion model showed that $^{137}$Cs migrated slightly and decayed out within the contaminated soil (the maximum concentration at a distance of 10 cm from the contaminated soil will be 1% of the concentration in the contaminated soil).

These results prove that the migration rate of radioactive Cs is low in soils in Japan and that the range of migration is limited. On-site burial, by which contaminated surface soil is removed from parks and accumulated in a trench on site then being backfilled with clean local soils, is an effective method for preventing direct exposure from the contaminated soil and contamination of the groundwater. It is a candidate disposal measure for contaminated soil.

The JAEA technically supported the Ministry of the Environment of Japan (MOE) and created these results.

**Reference**

Yamaguchi, T. et al., Demonstrative Experiments on the Migration of Radiocesium from Buried Soil Contaminated by the Accident at Fukushima Daiichi Nuclear Power Station, Genshiryoku Bakkuendo Kenkyu (Journal of Nuclear Fuel Cycle and Environment), vol.22, no.2, 2015, p.21-28.

# 1–17 Realization of Automatic Analysis of Radioactivity in Samples

## — Development of an Automatic Analysis System for Strontium-90 in an Environmental Sample —

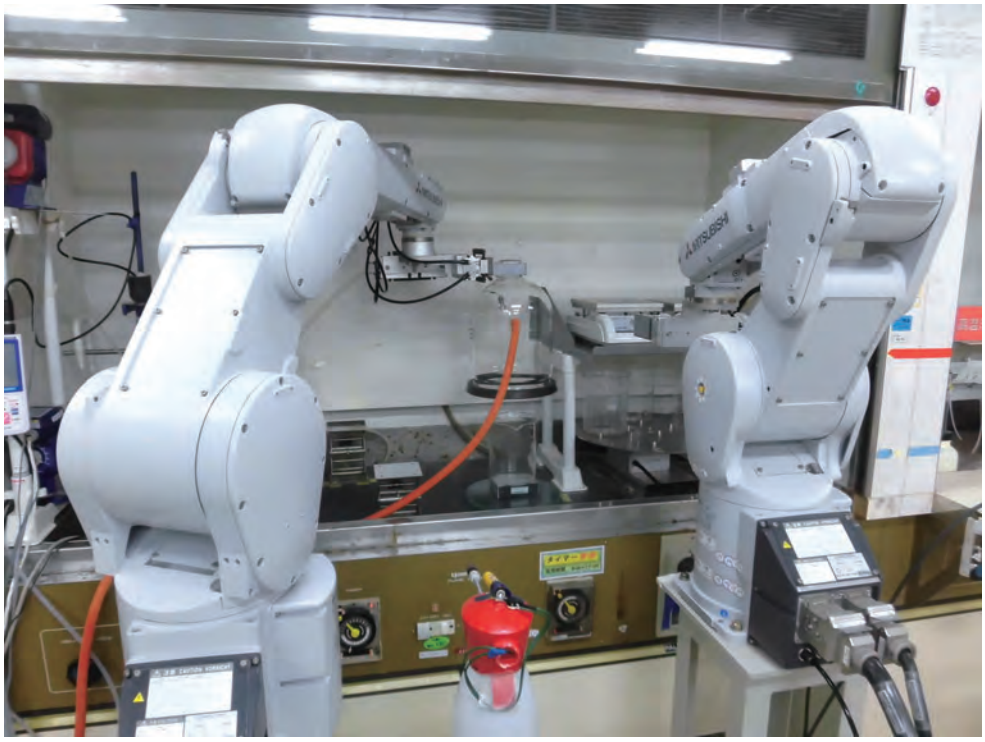

**Fig.1-40 Photograph of a chemical-separation system**
This is a photograph of the preparation of the filtration apparatus. This system can automatically perform pH adjustment, precipitation creation, maturation, filtration, and addition of reagent (solid or liquid) in combination with an industrial robot and apparatus-supply system.

The radioactivity concentrations of cesium-134 ($^{134}$Cs) and -137 ($^{137}$Cs), which were influenced by the accident at the TEPCO's Fukushima Daiichi NPS (1F), have been measured in environmental samples and reported by various institutions.

Conversely, there have been few reports of the radioactivity concentration of strontium-90 ($^{90}$Sr), owing to the fact that the analytical method for $^{90}$Sr is very complicated and takes more time than that for radioactive Cs. Therefore, various rapid analytical methods have been developed to measure $^{90}$Sr-radioactivity concentration in environmental samples since the 1F accident. However, these methods are limited by sample volume and difficulty in measuring $^{90}$Sr concentrations, similar to the environmental level of 0.02 Bq/kg·raw. In addition, workers must perform analysis using specific chemical techniques.

Thus, an automatic analysis system has been developed, capable of isolating Sr with a standard radioactivity-measurement method, in order to analyze and measure $^{90}$Sr radioactivity concentration in an environmental sample. Standard methods include the ion-exchange method, the white-fuming nitric acid method, the oxalate method, and the solvent-extraction method; the ion-exchange method was selected for this research. The method was divided into three processes such as (1) wet digestion, (2) chemical separation (Fig.1-40), and (3) ion-exchange, which were developed, respectively. Finally, the automatic analysis system was used to analyze ashed agricultural, farm, and marine products.

Previously, all analytical procedures have been conducted by a worker and the sample-size and duration of the analysis depended on their skill. However, the developed system can semi-automatically analyze $^{90}$Sr depending on sample type. Therefore, a person with basic knowledge of chemical analysis can perform analysis with the system, reducing their personal risk of exposure to a chemical reagent. In particular, using a wet-digestion process, the worker is not exposed to treatment risk because the addition of nitric acid and hydrogen peroxide need not be performed by the worker.

Moreover, the system may also be used to analyze other radionuclides such as plutonium, meaning it may have a large ripple effect on radiochemical analysis. With continuous research, our objective is to allow workers to automatically perform chemical analysis.

This research was sponsored by the Center for Revitalization Promotion, the Japan Science and Technology Agency (JST).

**Reference**

Nojima, T., Fujita, H. et al., Development of Automatic Analysis System of Strontium-90 in Environmental Sample, KEK Proceedings 2015-4, 2015, p.111-115 (in Japanese).

# 2 Nuclear Safety Research

## Implementing Continuous Improvements in Safety

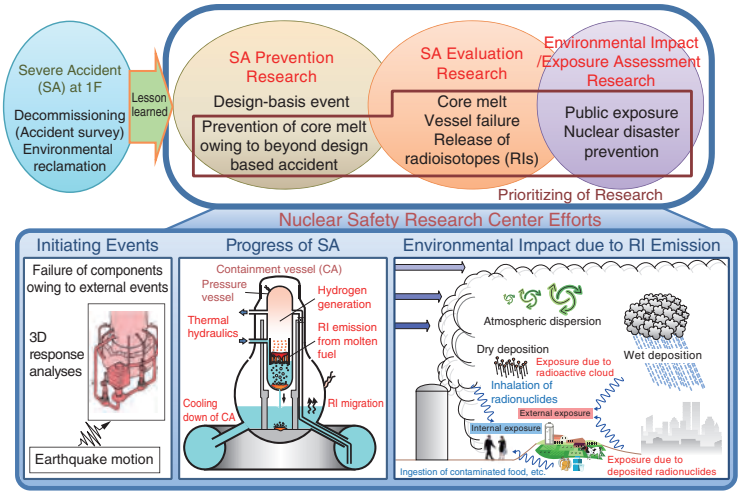


**Fig.2-1 Directions of nuclear-safety research**
In accordance with the lessons learned from the accident at 1F, we have promoted studies on severe-accident prevention efforts and nuclear-emergency preparedness activities such as environmental impact assessments in addition to safety assessments within design-basis events.

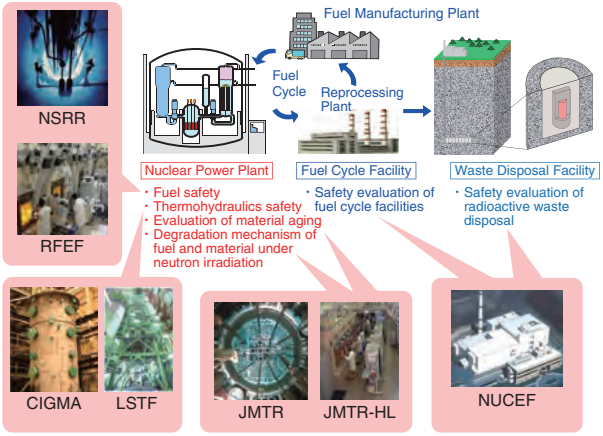


**Fig.2-2 Nuclear safety research areas and related JAEA facilities**
The NSRC acquires experimental data from various Japan Atomic Energy Agency (JAEA) facilities. These data, used for risk assessment and safety evaluation of nuclear facilities, contribute to international efforts to develop evaluation methods and criteria.

To ensure the safe use of current nuclear facilities, the Nuclear Safety Research Center (NSRC) is studying the possibility of serious accidents at nuclear installations and their consequences. A massive and severe accident (SA) occurred at the TEPCO's Fukushima Daiichi NPS (1F) as a result of the Great East Japan Earthquake and Tsunami. The NSRC has been collaborating with the Japanese government to institute appropriate emergency-response procedures. The specialists at the NSRC regret that they were unable to prevent the accident.

Continuous efforts should be made to avoid serious accidents while we utilize nuclear energy. A proper understanding of the situation is important for making the best and safest use of such technologies. In fact, the International Atomic Energy Agency, which investigated the accident at 1F, highlighted the importance of "continuous improvement". To contribute to continuous improvement aimed at the highest level of safety, we have promoted studies on SA prevention and evaluation so as to reduce the risk of accidents at nuclear facilities and prevent nuclear disasters using analyses such as environmental impact assessments, as shown in Fig.2-1.

We are committed to safety research and have devoted various facilities to this cause, as shown in Fig.2-2. These special facilities allow for the handling of radionuclides and the simulation of accident conditions.

This chapter presents the results of recent research on the following topics: prediction of hydrogen behavior in a reactor-containment vessel during SA using the international benchmark exercise (Topic 2-1); evaluation of the amount of fuel-cladding-tube deformation through simulated loss-of-coolant accident tests (Topic 2-2); evaluation of the effect of the chemical form of fission products upon the pH of coolant water during SA (Topic 2-3); evaluation of the radiation-health-risk estimation using disability-adjusted life years (Topic 2-4); evaluation of the release behavior of Ruthenium by evaporation to dryness of highly active liquid waste (Topic 2-5); and investigation of future critical experiments for clarifying the criticality characteristics of fuel debris (Topic 2-6).

The following topic, solicited by the NSRC and related to the accident at 1F, is described in Chapter 1: evaluation of the migration of radioactive cesium by experiments on the burial of contaminated soil at public parks (Topic 1-16).

# 2–1 Prediction of Hydrogen Behavior in a Reactor Containment Vessel during a Severe Accident

## — Thermal-Hydraulic Safety Research on Reactor Containment Vessels by the ROSA-SA Project —

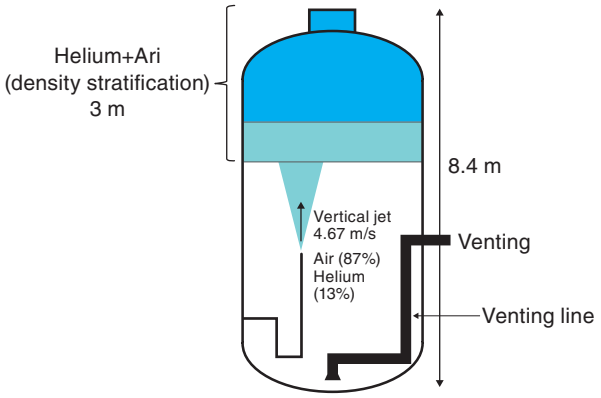


**Fig.2-3 Schematic view of the IBE-3 experimental condition**
Erosion of the density stratification formed with light gas in a large space is a major topic in investigating the behavior of light gas such as helium in a containment vessel.

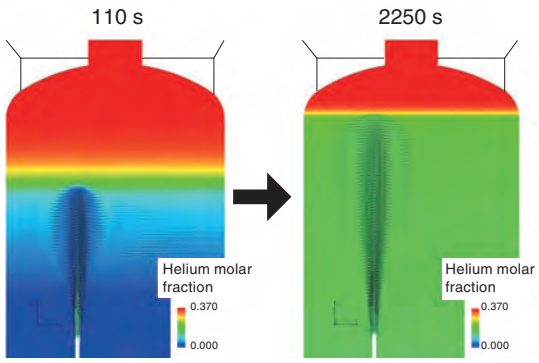


**Fig.2-4 Visualization of simulated instantaneous helium molar fraction and velocity vector**
The jet penetration and rebounding flow appeared, and the stratification gradually eroded with time.

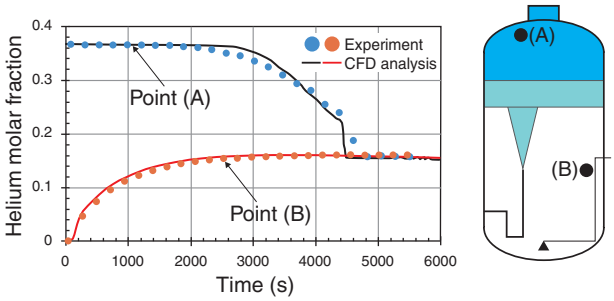


**Fig.2-5 Comparison between the experimental and CFD results for the time history of the helium molar fraction**
The helium molar fraction monotonically decreased in the upper region of containment vessel, whereas it gradually increased in the middle part. The CFD results quantitatively reproduced those of the experiment.

During severe accidents at light-water reactors, hydrogen explosions may occur owing to oxidation chemical reactions between the zirconium-alloy fuel-rod cladding and the coolant water because of severe core damage. Such a hydrogen explosion occurred during the accident at the TEPCO's Fukushima Daiichi NPS in 2011, severely damaging the reactor building. We have advanced the Rig of Safety Assessment-Severe Accident (ROSA-SA) project to investigate thermal hydraulic phenomena in reactor-containment vessels during severe accidents. One of the project objectives is to understand the hydrogen behavior in the containment vessel through experiments and numerical simulations.

Multi-dimensional and complicated flow appears in the containment vessel. Density stratification may form at the upper space of the containment vessel because hydrogen is a light gas. Several research projects in Europe have focused on the stratification formation and its erosion by a jet in a large space through experiments using test facilities to simulate the containment vessel. We participated in the OECD/NEA third international benchmark exercise (IBE-3) for the experiment conducted at the Paul Scherrer Institute (PSI) in Switzerland on the stratification erosion by a low-momentum vertical buoyant jet from below to understand the phenomena, improve the numerical-simulation method, and validate the computer code.

The experiment conducted at PSI simulated the density stratification to a height of 3 m by employing a helium–air mixture instead of hydrogen at the upper region of a simulated vessel approximately 90 $m^3$ in volume, as shown in Fig.2-3. The vertical buoyant jet was then injected from the lowest point of the test vessel to simulate the stratification erosion due to turbulent-flow mixing. We performed calculations for the PSI test using the open-source computational fluid dynamics (CFD) code OpenFOAM, which can be easily improved and made to implement new models. The calculation results shown in Fig.2-4 confirm that jet penetration and rebounding flow appeared; the stratification gradually eroded with time and thus helium was transported downwards. Fig.2-5 shows time histories of the helium molar fraction at two typical measuring points at the upper and middle regions of the simulated vessel. The helium molar fraction monotonically decreased owing to erosion of the stratification at the upper region, whereas it gradually increased at the middle region. We succeeded in calculating results that agreed well with the PSI-test results by modifying the turbulence model to consider turbulence dumping in the stratification. The calculated helium molar fraction thus reproduced the results calculated by other research organizations who participated in the IBE-3.

For future work, we will perform experiments with the Containment Integral Measurement Apparatus (CIGMA) as the main test facility of the ROSA-SA project, and use CFD analyses to clarify the mechanism of thermal-hydraulic phenomena under complicated accidental conditions.

**Reference**

Abe, S. et al., RANS Analyses on Erosion Behavior of Density Stratification Consisted of Helium-Air Mixture Gas by a Low Momentum Vertical Buoyant Jet in the PANDA Test Facility, the Third International Benchmark Exercise (IBE-3), Nuclear Engineering and Design, vol.289, 2015, p.231-239.

# 2–2 Evaluating the Degree of Deformation of the Fuel-Cladding Tube during Loss-of-Coolant Accidents — Effect of Oxidation and Crystal-Phase Condition of the Cladding Tube —

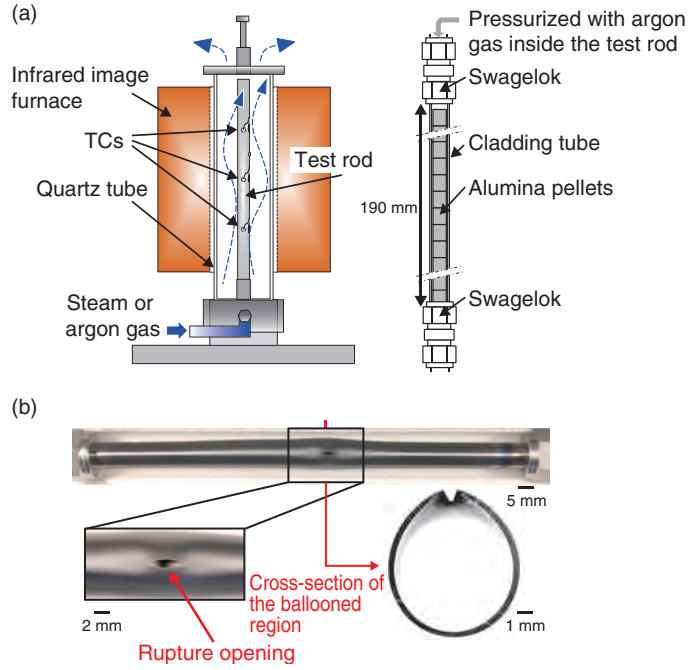


**Fig.2-6 (a) A schematic of the test apparatus used for a simulated LOCA test; (b) The appearance and cross-sectional macrograph of the ballooned region of a typical post-test cladding-tube specimen**
(a) A test rod is heated by an infrared image furnace in steam or argon-gas flow inside the quartz tube at a rate of ~3 K/s, close to the heating rate of a fuel rod in a typical postulated LOCA sequence. During the heat-up phase, the cladding tube balloons and ruptures due to a decrease in cladding mechanical strength and an increase in rod internal pressure. (b) The area of the rupture opening was estimated from the post-test appearance of the ruptured cladding tube, and the maximum circumferential strain was evaluated based on the macrograph of the cross-section at the largest ballooned region of the post-test cladding tube.

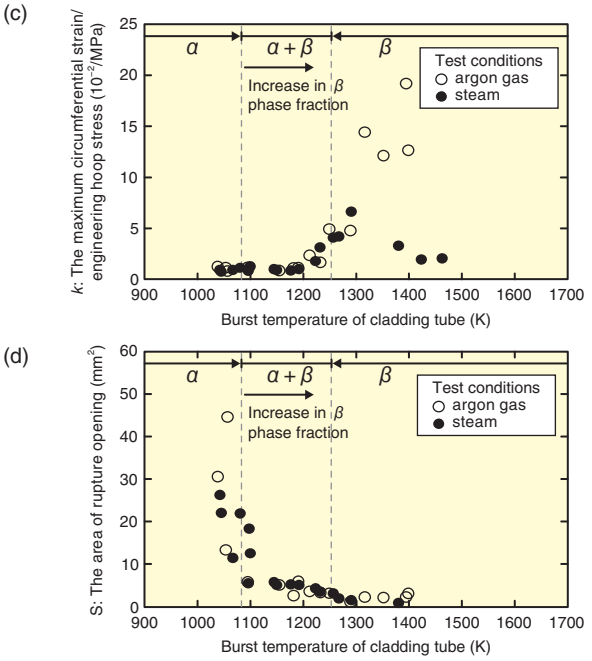


**Fig.2-7 Results of burst test under simulated LOCA conditions**
Symbols $\alpha$, $\alpha+\beta$, and $\beta$ show the crystal-phase conditions of Zircaloy-4, namely the $\alpha$ phase, the ($\alpha+\beta$) phase, and the $\beta$ phase, respectively. (c) The maximum circumferential strain, which was divided by the circumferential stress at the burst of the cladding tube ($k$), tended to increase as the burst temperature approached the $\beta$-phase region. When the burst temperature reached this region, a difference in $k$ was observed between the steam and argon gas conditions.
(d) The area of the rupture opening in the $\alpha$-phase region tended to be larger than that in the burst-temperature region where the $\beta$ phase existed.

Loss-of-coolant accidents (LOCAs), as caused by breaks in the primary piping or the like, are considered in the safety design of nuclear power plants. When the fuel-rod temperature reaches a certain value owing to a decrease in the core-water level during a LOCA, fuel cladding may balloon and rupture because of a decrease in cladding mechanical strength and an increase in the rod-internal pressure. In addition, fuel-fragmentation, -relocation, and -dispersal (FFRD) phenomena have been observed in several LOCA experiments on very high-burnup fuels conducted recently in European test facilities. Fragmented fuel pellets, which may possibly accumulate inside or outside of a ballooned region of fuel cladding, may deteriorate the coolable geometry of the reactor core during a LOCA. These fuel-pellet behaviors are thought to be greatly influenced by the ballooning and rupture behaviors of the cladding tube, leading to FFRD phenomena. In this study, therefore, we investigated the effect of the crystal-phase condition and the oxidation of the cladding tube upon the ballooning size and rupture-opening area of this tube, which has not been well-clarified thus far.

Simulated LOCA tests were conducted on non-irradiated Zircaloy-4 cladding tubes using the test apparatus shown in Fig.2-6(a) to investigate the ballooning size and rupture-opening area of the post-test cladding tube (Fig.2-6(b)). Steam or argon gas was caused to flow outside the test rod to evaluate the effect of oxidation upon the degree of deformation of the cladding tube. Moreover, the burst temperature of the test rod was changed by controlling the internal pressure to estimate the effect of crystal-phase condition upon the amount of deformation of the cladding tube.

To eliminate the effect of the rod-internal pressure at burst, the maximum circumferential strain which was divided by the nominal stress just before the burst of cladding tube, $k$, tended to increase as the burst temperature approached the $\beta$-phase region (Fig.2-7(c)). In contrast, when the burst temperature reached this region, $k$ tended to increase in the argon-gas condition and decrease in the steam condition with increasing burst temperature. These results suggest that the embrittlement of the cladding tube due to oxidation affects the ballooning and rupture behaviors of the tube in this burst-temperature region. In addition, based on the relationship between the area of the rupture opening and the burst temperature of the cladding tube, it is found that the area of the rupture opening in the $\alpha$-phase region tended to be larger than that in the burst-temperature region where the $\beta$-phase existed (Fig.2-7(d)).

The results obtained in this study will be useful for evaluating the effect of burnup upon the amount of deformation and the shape of the rupture opening of a cladding tube during a LOCA.

**Reference**

Narukawa, T. et al., The Effect of Oxidation and Crystal Phase Condition on the Ballooning and Rupture Behavior of Zircaloy-4 Cladding Tube-under Transient-Heating Conditions, Journal of Nuclear Science and Technology, vol.53, issue 1, 2016, p.112-122.

# 2–3 Chemistry of Fission Products during Severe Accidents

## — Effect of the Chemical Form of the Fission Products upon the pH of Coolant Water —

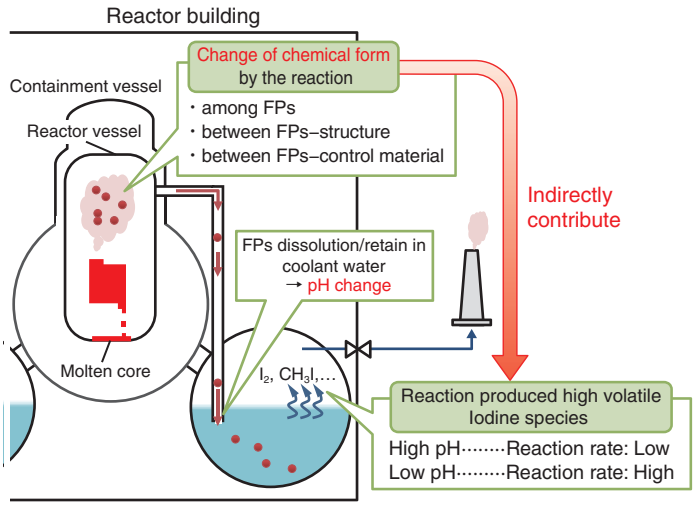


**Fig.2-8 Chemical behavior of fission products during severe accidents**
The chemical forms of fission products (FPs), which can change by reactions with other FPs and structure/control materials, may indirectly enhance the gaseous iodine compounds released from coolant owing to pH change.

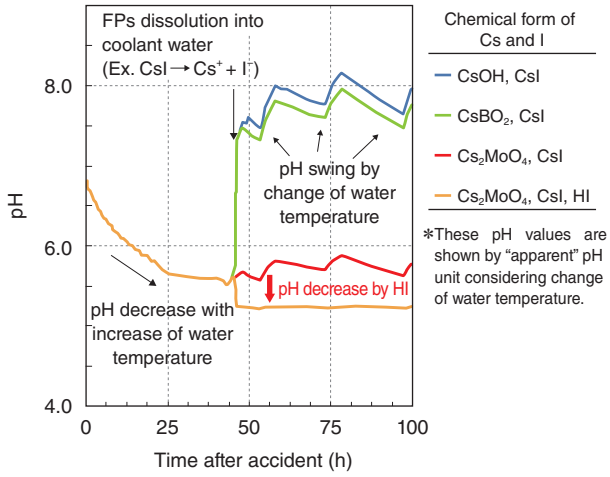


**Fig.2-9 Calculated pH histories depending upon the chemical forms of Cs and I**
Accident-progression analysis using the chemical forms of Cs and I as parameters was performed to determine the FP distribution using the THALES2 code developed by JAEA as an integral severe accident analysis code. The solution pH was evaluated based on the content of Cs and I of each of species in coolant water obtained through the analysis.

Evaluation of public exposure at severe accident (SA) with core melt requires source term information for easily released fission product (FP) such as Cesium (Cs) and Iodine (I), including the mass and chemical species of FPs released into environment. Although the source term can be generally evaluated with SA analysis codes based on various models for physical/chemical phenomena, these results include uncertainties attributed to difficulty in understanding phenomena under the severe condition. One important phenomenon with a large uncertainty and impact on the accident analysis at the TEPCO's Fukushima Daiichi NPS is the effect of boron (B) as a control rod material upon the chemical forms of Cs and I. The change of chemical form should affect the conversion of I ions dissolved in coolant water into highly volatile species (Fig.2-8), because the FP dissolution into coolant water can change pH. Chemical forms of decreasing pH are important because the reaction is accelerated, especially at lower pH.

Therefore, we estimated the chemical forms of Cs and I in gas phases that included B and other FPs based on thermodynamic equilibrium calculations and then evaluated pH considering the amount of FPs transported into the coolant water.

Consequently, it was found that CsI, CsOH, $Cs_2MoO_4$, and $CsBO_2$ were formed with Cs and that CsI and HI were formed with I in the gas temperature range from 500 to 3000 K. In addition, the amount of $CsBO_2$ and HI increased with the decrease in the amount of $Cs_2MoO_4$ and CsI in the case of lager amounts of B. Their effect on pH was dependent upon the chemical form of each species (Fig.2-9). CsOH or $CsBO_2$ with CsI contributed to the increase in pH. $Cs_2MoO_4$ with CsI did not significantly change pH, whereas $Cs_2MoO_4$ with HI decreased pH. Considering thermodynamic equilibrium for systems including Cs and B, the range of thermal stability differed between $Cs_2MoO_4$ and HI. However, from the viewpoint of kinetics, HI produced at high temperatures can exist with $Cs_2MoO_4$ stabilized at low temperature because the degradation rate of HI is lower at low temperature. Thus, the results obtained in this study indicate that boron's effect on pH is of significant importance to evaluate the amount of I released because B can enhance the production of HI as a contributor to pH decrease.

For future work, we will incorporate the static/dynamic evaluation function for chemical form into the THALES2 code to upgrade the source term evaluation technique.

**Reference**

Shiotsu, H. et al., Thermochemical Analysis for Cesium and Iodine Species and Their Impact on Aqueous pH under Severe Accident Conditions, Proceedings of 2015 International Workshop on Post-Fukushima Challenges on Severe Accident Mitigation and Research Collaboration (SAMRC 2015), Daejeon, Korea, 2015, paper 1514, 8p., in USB Flash Drive.

# 2–4 A New Attempt to Compare Radiation Risks with the Other Health Risks
## — Radiation-Health-Risk Estimation in Disability-Adjusted Life Years (DALY) —

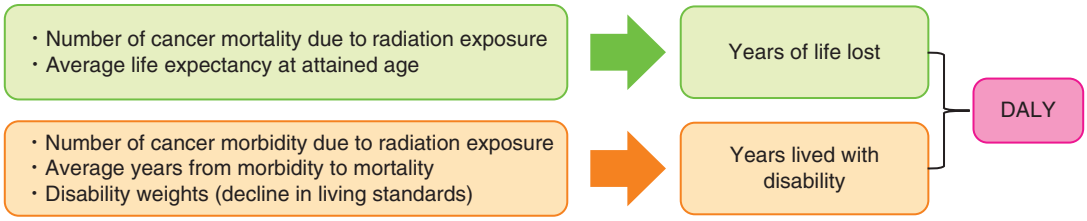


**Fig.2-10 Evaluation of DALY due to radiation exposure**
DALY due to radiation exposure are calculated as the sum of the years of life lost owing to cancer mortality and those lived with disability owing to cancer morbidity.

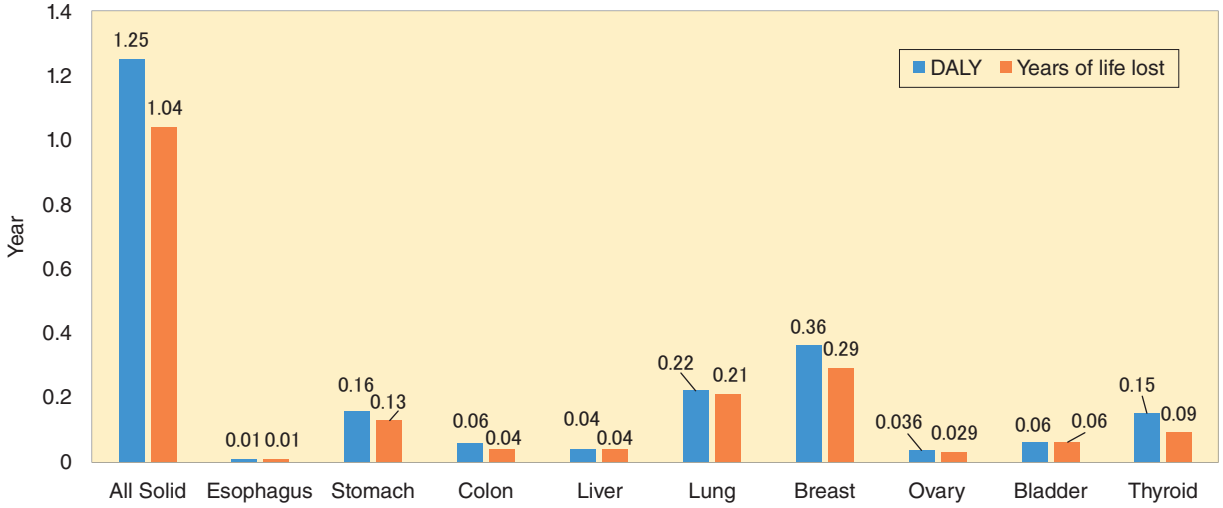


**Fig.2-11 Evaluation results of DALY and years of life lost by solid cancer in Japanese females owing to radiation exposure**
The DALY values of all solid cancer were approximately 16% higher than the number of years of life lost, owing to the influence of years lived with disability due to cancer morbidity; the survival fraction exceeding 5 years of breast and thyroid cancer are relatively high.

In Level-3 probabilistic risk assessment (Level-3 PRA), the risk indices of public health for severe accidents at nuclear power plant include cancer mortality, morbidity rates, and loss of life expectancy. However, these risk indices may underestimate the health risk to the public owing to radiation exposure because they do not consider the loss of health due to diseases. In contrast, in the field of public health, disability-adjusted life years (DALY), which are calculated as the sum of loss of life expectancy and years lived with disability, is used as a risk index for chemical materials and so on. DALY can compare various health risks to consider fatal and non-fatal diseases. Therefore, we have developed a health-risk-evaluation method for radiation exposure using DALY as a risk index.

Fig.2-10 shows the evaluation of radiation-exposure risk in terms of DALY. First, loss of life expectancies from cancer mortality due to radiation exposure are calculated. Second, years lived with disability are calculated to consider decreased quality of life from cancer morbidity. Finally, DALY values are calculated by summing loss of life expectancy and years lived with disability.

Fig.2-11 shows the DALY values and losses in life expectancy due to each type of solid cancer in Japanese females following a single exposure of 1000 mGy. The DALY values for all solid cancers were about 16% larger than the loss of life expectancy. Therefore, we can quantitatively evaluate the health risk due to radiation exposure considering decreased quality of life. Furthermore, we calculated the DALY values for all incidences of solid cancer spontaneously for the Japanese population in comparison with other health risks. The DALY values for all solid cancer incidences spontaneously were 4.26 years for males and 3.41 years for females. In contrast, the DALY values of all solid cancers due to 1000 mGy of radiation exposure were 0.73 years for males and 1.25 years for females. In other words, the health risk increased by approximately 17% (from 4.26 years to 4.99 years) for males and by approximately 37% (from 3.41 years to 4.66 years) for females as compared with normal life.

In summary, we performed a detailed health-risk assessment for radiation exposure to the public during nuclear-power-plant accidents. In the future, we will estimate the health risk to the public arising from hypothetical accident scenarios at nuclear power plants using level-3 PRA and examine the safety goals of nuclear power plants based on the risk information.

**Reference**

Shimada, K. et al., Calculating Disability-Adjusted Life Years (DALY) as a Measure of Excess Cancer Risk Following Radiation Exposure, Journal of Radiological Protection, vol.35, no.4, 2015, p.763-775.

# 2–5 Acquisition of Data Required for Severe-Accident Evaluation in a Reprocessing Plant

## — Understanding the Release Characteristics of Ruthenium from Highly Active Liquid Waste during a Drying Step —

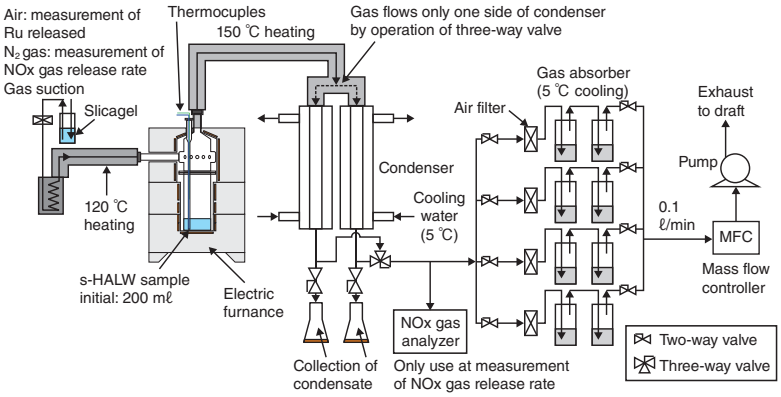


**Fig.2-12 Diagram of the experimental apparatus**
The temperature of the simulated highly active liquid waste (s-HALW) was increased, as shown in Fig.2-13. Released gases from the s-HALW containing steam and Ru were collected as the condensate in a condenser. The number of mols of Ru in the condensate samples was analyzed by inductively coupled plasma mass spectrometry (ICP-MS).

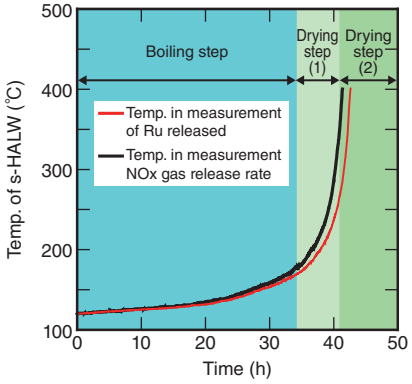


**Fig.2-13 Condition of temperature increase of the s-HALW**
The rate and time of temperature increase of the s-HALW were experimentally simulated based on the computer-code analysis of a HALW-storage tank in the postulated accident.

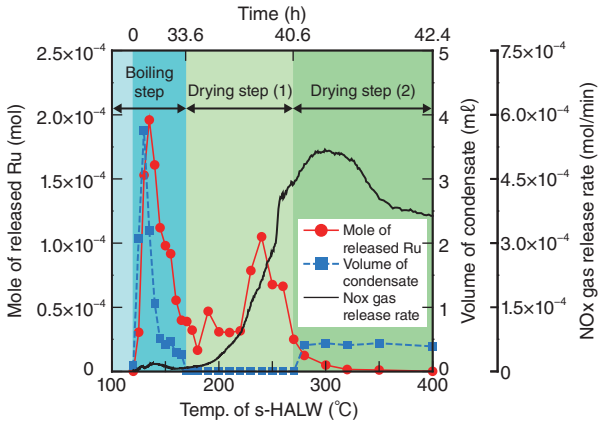


**Fig.2-14 Measurement results for mole of released Ru, volume of condensate, and NOx-gas release rate in terms of the s-HALW temperature**
Under the s-HALW-temperature condition shown in Fig.2-13, it was found that release behavior of Ru is dependent upon three divided zones of the s-HALW temperature during the period from the boiling step to the drying step.

When the cooling function for HALW in the fuel-reprocessing plant is lost, the HALW is heated by the decay of dissolved radioactive materials, which may cause boiling and dryout. Since the radioactive materials may be released from the HALW to the air, it is necessary to quantitatively understand their release and transport behavior to evaluate the safety at a plant during such an accident. In particular, since Ruthenium (Ru) can transform into volatile species during the boiling and drying steps, the release ratio of Ru from the HALW would be larger than those of other non-volatile elements. Therefore, Ru is considered an important element from the viewpoint of estimating the public dose from the accident.

Therefore, we performed experiments to acquire practical data on Ru-release behavior using s-HALW, which was prepared with stable isotopes including lanthanide elements based on the composition of HALW. The test conditions included a very slow rate and time of temperature increase based on the computer code analysis for an HALW-storage tank in a postulated accident.

The s-HALW was heated in the electrical furnace shown in Fig.2-12 under the experimental condition of s-HALW-temperature rise, as shown in Fig.2-13. Measurement results for the mole of released Ru, the volume of condensate, and the NOx-gas-release rate in terms of the s-HALW temperature are shown in Fig.2-14. It was found that the release behavior of Ru was dependent upon three divided zones of the s-HALW temperature during the period from the boiling step to the drying step.

The release mechanism of Ru in each region was considered as follows. In the boiling step, the concentration of s-HALW increased owing to steam release. Ru was released as a volatile species transformed by the oxidizability of highly concentrated nitric acid. When the release of steam went to the end, the amount of the Ru release was temporarily decreased. In the drying step (1), in which the condensate was not collected, Ru release resulted from progress of thermal decomposition of Ru nitrate with NOx release in the dried s-HALW. In the drying step (2), a small amount of steam was released, probably owing to desorption of hydrates of lanthanide nitrates. The NOx release was owing to thermal decomposition of lanthanide nitrates. In contrast, the amount of Ru released monotonically decreased because of the regress of thermal decomposition of Ru nitrate in the drying step (1). We are the first group to obtain detailed data on the amount of Ru released depending on the HALW temperature during the drying-step period. These data will be useful for investigating effective accident-management measures to mitigate the amount of the Ru release, considering the HALW temperature if the accident is in the drying step owing to loss of the cooling function.

**Reference**

Tashiro, S. et al., Release Characteristics of Ruthenium from Highly Active Liquid Waste in Drying Step, Nippon Genshiryoku Gakkai Wabun Ronbunshi (Transactions of the Atomic Energy Society of Japan), vol.14, no.4, 2015, p.227-234 (in Japanese).

# 2–6 Evaluation of the Criticality Characteristics of Fuel Debris
## — Study of the Critical Experiment using the Modified STACY —

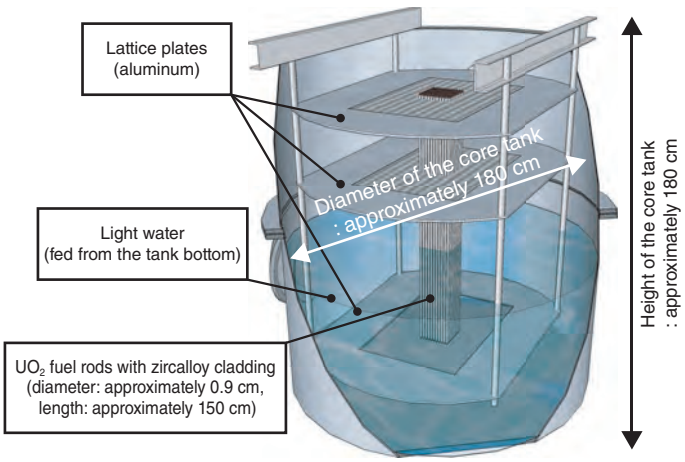


**Fig.2-15 Overview of the modified STACY**
Fuel rods will be supported by lattice palates. The moderator-to-fuel-volume ratio will be adjusted by changing the interval of the fuel rods. The modified STACY will be able to simulate various moderator conditions for the analysis of fuel debris.

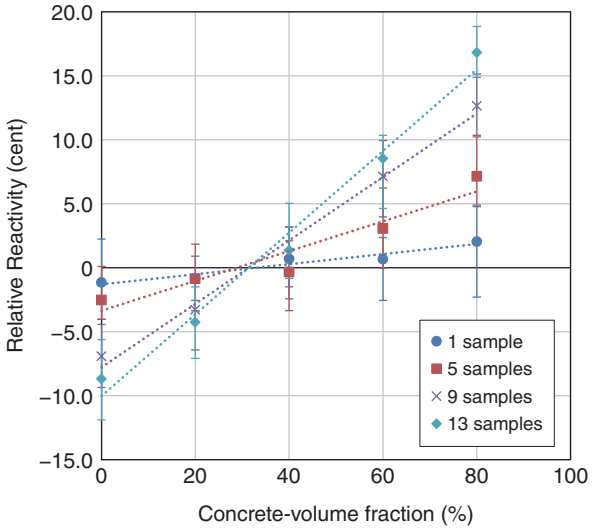


**Fig.2-16 Estimation of reactivity changes using a number of samples and the concrete volume fractions of pseudo fuel debris**
The reactivity changes of pseudo fuel debris under certain $V_m/V_f$ conditions are dependent on the number of samples and the concrete-volume fractions. We have studied the experimental core configurations to measure their reactivity changes with high accuracy.

In the accident at the TEPCO's Fukushima Daiichi NPS, it is conceivable that fuel debris may have formed from melted nuclear fuels and structural materials such as iron and concrete. It is important to evaluate the criticality characteristics of fuel debris using computational models for the decommissioning project including defueling. Furthermore, we should validate the uncertainties of the computations using critical experiments with pseudo fuel debris to clarify their criticality characteristics. For this purpose, the modification of STACY, whose core is being converted from a uranyl-nitrate-solution-fuel type to a $UO_2$-fuel-rod-and-water-moderator type, is now underway at JAEA.

As shown in Fig.2-15, the fuel rods will be arrayed at some interval and supported by lattice plates in the modified STACY core tank. The moderator-to-fuel-volume ratios ($V_m/V_f$) of the test core will be varied by changing the array interval. The criticality characteristics of fuel debris are largely influenced by $V_m/V_f$ as well as the total amount of fissile material and the geometries of fuel debris. Furthermore, the pseudo fuel debris including concrete will have specific critical characteristics because concrete includes water, contributing to neutron moderation. In the critical experiment, we will measure variation of the critical water heights; one of them is a base-core configuration comprising only a normal fuel-rod array; the other is a core configuration with pseudo fuel debris. The variation will be interpreted into a critical characteristic called "reactivity" (unit: cent).

We studied the experimental core configurations and the necessary numbers of samples for high-accuracy reactivity measurements of pseudo fuel debris using the radiation-transport-calculation-code system MCNP 5.1 and the evaluated nuclear-data library JENDL4 evaluated by JAEA. For example, when $V_m/V_f$ is 1.2, the calculation results of reactivity effects by the changing concrete-volume fraction are shown in Fig.2-16. This figure shows that the concrete-volume fraction has a big impact upon the reactivity, and there is a tendency for reactivity to become more positive with increase in the concrete-volume fraction. It is thought that the number of samples should be at least five to realize a condition with reactivity sufficiently large to be measured easily. In contrast, when the concrete-volume fraction is 30%, the reactivity change is too small to be measured. In this case, we should consider changing the experimental-core configuration. Following these studies, we are going to establish experimental conditions and procedures using the modified STACY. Furthermore, the measurement data from critical experiments will be useful for developing the methods for critical control of fuel debris.

This study includes the results of contract work funded by the Secretariat of the Nuclear Regulation Authority (NRA) of Japan.

**Reference**

Gunji, S. et al., Study of Experimental Core Configuration of the Modified STACY for Reactivity Worth Measurement of MCCI Products, Proceedings of PHYSOR 2016, Sun Valley, Idaho, USA, 2016, p.3927-3936, in USB Flash Drive.

# Advanced Science Pioneers the Future

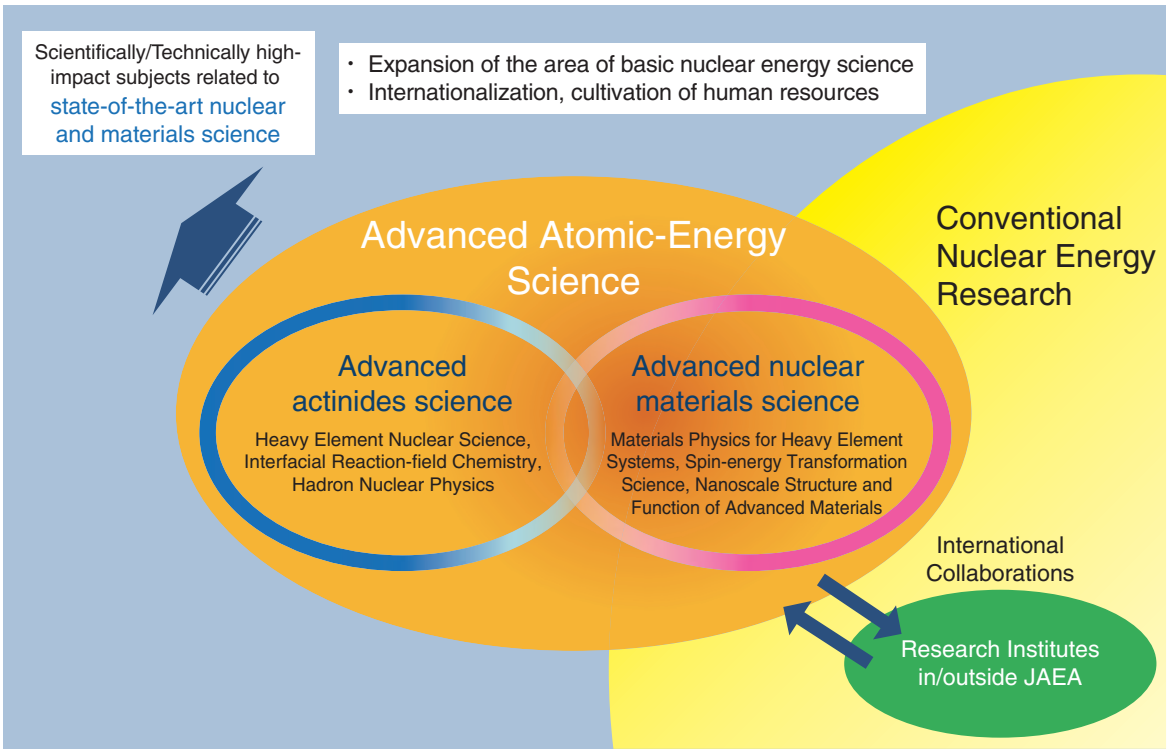


**Fig.3-1 The role of advanced nuclear scientific research**
Our aim is to perform high-impact scientific and technical studies related to state-of-the-art nuclear and materials science.

Basic science supports the greater part of nuclear-energy-related technology. In research, it is particularly crucial to respond to the new stage of nuclear energy development that we will be entering in the next few decades as well as to constantly seek solutions to today's energy problems.

The role of the Advanced Science Research Center (ASRC) is to explore the unlimited possibility of nuclear energy from the perspective of basic science. In this process, we aim to open up new research fields and strive to further develop science and technology. Beginning in FY2015, we started our mid-term plan, focusing on two main areas: advanced actinides science and advanced nuclear materials science (Fig.3-1). Research on the former has been conducted with the aim of creating a new concept for nuclear and heavy-element-based actinides science. For the latter, we have commenced investigation and development of new nuclear-energy-related materials. Through interactions between the two areas and collaboration with research institutes inside and outside of the Japan Atomic Energy Agency (JAEA), we have been working on cultivating new fields of nuclear-energy science (Fig.3-1).

We have made numerous highlighted achievements during FY2015. Through advanced actinides science, nuclear-charge-symmetry breaking by a strange particle was observed at the J-PARC Hadron Experimental Facility (Topic 3-4); this discovery may lead to a way to solve a mystery of the nuclear force among protons, neutrons, and so on. A large-scale nuclear-structure calculation to constrain the masses of neutrinos using the K supercomputer (Topic 3-5) was provided using extensive numerical simulations. A new technology for controlling the migration of cesium from forests to living areas had been developed, along with a means to regenerate village forests using polymers and clay (Chapter 1, Topic 1-15), which was demonstrated by verification tests in Iitate village, Fukushima. This accomplishment is expected to prevent recontamination of living areas.

Substantial results have been obtained by advanced nuclear-materials science. The discovery of a novel mechanism of superconductivity induced by strong magnetic fields (Topic 3-1) may allow the development of new functions of uranium-based compounds. Electrical generation from the quantum-mechanical-spinning motion in a liquid metal (Topic 3-2) may serve as a new electrical-generation source. This accomplishment in particular was published by Nature Physics and featured at the editors' choice (News&Views et al.) of Nature Physics, Nature Materials, and Science. A new material-surface-analysis, positron diffraction, revealed the interface structure between graphene and a metal substrate (Topic 3-3).

The ASRC thinks it important to develop nuclear human resources with expertise and to demonstrating their total abilities through nuclear basic research.

# 3–1 Reentrant Superconductivity Induced by a Strong Magnetic Field

## — New Functional Properties of Uranium Compounds Controlled by a Magnetic Field —

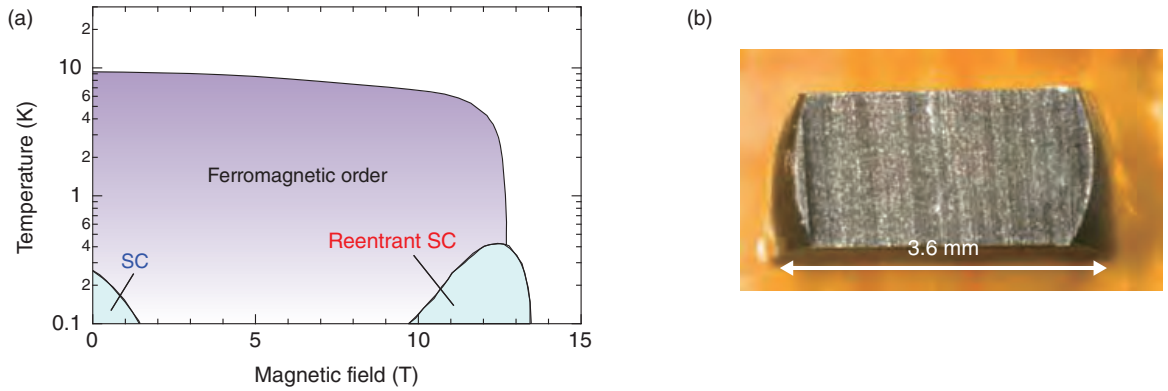


**Fig.3-2 Phase diagram of URhGe under a magnetic field and a single crystal prepared for NMR measurements**
(a) Superconductivity (SC) exists deep in the ferromagnetic state of URhGe under zero magnetic field. An applied magnetic field first suppresses the superconductivity around 2 T and then induces the reentrant superconductivity between 10 and 14 T. (b) Photograph of a single 10%-Co-doped crystal of URhGe.

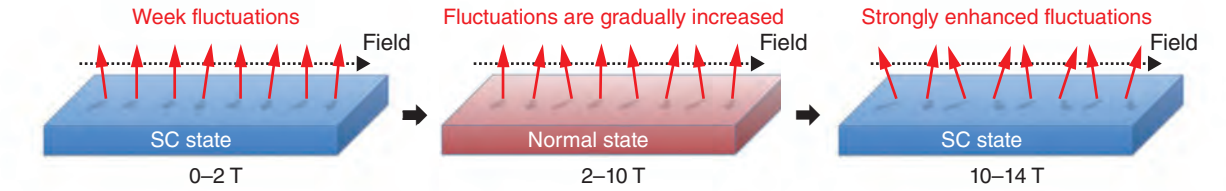


**Fig.3-3 The mechanism of reentrant superconductivity induced by strong magnetic fields (a schematic view)**
Superconductivity is mediated by week magnetic fluctuations of uranium 5f spin moments at lower magnetic fields, which are suppressed by an applied field around 2 T. A further increase in magnetic field enhances the magnetic fluctuations and finally induces reentrant superconductivity around 10–14 T.

Magnetic fields are incompatible in general with superconductivity. All superconductors possess an upper critical field above which superconductivity is completely suppressed. Therefore, the development of superconducting materials with higher upper critical fields has been a central issue in the industrial production of electrical wires and superconducting magnets. Recently, however, a field-induced reentrant superconductivity was discovered under strong magnetic fields in the uranium-based compound URhGe. In this compound, the applied magnetic field first suppresses superconductivity around 2 T, but then the reentrant superconducting phase appears between 10 and 14 T (Fig.3-2(a)). This unusual phenomenon tells us that the magnetic field is not always incompatible with superconductivity but can help its emergence in some cases. The existence of a novel superconducting mechanism is thus expected in URhGe, and might be available for the development of new superconducting devices controlled by strong magnetic fields.

To microscopically investigate the mechanism of reentrant superconductivity, we prepared a 10% Co-doped URhGe single crystal (Fig.3-2(b)) and performed Co nuclear-magnetic resonance (NMR) experiments using a strong magnet installed at the French National High Magnetic Field Laboratory (the maximum field of which is 34 T). The NMR experiments revealed the rapid increase of magnetic fluctuations of uranium 5f spin moments in the field region of 10–14 T, where reentrant superconductivity was observed. This provides strong evidence that superconductivity in URhGe is mediated by the magnetic fluctuations, and further, that reentrant superconductivity occurs owing to the enhancement of these fluctuations under strong magnetic fields (Fig.3-3).

Since the superconducting transition temperature of URhGe is very low, less than 1 K (−272 °C), it might be difficult to use it for industrial applications immediately. However, understanding of the mechanism behind reentrant superconductivity certainly increases our knowledge-base for developing new superconducting materials and devices working under strong magnetic fields. It is also important to notice that, so far, the reentrant superconductivity mediated by magnetic fluctuations has been discovered only in uranium-based compounds. This implies the crucial role of uranium-5f electrons in the occurrence of this exotic phenomenon. Further investigations are necessary to understand the complex and interesting nature of superconductivity and magnetism in uranium-based compounds.

Our research was accomplished as a collaborative study with the Tohoku University, and supported by the Japan Society for the Promotion of Science (JSPS) KAKENHI Grant-in-Aid for Scientific Research (C) (No.26400375).

**Reference**

Tokunaga, Y. et al., Reentrant Superconductivity Driven by Quantum Tricritical Fluctuations in URhGe: Evidence from $^{59}$Co NMR in $URh_{0.9}Co_{0.1}Ge$, Physical Review Letters, vol.114, issue 21, 2015, p.216401-1-216401-5.

# 3–2 Electrical Generation from Liquid-Metal Flow

## — Discovery of a New Principle of Electrical Generation via Electron-Spin Motion —

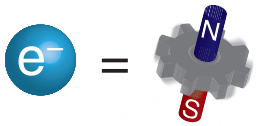


**Fig.3-4 Visualization of an electron**
Electrons have electric charge as well as spin, which can be visualized as a small magnet with a spinning gear.

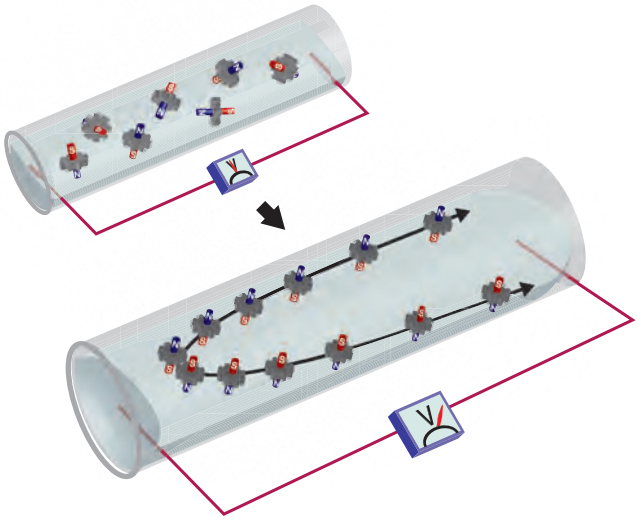

**Fig.3-5 Spin-current generation from a liquid-metal flow**
A "spin current," or flow of electron spins, is created by a pipe flow of a liquid metal.

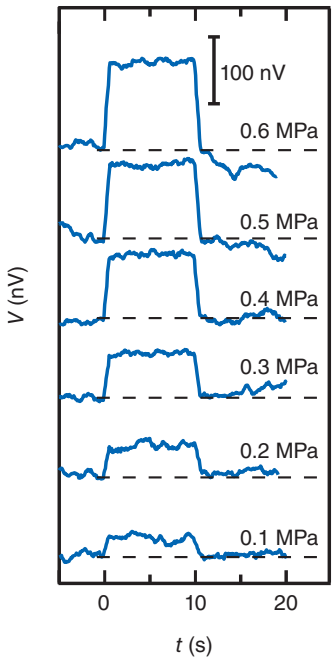


**Fig.3-6 Electric voltage from a liquid-metal flow**
We excited liquid-metal flows in a narrow channel, with spin current being generated by the vorticity fluctuation of the flow. The spin current is observed as the longitudinal-voyage generation.

Quantum mechanics reveals that electrons are charged elementary particles with spin. Owing to this quantum mechanical spin, electrons can be imagined as a spinning gear with a magnet whose poles are parallel to the spinning axis. Since the spinning motion is perpetual, the magnetism is permanent (Fig.3-4).

We benefit significantly from spin via magnetic materials such as iron wherein spins are intrinsically aligned. Conversely, it is difficult to utilize electron-spin functions in non-magnetic materials because the spinning axes are incoherent and thus, the spins cancel each other out.

Recent nanotechnological progress enables us to utilize spins in non-magnetic materials and generate a spin current (i.e., a flow of electron spins). Conventional electric devices consume power owing to the Joule heating of the charge current; in contrast, alternative devices based on the spin current are considered to save energy as its Joule heating is known to be much smaller than that of the charge current.

Spin currents have previously been generated only in solids, but we have discovered a new mechanism of spin-current generation using liquids.

Our theoretical calculation predicts that a spin current can be generated owing to the vorticity (i.e., the local rotational motion) of a liquid metal. When a liquid-metal flow is excited in a fine pipe by applying pressure, vorticity is induced in the liquid. The vorticity aligns the spinning axes of the "gears"; consequently, a spin current is created (Fig.3-5). The prediction is confirmed experimentally using a fine pipe of radius 400 $\mu$m. The electric voltage observed because of the spin current was several hundred nano volts (Fig.3-6).

The result proves the existence of a coupling between electron spin and fluid vorticity for the first time. Owing to this coupling, microscopic spinning motion can be controlled by macroscopic fluid motion. From an application point of view, the observed generation effects can be used to make an electric generator in an ultra-small device.

**Reference**

Takahashi, R., Matsuo, M. et al., Spin Hydrodynamic Generation, Nature Physics, vol.12, 2016, p.52-56.

# 3–3 Positron Diffraction Technique Reveals an Interface Structure between Graphene and Metal Substrates — Elements in Substrate Change the Bonding Character of Graphene —

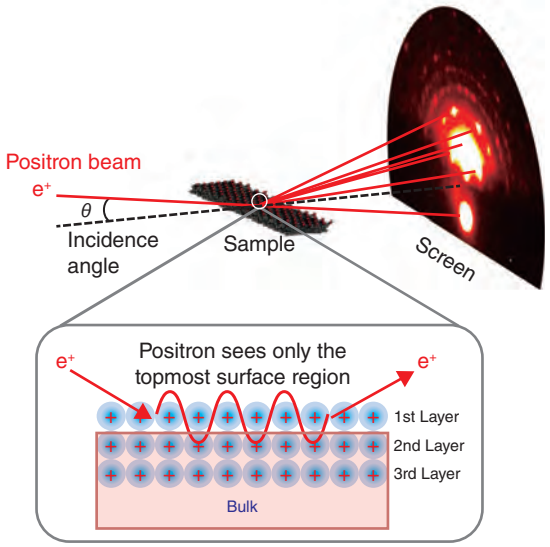


**Fig.3-7 Setup of total-reflection high-energy positron diffraction (TRHEPD) experiment**
The incident positron beam with an energy of 10 keV is scattered on the sample surface at a grazing angle, and diffracted positrons are observed on a screen. Since the positron, having a positive charge, is repelled by the sample surface, the diffracted positrons contain information only about the topmost- and near-surface layers.

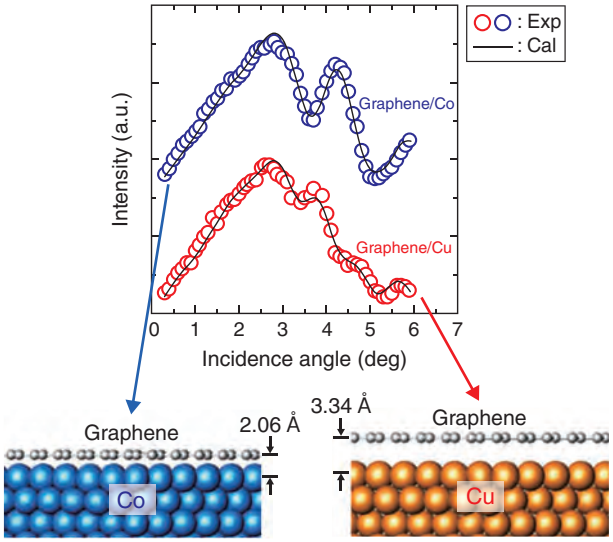


**Fig.3-8 Intensity of diffracted positrons for graphene/Co and graphene/Cu and analytical results**
Open circles in the upper part indicate the intensity of the diffracted positrons as a function of the incidence angle. Solid lines are the intensity calculated using the structure models depicted in the lower part. The peak positions reflect the height of the graphene from the substrate. Intensity analysis of the diffracted positions shows that the bonding character of graphene differs considerably for the Co and Cu substrates.

Recently, graphene, a two-dimensional atomic sheet of carbon, has been extensively investigated with a view to potential applications in future energy-saving and high-speed devices. Graphene, the discovery of which was awarded the 2010 Nobel Prize in Physics, is well known to have many promising features, including high carrier mobility and robust mechanical properties. There have been many studies on the properties of free-standing graphene. However, the properties of graphene in contact with other substances remain largely unknown. Because graphene has a very thin, one-atomic-layer thickness, its properties may be affected by substances with which it is in contact. In order to clarify this, it is necessary to investigate the graphene itself and the interface between the graphene and its substrate. Analyzing such a thin region near the topmost surface layer is difficult. Therefore, there are strong demands for experimental methods with limited penetration depth. We have developed a total-reflection high-energy positron diffraction (TRHEPD) technique and measured the interface between the graphene and the metal substrates. Fig.3-7 shows the experimental setup of the TRHEPD technique. Since the positron, the antiparticle of the electron, has a positive charge (opposite to that of the electron), it feels the repulsive force from materials. Thus, the positron beam does not penetrate the deeper bulk region. Therefore, the TRHEPD method enables us to accurately determine atomic configurations of the topmost- and near-surface layers.

In the present study, we fabricated graphene on two different metal substrates, namely cobalt (Co) and copper (Cu), and performed the TRHEPD experiments. We found that the peak positions of the diffracted positrons for the Co and Cu substrates are significantly different (Fig.3-8). As a result of this intensity analysis, the spacing between the graphene and the Co substrate was determined as 2.06 Å. For the Cu substrate, however, the spacing was observed to be 3.34 Å, which is more than 1 Å larger that of the Co substrate. It is known that the atomic layers of graphite, which is a stack of graphene layers, are weakly bonded to each other and that the interlayer distance is 3.3 Å. Therefore, graphene is strongly bonded to the Co substrate, whereas in the Cu case, the interaction is very weak. We experimentally verified that the bonding character of the graphene changes depending upon the element of the substrate.

Recently, two-dimensional atomic sheets such as silicene (the Si version of graphene) and germanene (the Ge version), which do not exist in nature, have been successfully fabricated on various substrates. Furthermore, atomic sheets of superconductors on insulator substrates give rise to high-temperature superconductivity. In the near future, we will investigate such novel atomic sheets and the interface with the substrate using the TRHEPD method.

This work has been conducted in collaboration with the High Energy Accelerator Research Organization (KEK).

**Reference**

Fukaya, Y. et al., Spacing between Graphene and Metal Substrates Studied with Total-Reflection High-Energy Positron Diffraction, Carbon, vol.103, 2016, p.1-4.

# 3–4 A "Strange Particle" Breaks the Charge Symmetry of a Nucleus

## — Successful Measurement of the Energy Levels of a Helium Hypernucleus —

(a) Experimental setup of J-PARC-E13

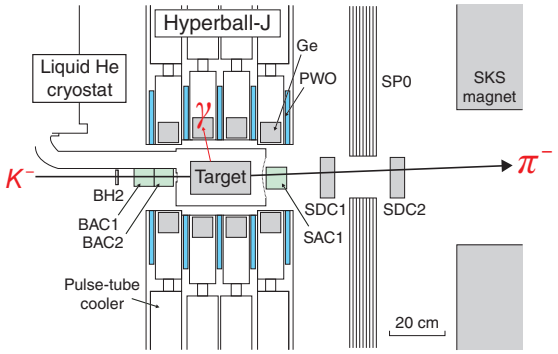


(b) Reaction of the hypernuclear production

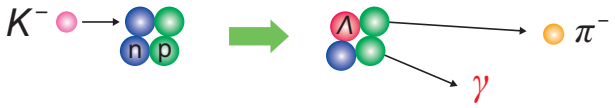


**Fig.3-9 (a) Experimental setup of J-PARC-E13 and (b) reaction of the hypernuclear production**
(a) The E13 setup comprises a $\gamma$-ray detector (Hyperball-J) and a $^4$He target as well as $K^-$ and $\pi^-$ identification detectors (BAC1, BAC2, and SAC1).
(b) A schematic view of the $K^- + {}^4\mathrm{He} \rightarrow {}^4_\Lambda\mathrm{He} + \pi^- + \gamma$ reaction.

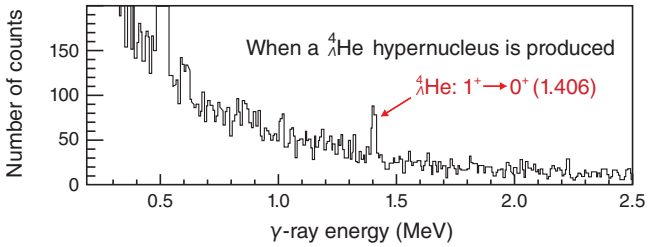


**Fig.3-10 Measured $\gamma$-ray-energy spectrum**
A $\gamma$-ray energy spectrum measured by the $\gamma$-ray detector. In this spectrum, only $^4_\Lambda$He-production-candidate events are selected.

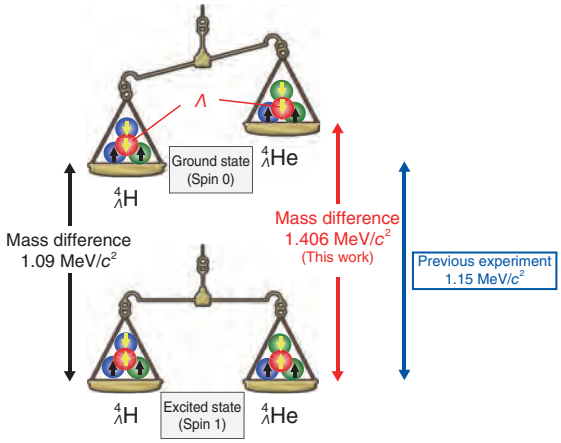


**Fig.3-11 Comparison of mass between $^4_\Lambda$H and $^4_\Lambda$He**
The mass difference between the excited states of $^4_\Lambda$He measured in this experiment is 1.406 MeV/$c^2$, whereas that of $^4_\Lambda$H is 1.09 MeV/$c^2$. There is a large mass difference of 0.32 MeV/$c^2$ between $^4_\Lambda$H and $^4_\Lambda$He, which shows a large charge-symmetry breaking.

Two normal nuclei for which the protons and neutrons are exchanged (known as mirror nuclei) have almost the same mass. This is known as the charge symmetry. Is this also the case for hypernuclei, which include a $\Lambda$ particle known as a "strange particle?" $\Lambda$ is a similar type of heavy particle (baryon) to a proton or a neutron but includes a rather heavy strange quark; this contrasts with protons and neutrons, which consist only of light up and down quarks.

A past experiment that involved measuring $\gamma$ rays emitted from $^4_\Lambda$He hypernucleus showed there was almost no mass difference from its mirror nucleus $^4_\Lambda$H in either the ground or excited states. Therefore, it was claimed that the charge symmetry held. However, since this experiment had poor energy resolution and signal-to-noise ratio, confirmation by an improved experiment has been required.

Therefore, we have proposed an experiment at the J-PARC Hadron Experimental Facility to measure $\gamma$ rays at high-energy resolution from $^4_\Lambda$He hypernuclei that are produced by injecting the world's highest-intensity $K^-$ beam (the total number of $K^-$ is $2.3 \times 10^{10}$) onto a $^4$He target. This reaction is $K^- + {}^4\mathrm{He} \rightarrow {}^4_\Lambda\mathrm{He} + \pi^- + \gamma$, as shown in Fig.3-9(b). For this experiment, we developed a $\gamma$-ray detector which can be operated at $10^6$ Hz $K^-$ beams as shown in Fig.3-9(a), and developed a fast-rejection technique for background $\gamma$ rays with mechanical refrigerators for Ge crystals and PWO (lead tungstate) crystal-scintillation counters. Consequently, we obtained the $\gamma$-ray spectrum shown in Fig.3-10 and succeeded in improving $\gamma$-ray energy resolution 20 fold.

In this experiment, we measured a mass difference of 1.406 MeV/$c^2$ between the excited and ground states, as shown in Fig.3-11. The precise experimental data excluded the previous experimental result of 1.15 MeV/$c^2$. Consequently, we discovered that the mass difference from the mirror nucleus $^4_\Lambda$H is significant, namely 0.32 MeV/$c^2$, in contrast to the small mass difference of 0.06 MeV/$c^2$ for normal nuclei. From this large mass difference, i.e., the charge-symmetry breaking, we learned that the forces between a $\Lambda$ and a neutron and between a $\Lambda$ and a proton differ largely depending upon the spin state (namely the excited state). This work provided important data concerning the nuclear force between baryons such as protons, neutrons, and $\Lambda$s.

**Reference**

Yamamoto, T.O., Sako, H. et al., Observation of Spin-Dependent Charge Symmetry Breaking in $\Lambda N$ Interaction: Gamma-Ray Spectroscopy of $^4_\Lambda$He, Physical Review Letters, vol.115, issue 22, 2015, p.222501-1-222501-5.

# 3–5 Exploring the Mystery of Neutrino Masses with Nuclear Physics
## — High-Precision Calculation of $\beta\beta$ Decay using the K Supercomputer —

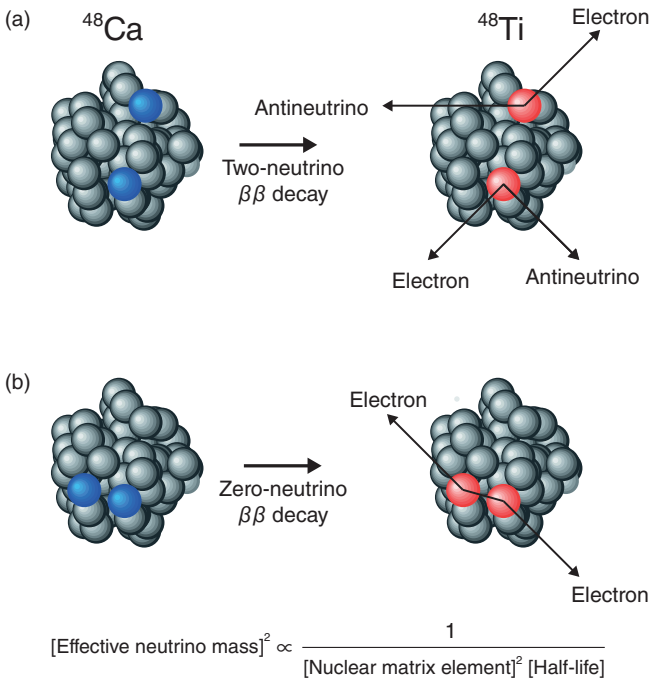


**Fig.3-12 Schematic illustration of $\beta\beta$ decay from $^{48}$Ca to $^{48}$Ti**
(a) Two-neutrino $\beta\beta$ decay and (b) zero-neutrino $\beta\beta$ decay are shown, both of which involve two protons (blue) changing into two neutrons (red). (a) Two neutrinos and (b) no neutrinos are emitted in addition to two electrons in common. (b) In the zero-neutrino $\beta\beta$ decay, the effective neutrino mass, i.e., a particular combination of the masses of three types of neutrinos, is related to the nuclear matrix element and the half-life by the equation displayed.

Neutrinos are a type of elementary particle. While the basic properties of neutrinos are indispensable for determining the theory of everything, most of them are still unknown. It has recently been established, on the basis of observations with Super-Kamiokande, that neutrinos are massive particles; however, their absolute masses have not been measured yet. In the present study, we provide reliable nuclear-structure data that are needed to determine neutrino masses from $\beta\beta$ decay by performing large-scale numerical calculations based on state-of-the-art nuclear theory.

$\beta\beta$ decay is a sort of nuclear decay in which two neutrons in a nucleus simultaneously change into two protons, as illustrated in Fig.3-12. This decay has been observed for ~10 nuclides, including $^{48}$Ca, and all the observed decay modes so far are so-called two-neutrino $\beta\beta$ decays, which emit two antineutrinos. It is nevertheless possible to detect another decay mode that does not emit any neutrinos (and is thus called zero-neutrino $\beta\beta$ decay) if neutrinos are their own antiparticles. When the half-life of zero-neutrino $\beta\beta$ decay is measured, neutrino masses can be determined using the equation shown in Fig.3-12(b). In order to derive neutrino masses in this way, however, one has to know how large the nuclear matrix element of zero-neutrino $\beta\beta$ decay is.

The nuclear matrix element is a value that characterizes how easily two neutrons are converted into two protons within a nucleus, depending on proton and neutron numbers. The value cannot be directly determined by nuclear experiment, and therefore, the only way to provide its quantity is calculation based on nuclear many-body theory. Before this study, the nuclear matrix element of $^{48}$Ca was estimated through a rather approximate calculation that took only eight nucleons as being active out of 48 nucleons in total. This restriction was owing to the computational limits on treating many nucleons. In the present study, we are successful in conducting a high-precision, large-scale quantum many-body calculation that assumes 32 active nucleons using the K supercomputer. The resulting nuclear matrix element in $^{48}$Ca becomes about 30% larger than that of the previous calculation. Since the present calculation considers the leading correction to the previous one, the obtained values should be quite reliable.

At present, zero-neutrino $\beta\beta$ decay is being sought worldwide. If this decay is observed in $^{48}$Ca in the near future, we expect that our value will be used to derive neutrino masses.

**Reference**

Iwata, Y., Utsuno, Y. et al., Large-Scale Shell-Model Analysis of the Neutrinoless $\beta\beta$ Decay of $^{48}$Ca, Physical Review Letters, vol.116, issue 11, 2016, p.112502-1-112502-6.

# 4 Nuclear Science and Engineering Research

## Promoting Basic R&D on Nuclear Energy and Creation of Innovative Technology to Meet Social Needs

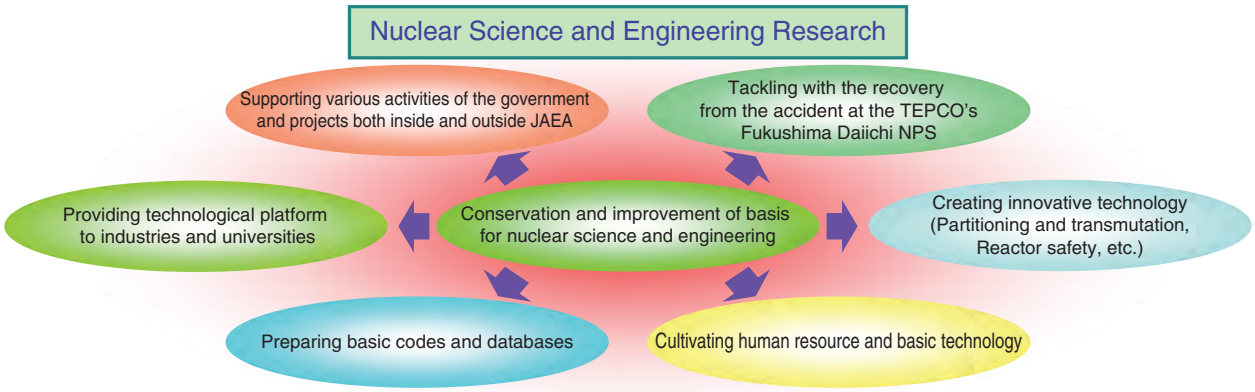


**Fig.4-1 Roles of nuclear science and engineering research**
We serve various roles to conserve and improve the foundation of nuclear science and engineering through fundamental research. Topics of study include nuclear science and reactor engineering, fuels and materials engineering, nuclear chemistry, and environmental and radiation science.

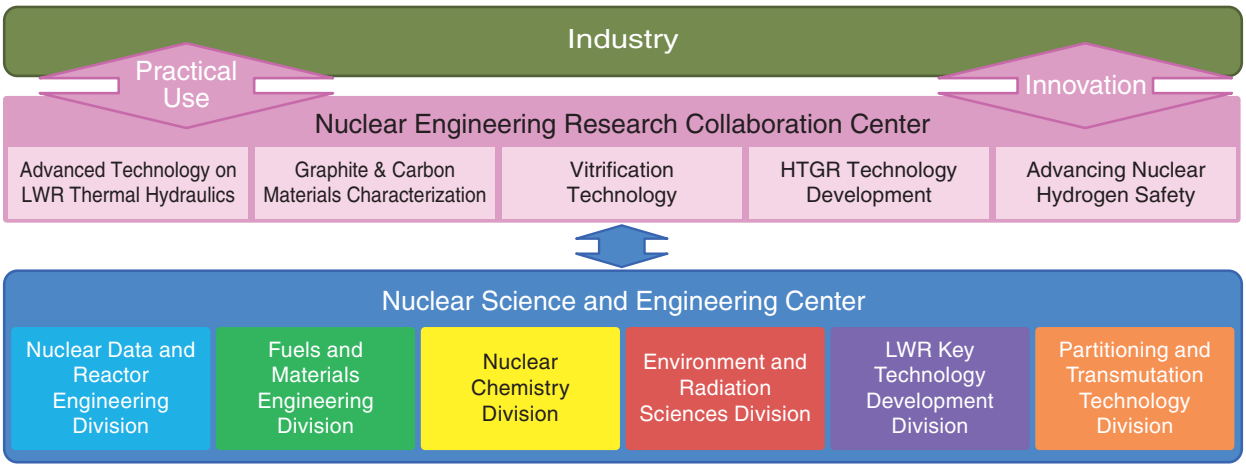


**Fig.4-2 Nuclear Engineering Research Collaboration Center**
Joint research with industry is being promoted to create innovative and practical products.

Nuclear science and engineering research aims to promote the activities shown in Fig.4-1, which include recovery from the accident at the TEPCO's Fukushima Daiichi NPS (1F), development of transmutation technologies to reduce the amount of long-lived radioactive waste, and key technology improving reactor safety. In the area of nuclear data and reactor engineering, we are revising the Japanese Evaluated Nuclear Data Library, measuring nuclear data, and developing a methodology for nuclear-reactor design based on advanced theoretical, experimental, and simulation approaches (Topics 4-1 and 4-2). In the area of fuels and materials engineering, research on the behavior of fuels and materials used in reactors and fuel-cycle facilities is also being promoted (Topics 4-3 and 4-4). In the area of nuclear chemistry, research is being promoted to obtain basic data for reprocessing and detection of extremely small amounts of nuclear materials (Topics 4-5 and 4-6). In the area of environmental and radiation sciences, studies of the behavior of radionuclides in the environment and on radiation protection with up-to-date scientific results are being advanced (Topics 4-7 and 4-8). Applying these results, we are conducting research on the improvement of nuclear safety (Topics 4-9 and 4-10). Based on the above fundamental technologies, joint research with industry is also being promoted via the Nuclear Engineering Research Collaboration Center (Fig.4-2).

Toward the development of fundamental technologies to aid the 1F recovery, we are studying the location of radioactive cesium (Cs) in the reactor building, prediction of the Cs dose distribution, melting-fuel behavior, fuel-cask soundness, recovering uranium (U) and plutonium (Pu) from fuel debris, and so forth. (Chapter 1, Topics 1-4, 1-5, 1-6, 1-7, 1-9, and 1-12).

In the field on technological developments to reduce the degree of hazard of radioactive wastes, the accelerator-driven subcritical system (ADS) is being studied for transmutation of minor actinide (MA) nuclides (ex. Neptunium and Americium) (Topic 4-11). Technologies to effectively partition MA and fission product nuclides and produce MA fuel are also being developed (Topics 4-12 and 4-13).

# 4–1 Pursuit of Accurate Nuclear-Reaction Cross-Sections in the Resonant Region
## — Synergy between Nuclear-Data Measurement and Theory —

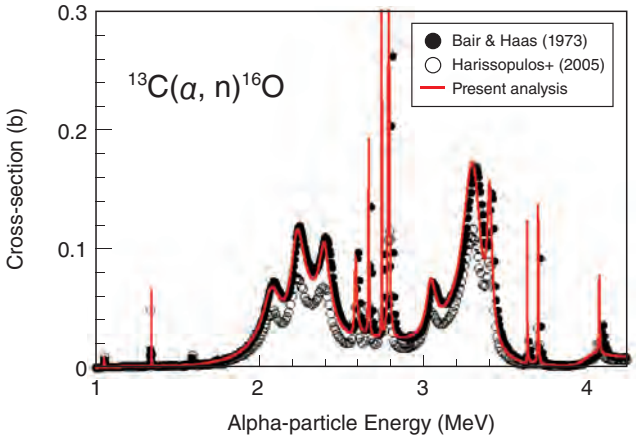


**Fig.4-3 The systematic difference between the measurements together with the estimated values from the present analysis**
We found that the systematic discrepancy among different experimental data could be resolved by a synergetic comparison between measurements and theory. In this example, an approximately 30% difference was observed between the old and recent measurements. Through shape analysis of the experimental data using R-matrix theory (which satisfies the quantum-mechanical conservation law), we obtained a result that supports the old measurement in this case.

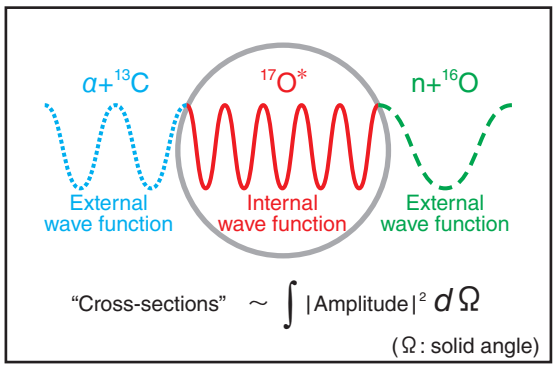


**Fig.4-4 Concept of the resonant nuclear-reaction theory (R-matrix)**
In the resonant nuclear-reaction theory adopted in this study, the matching condition of the internal and external wave functions is the parameter required for the calculation of the cross-sections. Note that the calculated cross-sections always satisfy the quantum-mechanical conservation law. In this study, we developed a computer code to obtain a value of the parameter from the shape of the experimental data.

Reactions occur in the nucleus with probabilities that depend on the energies of incident particles such as neutrons, protons, and alpha particles. Such probabilities, which are called nuclear-reaction cross-sections (or nuclear data), are fundamental values for nuclear engineering. With the recent progress of nuclear technology, cross-section data require ever-higher accuracy. Furthermore, the uncertainty values of these data must be fully accountable. To meet these demands, we are performing studies to enhance the general-purpose Japanese Evaluated Nuclear Data Library (JENDL; latest version is JENDL-4.0).

The cross-section shows resonant peaks in the low-energy particle reactions, reflecting the internal structure of the nucleus. Since those peaks are very difficult to predict only using nuclear theories, the most useful approach for determining the values is to conduct nuclear-data experiments at accelerator facilities with a combination of detectors. Here, let us indicate that we always see differences among measured data to a lesser or greater extent. An example is illustrated in Fig.4-3, in which an old measurement of the $^{13}C(\alpha, n)^{16}O$ reaction from 1970s and a recent one are systematically different by ~30%. Such a typical systematic difference is usually ascribable to uncertainty in the sample density.

In this study, we applied the R-matrix theory to the analysis of those experimental data (Fig.4-4). We adopted this theory essentially because it is strictly based on the quantum mechanics; hence, the theoretical calculation always obeys the quantum-mechanical conservation law (i.e., unitarity of the scattering matrix). The parameters in this theory are those for the matching condition of the internal and the external wave functions. We estimated those values from the shape of experimental data, assuming their absolute values to be unknown. The solid curve in Fig.4-3 shows the results of the present analysis, where the estimated values are consistent with the old experimental data. Moreover, the uncertainty of the present values is ~2.5% on average, which is significantly smaller than the difference in the measured data.

Uncertainty is always included in any measurement to a lesser or greater degree. However, we have presented a possibility for reducing the problem using a synergetic comparison between the measured nuclear data and the theory.

**Reference**

Kunieda, S. et al., Covariance of Neutron Cross Sections for $^{16}O$ through R-Matrix Analysis, Nuclear Data Sheets, vol.123, 2015, p.159-164.

# 4–2 Nuclear-Material Quantification by Observation of Transmitted Neutrons

## — A Non-Destructive Assay Technique for Measurement of Complex Nuclear Fuel using a Neutron-Resonance Reaction —

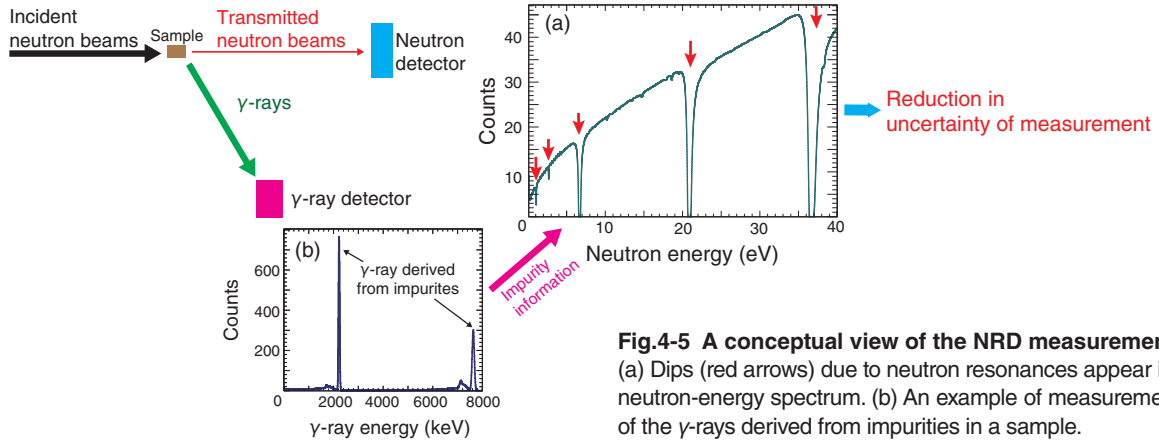


**Fig.4-5 A conceptual view of the NRD measurement**
(a) Dips (red arrows) due to neutron resonances appear in a neutron-energy spectrum. (b) An example of measurements of the γ-rays derived from impurities in a sample.

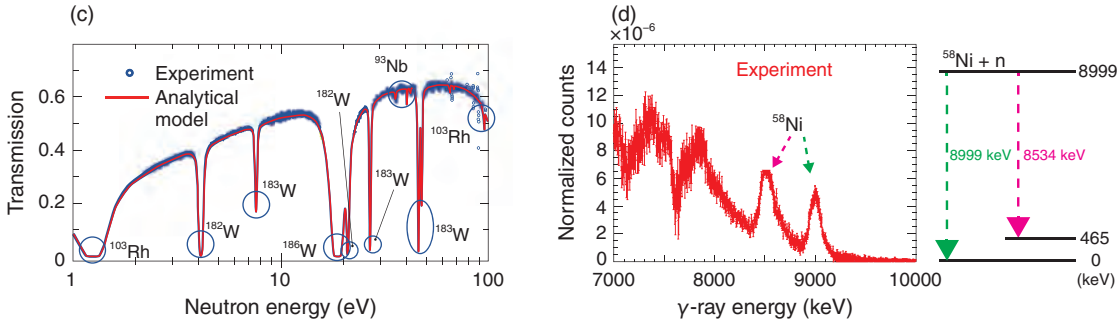


**Fig.4-6 Results of the NRD-demonstration experiment**
(c) Dips due to simulated NMs were measured with NRTA, enabling us to identify and quantify them.
(d) The presence of Ni was confirmed by observing the prompt γ-rays, as shown on the right side.

Recently, it has become important to determine the quantity of nuclear materials (NMs; namely uranium and plutonium) in nuclear fuel using a non-destructive-assay (NDA) technique. One particular unresolved problem is the accurate quantification of NMs in the fuel debris produced by severe accidents such as that at the TEPCO's Fukushima Daiich NPS. To overcome this problem, we have developed a new NDA technique for neutron-resonance densitometry (NRD) in collaboration with the European Commission - Joint Research Centre (EC-JRC).

To quantify the NMs in a sample, NRD combines measurements of both neutrons and γ-rays utilizing pulsed neutron beams. Neutrons at specific energies tend to be drastically absorbed by a nucleus. Such a neutron resonance absorption causes dips in the energy spectrum measured by a neutron detector, as shown in Fig.4-5. The specific energy of a dip and its depth enable us to identify and quantify NMs; this technique is called neutron-resonance-transmission analysis (NRTA). However, it is expected that fuel debris will contain not only NMs but also impurities such as structural materials (e.g., stainless steel) and strong neutron absorbers (e.g., boron derived from control rods). Impurities that cannot be measured with NRTA complicate the accurate quantification of NMs. Therefore, the isotopic identification of such impurities is performed via measurement of γ-rays that are emitted when an impurity absorbs a neutron, and it is useful to reduce the uncertainty of the NM quantification by allowing us to evaluate the impact of contaminants upon a neutron-energy spectrum measured with NRTA.

In March 2015, an NRD-demonstration experiment was conducted at EC-JRC. Various samples were prepared for the experiment to simulate NMs, structural materials, and control rods. The experiment was performed blind by allowing a third party (including an IAEA official) to select several of prepared samples and seal them in Al boxes. As shown in Fig.4-6, the NRTA measurement confirmed that the simulated NMs of tungsten (W), niobium (Nb), and rhodium (Rh) were present in the sealed sample box. The γ-ray measurement also proved the presence of nickel (Ni) as a representative of the structural materials. Consequently, this demonstration experiment determined the amount of simulated NMs to an accuracy of 2% or better.

This research was partly supported by the Ministry of Education, Culture, Sports, Science and Technology of Japan (MEXT) and given the award for technical development by the 48th Atomic Energy Society of Japan. As a next step, we are currently tackling the development of a technique that is applicable to measurements of NMs in spent and reprocessed fuels.

**References**

Tsuchiya, H. et al., Impact of Systematic Effects on Results of Neutron Resonance Transmission Analysis, Nuclear Instruments and Methods in Physics Research A, vol.767, 2014, p.364-371.
Paradela, C., Tsuchiya, H. et al., NRD Demonstration Experiments at GELINA, EUR 27507 EN, 2015, 16p.

# 4–3 Measurement of the Corrosive Environment in High-Temperature, High-Pressure Water within Light Water Reactors

## — Development of an Electrochemical Measuring Technique and Evaluation of the Corrosive Condition in High-Temperature Pure Water —

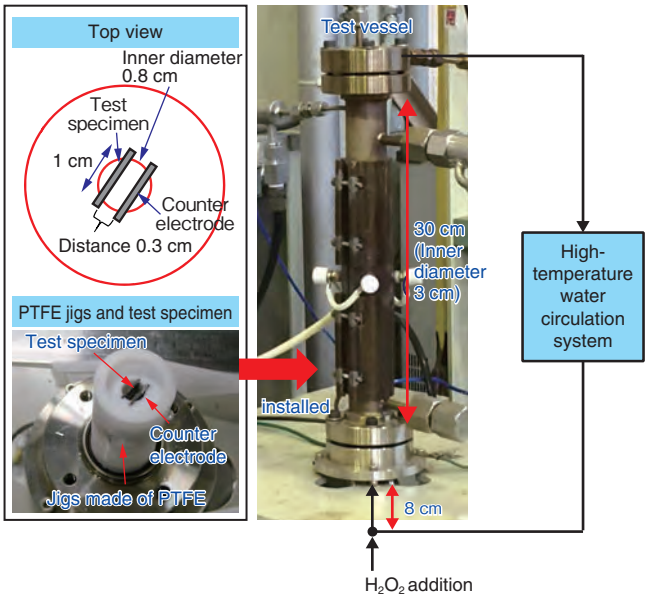


**Fig.4-7 Electrochemical-test vessel**
This vessel is designed for use under high-pressure; high-temperature water is caused to flow inside it via a circulation system. The size of the vessel was logically minimized and PTFE jigs have been installed. Such special designs could permit electrochemical measurements with high accuracy under simulated BWR conditions. The test pressure was 80 atm, larger than that in the BWRs, to prevent the boiling of the water.

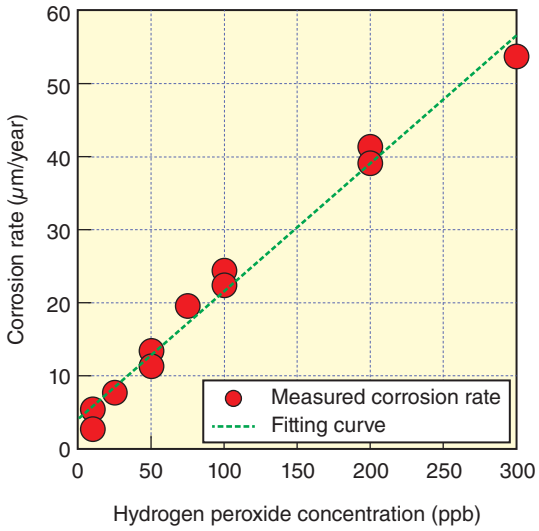


**Fig.4-8 The relationship between the corrosion rate determined by the resistance measurements and the hydrogen peroxide concentration**
The relationship confirmed that the corrosion rate of stainless steel in high-temperature water containing hydrogen peroxide was proportional to the hydrogen peroxide concentration.

Degradation of materials owing to corrosion (e.g., stress corrosion cracking) is a major problem in boiling water reactors (BWRs). Electrochemical measurement in simulated BWR cooling-water conditions is a major approach to understand the mechanism of corrosion. The cooling water in a BWR is pure light water with high temperature (288 °C) and high pressure (70 atm). Hydrogen peroxide ($H_2O_2$), which has high oxidizability, is generated owing to irradiation. The hot pure water has a high electric resistance, while $H_2O_2$ decomposes easily at high temperature (it disappears after approximately 1 min) and this decomposition is further enhanced by contact with the surfaces of the metals. Thus, electrochemical measurements in simulated BWR conditions are difficult to perform. Therefore, we developed a system to measure electrochemical data under such conditions.

A test vessel designed to maintain high pressure is shown in Fig.4-7. High-temperature water flows into the test vessel in which the vessel specimen was installed for electrochemical examinations. The high electric resistance of water caused a potential drop in the water when the current flowed. To reduce this drop, we minimized the path of current flow between the test specimen and the counter electrode to a distance of 0.3 cm. To prevent the disappearance of $H_2O_2$ through decomposition, we performed the measurements as quickly as possible after the $H_2O_2$ was added to the test specimen. We also minimized the distance between the addition point of the $H_2O_2$ and the test vessel to approximately 8 cm as well as the volume of the test vessel. To prevent the decomposition of $H_2O_2$ at the vessel surface, we installed jigs composed of polytetrafluoroethylene (PTFE), in which the decomposition was much smaller than that of the metals. These enabled us to obtain the electrochemical data with greater precision in simulated BWR conditions.

The measurements of the impedances, which are electrochemical parameters, were performed. The impedances were measured by supplying a sinusoidal AC voltage between two stainless-steel specimens installed inside the vessel. The impedances corresponding to the conductivity, the composition, and the thickness of the oxide film as well as the corrosion rate could be measured by changing the frequency of the supplied AC voltages. Obtained impedances were inversely proportional to the current that flowed at the surface of the stainless steel, which was proportional to the stainless steel's corrosion rate. Therefore, the corrosion rate could be determined by measurements of the impedances. The obtained stainless-steel corrosion rates are shown in Fig.4-8 alongside $H_2O_2$ concentrations; we confirmed that the two quantities were proportional. This is expected to be important information in understanding the mechanism of degradation due to the corrosion. Moreover, we will improve this electrochemical test equipment such that it can be applied to the measurements of other electrochemical parameters.

**Reference**

Satoh, T. et al., In-situ Measurement of Corrosion Environment in High Temperature Water without Electrolyte Utilizing Electrochemical Impedance Spectroscopy, Zairyo to Kankyo (Corrosion Engineering of Japan), vol.64, no.3, 2015, p.91-97 (in Japanese).

# 4–4 Predicting the Property Changes in Nuclear Reactor Materials

## — Understanding the Hardening Mechanism owing to Nano-Sized Defects: Molecular Dynamics Simulation —

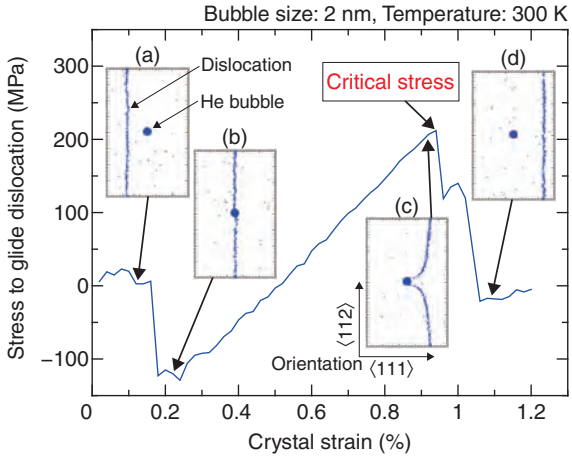


**Fig.4-9 Interaction process of a dislocation gliding through a He bubble**
Successive images of the interaction at some characteristic stages are presented in (a)–(d) with the corresponding stresses required for the dislocation to glide. Just before the release from a He bubble, the stress reaches a maximum, which is defined as the critical stress.

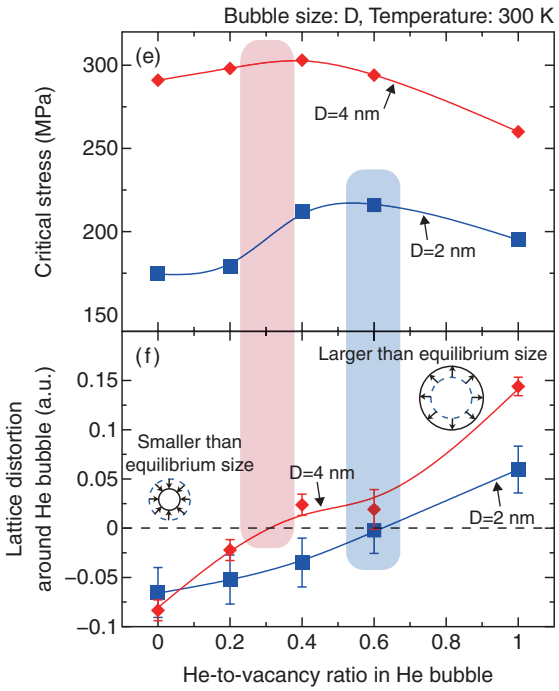


**Fig.4-10 Relationship between (e) critical stresses and (f) lattice distortions around He bubbles**
Higher critical stresses are correlated with smaller lattice distortions (the horizontal broken line presents a zero value), as indicated by the colored areas. Bubbles with negative and positive distortions have smaller and larger sizes, respectively, compared with the equilibrium size with zero distortion.

In the main structural materials comprising nuclear reactors, helium (He) atoms are produced by transmutation reactions; in addition, spherical voids are formed by supersaturation of vacancies under significantly high-energy neutron irradiation, such as those in fast-breeder reactors. He atoms are known to accumulate in the voids, coalescing in the form of He bubbles. These nanometric defects induce hardening of irradiated materials by preventing the dislocation motion that governs material deformation, and are thus responsible for the degradation of mechanical properties. Therefore, understanding the hardening mechanism owing to the interaction of a dislocation with nanometric defects is an important issue for predicting property changes in nuclear-reactor materials.

To address this issue, we have performed a detailed investigation of the interaction of a dislocation with a He bubble using a molecular dynamics simulation capable of dynamically predicting the motion of each atom based on Newton's equation of motion. Fig.4-9 shows a typical case of the temporal behavior of the interaction of a dislocation gliding through a He bubble in pure iron, which is the base material of nuclear reactors. Just before the dislocation escapes from the He bubble, the stress reaches a maximum value, referred to as the critical stress, which is used as a measure of the extent of hardening. By focusing attention on the fact that the estimated lattice distortion around a He bubble varies with the He-to-vacancy ratio, we investigated the influence of this ratio upon the critical stress. Fig.4-10 shows the relation between (e) critical stresses and (f) lattice distortions around He bubbles for 2- and 4-nm bubbles as a function of the He-to-vacancy ratio. We found that the higher critical stress is correlated with smaller lattice distortion for each bubble size. Using the visualization technique for extracting the specified atoms, it was revealed that through atomic exchange between the intersecting dislocation and the bubble surface, the number of vacancies in the bubble varied so as to reduce the lattice distortion, i.e., the energy relaxation. This indicates that bubbles with larger lattice distortions are subjected to larger energy relaxation owing to the intersecting dislocation, resulting in lower critical stresses.

This result has extended our understanding of the hardening mechanism induced by He bubbles, which are nanometric defects in irradiated materials. The prediction accuracy of the property changes in nuclear reactor materials under high-energy neutron irradiation is expected to be improved.

This work was partly supported by the Japan Society for the Promotion of Science (JSPS) KAKENHI Grant-in-Aid for Challenging Exploratory Research (No.24656425).

**Reference**

Abe, Y. et al., Effect of The Dilation Caused by Helium Bubbles on Edge Dislocation Motion in $\alpha$-Iron: Molecular Dynamics Simulation, Journal of Nuclear Science and Technology, vol.53, issue 10, 2016, p.1528-1534.

# 4–5 Exploring the Valence of Uranium by Luminescence

## — Time-Resolved Laser-Induced Fluorescence Spectroscopy for Short-Lived Species —

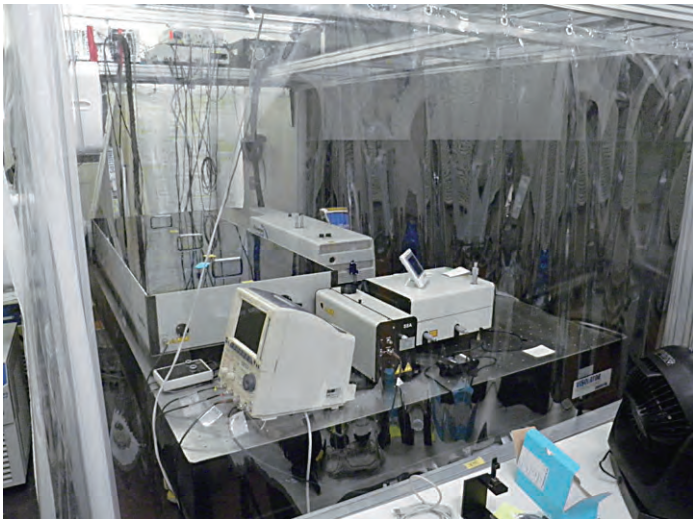

**Fig.4-11 System using an ultrashort pulsed laser**
The regenerative amplifier of a Ti:sapphire laser with a fast CCD camera hyphenated to a spectrometer enables us to obtain time-resolved luminescence spectra and lifetimes.

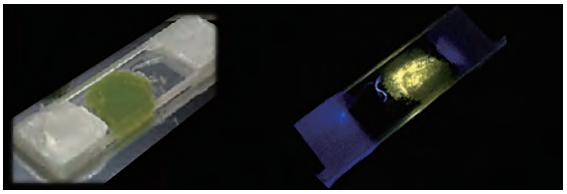

**Fig.4-12 The color and luminescence of the U(IV) compound**
The green U compound (left) emits white-to-light-yellow luminescence (right) under irradiation by ultraviolet light (365 nm).

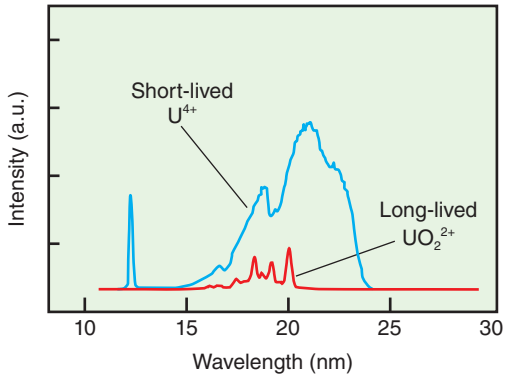


**Fig.4-13 Time-resolved luminescence spectra of $UI_4$ in [emim][SCN]**
Upon the irradiation of ultraviolet pulsed light, emission from the short-lived $U^{4+}$ occurs from 0–10 ns, and then that from the long-lived $UO_2^{2+}$ occurs from 1–10 $\mu$s.

The environmental behavior of uranium (U), which is the major component of spent nuclear fuel, and techniques to analyze are key issues for future studies of the direct disposal of such fuel. U exhibits various valences. Among them, U(VI) is chemically favorable as the most stable state, which is abundant in the ambient condition. In the liquid state, the U(VI) ions bind oxygen, resulting in uranyl ions ($UO_2^{2+}$). Since these ions are intensely luminescent under the irradiation of UV light, this luminescence has been investigated in many analytical studies to understand the chemical state of U compounds. In contrast, U exists as uranous ions ($U^{4+}$) in reductive conditions such as in groundwater, where analytical observation of $U^{4+}$ is of greater importance. The conventional absorption spectroscopy records spectra in which photon energy ranges widely from the ultraviolet to the near infrared. Conversely, the luminescence intensity is so weak and the luminescence lifetime so short that the measurement of $U^{4+}$ might be difficult. Therefore, the spectral information available for $U^{4+}$ is less than that for $UO_2^{2+}$ and it is often challenging to determine the chemical states of U(IV) and U(VI) in a mixture solution by simultaneous observation.

Hence, we develop a laser system for the *in situ* detection of $U^{4+}$ using state-of-the-art laser technology with an intense light source. The laser, having ultra-short pulses of approximately 100 fs, was introduced to provide excitation pulses for samples having short-lived species. Moreover, a fast and highly sensitive CCD camera as was utilized as a detector to facilitate time-resolved laser-induced fluorescence spectroscopy (Fig.4-11). We aim to extend the spectral database of uranium in solutions.

To demonstrate the luminescence of U(IV) compounds, $UI_4$ was dissolved in 1-butyl-3-methylimidazolium thiocyanate ([emim][SCN]), which is suitable for spectroscopy owing to its transparency (Fig.4-12). Consequently, we have succeeded in obtaining the luminescence data for $U^{4+}$ and in distinguishing U(IV) from U(VI) in their mixture solution by changing the delay time after the irradiation of the excitation pulses; the lifetime of $U^{4+}$ is 18.6 ns and that of $UO_2^{2+}$ is 35.7 $\mu$s (Fig.4-13).

This work was partly supported by the Japan Society for the Promotion of Science (JSPS) KAKENHI Grant-in-Aid for Scientific Research (C) (No.24561046) and performed under the Cooperative Research Program of "Network Joint Research Center for Materials and Devices" (No.2014139).

**Reference**

Aoyagi, N. et al., Optical Properties of Tetravalent Uranium Complexes in Non-Aqueous Media, Journal of Radioanalytical and Nuclear Chemistry, vol.303, issue 2, 2015, p.1095-1098.

# 4–6 Preparation of a Micro-Sized Solid-Phase Extraction Cartridge

## — Separation Cartridge Designed for Trace Analysis of Difficult-to-Measure Nuclides —

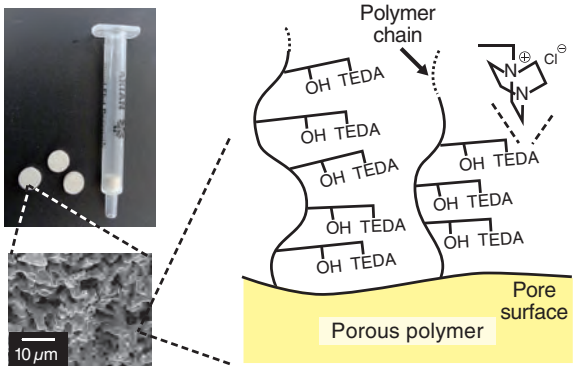


**Fig.4-14 Schematic interfacial structure of a micro-volume cartridge (TEDA cartridge)**
A disk-shaped highly permeable microporous polymer is packed inside the cartridge. Anion-exchange-group (TEDA)-bound polymer chains, which are closely attached to the polymer surface, enable highly efficient separation.

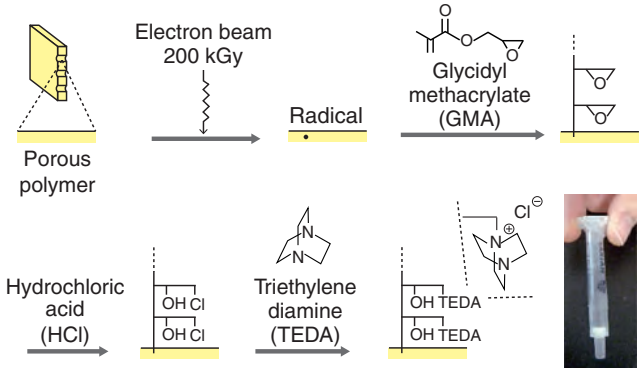


**Fig.4-15 Preparation of the TEDA cartridge by electron-beam-induced graft polymerization**
Graft polymerization is induced by electron-beam irradiation, producing polymer chains that extend from the pore surface of the polymer. Subsequently, ion-exchange groups are introduced to the polymer chains via reaction with HCl.

**Table 4-1 Comparison of separation performances between the TEDA cartridge and conventional adsorbent**
The TEDA cartridge can maintain separation performances that are comparable with or higher than those of the commercially available anion-exchange resin-packed column when solutions are fed up to 10 times faster than a typical flow rate for the use of the anion-exchange resin.

| | Flow rate (mℓ/min) | Total feeding vol. (mℓ) | $^{237}$Np recovery | Contamination rate | |
|---|---|---|---|---|---|
| | | | | Am | U |
| TEDA cartridge | 1.5 | 2.5 | 90% | <0.001% | <0.1% |
| Commercially available anion-exchange resin ※1 | 0.15 | 41.3 | 78% | <0.001% | 2.3% |

$^{237}$Np: neptunium-237
Am: americium
U: uranium

※1 BIO-RAD AG® 1-X8

Radionuclides are commonly determined with radiometry and mass spectrometry. For $\gamma$-emitting nuclides, the activities can be measured without any pretreatments owing to strong penetration ability. In contrast, the measurements of $\alpha$ and $\beta$-emitting nuclides are associated with pretreatments comprising mostly chemical separations to remove concomitants that may cause interference of the energy spectra. Mass spectrometry, which identifies the mass number of an analyte rather than its radiation energy, also requires separation of isobars and molecular ions with the same mass number. Thus, simplifying such cumbersome and time-consuming separation procedures can be an effective approach to reducing operation time and workload.

Our study has focused upon facilitating the separation procedures by preparing a micro-volume solid-phase extraction cartridge that achieves rapid separation. A disk-shaped, highly-permeable microporous polymer (average pore diameter: 1.0 μm) with a diameter and thickness of 5.9 and 3.0 mm, respectively, is packed inside the cartridge. Triethylenediamine (TEDA), which has two anion-exchange groups per molecule, is uniformly present on the pore-surface of the polymer, forming a high-density ion-exchange-interfacial phase (Fig.4-14). This ideal structure for rapid separation can be realized by the electron-beam-induced graft-polymerization technique (Fig.4-15).

The separation performances of the prepared (TEDA) cartridge were evaluated using a spent nuclear-fuel sample. $^{237}$Np, one of the difficult-to-measure long-lived nuclides generated through nuclear reactions, was selected as an analyte. The separation performances of the TEDA cartridge were compared with a conventional chromatography column with a commercially available anion-exchange resin (Table 4-1). The TEDA cartridge could maintain comparable or higher separation performances than those of the conventional column when solutions were fed up to 10 times faster than a typical flow rate for the use of the anion-exchange resin, thus demonstrating that the TEDA cartridge significantly reduced the separation time.

The technique employed for the preparation of the TEDA cartridge is applicable to various molecules that have specific-adsorption ability. Optimal combinations of a molecule to be bound and a base polymer for grafting will provide the capability to meet a wide range of analytical needs.

**Reference**

Asai, S. et al., Preparation of Microvolume Anion-Exchange Cartridge for Inductively Coupled Plasma Mass Spectrometry-Based Determination of $^{237}$Np Content in Spent Nuclear Fuel, Analytical Chemistry, vol.88, issue 6, 2016, p.3149-3155.

# 4–7 Understanding the Migration Behavior of Transuranic Elements from Forests to Rivers

## — Migration Behavior Research using Rare Earth Elements that Exhibit Chemical Similarity to Transuranic Elements —

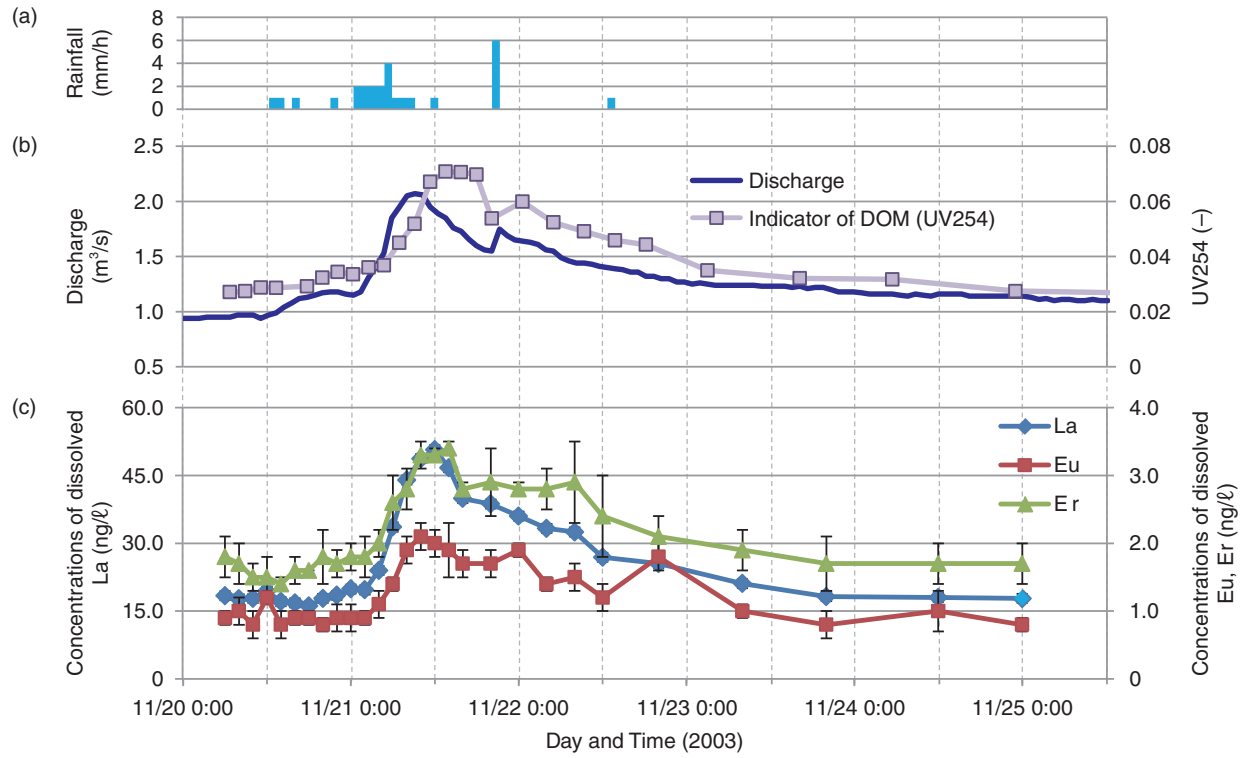


**Fig.4-16 Observation results from November 20 to November 25, 2003**
Temporal changes of (a) rainfall and (b) river-water discharge, as well as absorbance at 254 nm (UV254), which is an indicator of the concentration of dissolved organic matter (DOM); (c) concentrations of dissolved REEs (lanthanum (La), europium (Eu), and erbium (Er)). The concentrations of DOM and REEs increased at the same time and these changes occurred shortly after an increase in discharge during a rainfall event.

The environmental behavior of transuranic elements (TRU) is an important issue when assessing the impact and measuring long-lived radionuclides such as TRU, which are released into the environment. It is generally difficult to use nuclear-bomb-test-derived TRU in environmental-behavior research, owing to their limited presence on the ground.

We performed migration behavior research based on field observations using rare earth elements (REEs), which are known to exhibit chemical similarity to TRU in laboratory experiments. We observed temporal changes of discharge, dissolved organic matter (DOM) concentrations and concentrations of dissolved REEs during rainfall events in a small catchment (Fig.4-16). The concentrations of DOM, especially humic substances, increased following a short delay from the increase in discharge. The concentrations of dissolved REEs also increased at this time. We observed that the DOM and the dissolved REEs migrated together, owing to the fact that their temporal changes were consistent. This result suggests that humic substances, which are widely distributed in forest soil, are involved in the migration behavior of TRU. It has been reported in previous literature that REEs and humic substances attach strongly to one another. These results suggest that some of the dissolved REEs in soil migrate into river water in a form attached to DOM during rainfall events.

By analyzing the distribution of the data, most of the REEs dissolved during rainfall events were shown to exist as particles with diameters of 1–200 nm. This result also suggests that dissolved REEs and humic substances are strongly attached to one another. Furthermore, as a result of analyzing the relationship between the REE concentration and the characteristics of the humic substances, it was suggested that the quantity of a cyclic compound such as the benzene included in the humic substances was significantly involved in forming complexes with REEs. The findings will improve our understanding the migration behavior of TRU from forests to rivers.

**Reference**

Matsunaga, T., Tsuduki, K. et al., Increase in Rare Earth Element Concentrations Controlled by Dissolved Organic Matter in River Water During Rainfall Events in a Temperate, Small Forested Catchment, Journal of Nuclear Science and Technology, vol.52, issue 4, 2015, p.514-529.

# 4–8 Toward Detailed Prediction of the Radiation Damage to Structural Materials in Accelerators

## — Development of a Cryogenic Irradiation Device for Validation of the Radiation-Damage Model —

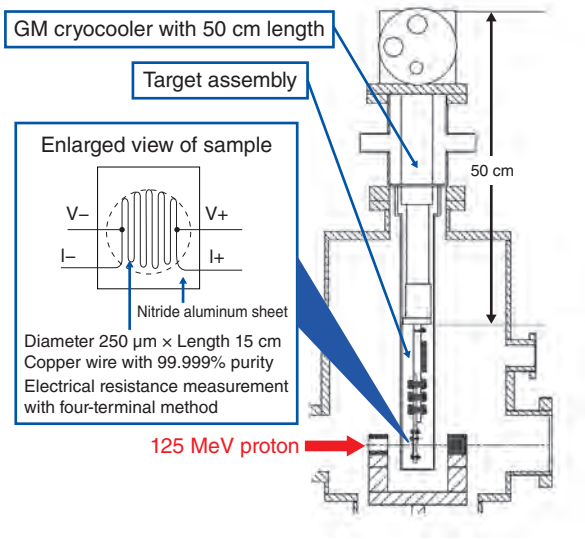


**Fig.4-17 Cryogenic irradiation device developed by this research**
A sample of a copper wire fixed by two aluminum nitride sheets with superior thermal conductivity and insulation properties is attached to the target assembly. A sample is cooled by thermal conduction via the target assembly attached to a GM cryocooler.

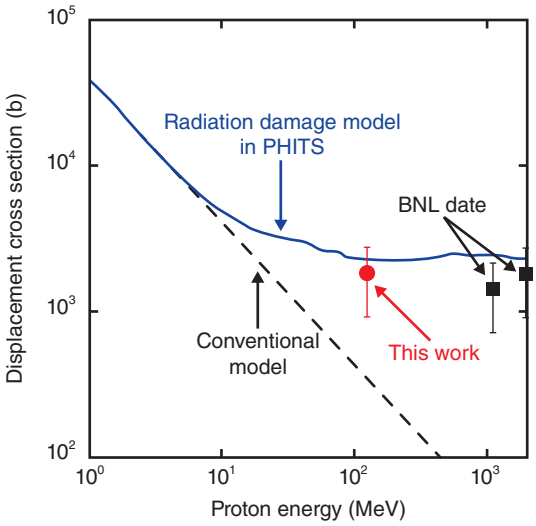


**Fig.4-18 Displacement cross-section of copper owing to proton energy**
From experimental data obtained by this research and BNL, we found that our radiation-damage model based on the PHITS code can reproduce the experimental data very well compared with the conventional model.

Displacement per atom (DPA), which is defined as the ratio of the number of displaced atoms to the total number of atoms in an irradiation area, is used as an index for evaluating radiation damage to constructional materials in accelerators. The DPA value is proportional to the displacement cross-section, which shows the probability of displacement, and it is an index of the lifetime of the structural materials. Therefore, accurate prediction of DPA value assists in planning the frequencies of exchanging devices. To improve the accuracy of the predicted displacement cross-section at energies above a few MeV, we have developed a radiation-damage model in the Particle and Heavy Ion Transport-code System (PHITS) that includes nuclear reactions that are not considered in the conventional model.

Validating the displacement cross-section using experimental data is important. For this purpose, we measured the increase in the electrical resistivity of metal induced by defects displaced atoms and vacancies) in the sample under irradiation. Here, it is necessary to set the sample under a cryogenic environment so as not to improve defects. During the only experiment on this subject performed at the Brookhaven National Laboratory (BNL) in the United States, the sample was cooled by liquid helium. However, many facilities cannot use this coolant owing to safety concerns. Therefore, we have developed a cryogenic irradiation device using a movable Gifford–McMahon (GM) cryocooler, which does not use a cryocoolant (Fig.4-17); rather, this device cools samples via a target assembly that includes copper and aluminum plates with high thermal conductivities attached with a GM cryocooler, which has a length of approximately 50 cm and a cooling ability of 4 K (Fig.4-18). We have successfully measured very small electrical-resistivity increases in the copper sample irradiated by protons with energies of 125 MeV at the FFAG accelerator facility at the Kyoto University Reactor Research Institute, and we have deduced the displacement cross-section using this measured value. Using new experimental data obtained by this research, as well as BNL data, we found that our radiation-damage model for the PHITS code can reproduce experimental data very well compared with the conventional model.

From this research, we have established a cryogenic irradiation device for measurement of the displacement cross-section available in various accelerator facilities, and it is possible to validate the radiation-damage model against various types of radiations with wide energy ranges. The experimental data are also used in coordinated research activities of the International Atomic Energy Agency (IAEA) related to the displacement cross-section.

**Reference**

Iwamoto, Y. et al., Measurement of the Displacement Cross-Section of Copper Irradiated with 125 MeV Protons at 12 K, Journal of Nuclear Materials, vol.458, 2015, p.369-375.

# 4–9 Visualization of Water–Steam Fractions under High-Pressure and High-Temperature Conditions in Reactor Cores

## — Development of Technology for the Measurement of Steam Volumetric Fractions in Fuel Assemblies with Wire-Mesh Sensors —

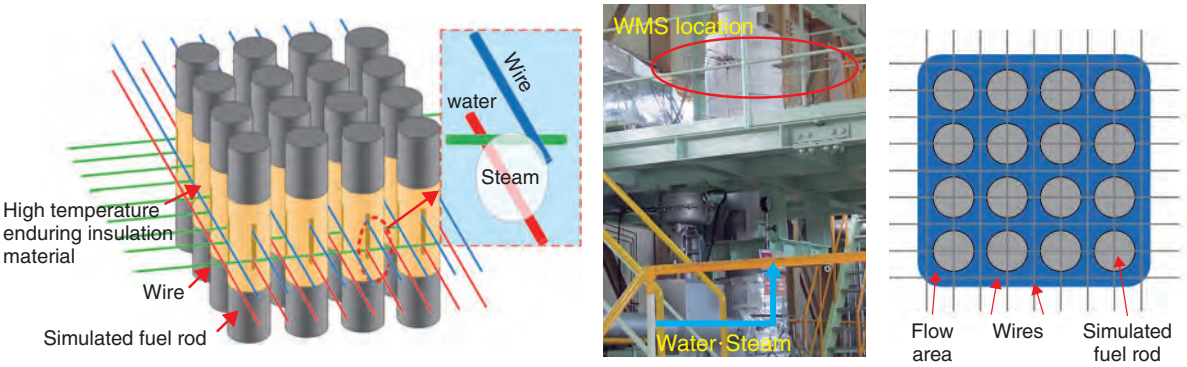


(a) Structure of the WMS (b) Outline of the test apparatus (c) Cross-sectional view of the WMS location

**Fig.4-19 Test apparatus and principles for the measurement of steam volumetric fractions in fuel assemblies**
WMS measures the electrical current flowing through the small space between two wires by applying electrical voltages over these wires. If steam exists in the small space between them, electricity will have difficulty flowing, resulting in a lower current. For example, the current is low between the red and green wires in (a); however, it is high between the green and blue wires. To enhance the measuring technology for application to two-phase flow under high-pressure and -temperature conditions, materials with high temperature endurances and electrical insulation were adopted for the setting of the wires during manufacture of the test apparatus.

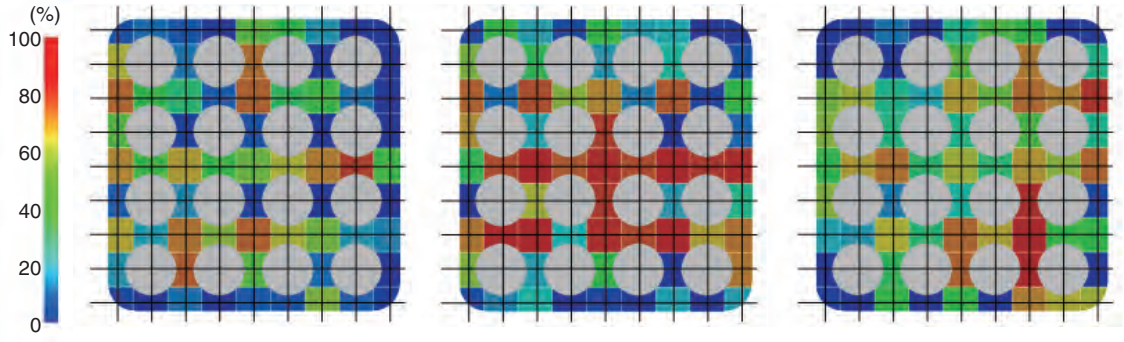


(d) At measurement starting time (e) 0.012 s after start (f) 0.024 s after start

**Fig.4-20 Changes in the measured steam volumetric-fraction distribution with time**
These figures show the measurement results at pressure = 2.6 MPa, temperature = 226 °C, water velocity = 0.58 m/s, and steam velocity = 1.74 m/s. The high-steam-volumetric-fraction region appears in the central part of the test channel (e); however, it becomes low (f). These figures show that the steam volumetric-fraction distribution changes significantly over a short time.

In boiling-water reactor cores, the coolant is heated by fission energy, resulting in boiling. Water flow (liquid phase) mixed with steam (vapor phase) is called water–steam two–phase flow (abbreviated to two-phase flow in the following). The temperature distributions in the reactor cores are affected significantly by the two-phase-flow conditions, especially the steam volumetric fraction. Therefore, when designing a reactor core or analyzing an accident, it is very important to evaluate the steam volumetric fraction inside the cores. However, the measurement of this fraction inside a reactor core under high-pressure and high-temperature conditions is very difficult because the flow area of the coolant is very small owing to the existence of fuel rods. This is the reason that most experiments have been performed under low-pressure and low-temperature conditions. To evaluate the steam volumetric fraction in the reactor cores, we developed a measurement technology that can be applied to high-pressure, high-temperature test apparatuses that simulate reactor cores as based on wire-mesh sensor (WMS) technology.

Fig.4-19(a) shows the structure of the constructed WMS and the basic principle of its operation. Metals with high electrical conductivity affect the WMS measurement, which is based on the measurement of electrical current. Therefore, as shown in Fig.4-19(a), an electricity insulation material capable of enduring very high temperatures was inserted between the upper and lower metal tubes that simulated fuel rods, with very small holes drilled in the material for the setting of wires. Fig.4-19(b) shows the outer appearance of the test apparatus. To simulate the reactor cores, the test section has a height of approximately 4 m and comprises four rods in both the vertical and horizontal directions, meaning a total of 16 rods (Fig.4-19(c)). As an example of the test results, Fig.4-20 shows how the measured steam volumetric fraction changes with time. The red part (representing a high fraction of steam) and the blue part (representing a high fraction of water) change complicatedly over a short time interval. In the future, to contribute to evaluations of the temperature distribution and boiling condition inside real reactor cores, we will obtain more experimental data to validate simulation codes, and to evaluate and improve experimental correlations.

**Reference**

Liu, W. et al., Measurement of Void Fraction Distribution in Steam–Water Two–Phase Flow in a 4×4 Bundle at 2 MPa, Transactions of the American Nuclear Society, vol.114, 2016, p.875-878.

# 4–10 Prevention of Severe-Accident Progression by Delaying Core Overheating and Melting
## — Development of Fuel-Cladding Materials with High Resistance to Oxidation —

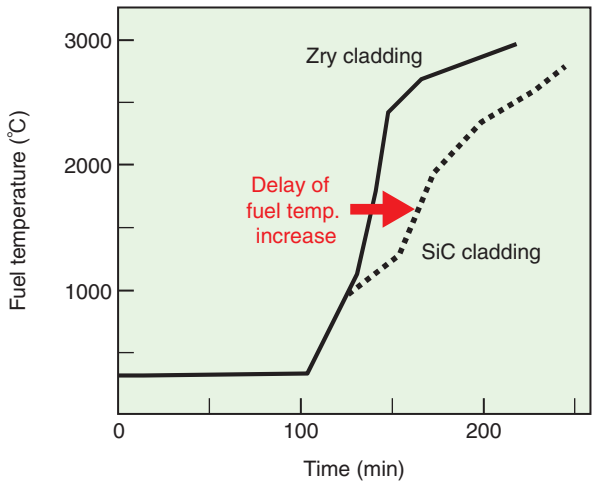


**Fig.4-21 Schematic illustration indicating the relationship between fuel temperature and oxidation time in both SiC and Zry claddings**
Since SiC cladding has a relatively slow oxidation rate compared with that of Zr-based-alloy cladding, it was considered that the possibility approaching to core damage could be much lower or that there were the possibility mitigating the influence when the core damaged by suppressing fuel-temperature escalation.

Zirconium alloys, which are used as fuel cladding and other core components in light-water reactors, are readily oxidized at higher temperatures. The reaction of zirconium (Zr) with water or steam is accompanied by the release of hydrogen gas as well as the formation of an oxide. In addition, the reaction is highly exothermic and the reaction rate becomes very high beyond 1500 °C. The cooling capability at the TEPCO's Fukushima Daiichi NPS (1F) was lost owing to the tsunami caused by the Great East Japan Earthquake. It is believed that the Zr-alloy fuel cladding was oxidized in the heated core and that the subsequent temperature escalation due to oxidation caused core melting. It is also presumed that hydrogen generated by the oxidation leaked from the primary containment vessel, causing the reactor building to explode. Based on lessons learned from the 1F accident, we are developing advanced fuel and core components with enhanced accident tolerance to prevent extensive core damage and hydrogen generation and mitigate these phenomena in accidents beyond the design basis.

High-temperature oxidation is an indication of accident tolerance. Fig.4-21 schematically compares fuel-temperature increases during accidents in reactor cores with silicon-carbide and Zr-alloy fuel cladding. The figure shows that the remarkably lower oxidation rate of silicon carbide (SiC) can suppress fuel-temperature escalation and consequently the core damage experienced in 1F may be prevented or mitigated. Therefore, it is commonly recognized that development of the cladding with high oxidation resistance is the most effective way to enhance accident tolerance.

We have chosen SiC/SiC composites reinforced by SiC-fibers and FeCrAl-steel strengthened by the dispersion of fine-oxide particles (FeCrAl-ODS steel) as promising candidates for advanced fuel components with enhanced accident tolerance. We have started R&D to establish a technical basis for implementing advanced fuel components in existing LWRs. The R&D is conducted in cooperation with power-plant providers, fuel vendors, research institutes, and universities that have been involved in the development of advanced fuel components to utilize their accumulated experience, intelligence, and analytical tools for fuel design, fabrication, practical use, safety evaluation, and materials development.

We have clarified technical subjects including crucial showstoppers, factors that stops or could stop the progress, for the implementation by investigating the development status of advanced core-component materials and reviewing the current technical-readiness level (TRL) assuming implementation in existing LWRs. The R&D will be conducted to address technical challenges that have been clarified for candidate advanced-fuel components.

A part of this study is the result of the Development of a Technical Basis for Introducing Advanced Fuels Contributing to Safety Improvement of Current Light Water Reactors, as carried out under the Project for the Development of a Technical Basis for Safety Improvement at Nuclear Power Plants by the Agency for Natural Resources and Energy, the Ministry of Economy, Trade and Industry of Japan (METI).

**Reference**

Yamashita, S. et al., Establishment of Technical Basis to Implement Accident Tolerant Fuels and Components to Existing LWRs, Proceedings of Top Fuel 2016, Boise, Idaho, USA, 2016, paper 17550, 10p., in USB Flash Drive.

# 4–11 Investigation of a New Transmutation System Concept

## — Implementation of an Analysis Code for an Accelerator-Driven System with a Subcriticality Adjustment Mechanism —

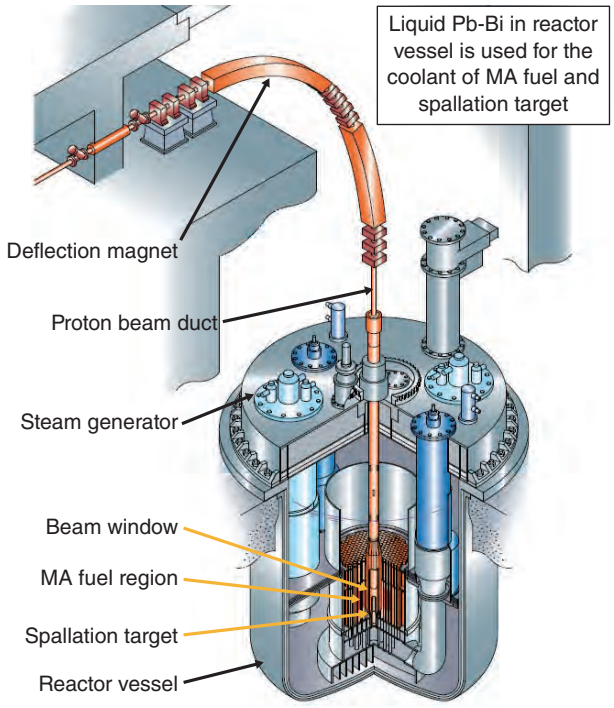


**Fig.4-22 Conceptual diagram of the ADS**
A proton beam is injected from a superconducting proton accelerator to a spallation target in the subcritical core. Spallation neutrons are generated in this target and used to transmute MAs loaded in the subcritical core.

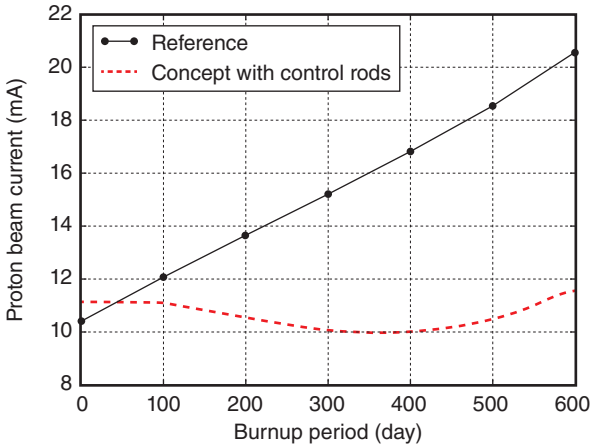


**Fig.4-23 Change of the proton beam current for ADS with control rods**
The proton beam current at the end of the cycle was 20 mA in the reference case (black line). Conversely, the value was reduced below 12 mA by the installation of the control rod (red line) during the burnup cycle.

To reduce the burden of geological disposal of the high-level waste (HLW) discharged from nuclear power plants, transmutation technology capable of transmuting long-lived nuclides into short-lived ones, has been investigated. It is expected that this technology can reduce the area of repository sites for HLW and the time at which the radioactivity of HLW decays to that of natural uranium from the order of tens of thousands of years to the order of a few hundred years. We have performed research and development on an accelerator-driven system (ADS) to transmute minor actinides (MAs) separated from the HLW.

The ADS is a hybrid system comprising an accelerator and a subcritical core with MA fuel (Fig.4-22). Although the ADS can efficiently transmute the MA, there are many inherent issues. One important issue is the design of a beam window that acts as a boundary of the accelerator and the subcritical core.

The important factor affecting the design of this window is heat generation by the proton beam. To maintain the subcritical core power at a constant level, it is necessary to increase the proton beam current to compensate for the decrease in the effective multiplication factor during the burnup cycle. The investigation of a new ADS concept with a subcritical adjustment mechanism began to prevent the increase of the proton beam current. In this study, a control rod used often in an existing nuclear power plant was employed as the subcritical adjustment mechanism. However, we lacked an ADS neutronics analysis tool to treat large absorbers such as the control rod because simple RZ-calculation geometries had been employed in the design of ADS neutronics in the past.

The ADS3D code system was developed on MARBLE, a next generation reactor analysis code system developed by JAEA to achieve ADS neutronics calculation with the control rod. The ADS3D code system was able to calculate the transportation of protons and neutrons, the burn-up calculation, and the fuel exchange in a three-dimensional calculation model.

Fig.4-23 shows the calculation results for the ADS concept with the control rod using ADS3D. In the reference case, the proton beam current at the end of the cycle was 20 mA, so a heat generation condition of 20 mA was employed for the design of the beam window. By installing the control rod, it was observed that the maximum proton beam current was less than 12 mA during the burnup cycle. A decrease of 40% in the proton beam current was achieved. Since the heat generation condition is mitigated by the installation of the control rod, a new beam window concept will be investigated.

**Reference**

Sugawara, T. et al., Development of Three-Dimensional Reactor Analysis Code System for Accelerator-Driven System, ADS3D and Its Application with Subcriticality Adjustment Mechanism, Journal of Nuclear Science and Technology, vol.53, issue 12, 2016, p.2018-2027.

# 4–12 Recovery of Valuable Rare Metals from High-Level Radioactive Waste
## — Separation of Rhodium with Ion-Exchange Resin —

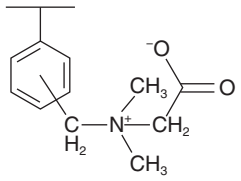


**Fig.4-24 Schematic formula of betaine resin, AMP03**
Functional groups with ion exchangeability have been connected to the structure of cross-linked polystyrene, which is an amphoteric ion-exchange resin having a positive and a negative charge in a functional group. The structure of the resin contains carbon, hydrogen, oxygen, and nitrogen.

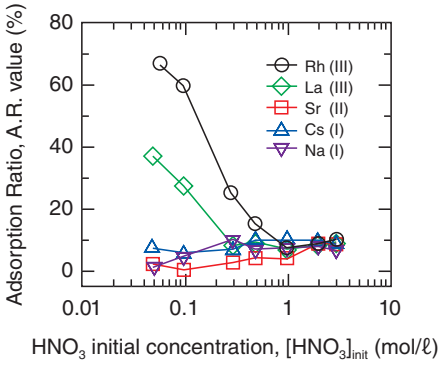


Experimental conditions
[Rh(III)] = 0.10 mmol/ℓ, [La(III)] = 0.072 mmol/ℓ, [Sr(II)] = 0.12 mmol/ℓ, [Cs(I)] = 0.075 mmol/ℓ, [Na(I)] = 0.43 mmol/ℓ, Solution volume = 1.0 mℓ, AMP03 = 0.099 g, Shaking time = 60 min.

**Fig.4-25 Adsorption behavior of metal ions with AMP03**
Plots of the extraction rate (A.R., %) value against initial concentration of nitric acid for the adsorption of Rh(III), La(III), Sr(II), Cs(I), and Na(I).

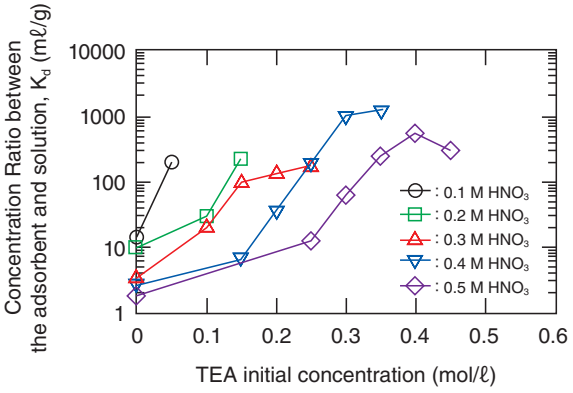


Experimental conditions
[Rh(III)] = 0.10 mmol/ℓ, Solution volume = 1.0 mℓ, AMP03 = 0.099 g, Shaking time = 60 min.

**Fig.4-26 Adsorption behavior of Rh(III) with AMP03**
Plots of Kd versus TEA concentration in initial solutions. The Rh(III)-adsorption ability of AMP03 greatly increased after the additions of amine compounds, such as trimethylamine, TEA, to the aqueous phase.

High-level radioactive waste (HLW) from reprocessing process contains various elements. Some of these are valuable, such as rare metals. If the valuable rare metal in HLW is recovered for industrial usage, it may become an important resource. Rhodium (Rh) is a platinum-group metal that is necessary for the production of catalytic agents used in automobiles. The price of Rh is relatively high and will increase further with growing automobile demand. Relatively large amounts of Rh are generated as fission products. Although radioactive $^{102}$Rh and $^{102m}$Rh, with half-lives of 2.9 and 0.57 years, respectively, are present in minor amounts, almost all Rh generated in fission reactors is of the stable isotope $^{103}$Rh. Therefore, after suitable storage, Rh can be used in industrial applications.

We examined Rh(III) adsorption using styrenedivinylbenzene copolymer functionalized with betaine (AMP03, Fig.4-24). AMP03 is generally used to separate sugar groups and salts. Consequently, AMP03 was found to successfully adsorb Rh(III) from the $HNO_3$ solution with pH 1.72. AMP03 is composed of C, H, O, and N and is favorable for reducing secondary radioactive waste. This point is advantageous for application to Rh(III) recovery from HLLW.

The adsorption of Rh(III), La(III), Sr(II), Cs(I), and Na(I) from an $HNO_3$ solution was also studied by varying the $HNO_3$ concentration in the initial solution, $[HNO_3]_{init}$. The results are shown in Fig.4-25;Rh(III) and La(III) were adsorbed in the low-$[HNO_3]_{init}$ range. The adsorption-ratio (AR) values of Rh(III) and La(III) decreased with increasing $[HNO_3]_{init}$. By contrast, AMP03 showed lower affinity for Sr(II), Cs(I), and Na(I) across the entire range of $[HNO_3]_{init}$ values (AR < 10%). The order of the adsorption selectivity for AMP03 (Rh(III) > La(III) > Cs(I), Sr(II), Na(I)) is advantageous for the selective recovery of Rh(III).

The $K_d$ values of Rh(III) for AMP03 greatly increased with the addition of trimethylamine (TEA). To obtain detailed data for the efficient recovery of Rh(III), adsorption experiments were performed using 0.1–0.5M $HNO_3$ solution containing Rh(III) and TEA. Fig.4-26 shows plots of $K_d$ against the concentration of TEA contained in the initial solutions $[TEA]_{init}$. All $K_d$ values in Fig.4-26 significantly increased with the addition of the amine compound. Effective Rh(III) adsorption with $K_d$ > 100 was also observed.

R&D activities aimed at establishing reasonable treatment processes for HLW will be conducted.

**Reference**

Suzuki, T., Matsumura, T. et al., Recovery of Rhodium(III) from Nitric Acid Solutions using Adsorbent Functionalized with *N,N,N*- Trimethylglycine, Bulletin of the Chemical Society of Japan, vol.89, no.5, 2016, p.608-616.

# 4–13 Toward the Establishment of a Method for Treating MA Transmutation Fuels

## — Development of the Technology for Pyrochemical Treatment of MA Nitride Fuel —

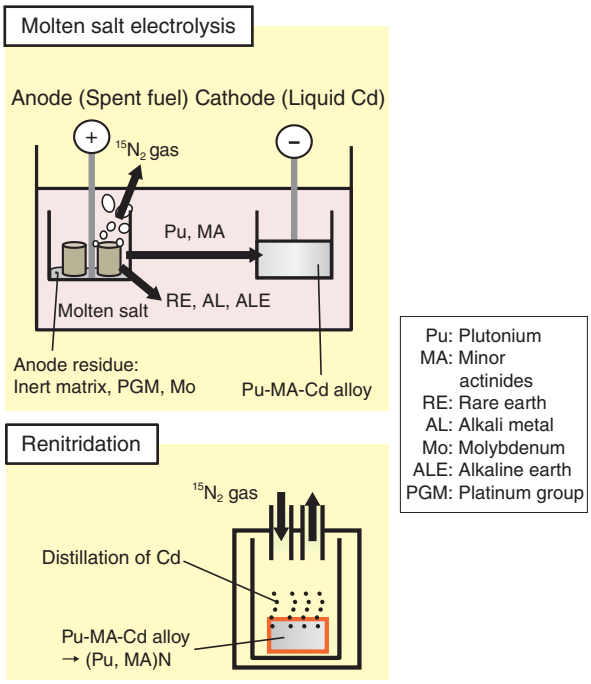


**Fig.4-27 Outline of the pyrochemical treatment of MA nitride fuel**
Pu and MA in the spent MA nitride fuels are dissolved into molten salt, separated from the FP elements, and recovered into the Cd cathode by molten salt electrolysis. The recovered Pu and MA are converted into nitrides to be used as fuels.

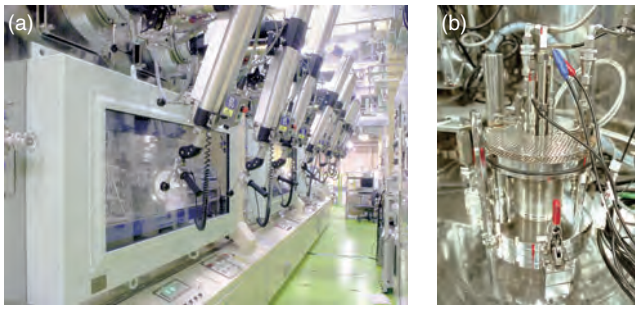


**Fig.4-28 Experimental apparatus for the study of pyrochemical-treatment of MA nitride fuel**
Experiments using highly radioactive MAs such as Am have been conducted with the apparatus including the molten salt electrorefiner (b) installed in the module for TRU high temperature chemistry (TRU-HITEC) (a), which comprises hot cells and a glove box with an inert gas atmosphere.

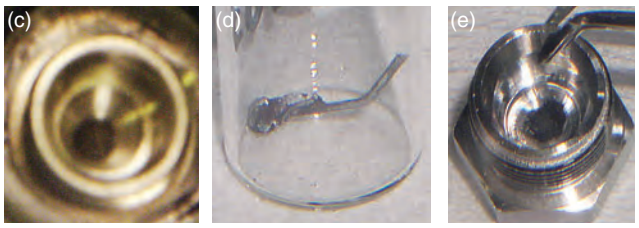


**Fig.4-29 Am compounds and alloys obtained in our study**
Molten salt electrolysis using a disk-shaped AmN sample (diameter: 4 mm, thickness: 1 mm) as an anode (c) has been conducted to recover Am in a Cd cathode. From the Am–Cd alloy obtained by molten salt electrolysis (d), an AmN powder sample (e) was prepared.

Partitioning and transmutation (P&T) technology serves to separate elements in high level radioactive wastes discharged from reprocessing plants depending on their intended use and chemical character, and to transmute long-lived nuclides to short-lived or stable ones. This technology aims at reducing the burden of high level waste and using repositories efficiently.

We have been conducting research and development of the technology for transmuting highly radioactive long-lived nuclides including minor actinides (MA: neptunium (Np), americium (Am), and curium (Cm)) using a dedicated accelerator-driven system (ADS). To transmute MA using ADS, neutrons produced by injection of an accelerated proton beam to a metal target will be supplied successively to a subcritical core to maintain fission chain reactions of MA and other elements in the core. The composition and chemical form of the fuel pellets containing MA elements in the core should be appropriate for MA transmutation. Uranium-free MA nitride has been selected as the first candidate for the MA transmutation fuel. Previous feasibility studies on the transmutation system show that approximately 20% of the MAs in the fuel can be transmuted in one burning cycle of approximately two years. To increase the transmutation ratio, reprocessing of spent MA transmutation fuels and reuse of the MA elements existing in spent MA transmutation fuels are necessary. Therefore, a method suitable for reprocessing MA transmutation fuel should be developed.

We have been researching and developing spent MA transmutation fuel reprocessing technology to recover and reuse the MA in spent fuels. One of our concerns is pyrochemical treatment technology (Fig.4-27), which is based on that developed to reprocess metal fuels for fast reactors. This technology, in which molten salts and liquid metals are used as solvents, is suitable for treatment of MA transmutation nitride fuels because solvents are resistant to radiation damage and decay heat. Advantages such as the feasibility of recycling the expensive and highly enriched $^{15}N$ used in the nitride fuels have also been pointed out. Conversely, one disadvantage is the necessity of an inert gas atmosphere because the salts used as solvents are hygroscopic.

Our experimental results with plutonium (Pu) and MA (Np and Am) samples at the lab-scale (Figs.4-28 and 4-29) indicate that the elemental technologies are feasible. The similarity of the behaviors of MA and Pu, which suggest that the technology has advantages in terms of proliferation resistance in principle, have been certified. At present, our focus is on evaluating the detailed behavior of the elements that are thought to exist in spent MA transmutation fuels, including fission product elements and inert matrix elements such as zirconium (Zr) and titanium (Ti). We also focus on the development of an engineering-scale apparatus for nitride fuel treatment.

**Reference**

Hayashi, H. et al., Pyrochemical Treatment of Spent Nitride Fuels for MA Transmutation, Science China Chemistry, vol.57, issue 11, 2014, p.1427-1431.

# 5 Quantum Beam Science Research

## Contributing to the Production of Innovative Outcomes in Science and Technology using Quantum Beam Facilities

In accordance with the "Science and Technology Basic Plan" formulated by the Government of Japan, we are aiming to contribute to the advance of science and technology and the promotion of industry in Japan through the production of innovative results using quantum beams.

In particular, we are making use of various quantum beam facilities, including the high-intensity proton accelerator at the Japan Proton Accelerator Research Complex (J-PARC), the ion-beam irradiation facility known as the Takasaki Ion Accelerators for Advanced Radiation Application (TIARA), the JAEA-Kansai Advanced Relativistic ENgineering (J-KAREN) laser system, and the JAEA synchrotron radiation beamlines at Super Photon ring-8 GeV (SPring-8) for two main purposes, namely, (1) upgrading neutron facilities and devices and utilizing neutron and other quantum beams for nuclear, materials, and life sciences, etc., and (2) developing and advancing the latest technologies for the generation, control, and measurement of quantum beams such as ion beams, light quanta, and the like, and pursuing world-leading research by making comprehensive use of their superior functions.

In this chapter, we will report recent highlights of quantum beam science and technology research in various fields.

### 1. Upgrade of Neutron Facilities and Devices / Neutron-utilization Research, etc.

J-PARC comprises a series of three proton accelerators, namely, a LINear ACcelerator (LINAC), a 3 GeV Rapid Cycling Synchrotron (RCS), and a 50 GeV synchrotron as well as three experimental facilities. These facilities include the Materials and Life Science Experimental Facility (MLF) for a wide range of research fields using neutron and/or muon beams, the Hadron Experimental Facility for nuclear- and particle-physics experiments using K-mesons and other particles, and the Neutrino Experimental Facility for the T2K particle physics experiment using neutrinos. All these experimental facilities are open to users from across the globe. In FY2015, use of the J-PARC Research Building (Fig.5-1) began, offering opportunities to users to develop experimental devices, prepare samples, and facilitate interaction among users. The accelerators have restarted beam delivery to the Hadron Experimental Facility, which was shut down owing to the radioactive-materials leak accident in May 2013. The user operations of the Hadron Experimental Facility and the Neutrino Experimental Facility were conducted almost as planned throughout the year. On the other hand, the MLF twice experienced the failures in the water shroud of the neutron-production target after the beam intensity was ramped up from 300 kW to 500 kW. Owing to these failures, the beam time allocated to the user programs was diminished. However, both experimental programs and international programs for bringing up future researchers, such as the Asia–Oceania Neutron School, were conducted at 19 neutron instruments and 2 muon beamlines over a wide materials science research field. In this chapter, outcomes from accelerators (Topics 5-1 and 5-2) and from MLF (Topics 5-3 and 5-4) are presented.

**Fig.5-1 Photo of the J-PARC Research Building**
The four-story building on the ground includes living spaces, various experiment-preparation rooms, computer rooms, and meeting rooms along with an atrium and conversation spaces to facilitate interaction among users.

Taking advantage of steady-state neutron beams from research reactors such as Japan Research Reactor-3 (JRR-3), we have developed neutron-utilization techniques and applied them to both improving the performance of advanced materials and evaluating the structural reliability of large industrial components based on investigation of the correlation between function and structure. Moreover, we are developing a novel extractant for the separation of minor actinides (MA) and the clarification of the adsorption/desorption reaction mechanisms of radioactive nuclides in soil, thereby contributing to the decommissioning of nuclear-power plants, treatment of radioactive wastes, and improvement of safety (Topics 5-5, 5-6, 5-7, and 5-8).

### 2. Development of Highly Advanced Quantum Beam Technology / Quantum Beam Science Research

At the Takasaki Advanced Radiation Research Institute, the TIARA, which comprises four ion accelerators, an electron accelerator, and a $\gamma$-ray irradiation facilities are available to researchers at JAEA and other organizations for R&D activities related to environmental and energy materials, medical research, and biotechnology. In addition, technological developments currently in progress involve the development of a beam-analysis apparatus for efficient transmission and acceleration of ion beams and techniques for large-area uniform ion irradiation as well as three-dimensional in-air micro-PIXE analysis (Topic 5-9) and microfabrication techniques. FY2015 marked the first year of the development of generation and acceleration techniques for MeV fullerene ($C_{60}$) ion beams and their applications. We created a conceptual design of an ion source for a Tandem accelerator,

capable of generating negative-ion beams of $C_{60}$ at several hundred nA. We constructed a test ion source on a trial basis (Fig.5-2), with which we have determined the conditions for generating high-intensity negative-ion beams.

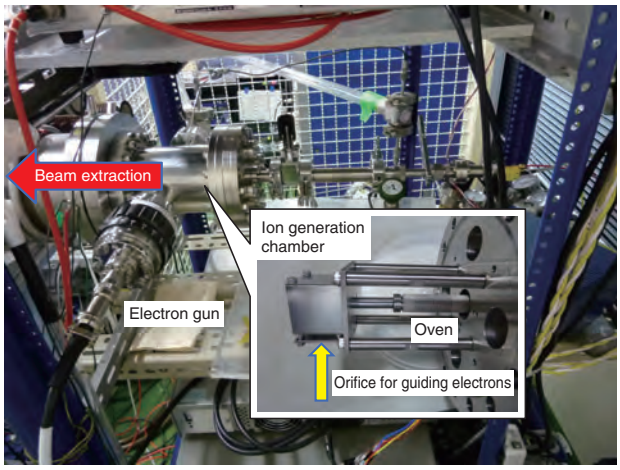


**Fig.5-2 Test ion source**
The device generates negative $C_{60}$ ions by means of an electron-attachment method.

In the Kizu District of Kansai Photon Science Institute (KPSI), the most advanced academic research on laser acceleration of electrons and ions, as well as on the industrial and medical applications of lasers, has been conducted using the world's top class high-peak-power laser technology for innovation. In FY2015, the installation of a final amplifier in the J-KAREN laser system was completed and the system is now called J-KAREN-P ("P" for peta-watt, Fig.5-3); it has been upgraded to generate sufficient energy to obtain a peak power in the PW range at a 0.1 Hz repetition rate (Topic 5-10). Moreover, in the development of high-speed inspection of the soundness of tunnel concrete with lasers, which is financially supported under the cross-ministerial Strategic Innovation Promotion Program (SIP) of the Cabinet Office of the Government of Japan, we have succeeded in accelerating the inspection of defects by 50 fold over conventional methods (Fig.5-4).

**Fig.5-3 Upgrade of the J-KAREN laser system to J-KAREN-P**
This system is aimed at realizing a peak power over the world-top-class 1 PW level at a 0.1 Hz repetition rate.

In the Harima District of KPSI, the JAEA synchrotron-radiation beamlines at SPring-8 have been utilized to develop

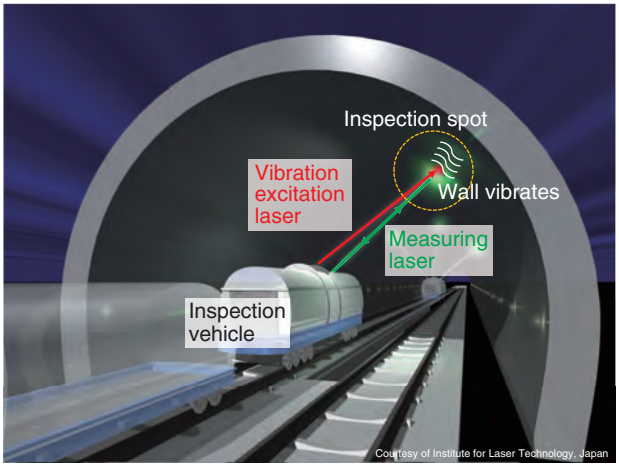


**Fig.5-4 A defect-detection method using laser beams**
Using laser beams, one can perform remote, non-contact detection of the defects in tunnel concrete over a very short time.

a state-of-the-art analytical technique for materials science research. Furthermore, external researchers are being supported as part of the Nanotechnology Platform Project entrusted to us by MEXT. About 28% of all user time was provided for external use in FY 2015.

We are making the most of these quantum beam facilities for the production of radionuclides and the development of structural analysis techniques for biopolymers, and the like for the sake of medical treatment and diagnosis (Topics 5-11 and 5-12). In addition, we are also developing analytical and evaluation methods to clarify the mechanisms of radiation-induced biological actions (Topic 5-13). Through these R&D activities, we expect to contribute to the realization of a healthy and active aging society, the production of biological and regional resources, and the strengthening of the primary industries (namely agriculture, forestry, and fishing), of our nation (Topic 5-14).

In the field of materials science, we are utilizing charged particle beams and radioisotopes to research and develop technologies to create advanced functional materials as well as techniques for controlling and measuring spin information for realization of innovative electronic devices (Topics 5-15 and 5-16). Toward industrial applications, we are also utilizing lasers as well as the laser-driven quantum beams to develop sophisticated techniques for material detection, vibration measurement, microanalysis of radioactive nuclides, and separation of elements (Topics 5-17 and 5-18). Furthermore, using synchrotron radiation and computational science, we are promoting research and development on the analysis and evaluation of the structures, qualities, and functional origins of environmental and energy materials such as hydrogen-storage materials (Topic 5-19).

Other research subjects related to application of quantum beams to recovery from the accident at the TEPCO's Fukushima Daiichi NPS, are described in Topics 1-13 and 1-14 in Chapter 1.

A part of quantum beam science research was taken over to the National Institutes for Quantum and Radiological Science and Technology (QST) established in April 2016 (reported in section 2 of this article).

# 5–1 Realization of High-Accuracy Orbit Control of a High-Intensity Proton Beam

## — Development of a New Pulsed Power Supply for Eliminating Current Ripple —

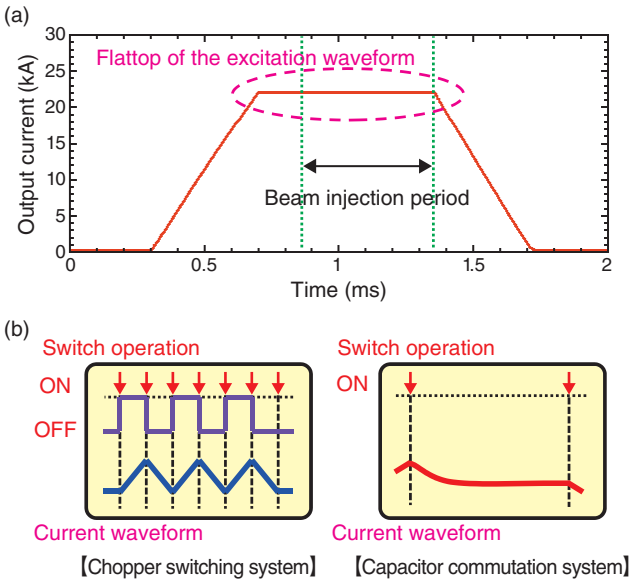


**Fig.5-5 (a) Trapezoidal waveform of a pulsed power supply and (b) current waveform-formation methods using pulsed power supplies of different circuit configurations (blue: chopper-switching system, red: capacitor-commutation system)**
(a) The trapezoidal waveform for exciting an electromagnet with a pulsed power supply is indicated. Ideally the waveform should be flat and without ripples during the beam-injection period to fix a beam orbit.
(b) The current ripple is caused by continuous switching in the chopper-switching system. However, the capacitor-commutation system eliminates this ripple during beam injection as the number of switch operations is limited.

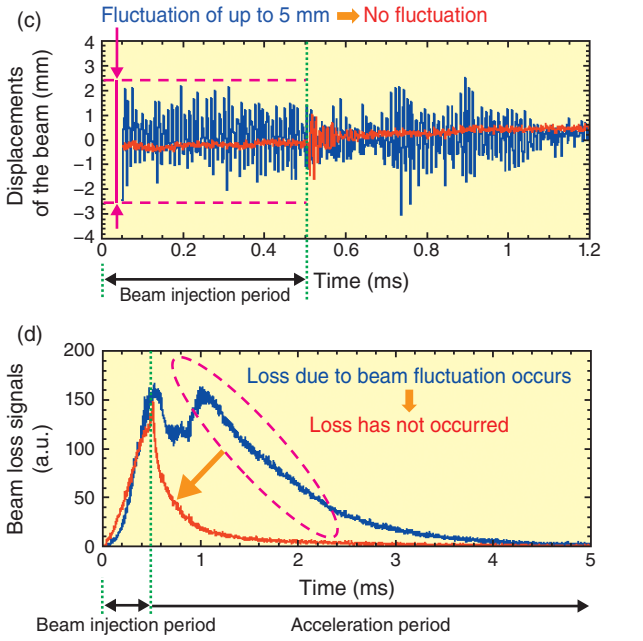


**Fig.5-6 (c) Beam-orbit displacements and (d) beam-loss signals with a beam intensity of 550 kW (blue: chopper-switching system, red: capacitor-commutation system)**
(c) Fluctuation of the beam orbit was at most 5 mm during a beam-injection period with the chopper system. However, in the case of the capacitor-commutation system, the displacement of the beam orbit became approximately zero and beam fluctuation did not occur.
(d) Suppression of the beam loss by the capacitor-commutation system is indicated. A fluctuation in the beam-injection period resulted in beam instability in the course of the acceleration.

Located at the Japan Proton Accelerator Research Complex (J-PARC), the 3 GeV Rapid Cycling Synchrotron (RCS) accelerates injected protons up to 3 GeV with a repletion rate of 25 Hz and is intended to output a 1-MW beam power. The injection-pulsed magnets of the RCS control the injection-beam orbit using the flat tops of the trapezoidal waveform (Fig.5-5(a)) and merge the many protons into a circulating beam.

The original pulsed power supply adopted a chopper-switching system for the main circuit, which formed the trapezoidal waveform by continuous ON/OFF-switching operation of the semiconductor switch (Fig.5-5(b): left). Thus, an arbitrary waveform change was possible and various injection parameters were produced in an acceleration-beam test. However, the continuous current ripple caused by the switching operation caused beam fluctuation (Fig.5-6(c): blue) and beam loss occurring owing to beam instability was observed during beam power ramp-up (Fig.5-6(d): blue).

We paid attention to ensure that the output current of the trapezoidal waveform of the capacitor-commutation system switched only three times per period. The power supply adopting this system is suitable for eliminating current ripple (Fig.5-5(b): right) during the beam-injection period. However, this current-waveform-formation technique is limited by the capacitance value and thus, the design of a control system is a problem that must be solved for RCS beam commissioning. In particular, distortion occurs in a flattop owing to an eddy current effect when the rise time of the waveform is changed.

To decide the basic capacitance value of the capacitor-commutation system, we constructed an equivalent circuit model by understanding the characteristic of the load exactly and analyzed it using circuit simulation. In addition, we devised a new correction circuit capable of controlling the waveform and realized high flattop flatness. Furthermore, in order to reliably reduce current ripple, we worked to reduce high-frequency noise due to the current route of the main circuit.

According to our results, various injection parameters could be produced. Thus, high-accuracy trajectory control without fluctuation has been realized (Fig.5-6(c): red) and a significant reduction of beam loss has been demonstrated (Fig.5-6(d): red). Consequently, there is a prospect of realizing stable user operation with a 1-MW high-intensity proton beam.

**Reference**

Takayanagi, T. et al., Comparison of the Pulsed Power Supply Systems using the PFN Switching Capacitor Method and the IGBT Chopping Method for the J-PARC 3-GeV RCS Injection System, IEEE Transactions on Applied Superconductivity, vol.24, no.3, 2014, p.3800905-1-3800905-5.

# 5–2 A New Tuning Apparatus for High-Intensity Beams in a Linac
## — Beam-Phase-Distribution Measurement for Loss Reduction —

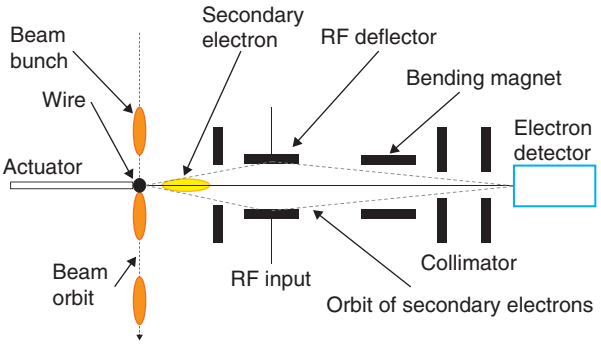


**Fig.5-7 Principle of the bunch-shape monitor**
The bunch-shape monitor comprises an actuator with a target wire, an RF deflector, a bending magnet for adjusting a secondary-electron orbit, a collimator to remove excess electrons, and an electron detector.

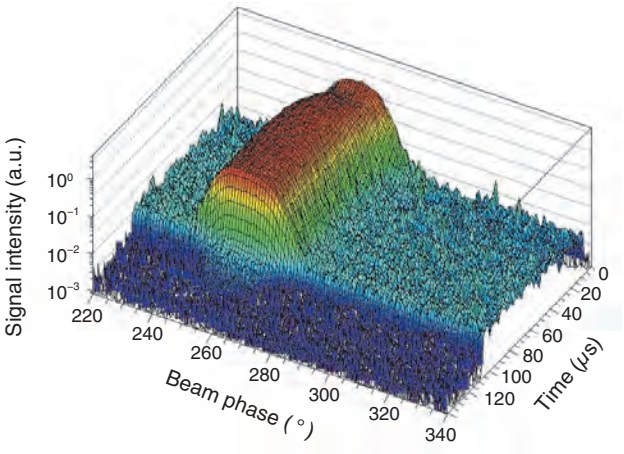


**Fig.5-8 Waveform of the phase distribution**
The distribution of the mountain plots indicates the phase width. The beam direction is from back (t = 0) to front (t = 100 $\mu$s).

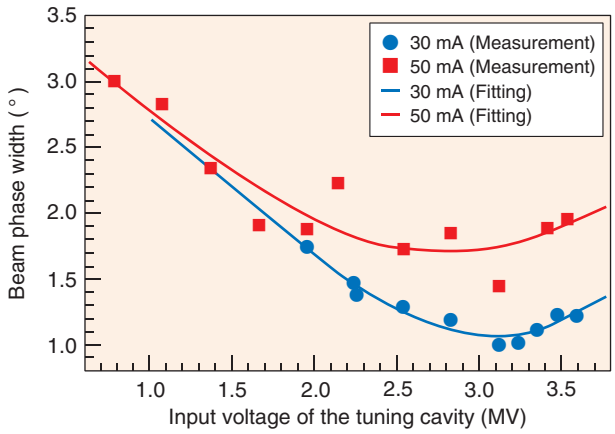


**Fig.5-9 The dependence of phase width upon tuning-cavity amplitude**
When the input voltage is scanned, the tendencies of the phase width are obtained. Measurement results for 30- and 50-mA peak beam currents with the with fitting curves are shown by blue circles and red squares, respectively.

At J-PARC, the linac, which serves as the injector for the 3-GeV synchrotron, accelerates a negative-hydrogen-ion beam ($H^-$) to obtain a 400-MeV beam energy. For radio-frequency (RF) accelerators, a beam-phase monitor for the centroid phase-measurement device is usually employed to determine the set point of the RF phase. We use an accelerating frequency of 324 MHz for the cavities in the middle of the linac and of 972 MHz for the downstream linac cavities. Because the high-brightness accelerators at J-PARC should suppress beam loss (which leads to radiation during operation and the activation to the machine components), both the centroid-phase set point at the frequency jump from 324 MHz to 972 MHz and the phase-width control are key issues for suppressing the excess beam loss. We developed a bunch-shape monitor (BSM) to measure the phase width as well as a tuning strategy to minimize the beam loss below 1 W/m along the linac beam line.

Fig.5-7 shows a schematic view of the BSM. The device is based on secondary electrons emitted from an interaction between the beam and tungsten wire. Because the secondary electrons are generated rapidly and retain their original phase distribution, the device can obtain the phase distribution of the charge in bunches by adjusting the phase of the deflecting field. Fig.5-8 shows the waveform of the phase distribution. The time duration of a pulse length is 100 $\mu$s and the Gaussian distribution can be obtained every 1 $\mu$s. We define the root-mean-square (rms) phase width by the standard variations calculated from the distribution. Amplitude-scanning results of the tuning cavity, which is located in front of the bunch-shape monitor, is shown in Fig.5-9. Once the phase width is decreased on the amplitude of the tuning cavity, because the bunching force depends on the gradient of supplied RF. As per the theory of geometric optics, the focalusing point is shifted closer to the tuning cavity and over-focusing occurs owing to the excess amplitude. We compare these curves with a beam-dynamics simulation and estimate the optimal set point of the amplitude of the tuning cavity. This tuning suppresses the beam loss within 1 W/m along the linac beam line.

BSMs are presently used at high-brightness accelerator facilities around the world. We proposed to use the phase-width measurement and refer to beam-dynamics simulations to obtain the optimal amplitude of the tuning cavity at the frequency-jump point. This validated the suppression of the beam loss and established a new cavity-tuning method.

**Reference**

Miura, A. et al., Bunch Shape Measurement of 181 MeV Beam in J-PARC Linac, JPS Conference Proceedings, vol.8, 2015, p.011003-1-011003-6.

# 5–3 Successful Impact Mitigation with Microbubbles in Liquid Metal

## — Development of a Microbubble Generator in Mercury for Realizing the Most Intense Spallation Neutron Source in the World —

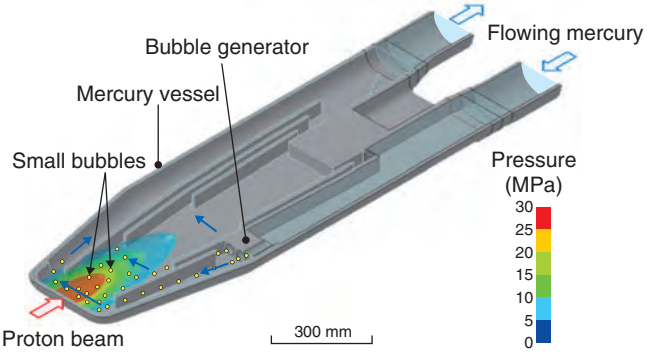


**Fig.5-10 Schematic of the initial pressure generated in mercury by proton-beam bombardment**
A maximum initial pressure of approximately 40 MPa is generated in mercury by bombardment of a 1-MW pulsed proton beam.

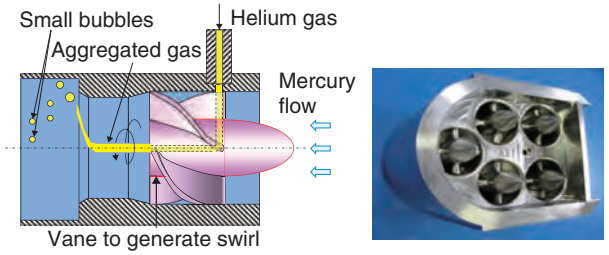


(a) Bubble generator (Single element)

(b) Bubble generator installed into real mercury vessel

**Fig.5-11 Swirl-type bubble-generator**
(a) Gas is broken into small bubbles by swirl flow of the liquid metal. (b) Coalescence of the generated bubbles is prevented by arranging several generators in parallel, alternating each swirl direction with the one next to.

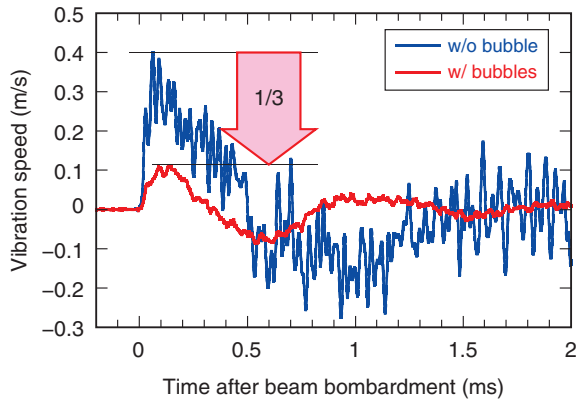


**Fig.5-12 Effect of small bubbles on the pressure load of the mercury vessel**
It was demonstrated that bubble injection under 300-kW proton-beam operation reduces the vibration speed of the mercury vessel to 1/3 of its value in the case without bubbles.

At the spallation neutron source in J-PARC, pulsed proton beams (pulse duration: 1 $\mu$s; repetition rate: 25 Hz; Power: 1 MW) are bombarded onto a mercury target to generate neutrons for various innovative material science research purposes. A mercury target contains mercury in a vessel composed of stainless steel such that proton-beam bombardment rapidly increases the mercury temperature, inducing rapid increase of pressure in the mercury (Fig.5-10). According to a numerical simulation, a maximum stress of 150 MPa was generated cyclically and cavitation erosion occurred at the forefront of the mercury vessel owing to rapid increase of pressure. Therefore, it is critical to reduce the pressure generated in mercury to prevent fatigue fracture and mitigate cavitation erosion.

As a countermeasure against this issue, we proposed that pressure can be reduced by absorbing the thermal expansion of mercury by contraction of a helium-gas bubble. Since rapid thermal expansion cannot be absorbed owing to the low natural frequency of a large bubble, it is necessary to generate small bubbles of less than 100 $\mu$m in radius in the flowing mercury.

We first attempted to generate bubbles by injecting gas into mercury through a narrow needle. However, gas adhered to the surface of nozzle because of the poor wettability of mercury to steel, resulting in a generated bubble size reaching several mm. Then, we developed a novel swirl-type bubble-generator (Fig.5-11). In this generator, a swirl flow of mercury is generated inside cylinder and the gas aggregated in the center of swirl is broken into small bubbles owing to changes in swirl speed and pressure along the radial direction at the exit of cylinder. We also devised an original idea to arrange several generators in parallel, alternating each swirl direction with the one next to, in order to eliminate mercury swirl downstream the exit, which causes coalescence of bubbles. Furthermore, we investigated the relationship between the vane angle set in the cylinder and the size of the generated bubbles by experimentally considering the discharge pressure of the mercury pump. Consequently, we optimized the geometry of the bubble generator, succeeding in generating small bubbles of 90 $\mu$m in radius.

This swirl-type bubble-generator was installed in the mercury vessel. As shown in Fig.5-12, we demonstrated that injection of small bubbles reduced the vibration speed of the mercury vessel to 1/3 of its value in the case without bubbles. This result indicated that the stress generated in the mercury target was reduced to 50 MPa under 1-MW beam bombardment, satisfying the criterion against fatigue fracture (less than 90 MPa).

Toward the realization of the most intense spallation neutron source in the world, we must quantitatively ensure the effectiveness of small bubbles for suppressing cavitation erosion in a real target step-by-step as beam power is increased up to 1 MW.

**Reference**

Kogawa, H. et al., Development of Microbubble Generator for Suppression of Pressure Waves in Mercury Target of Spallation Source, Journal of Nuclear Science and Technology, vol.52, issue 12, 2015, p.1461-1469.

# 5–4 Opening up a New Frontier of Material Science using Single-Crystal Neutron Diffraction
## — Development of the Extreme Environment Single Crystal Diffractometer SENJU —


**Fig.5-13 Photograph and schematic view of SENJU**
(a) Photograph and (b) schematic view of SENJU. The sample crystal is set in a vacuum sample chamber. Scattered neutrons are detected by area detectors arranged around the chamber.

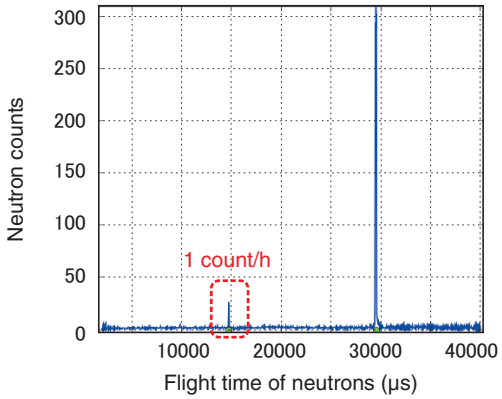


**Fig.5-14 Neutron-diffraction data for a small taurine single-crystal detected by SENJU**
Part of the diffraction data detected by SENJU. Even a weak diffraction peak, 1 count per 1 hour, was successfully observed as a significant signal.

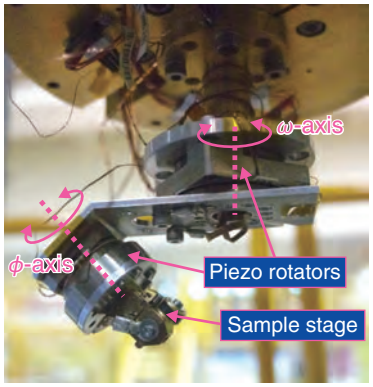


**Fig.5-15 Sample rotation device for SENJU**
A sample crystal fixed on an aluminum rod is set on the sample-mounting table. The sample can be rotated with along the $\omega$- and $\phi$-axes using piezo-rotators.

Single-crystal neutron diffraction is one of the most fundamental and powerful techniques for determining the arrangement of light elements and magnetic moments in crystalline materials with high accuracy and reliability. Thus, this technique has been used in various scientific fields, including physics, chemistry, molecular biology, material science, and energy science, and has the potential to be an irreplaceable analytical tool for the development of new functional materials such as proton conductors, hydrogen-absorbing materials, and magnets. However, because a large (over 1.0 $mm^3$ in volume) single-crystal sample is required, the number of experiments has been limited. Recently, we developed a new single-crystal neutron diffractometer called SENJU at MLF to alleviate this limitation.

SENJU has a vacuum sample chamber around which 37 area detectors are arranged cylindrically, as shown in Fig.5-13. Because the chamber and collimators were designed properly, a very low background was achieved; consequently, weak Bragg spots from the small sample crystal were significantly observed. In addition, large amounts of neutrons scattered from the sample were efficiently collected by covering a large solid angle with area detectors. Besides being used to achieve a high-intensity neutron beam at J-PARC, these features have also allowed diffraction measurements of 0.1-$mm^3$-volume single crystals at SENJU.

As an example of such a measurement at SENJU, Fig.5-14 shows Bragg peaks of a single 0.1-$mm^3$-volume taurine crystal measured by SENJU. Even though the intensity of the peak indicated by the red frame was very weak (only one neutron counted per hour), this peak was measured as a significant signal because of the low background of SENJU. 980 Bragg peaks of the taurine crystal (including such weak peaks) were collected over a 7-day measurement, and the molecular structure of taurine including hydrogen atoms was successfully determined.

At SENJU, a two-axis sample-rotation system at temperatures below 10 K was also developed using piezo-rotators that work under low-temperature and evacuated conditions, as shown in Fig.5-15. In previous low-temperature devices, sample rotation has only been possible on one axis and, consequently, some of the Bragg peaks required for structural analysis were immeasurable. Using the new sample-rotation system, almost all peaks required for structural analysis became measurable by SENJU, even under low temperature.

The measurable size of a sample crystal by SENJU is compatible with that for measurements of various types of physical properties. This means that the development of SENJU enables both crystal structure and physical properties to be determined with the same sample in the same condition. We believe that SENJU will open up a new frontier of material science using single-crystal neutron diffraction.

**Reference**

Ohhara, T. et al., SENJU: A New Time-of-Flight Single-Crystal Neutron Diffractometer at J-PARC, Journal of Applied Crystallography, vol.49, part 1, 2016, p.120-127.

# 5–5 Probing Novel Characteristics of Unconventional Superconductors via Neutron Scattering under a Magnetic Field
## — Magnetic-Field-Enhanced Antiferromagnetism in Unconventional Superconductors —

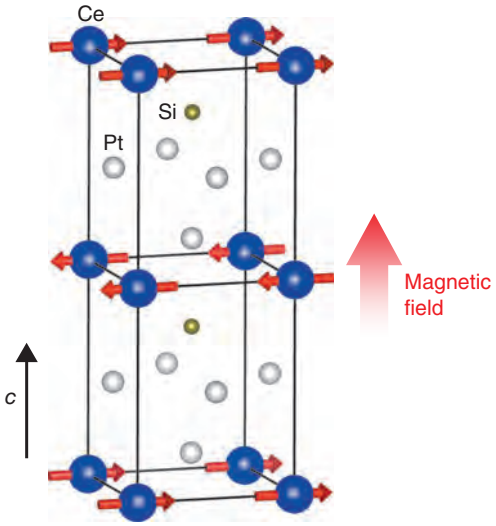


**Fig.5–16 Crystal and antiferromagnetic structure of $CePt_3Si$ with a schematic experimental configuration**
Arrows in the figure represent the magnetic moment of Ce.

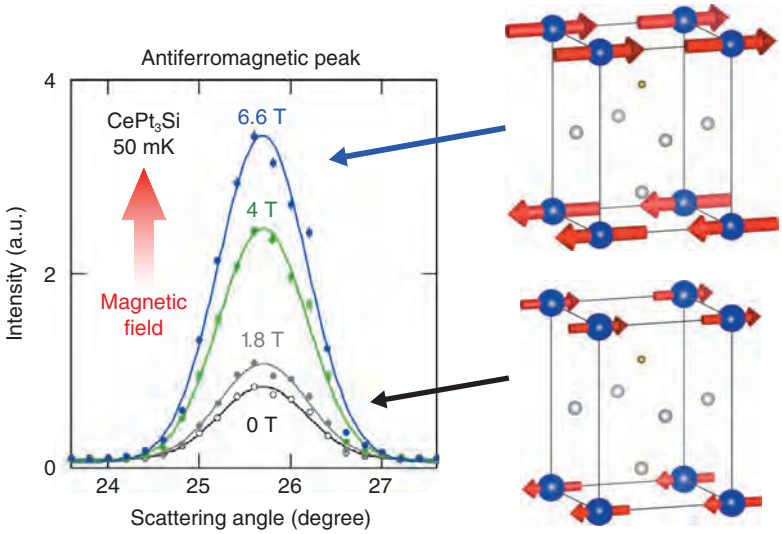


**Fig.5–17 Magnetic-field response of the antiferromagnetic peak**
The intensity of the antiferromagnetic peaks is strongly enhanced under application of the magnetic field.

Superconductivity emerges from the formation of bound pairs of electrons, the so-called Cooper pairs, which originate from an attractive force between electrons. Whilst lattice vibration plays a dominant role in conventional superconductors, unconventional superconductivity is believed to arise mostly from magnetic fluctuation. In fact, the majority of unconventional superconductors have been discovered in the vicinity of a magnetic critical point, where magnetic fluctuation is strongly enhanced.

Conversely, superconductivity in $CePt_3Si$ is realized in a long-range antiferromagnetic ordered state. The antiferromagnetic order in $CePt_3Si$ is characterized as a ferromagnetic basal *c*-plane stacked alternatively along the *c*-axis (Fig.5-16). It is of great interest to determine how antiferromagnetic order can coexist with superconductivity.

Determining an external field response is a useful approach to unveiling the true nature of the state of matter. Here, we applied an external magnetic field to understand antiferromagnetism in $CePt_3Si$. Owing to its transparent character, neutron scattering is highly compatible with an extreme sample environment such as high-magnetic-field and low-temperature as well as a sensitive probe for studying antiferromagnetism. Therefore, we conducted neutron-scattering experiments under high magnetic field at temperatures as low as 50 mK using the V2 spectrometer at Helmholtz-Zentrum-Berlin (Germany) and the IN14 spectrometer at Institut-Laue-Langevin (France). In typical antiferromagnets, a staggered moment arrangement is unfavorable against a uniform magnetic field and collapses with an increasing applied field. Contrarily, the antiferromagnetic peak intensity is strongly increased by a factor of more than 4 with magnetic fields (Fig.5-17). This increase in intensity suggests an enhancement of the antiferromagnetic moment. This enhanced magnetic moment under a magnetic field implies an underlying hidden magnetic moment at a zero field, a unique character of the antiferromagnetic order of $CePt_3Si$. Therefore, it may help to reveal the mechanism of this field-induced moment enhancement for understanding the coexistence of superconductivity and magnetism in $CePt_3Si$.

This work is performed under a framework for collaborations on actinide-compound research among the JAEA, the CEA (Grenoble, FR), and the ITU (Karlsruhe, DE).

**Reference**

Kaneko, K. et al., Magnetic–Field–Enhanced Antiferromagnetism in the Noncentrosymmetric Heavy–Fermion Superconductor $CePt_3Si$, Physical Review B, vol.89, issue 24, 2014, p.241105–1–241105–5.

# 5–6 Elucidation of the Selective Separation of Cesium by Small-Angle Neutron Scattering — Toward Selective Separation of Cesium using a $\pi$–$d$ Hybrid Orbital —

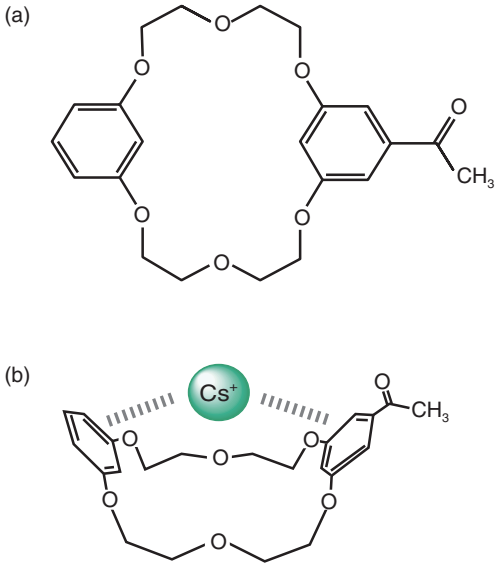


**Fig.5-18 Coordination structure composed of DB20C6 and $Cs^+$**
(a) The chemical structure of a derivative of benzo-crown ether (DB20C6), which coordinates preferentially with $Cs^+$ compared with other alkali metal ions. (b) Proposed coordination structure formed by DB20C6 and $Cs^+$ ($DB20C6/Cs^+$) based on a DFT calculation. The two benzene rings of DB20C6 fold around $Cs^+$ above the center of the crown-ether ring of DB20C6 based on hybridization between the $\pi$ electron orbital of the benzene rings and the $d$ orbital of $Cs^+$.

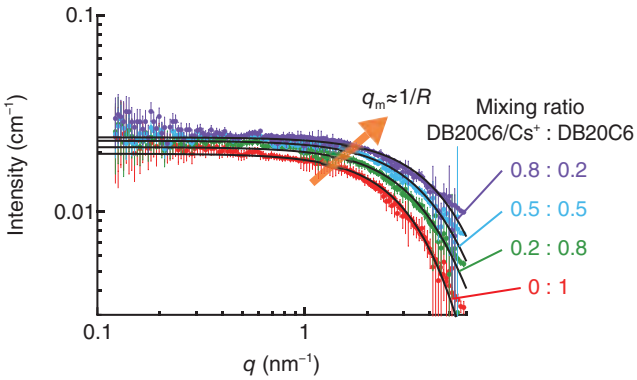


**Fig.5-19 SANS profiles obtained for the mixtures of DB20C6 and $DB20C6/Cs^+$**
Double-logarithmic plots of the SANS profiles obtained for the mixture of $DB20C6/Cs^+$ and DB20C6 in DMSO-$d_6$ at different mixing ratios: 0.8:0.2 (purple), 0.5:0.5 (blue), 0.2:0.8 (green), and 0:1 (red). The average radius of gyration of the solutes ($R$) is in inverse proportion to the characteristic $q$ position ($q_m$), that is, $q_m \approx 1/R$, which starts to decrease in small-angle scattering intensity at this position. $q_m$ moves toward higher $q$ as the proportion of $DB20C6/Cs^+$ in the solution increases, which agrees with the result of DFT calculation (solid black lines). SANS measurements were performed with the time-of-flight extended $q$-range SANS spectrometer of the Spallation Neutron Source (SNS), the Oak Ridge National Laboratory, USA.

Following the accident at the TEPCO's Fukushima Daiichi NPS in Japan in 2011, radioactive cesium was released into the northern Kanto and southern Tohoku areas. The development of physicochemical techniques for removing cesium ions ($Cs^+$) is required to decrease the radioactivity in these areas. In particular, the selective separation of $Cs^+$ from other cations contributes to remediation and reduction of the volume of contamination. Crown ethers are macrocyclic organic compounds that exhibit electrostatic interactions between an alkali-metal ion and multiple oxygen atoms in the ether ring and are thus difficult to use for selective separation of $Cs^+$. Against this background, we found a derivative of benzo-crown ether, mono-acetyl substituted dibenzo-20-crown-6-ether (DB20C6) (Fig.5-18(a)), which preferentially forms stable complexes with $Cs^+$ as compared with $Na^+$ and $K^+$. Understanding the selectivity mechanism contributes to the development of more effective adsorbents for $Cs^+$ in solution.

In this study, we used density-functional-theory (DFT) calculation and small-angle neutron scattering (SANS) to elucidate the mechanism of this selectivity. The result of DFT calculation suggested that the stability of the complex formed by DB20C6 and $Cs^+$ ($DB20C6/Cs^+$) arose from the interaction between the $\pi$-orbitals of the two benzene rings and the $d$-orbital of $Cs^+$. That is, the $\pi$-electrons of the benzene rings are donated to the vacant $d$-orbitals. This calculation indicates that $Cs^+$ is stably bound above the center of the ether-oxygen ring by the two benzene rings and that DB20C6 adopts the folded structure shown in Fig.5-18(b). Note that neither $Na^+$ nor $K^+$ can form the $\pi$–$d$ hybrid orbital because there are no electrons in their $d$-orbitals. Therefore, hybridization would be attributed to the high selectivity of $Cs^+$ among alkali metal ions.

Fig.5-19 shows the SANS profiles obtained for mixtures of $DB20C6/Cs^+$ and free DB20C6 in deuterated dimethyl sulfoxide (DMSO-$d_6$) as functions of their mixing ratios. The characteristic $q$ position, which starts to decrease in small-angle scattering intensity at this position, moves toward higher $q$ as the fraction of $DB20C6/Cs^+$ in the solution increases, indicating that the size of $DB20C6/Cs^+$ is smaller than that of free DB20C6 in accordance with the coordination structure predicted by DFT calculation. The experimental data agreed well with SANS profiles calculated using the Debye function for scattering on an absolute scattering-intensity scale. Here, the structures of $DB20C6/Cs^+$ and free DB20C6 from the DFT calculation were used for this theoretical calculation of the scattering profiles. This result leads us to the conclusion that SANS analysis experimentally supports the coordination structure of $DB20C6/Cs^+$ and lends credence to the prediction that the driving force behind $Cs^+$ selective coordination is hybridization between the $\pi$ electrons of the two benzene rings and the $d$-orbital of $Cs^+$. This work will contribute to the further development of materials for separating radioactive $Cs^+$ in solution.

**Reference**

Motokawa, R. et al., Small-Angle Neutron Scattering Study of Specific Interaction and Coordination Structure Formed by Mono-Acetyl-Substituted Dibenzo-20-Crown-6-Ether and Cesium Ions, Journal of Nuclear Science and Technology, vol.53, issue 8, 2016, p.1205-1211.

# 5–7 Electric Power Generation by Temperature Variation

## — Observation of Ferroelectric Materials under Power Generation using Synchrotron X-ray Diffraction —

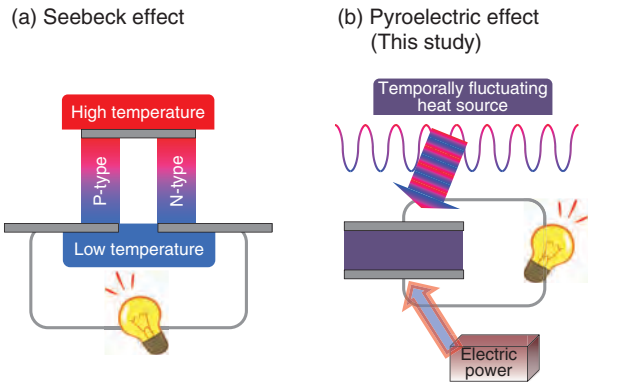


**Fig.5-20 Typical thermoelectric-conversion methods**
(a) The conversion of a spatial temperature gradient into electric power using the Seebeck effect. (b) The conversion of temporal temperature variation into electric power using the pyroelectric effect. In addition to this, our study uses a synchronized external power supply.

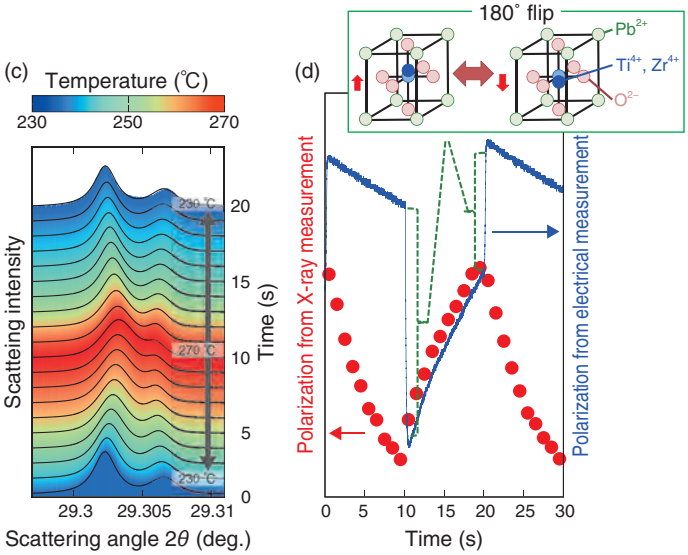


**Fig.5-21 Synchrotron X-ray spectra and polarizations of the sample**
(c) X-ray-spectrum change under temperature variation. (d) Polarization change derived from X-ray (red circle) and electrical (blue dot) measurements. Inset shows the positions of the atoms in the 180˚ flip state. The difference between the X-ray and electrical measurements (discrete green jump of electrical measurement) shows a 180˚ flip.

In modern society, only one quarter of the total energy consumed is effectively utilized. The remaining three quarters are released in the form of waste heat and the like. Therefore, it is essential to develop a technology for converting waste energy into reusable electric power to realize an energy-saving society. The most widely studied method for converting heat into electricity is the application of the Seebeck effect using the spatial-temperature gradient in semiconductors and the like (Fig.5-20(a)); however, this method requires two types of elements, n-type and p-type, and there is a tradeoff between low thermal conductivity and high electrical conductivity when achieving higher efficiency. In contrast, the temperature of waste heat sometimes fluctuates and this temporal change can be converted to electrical energy using the pyroelectric effect of ferroelectric materials (Fig.5-20(b)). This method requires only one element, but its efficiency is currently rather low. However, by applying an external electric field synchronized with the temperature variation, the output electric power can be dramatically enhanced compared with the electrical-energy input.

We have been promoting research on power-generation mechanisms using the temporal temperature change of vehicle exhaust gas. Under the simulated exhaust gas environment in laboratories, the output power is enhanced both by applying an external electric field in sync with the temperature variation and by improving the electrical circuit. We could also remove actually available power using the exhaust gas from an automobile engine. Furthermore, we succeeded in examining the sequence of polarization change of the ferroelectric element using synchrotron X-ray diffraction at beamline BL14B1 of SPring-8 under power-generation operation (Fig.5-21(c)). By comparing the simultaneously measured polarization results of the X-ray and electrical measurements, the rotation of the polarization by 180° (180° flip) is found to be more important than the rotation by 90° (90° flip) (Fig.5-21(d)). This result has been fed back to the selection and growth steps of the elements and is expected to be applied to various types of waste heat from plants in the future.

Our research was accomplished as a collaborative study with the Daihatsu Motor Co., Ltd. and the Nagaoka University of Technology.

**Reference**

Kim, Y., Fukuda, T. et al., Novel Electrothermodynamic Power Generation, Advanced Energy Materials, vol.5, issue 13, 2015, p.1401942-1-1401942-6.

# 5–8 Unmasking the Ferromagnetism in Magnetically-Doped Topological Insulators
## — Toward Ultra-Low Power-Consumption Spintronic Devices —

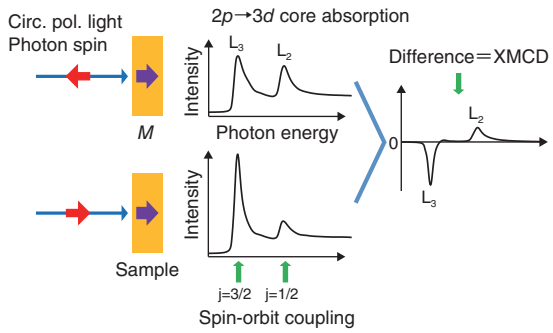


**Fig.5-22 XMCD schematics in core-level absorption**
The XMCD is defined as the difference in absorption intensity between left- and right-polarized light.

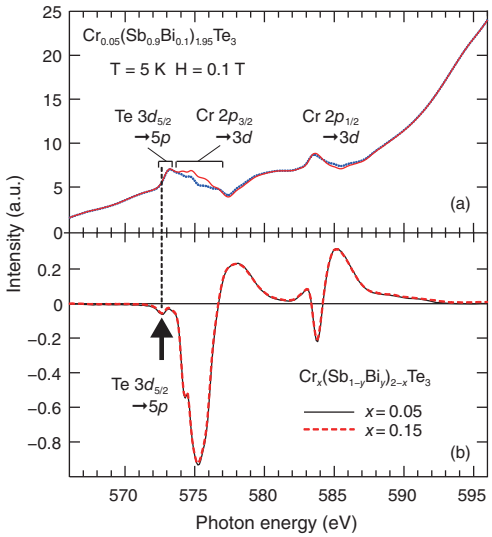


**Fig.5-23 Experimental spectra of $Cr_x(Sb_{1-y}Bi_y)_{2-x}Te_3$ at the Cr $2p \rightarrow 3d$ and Te $3d \rightarrow 5p$ edges**
XAS (a) and XMCD (b) spectra measured at 5 K and 0.1 T.

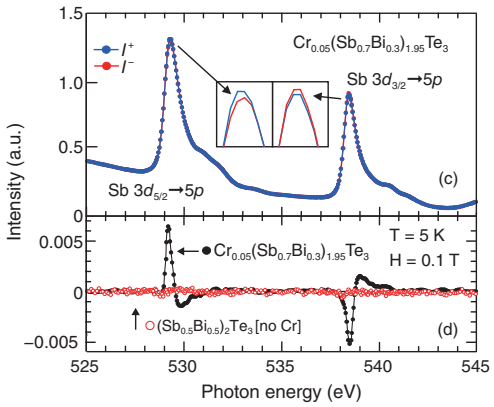


**Fig.5-24 Experimental spectra of $Cr_x(Sb_{1-y}Bi_y)_{2-x}Te_3$ at the Sb $3d \rightarrow 5p$ edges**
XAS (c) and XMCD (d) spectra measured at 5 K and 0.1 T.

Recently, topological insulators (TIs), characterized as bulk insulators with conducting states on their surface, have attracted attention globally owing to the quantum-anomalous Hall effect (QAHE) discovered in ferromagnetic Cr-doped $(Sb,Bi)_2Te_3$ TI at very low temperatures. The QAHE enables electric currents to flow with little energy consumption. To realize QAHE at room temperature, unmasking the underlying physics behind the ferromagnetism is required. We have performed an X-ray magnetic-circular dichroism (XMCD) experiment at the BL23SU of SPring-8 and revealed the origin of ferromagnetism by detecting not only the magnetic moment of Cr $3d$ electrons but also those of "nonmagnetic" Sb and Te $5p$ electrons. The XMCD spectrum is defined as the difference between the core-absorption spectra (XAS) of the left- and right-handed circularly polarized light, as schematically shown in Fig.5-22.

Fig.5-23(a) shows the Cr $2p \rightarrow 3d$ XAS spectra of $Cr_x(Sb_{1-y}Bi_y)_{2-x}Te_3$ ($x = 0.05$, $y = 0.1$, $T_C = 15$ K) measured at a magnetic field of 0.1 Tesla and a temperature of 5 K. Fig.5-23(b) shows the XMCD spectra for two different Cr contents ($x = 0.05, 0.15$). We find that the signals are negative and positive at the $2p_{3/2} \rightarrow 3d$ and $2p_{1/2} \rightarrow 3d$ edges, respectively, which signifies that the Cr $3d$ electrons are responsible for ferromagnetism. As indicated by an arrow in Fig.5-23(b), a negative signal at the Te $3d_{5/2} \rightarrow 5p$ edge below the Cr $2p_{3/2}$ edge is observed. This tells us that the magnetic moments of the Te $5p$ and Cr $3d$ electrons are coupled in an antiparallel manner.

Fig.5-24 shows the Sb $3d \rightarrow 5p$ XAS (c) and the associated XMCD (d) spectra for $Cr_{0.05}(Sb_{0.7}Bi_{0.3})_{1.95}Te_3$. Here, we find positive and negative signals at the $3d_{5/2} \rightarrow 5p$ and $3d_{3/2} \rightarrow 5p$ edges, respectively. No XMCD spectrum is found for the sample without Cr doping [$(Sb_{0.5}Bi_{0.5})_2Te_3$]. The result tells us that the Sb $5p$ moment is aligned parallel to the Cr $3d$ magnetic moment. Therefore, we confirm that the Cr $3d$ magnetic moments are mediated by the Te and Sb $5p$ holes, which work as a glue for the largely separated Cr spins in the crystal and should be a key to the ferromagnetism of magnetic TI $Cr_x(Sb_{1-y}Bi_y)_{2-x}Te_3$.

Our results will open the way to the future material design of QAHE systems and may provide a guideline for practical application of next-generation ultra-low power-consumption devices using TIs.

**Reference**
Ye, M., Saitoh, Y. et al., Carrier-Mediated Ferromagnetism in the Magnetic Topological Insulator Cr-Doped $(Sb,Bi)_2Te_3$, Nature Communications, vol.6, 2015, p.8913-1-8913-7.

# 5-9 Nondestructive Three-Dimensional Elemental Analysis using an Ion Microbeam
## — Development of Particle-Induced X-ray-Emission Tomography —

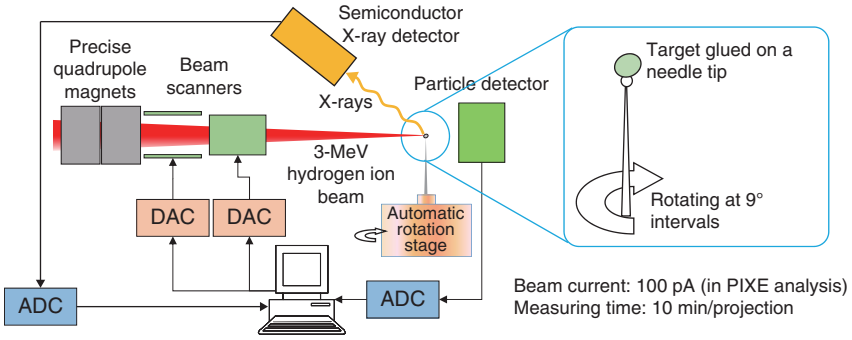


**Fig.5-25 Schematic diagram of the PIXE Tomography system**
A 3-MeV hydrogen-ion beam is focused to a diameter of 1 μm by precise quadrupole magnets and used to scan across a 100 μm × 100 μm area on a target. The three-dimensional elemental distribution is reconstructed from the location and energy of the X-rays emitted from the target by a computer.

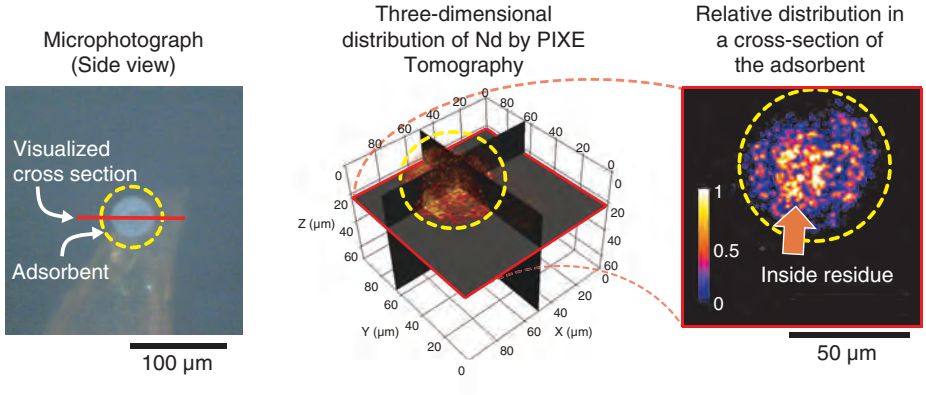


**Fig.5-26 Optical micrograph of a porous silica-adsorbent particle for EXC (left figure) and the results of PIXE tomography (center and right figures)**
The left figure exhibits a porous silica-adsorbent particle fixed on the tip of a needle. An arbitrary tomographic image of the Nd distribution in the particle was obtained by PIXE tomography, as shown in the right figure.

We developed a particle-induced X-ray emission (PIXE) tomography system (Fig.5-25) based on the micro-PIXE analyzer using a MeV-class hydrogen-ion microbeam in the TIARA facility. In our system, a three-dimensional elemental distribution was obtained by image reconstruction from 40 two-dimensional projections measured by micro-PIXE. Moreover, to compensate for the decrease of X-ray production with decreasing energy of the beam and the absorption of X-rays, the modified maximum-likelihood-expectation-maximization (ML-EM) image-reconstruction method has enabled us to know the internal elemental distribution, even in a target several dozen $\mu$ms thick.

Using our PIXE tomography system, we analyzed a 50-$\mu$m-diameter porous silica-adsorbent particle for extraction chromatography (EXC). In EXC, dissolved ions are first adsorbed to the adsorbent packed in a column and then eluted. Although EXC is promising for selectively removing long-half-life minor actinides (MAs) from high-level radioactive waste, its elution rate is insufficient at present. Even after the elution process, neodymium (Nd) substituting for MAs was detected by micro-PIXE. However, it was difficult to not only estimate the residual quantity inside the particle because of the overlapping surface distribution but also directly analyze a cross-sectional surface because of fragility. Therefore, we made an effort to measure the cross-sectional distribution of the residual Nd nondestructively using PIXE tomography. Consequently, we identified locally-concentrated Nd inside the eluted particle, as shown in Fig.5-26. Such a distribution is considered to depend upon the size of the micropores in the adsorbent, the concentration, and the passing speed of eluent. We will decide the optimal conditions of these parameters using PIXE tomography from now on.

**Reference**

Satoh, T. et al., Particle Induced X-Ray Emission-Computed Tomography Analysis of an Adsorbent for Extraction Chromatography, Nuclear Instruments and Methods in Physics Research B, vol.371, 2016, p.419-423.

# 5–10 The Challenge of Realizing Unexplored Super-Strong Electromagnetic Fields with a Laser
## — J-KAREN-P Laser Development —

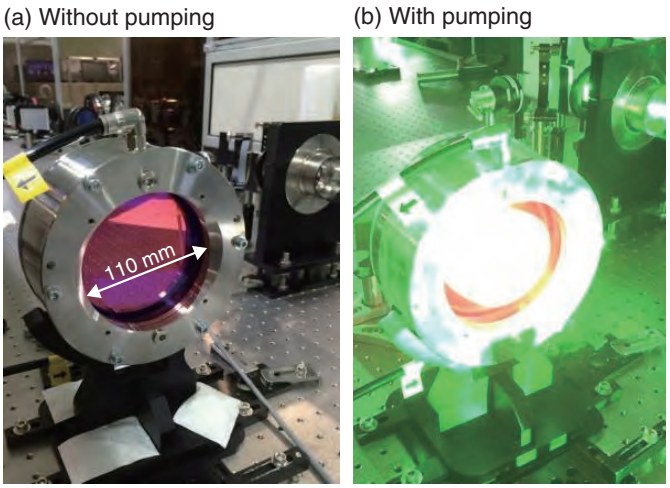


**Fig.5-27 A T:Sap crystal for energy amplification in J-KAREN-P**
The world's largest 120 mm crystal in a water-cooled holder for J-KAREN-P (crystal clear aperture: 110 mm). The energy is stored in the central white part by strong green pump lasers.

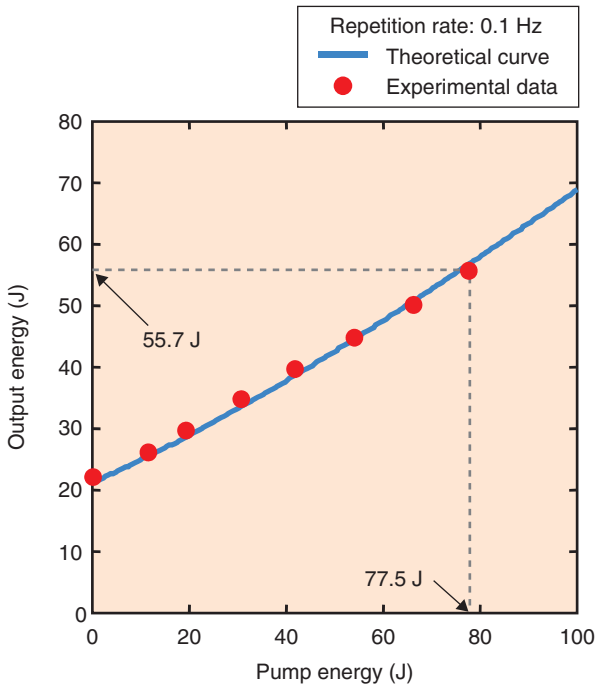


**Fig.5-28 Output energy from the final Ti:Sap amplifier**
According to theory, the output energy as a function of pump energy is increased with the suppression of parasitic oscillation. The output energy of 55.7 J enables a PW peak power, which is our aim.

A super-strong electromagnetic field is created when an ultra-high-intensity laser is focused down to a very small area. High-energy particles such as electrons and ions as well as X-rays are generated by the interaction of atoms with the electric field in this condition. We have developed the world's top-class ultra-high intensity and ultra-short-pulse laser (J-KAREN) to realize an unexplored super-strong electromagnetic field of $10^{22}$ W/cm$^2$ for generating higher-energy particles. In the J-KAREN-P, the goal is to generate a $10^{15}$ W (1 PW: petawatt) ultra-high-intensity pulse at a 0.1-Hz repetition rate (0.1 Hz) by concentrating 30 J of energy into an ultra-short pulse duration of 30 fs (fs = $10^{-15}$ s).

A titanium-doped sapphire crystal (Ti:Sap crystal) is used for energy amplification of the laser. The energy is stored in the Ti:Sap crystal when the crystal is pumped by green lasers (Fig.5-27). Energy amplification occurs owing to stimulated emission when the laser passes through the pumped region. In J-KAREN-P, the laser energy is increased by gradually increasing the laser-beam size.

Before now, the laser was fired every 30 min owing to thermal distortion in the glass-laser material because a large-aperture glass laser was used for pumping the final Ti:Sap amplifier. With this upgrade, thermal distortion is significantly suppressed and the laser can be fired at 0.1 Hz because the pump-glass laser was divided into 6 lasers with small aperture.

Furthermore, the energy loss due to parasitic oscillation in the large-aperture Ti:Sap crystal was suppressed by putting a light-absorption-liquid (methylene iodide) around the crystal. As a result, the output energy as a function of pump energy is achieved according to theory at 0.1 Hz (Fig.5-28). The throughput is about 70% to obtain compression pulse of 30 fs after amplification. Thus, the design goal of 30 J of compressed energy at 0.1 Hz and PW-order peak power can be expected because of the achievement of a 55.7-J output energy (pump energy 77.5 J).

With this, the world's best-performing laser developed by our research; rapid progress in the study of new phenomena under unexplored super-strong electromagnetic fields is expected, together with various applications, such as a compact particle accelerators or cancer-therapy machines.

**Reference**

Kiriyama, H. et al., High-Contrast, High-Intensity Petawatt-Class Laser and Applications, IEEE Journal of Selected Topics in Quantum Electronics, vol.21, no.1, 2015, p.1601118-1-1601118-18.

# 5–11 Dual Treatment and Diagnosis Role Played by Simultaneous Emission of β- and γ-rays
## — Production of Highly Purified Lutetium-177 for Radioimmunotherapy —

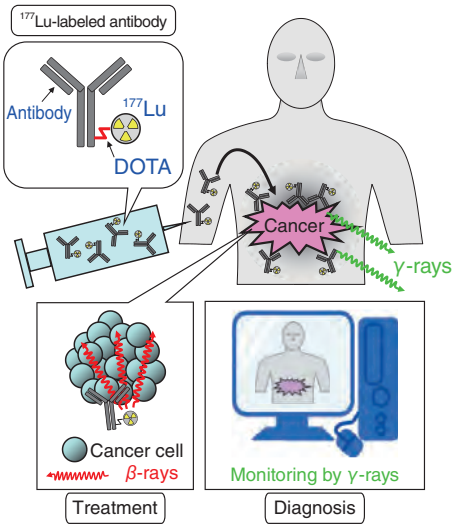


**Fig.5-29 Treatment and diagnosis of cancer by a $^{177}$Lu-labeled antibody**
$^{177}$Lu is bound to an antibody through the chelator 1,4,7,10-tetraazacyclododecane-1,4,7,10-tetraacetic acid (DOTA). The $^{177}$Lu-labeled antibody administrated within the body binds to an antigen that is specifically expressed on a cancer cell. During treatment, β-rays emitted from $^{177}$Lu kill the cancer cells. Simultaneously, diagnostic imaging to investigate the biodistribution in the body can be performed by measuring γ-rays from outside.

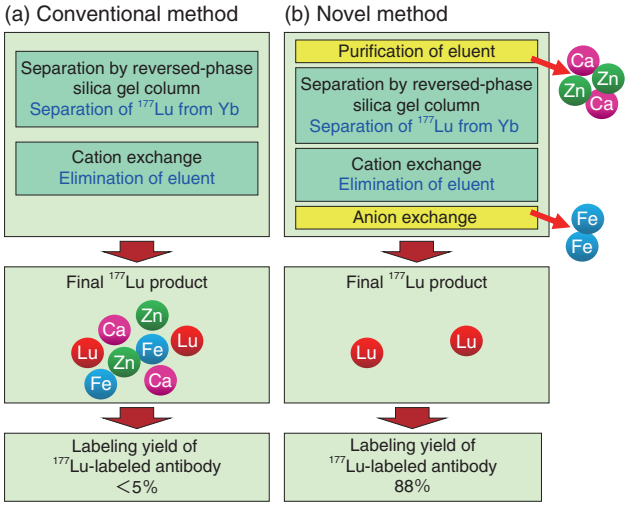


**Fig.5-30 Separation of $^{177}$Lu from neutron-irradiated Yb**
In the conventional method (a) that we have developed, the labeling yield of the $^{177}$Lu-labeled antibody was < 5%, owing to inhibition by Ca, Fe, and Zn included in final $^{177}$Lu product. In the novel method (b), the Ca, Fe, and Zn were eliminated by both purification of eluent and addition of an anion exchange. Consequently, the labeling yield of the $^{177}$Lu-labeled antibody increased up to 88%.

At present, beta-emitting radionuclides are used for cancer treatment. Lutetium-177 ($^{177}$Lu) is regarded as a promising novel radionuclide because it emits not only β-rays but also γ-rays. By measurement of the γ-rays from outside of the body, diagnostic imaging to investigate the biodistribution within the body can be performed (Fig.5-29).

Fig.5-29 shows a schematic diagram of radioimmunotherapy. $^{177}$Lu is transported to a cancer cell by the antibody, which binds to an antigen that is specifically expressed on the cancer cell. By this therapy, if the purity of $^{177}$Lu for the whole Lu isotope is low, the amount of $^{177}$Lu transported to the cancer cell is reduced. Consequently, the therapeutic effect of $^{177}$Lu upon the cancer cell is reduced. Two methods have been proposed to produce high purity $^{177}$Lu. One is the direct method via the $^{176}$Lu (n, γ) $^{177}$Lu reaction. In this method, stable lutetium ($^{176}$Lu) is irradiated at reactors in Europe and America with large amounts of neutron-generation over a limited area. The other is the indirect method via the $^{176}$Yb (n, γ) $^{177}$Yb (half-life: 1.91 h) → $^{177}$Lu reaction. In this method, stable ytterbium ($^{176}$Yb) is irradiated at reactors throughout the world with a low quantity of neutrons, and $^{177}$Lu is separated from Yb. Therefore, to produce high-purity $^{177}$Lu with the indirect method, various separation methods of $^{177}$Lu from Yb have been investigated in many countries.

We have developed a method for completely separating $^{177}$Lu from Yb using a reversed-phase silica gel column (Fig.5-30(a)) and have synthesized $^{177}$Lu-labeled antibodies using the $^{177}$Lu produced by our separation method. However, the labeling yield was < 5%. From the results of elemental analysis, it was found that calcium (Ca), iron (Fe), and zinc (Zn) were included in the final $^{177}$Lu product, and that these metallic elements competitively inhibited the complexation between $^{177}$Lu and 1,4,7,10-tetraazacyclododecane-1,4,7,10 -tetraacetic acid. Consequently, the labeling yield of $^{177}$Lu-labeled antibody decreased. It was also found that these metallic elements were included as impurities in the regents of both 2-hydroxyisobutyric acid (2-HIBA) and 1-octanesulfonic-acid sodium salt (1-OS), eluents of the reversed-phase silica-gel column. Therefore, the eluents of 2-HIBA and 1-OS were purified by cation-exchange and chelating-ion-exchange columns in advance, respectively. Furthermore, an anion exchange was added as a final purification step (Fig.5-30(b)). The concentrations of Ca, Fe, and Zn in the final $^{177}$Lu product were reduced from 87, 340, and 77 ppb to 13, 18, and 9 ppb, respectively, and the labeling yield of the $^{177}$Lu-labeled antibody increased up to 88%. Consequently, we successfully produced highly purified $^{177}$Lu capable of being applied to radioimmunotherapy.

If the highly purified $^{177}$Lu can be produced using our method all over the world, radioimmunotherapy with $^{177}$Lu will spread widely.

**Reference**
Watanabe, S. et al., Production of Highly Purified No-Carrier-Added $^{177}$Lu for Radioimmunotherapy, Journal of Radioanalytical and Nuclear Chemistry, vol.303, issue 1, 2015, p.935-940.

# 5–12 Elucidation of the Reaction Mechanism of an Anti-Cancer Drug at the Atomic Level

## — Precise Structural Analysis of a Drug's Target Protein using Synchrotron X-ray Radiation —

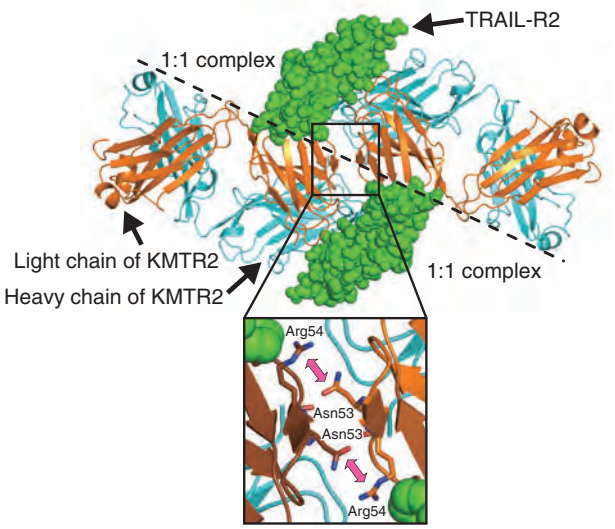


**Fig.5-31 Functional unit for the reaction mechanism of KMTR2**
The dimeric structure of a 1:1 KMTR2-Fab/ecTRAIL-R2 complex is rendered by two-fold crystallographic symmetry (dash line). A close-up view of the interface between two KMTR2-Fab molecules (rounded square) shows that Asn53 and Arg54 in the light chain of KMTR2 recognize each other at the interface.

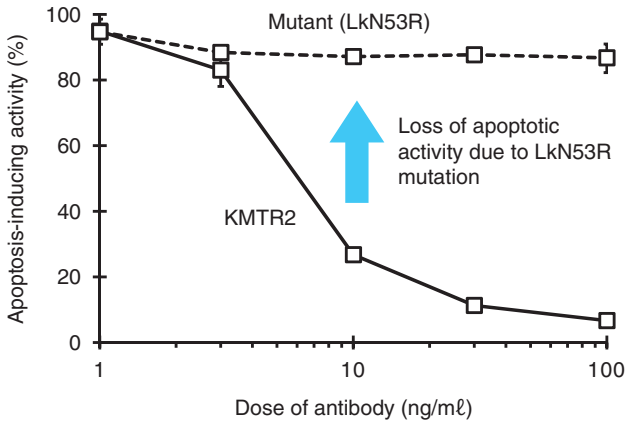


**Fig.5-32 Apoptosis-inducing activity of KMTR2 and its mutant form**
Dose-dependent responses of apoptosis-inducing activity by KMTR2 (solid line) and the LkN53R mutant (dashed line). These results clearly indicate that the mutation of Asn53 to Arg at the two-fold interface in the KMTR2 resulted in a loss of its apoptotic activity.

Tumor-necrosis-factor-related apoptosis-inducing ligand (TRAIL) induces apoptosis in various human cancer-cell lines but not in most normal human cells. TRAIL activates two distinct receptors, TRAIL-R1 and TRAIL-R2, both of which possess a death domain (DD) in their cytoplasmic tail that can interact with the apoptotic machinery. The fully human monoclonal antibody KMTR2, clusters TRAIL-R2 on tumor-cell surfaces and acts as a strong direct agonist for TRAIL-R2. Therefore, specifically targeting the apoptotic pathway with TRAIL-R2 using direct agonistic antibodies including KMTR2 may offer a novel therapeutic strategy for malignant tumors.

To investigate the mechanism of direct agonistic activity induced by KMTR2, the 1:1 complex structure of the extracellular region of TRAIL-R2 (ecTRAIL-R2) and a Fab fragment derived from KMTR2 (KMTR2-Fab) was determined to a 2.1-Å resolution by X-ray crystallography. The dimeric structure of two 1:1 KMTR2-Fab/ecTRAIL-R2 complexes rendered by crystallographic symmetry is shown in Fig.5-31. Two KMTR2-Fab molecules interacted with the second complementarity-determining region (CDR2) of the light chain via two-fold crystallographic symmetry, and consequently, two ecTRAIL-R2 molecules were situated in parallel within a C-terminal distance of 20 Å. It is believed that this adjacent configuration of the extracellular region resulted in access to each DD in the intracellular regions of the TRAIL-R2 molecules, leading to activation of a caspase-dependent apoptotic pathway. We assumed that Fab dimerization based on this two-fold symmetry was essential for the direct agonistic activity of KMTR2.

To confirm this assumption, we designed a mutant, replacing Asn53 with Arg in the light kappa chain of KMTR2 (LkN53R) to prevent dimerization at this site (close-up view in Fig.5-31). Because Asn53 in the CDR2 of the light chain was located near the two-fold axis between the two KMTR2-Fab fragments, the Asn53-to-Arg mutation should have introduced both steric hindrance and charge repulsion from the associations of four positive charges, two from Arg53 after mutation and two from Arg54.

Several biochemical experiments using KMTR2 and its mutant LkN53R were performed to confirm this assumption. Both flow cytometry and ELISA analyses clearly indicated that the Asn53-to-Arg mutation had little effect upon the binding activity of TRAIL-R2. In addition, both size-exclusion chromatography and confocal-microscopy techniques showed that the LkN53R mutation abolished the higher oligomerization. Furthermore, the LkN53R mutation resulted in a loss of its apoptotic activity (Fig.5-32) in conjunction with its caspase activation. These results indicate that strong agonistic activity induced by KMTR2, such as apoptotic signaling and tumor regression, can be attributed to TRAIL-R2 superoligomerization induced by the interdimerization of KMTR2, shown in Fig.5-31 as an essential functional unit.

The present study was accomplished in collaboration with the JAEA and the Kyowa Hakko Kirin Co., Ltd.

**Reference**

Tamada, T. et al., TRAIL-R2 Superoligomerization Induced by Human Monoclonal Agonistic Antibody KMTR2, Scientific Reports, vol.5, 2015, p.17936-1-17936-12.

# 5–13 Toward Advancement of Heavy-Particle Cancer Therapy

## — Successful Development a New Radial Dose-Simulation Model —

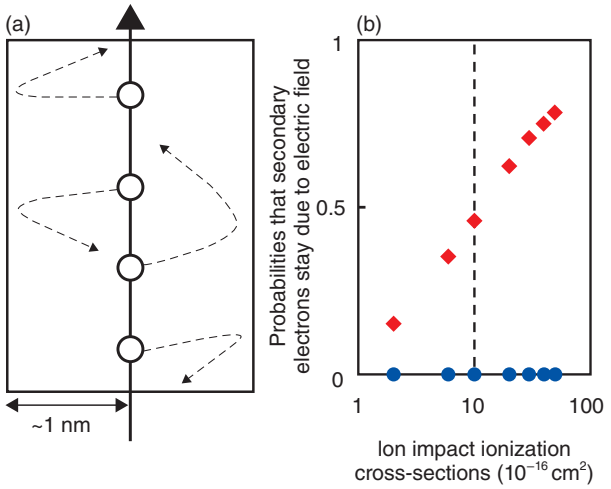


**Fig.5-33 (a)Images of the movement of secondary electrons and (b) probabilities that secondary electrons stay near the heavy-ion path for various impact-ionization cross-sections**
(a) Solid and dashed arrows express the movement of an incident ion and secondary electrons, respectively, and white open circles express the ions produced from heavy-ion-impact ionization. (b) Red rhombi and blue circles express the probabilities obtained from our proposed and the conventional models, respectively. The broken line expresses the cross-section of a carbon-ion-impact ionization at 36 MeV.

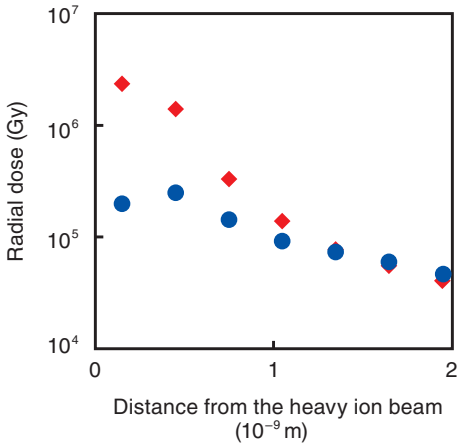


**Fig.5-34 Radial dose vs. distance from the incident-ion path for the irradiation of 36-MeV carbon-ion beams into water**
Red rhombi and blue circles express the radial dose obtained from our model and the conventional model, respectively.

Heavy-particle cancer therapy is one of the most important techniques for realizing a healthy and long-living society because it offers a smaller exposure to normal tissues than do other forms of radiation therapy such as that using X-rays. This is because heavy ions can be directed only toward cancer cells. Secondary electrons, which are produced from the heavy-particle-impact ionization in the tissue (of which the main component is water), as well as the heavy particles (ions) themselves, significantly contribute to the dose. Therefore, it is important to estimate the radial dose (which is the dose as a function of distance from the heavy-ion path) produced by secondary electrons in planning heavy-particle cancer-therapy systems.

In order to simulate radial dose, firstly, we construct a model. Then, we make a simulation code using this model. Finally, we operate this code on the super-computers. Conventional models suffer from the weakness that electric fields formed from positive molecular ions are ignored because the continuum is treated as a target. To overcome this weakness, we treat individual molecules in the target and the Coulomb interaction between each individual molecular ion and each individual secondary electron. This allows our model to become closer to reality than conventional ones. We find that all secondary electrons move away from the heavy-ion path in the conventional model. However, numerous secondary electrons are trapped near this path (Fig.5-33(a)). We also find the probability of secondary electrons being trapped near this path increases with increasing ion-impact-ionization cross-sections (Fig.5-33(b)).

Fig.5-34 shows radial-dose distributions obtained from our proposed and the conventional models. In our simulations, the radial dose obtained from our model is approximately 10 times as large as that from the conventional model on the heavy-ion path. This may be owing to the secondary electrons trapped near the heavy-ion path interacting multiple times with the target molecules.

The present planning systems for heavy-particle cancer therapy employ a radial dose-distribution estimated in the μm-order region according to the sizes of the chromosomes. However, our simulation results indicate that it is important to estimate the radial dose distribution in the nm-order region, which corresponds to the size of the DNA. We will study the effect of DNA in the nm-sized region in more detail to advance this therapy.

This study was partly supported by the Japan Society for the Promotion of Science (JSPS) KAKENHI Grant-in-Aid for Scientific Research (C) (No.25390131).

**Reference**

Moribayashi, K., Simulation Study of Radial Dose due to the Irradiation of a Swift Heavy Ion Aiming to Advance the Treatment Planning System for Heavy Particle Cancer Therapy: The Effect of Emission Angles of Secondary Electrons, Nuclear Instruments and Methods in Physics Research B, vol.365, part B, 2015, p.592-595.

# 5–14 Which Liver-Sashimi was Treated by Radiation?

## — Development of a Method to Distinguish Disinfected Liver —

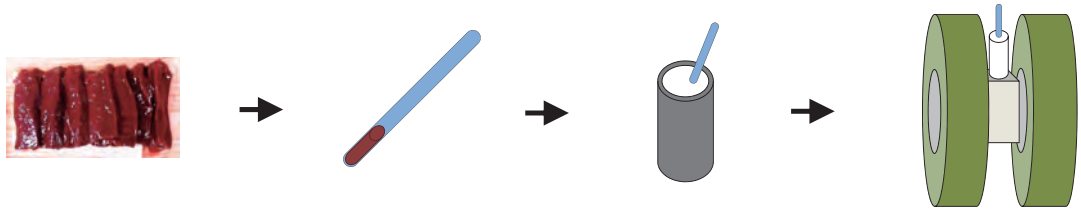


**Fig.5-35 Schematic of electron spin resonance (ESR) measurements**
Raw bovine livers were irradiated with 1.0, 2.6, 5.2, and 7.8 kGy γ-rays at 0 °C. The irradiated samples were inserted into ESR tubes, frozen at –196 °C with liquid nitrogen, and measured on an ESR at their frozen temperature.

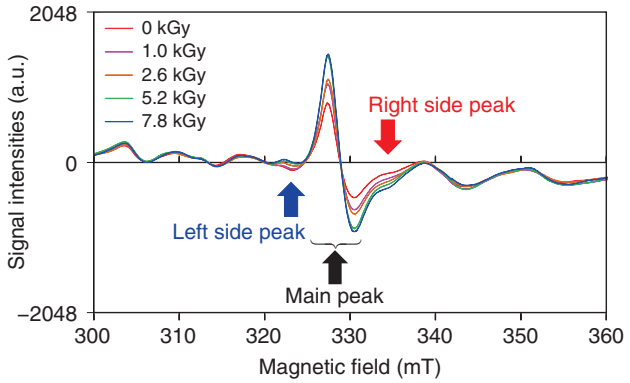


**Fig.5-36 Changes of ESR spectra of irradiated raw bovine livers**
ESR spectra of raw bovine livers irradiated with different doses are depicted on this plot. Arrows indicate the dose-responsible peaks after irradiation. A large peak in the center is called the main peak, and the two small peaks to the left and right of the main peak are called side peaks.

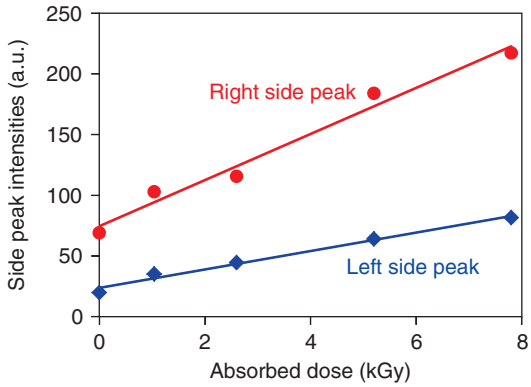


**Fig.5-37 Dose responses of side peaks on bovine livers**
The intensities of the right and left side peaks were plotted against absorbed doses. The peak intensities on the plot increased linearly according to increasing dose at each different slope.

To prevent foodborne illness in Japan, after the outside of raw meat had been roasted and then the cooked parts were trimmed off, the steak tartare must be prepared from only the inside meat in restaurants. However, since pathogenic bacteria such as some *E. coli* were found inside raw bovine livers where no disinfection method is effective, the sale of any raw bovine liver to eat as "liver-sashimi" has been prohibited since July 1, 2012. Providing for the radiation exposure that is used to sterilize bacteria out of a sealed food package without heating, detection methods have been developed to distinguish raw livers that have been disinfected by radiation.

At first, the irradiated raw bovine livers were subjected to the ELISA method, which was developed as for irradiated ground meats. The ELISA method could distinguish irradiated livers when such irradiation was done in the chilled condition (0 °C), but not at all could be detected when irradiation was done in the frozen condition (–80 °C).

The ELISA method can detect an oxidative lesion in DNA that reacts with active species (radicals) caused by ionizing radiation. Therefore, the radical migration to DNA might be inhibited in the frozen condition. Next, we tried to detect the radical itself. Basically, unpaired electrons of radicals can be measured using electron spin resonance (ESR) spectroscopy. This apparatus utilizes an electromagnetic wave similar to a microwave oven. Therefore, the method has a weak point in that the electron cannot resonate when the water within the samples absorbs the microwave. However, we have demonstrated that ESR can measure radicals in the flesh of fresh fruits irradiated as a disinfestation treatment for the plant quarantine. Thus, we thought that it might be possible to measure radicals in livers using ESR.

After raw bovine livers were irradiated in the chilled condition, they were measured at liquid-nitrogen temperature to suppress microwave absorption by stopping the motion of the water molecules during ESR measurement (Fig.5-35). According to the results, we found a main peak and two side peaks in the livers (Fig.5-36), and the side-peak intensities increased according to the increasing doses (Fig.5-37). Since the measuring errors were involved in experimental values, we assumed that the side-peak intensities of the raw bovine livers irradiated at approximately 3 kGy could be clearly distinguished from those that were not irradiated. Therefore, it is suggested that raw bovine liver treated by irradiation beyond 3 kGy can be distinguished using the ESR method.

Since the ESR method can be used to investigate the raw bovine livers being irradiated for disinfection, we believe that this technique can help consumers to choose reliable liver-sashimi.

**Reference**

Kikuchi, M. et al., ESR Signal Changes Recorded in γ-Irradiated Bovine Livers, Shokuhin Shosha (Food Irradiation, Japan), vol.50, no.1, 2015, p.9-12 (in Japanese).

# 5–15 A Polymer-Electrolyte-Membrane Fuel Cell with the World's Highest Power Density

## — Preparation of Polymer-Electrolyte Membranes by Radiation-Induced Graft Polymerization —

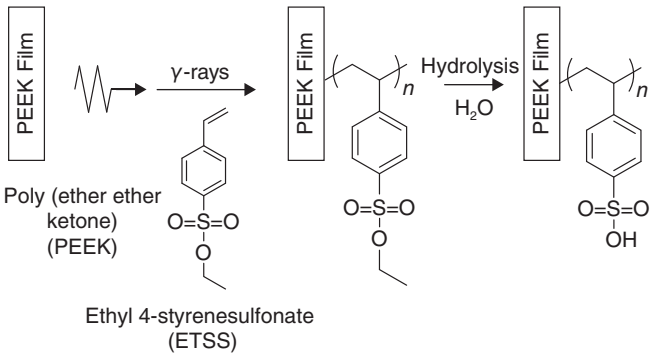


**Fig.5-38 Synthetic scheme of an aromatic hydrocarbon-type PEM**
Radiation induced-graft polymerization of ETSS onto radiation-resistant PEEK substrates and subsequent hydrolysis of ethyl ester groups.

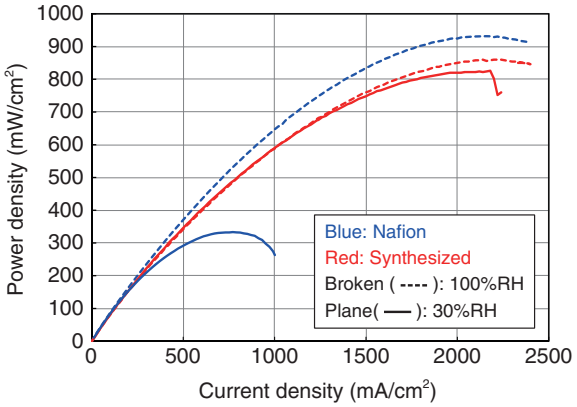


**Fig.5-39 Comparison of fuel cell tests at 80 °C under different relative humidity conditions**
The $E_{max}$ of the PEEK-PEM-based MEA was 2.5 times higher than that of the Nafion-based MEA at 80 °C under a lower-RH condition.

Polymer-electrolyte-membrane (PEM) fuel cells have received attention as energy sources for next-generation applications such as fuel-cell vehicles and stationary-cogeneration systems. PEMs, which are used as the separator between the cathode and the anode, are key components because their ionic resistance directly determines the power-generation efficiency. PEMs that afford high power density are desirable for the extraction of large amounts of electric power per unit area. Thus far, sulfonated perfluoropolymers such as Nafion have been predominantly used as PEMs. However, these materials cause several critical problems, including high fuel crossover and power-density decreases under low relative humidity (RH) at 80 °C.

To solve these issues, graft-type PEMs based on poly (ether ether ketone) (PEEK) with high gas-barrier properties (PEEK-PEM) were prepared by radiation-induced graft polymerization. Ethyl 4-styrenesulfonate (ETSS) was selected as a grafting monomer to prevent damage to the PEEK substrate during the sulfonation process. After graft polymerization, the sulfonate of the ETSS-grafted PEEK films could be converted to the sulfonic-acid group by hydrolysis (Fig.5-38). Radiation-induced graft polymerization of the ETSS monomer was attempted under numerous reaction conditions since there have been few reports of grafting based on PEEK film. Consequently, we found that the graft reaction of ETSS with PEEK films irradiated with $\gamma$-rays occurred efficiently in ETSS/dioxane mixtures, enabling a PEEK-PEM with high ion conductivity to be obtained.

Fuel-cell tests of the membrane-electrode assemblies (MEAs) fabricated with PEEK-PEM and Nafion were performed under 100%RH and 30%RH at 80 °C, respectively; the current-density (I-W) polarization curves of the fuel cells are plotted in Fig.5-39. Nafion-based MEA under the low-humidity condition (30%RH) showed a maximum power density ($E_{max}$) of 333 mW/cm$^2$, which was 1/3 times lower than that of Nafion-based MEA under 100%RH at 80 °C. In contrast, PEEK-PEM-based MEA under 30%RH at 80 °C maintained an $E_{max}$ level of 96% of that at 100%RH, where it exhibited the world's highest power density of 826 mW/cm$^2$.

Practical application of the developed PEEK-PEM is expected. PEEK-PEM fuel cells would be useful as energy sources for fuel-cell vehicles.

**Reference**

Hamada, T., Hasegawa, S. et al., Poly(Ether Ether Ketone) (PEEK)-Based Graft-Type Polymer Electrolyte Membranes Having High Crystallinity for High Conducting and Mechanical Properties under Various Humidified Conditions, Journal of Materials Chemistry A, vol.3, issue 42, 2015, p.20983-20991.

# 5–16 Toward the Realization of Quantum-Information Communication and Quantum Computing — Exploring Single-Photon Sources in Silicon Carbide —

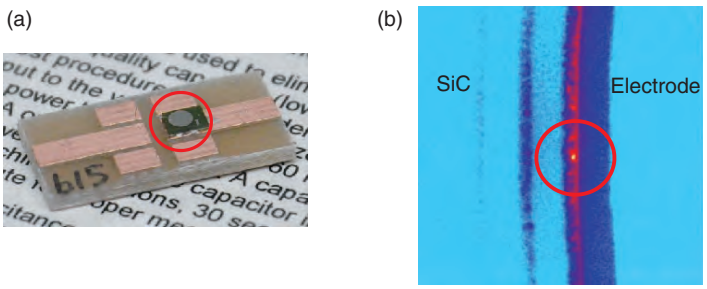


**Fig.5-40 (a) Photo of a diode (b) Confocal-laser-scanning-fluorescence-microscope-observation image of the diode**
(a) Within the red circle is the diode. This diode is fixed on a chip carrier for electrical-characteristic measurements. (b) An area just outside of the electrode for the diode. Yellow-colored spots inside of the red circles indicate the luminescence from an SPS.

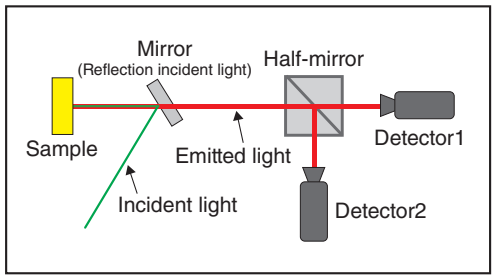


**Fig.5-41 Schematic of photocount-time-correlation-function measurement**
Light from the sample (red) excited by an incident laser (green) either goes straight or turns at 90° at the half-silvered mirror and then reaches one of two detectors.

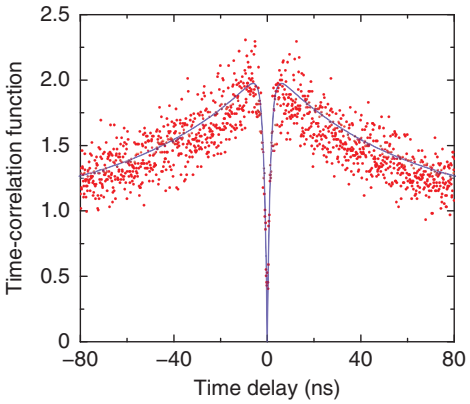


**Fig.5-42 Result of photocount-time-correlation-function measurement for the luminescent spot**
Red and blue lines indicate measurements and fitting results, respectively.

Quantum computing with extremely high capability compared with conventional computers and perfectly secure quantum-cryptographic communication have attracted attention as next-generation technologies. For such quantum technologies, the realization of a "quantum bit," which has an intermediate state between 0 and 1 in addition to the binary values, is a key issue. Some crystal defects in semiconductor materials act as single-photon sources (SPSs), emitting one photon under the absorption of one photon. Efforts have been made to apply SPSs to quantum bits.

We focus on silicon carbide (SiC) and explore SPSs, which can be operated at room temperature in SiC. SiC is a wide-bandgap semiconductor, and the luminescence from SPSs is not disturbed by the characteristics of SiC. In addition, since SiC has been well developed for use in power electronics, large wafers with high quality are available and the development of the device-fabrication process is progressing. Therefore, SiC also has advantages from the viewpoint of the development of quantum computers and devices for quantum communication/information. We have to discover SPSs with excellent features such as high thermal stability even after a high-temperature annealing process and high brightness at room temperature. Pn diodes were fabricated on high-quality SiC epitaxial substrates using aluminum (Al)-ion implantation at 800 °C and annealing at 1800 °C (Fig.5-40(a)). A very bright luminescent spot with 300 thousand photons per second was found near the edge of electrode for the pn diode by a confocal laser-scanning fluorescence microscope (Fig.5-40(b)). To confirm whether it was an SPS, we measured its photocount-time correlation function. Two detectors are set with a half-silvered mirror (Fig.5-41). Since an SPS emits one photon under the incidence of one photon, the two detectors never collect photons simultaneously. Thus, if the two detectors do not collect photons from a luminescent spot at the same time, the spot is confirmed to be an SPS. For the spot shown in Fig.5-40(b), the value of the time-correlation function was zero at zero seconds. Thus, two photons were not detected simultaneously (Fig.5-42). Therefore, we can conclude that the luminescent spot found in this study is an SPS that cannot be annihilated even by annealing at 1800 °C.

We must determine the spin properties of the SPS in order to consider the possibility of its use as a quantum bit.

This study was partly supported by the Japan Society for the Promotion of Science (JSPS) KAKENHI Grant-in-Aid for Scientific Research (B) (No.26286047).

**Reference**

Lohrmann, A., Ohshima, T. et al., Single-Photon Emitting Diode in Silicon Carbide, Nature Communications, vol.6, 2015, p.7783-1-7783-7.

# 5–17 Isotope Separation Utilizing Control of Molecular Rotation

## — An Isotope-Separation Method Effective for Heavy Isotopes —

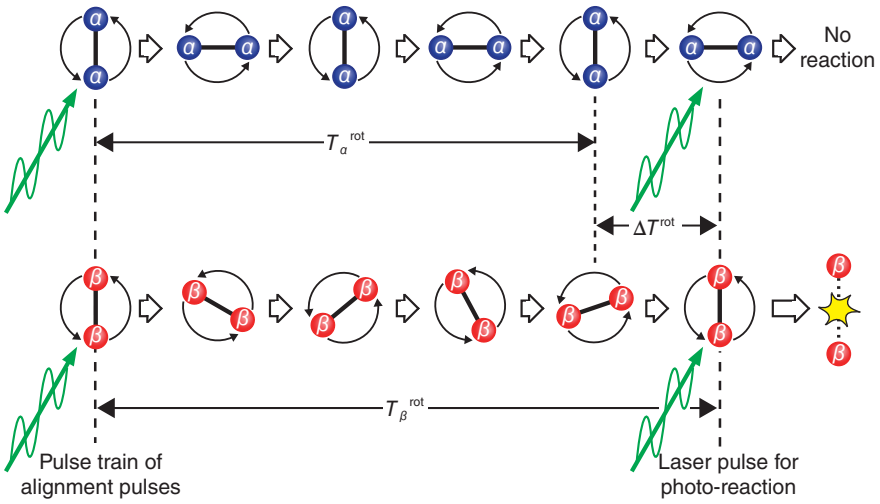


**Fig.5-43 Diagram of laser-isotope separation utilizing control of molecular rotation**
After the irradiation of a laser-pulse train (left side), the isotopologues show a periodic alignment condition with a rotational period of $T_i^{rot}$ (i = $\alpha$ or $\beta$). Isotope-selective photoreaction can be induced by additional laser-pulse irradiation when one of the isotopologues is aligned.

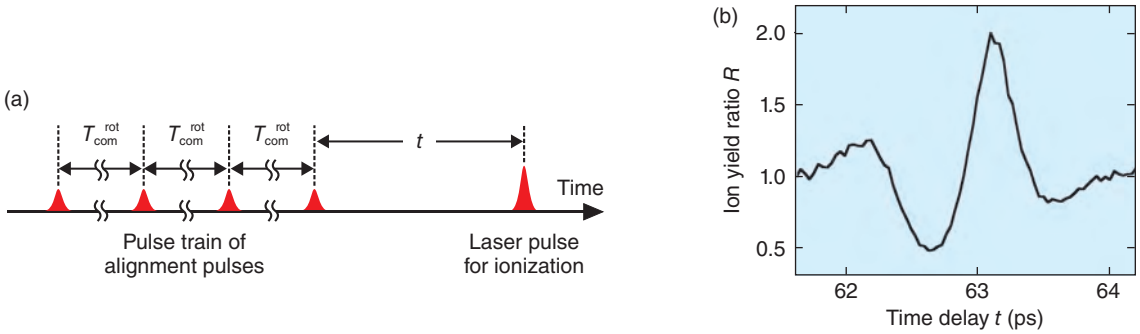


**Fig.5-44 Experimental result of $N_2$-isotope-selective ionization with a femtosecond-laser-pulse train**
(a) Schematic of the laser-pulse sequence and (b) time-delay ($t$) dependence of the ion-yield ratio, $R$.

A conventional molecular-laser isotope-separation (MLIS) method uses isotope-selective vibrational excitation of isotopologues. The isotope selectivity originates from differences in the vibrational frequencies of the isotopologues. Because the frequency difference decreases as isotope mass increases, the isotope selectivity is significantly lowered when we apply this method to heavy isotopes.

We have proposed a new MLIS utilizing control of molecular rotation. According to this method, isotopologues are selected depending on their rotational periods (Fig.5-43). Femtosecond (fs) laser pulses with linear polarization (alignment pulses) create rotational wave packets in the isotopologues, which show an alignment condition just after the fs-pulse irradiation (the left side of Fig.5-43). The alignment condition disappears under time evolution of the wave packets and revives periodically with a rotational period of $T^{rot}$. $T^{rot}$ of one isotopologue is different from that of the other. Additional fs-laser-pulse irradiation when one of the isotopologues aligns can induce isotope-selective photoreaction. Because the difference of $T^{rot}$ ($\Delta T^{rot}$) does not depend significantly upon the isotope mass, the isotopic selectivity of the new method is not significantly lowered for heavy isotopes.

To demonstrate the new method, a gas mixture of $N_2$ isotopologues ($^{14}N_2$ and $^{15}N_2$) was used. After a time delay $t$ following pulse-train irradiation of four alignment pulses with the pulse interval being equal to the common rotational period of the isotopologues ($T_{com}^{rot} = 15T_{14}^{rot} = 14T_{15}^{rot}$), an additional laser pulse ionized the $N_2$ isotopologues (Fig.5-44(a)). As shown in Fig.5-44(b), the ion-yield ratio $R$ [$= I(^{15}N_2)/I(^{14}N_2)$] varies in the range of 0.49–2.00, depending on the time delay $t$. This result indicates that isotope-selective ionization can be realized by simply tuning $t$.

We expect that the new method will be applicable for separation of heavy isotopes, leading to advances in radioactive-waste management.

This research was partly supported by the Japan Society for the Promotion of Science (JSPS) KAKENHI Grant-in-Aid for Challenging Exploratory Research (No.23656594), and by the Consortium for Photon Science and Technology.

**Reference**

Akagi, H. et al., Isotope-Selective Ionization Utilizing Field-Free Alignment of Isotopologues with a Train of Femtosecond Laser Pulses, Physical Review A, vol.91, issue 6, 2015, p.063416-1-063416-7.

# 5–18 A Quantitative Liquid-Analysis Method using Laser-Induced Plasma-Emission Light

## — A Highly Sensitive In situ Liquid-Analysis Technique under Severe Environments —

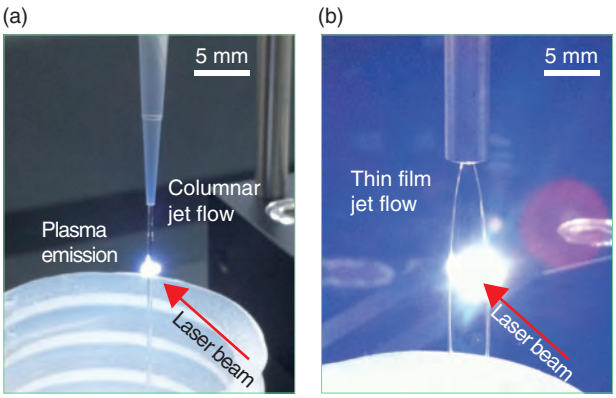


**Fig.5-45 Plasma-emission light at the liquid surface produced by laser-induced breakdown**
When a pulsed laser beam is irradiated upon the liquid surfaces of a thin-film jet flow and a columnar jet flow under the same condition, the thin-film jet flow (b) causes stronger plasma-emission light than the columnar jet flow (a). Also, the thin-film jet flow enables us to reduce the risk of contamination propagation and to avoid contamination of optical components.

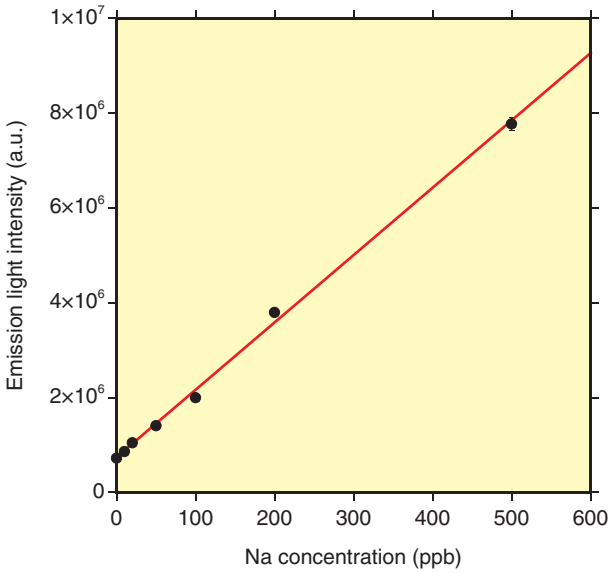


**Fig.5-46 Relationship between emission-light intensity and the concentration of Na atoms in aqueous NaCl solution (Calibration curve)**
This figure shows good correlation between the emission-light intensity and the concentration of Na atoms. The large slope of the line denotes high sensitivity.

Recent years have seen remarkable development and spread of atomic-spectrum-analysis devices. As for spectroscopic analysis, devices based on inductively-coupled-plasma (ICP) optical-emission-spectroscopy (OES) methods that offer immediate or instantaneous quantitative analysis are possible for various elements. However, the ICP-OES apparatus requires the sample to be pretreated before the analysis and is operated at an off-site area. Furthermore, at the site, an analysis operator separately collects liquid samples under severe environments.

In contrast, the laser-induced breakdown-spectroscopy (LIBS) analysis method does not require sample preparation because this method directly irradiates the sample being measured. This method can also perform remote, online, *in situ,* and real-time quantitative analysis of multiple elements. Despite the wide application of LIBS to elemental analysis of solid samples, it is difficult to use this method with liquid samples because splashes and ripples that form on the liquid prevent efficient detection of plasma emission in the ablation. Moreover, laser optics contaminated by splashes compromise the reliability of LIBS.

To overcome these difficulties, we performed feasibility studies on liquid LIBS using the free jet. A laminar columnar jet flow of water (Fig.5-45(a): water flow from the tap at low speed) or a jet flow of a film with 10 μm thickness (Fig.5-45(b): effusion of pressurized and flattened water at high speed). When we irradiated a pulsed laser beam on the free surface of a liquid, plasma emission occurred effectively with the thin-film jet flow, as shown in Fig.5-45(b), and we found that emission-light intensity improved significantly. The calibration curve for Na showed good linearity when this method was applied to the NaCl aqueous solution (Fig.5-46). The limit of detection estimated from the slope of the calibration curve and the relative standard deviation of background signal was 0.1 ppb. The value exceeded 0.5 ppb (i.e., the general-detection limit of the commercial ICP-OES device).

This method is applicable to alkali metal elements such as Rb and Cs, which are difficult to measure with an ICP-OES device. In the future, it is expected that this method may be useful for mass-transfer monitoring of the radioactive solution in nuclear reprocessing, and for monitoring of contaminated water during the decommissioning of the TEPCO's Fukushima Daiichi NPS, as it operates under severe environments at high radiation doses.

The present study includes the result of the Development of laser remote analysis for next generation nuclear fuel and applied study by MOX sample project entrusted to the JAEA by the Ministry of Education, Culture, Sports, Science and Technology of Japan (MEXT). This work was partly supported by the Japan Society for the Promotion of Science (JSPS) KAKENHI Grant-in-Aid for Scientific Research (C) (No.24560068).

**Reference**

Ohba, H. et al., Effect of Liquid-Sheet Thickness on Detection Sensitivity for Laser-Induced Breakdown Spectroscopy of Aqueous Solution, Optics Express, vol.22, issue 20, 2014, p.24478-24490.

# 5–19 Real-Time Observation of Lattice Deformation in Nitride Semiconductors

## — Proposal for a New Lattice-Deformation Model that Defies Conventional Theory —

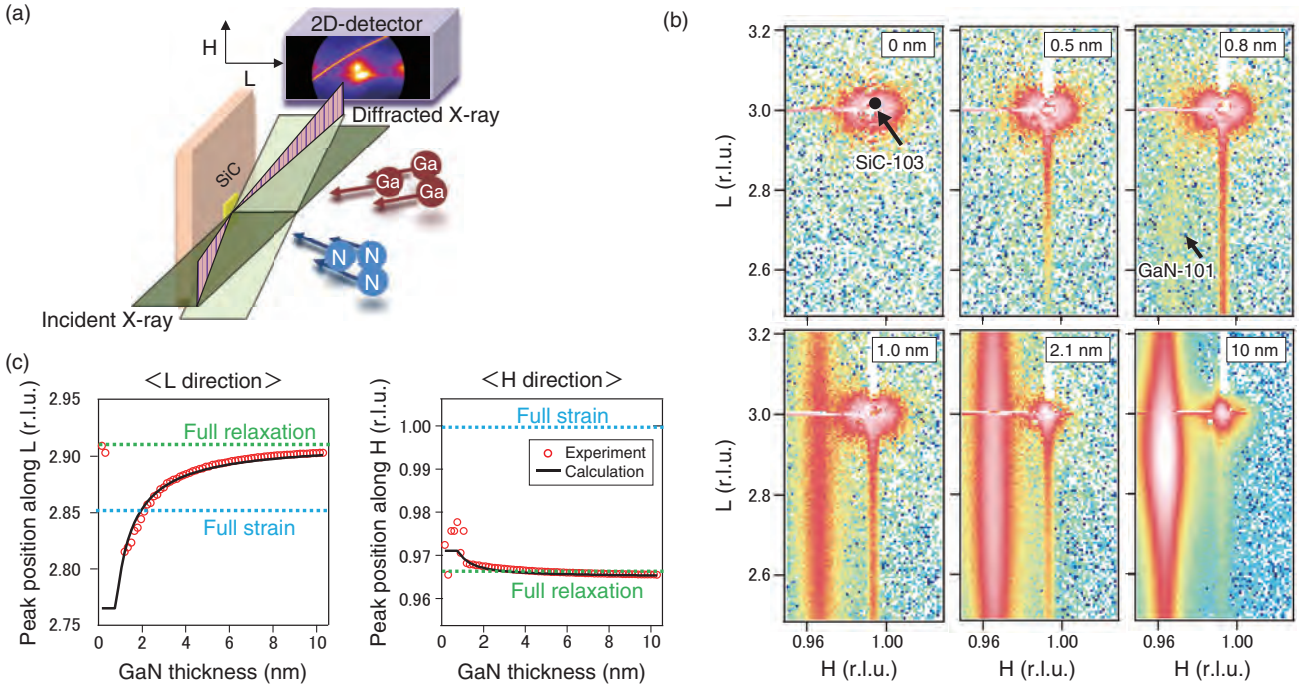


**Fig.5-47 *In-situ* synchrotron X-ray diffraction during the growth of gallium nitride (GaN) films**
We measured the synchrotron X-ray diffraction during the growth of GaN films on silicon carbide (SiC) substrates (a). With increasing GaN-film thickness, the diffraction peak of GaN becomes larger and its peak position is gradually shifted as indicated in (b). The film-thickness dependence of the peak position is shown in (c). It is clear that a lattice spacing along the L-direction shifted more drastically than that along the H-direction, indicating a difference from conventional elastic theory. "r.l.u." indicates reciprocal lattice unit and the large (small) value corresponds to the small (large) lattice spacing of GaN.

Gallium nitride (GaN) is widely used for LEDs and high-frequency power devices and has the potential to drastically reduce power consumption beyond what has been achieved by conventional materials such as silicon (Si) or gallium arsenide (GaAs). Thus, a further spread of GaN-based devices is expected to help realize a future low-energy society. Despite these technological advances, many challenges affecting the crystal growth of GaN still remain. For example, surface structures, lattice deformation, and detailed defect structures in GaN films have not been fully clarified. Understanding such fundamental knowledge in terms of crystal growth is imperative for dramatically improving device performance. In this study, the lattice deformation of the GaN film is observed in real-time and a new deformation model that defies conventional theory is proposed.

Experiments were performed at the SPring-8 synchrotron-radiation facility (Beamline 11XU) using a plasma-assisted molecular-beam-epitaxy system that is directly coupled to the X-ray diffractometer (XRD). As shown in Fig.5-47(a), *in situ* X-ray diffraction was measured while a GaN film was grown on a silicon carbide (SiC) substrate. Fig.5-47(b) shows typical obtained experimental data. The diffraction peak of GaN was confirmed to emerge as the thickness of the GaN film reached 0.8 nm, corresponding to approximately two atomic layers. This means that our real-time measurement is quite effective at evaluating lattice deformation quantitatively at the atomic-layer scale. Fig.5-47(c) shows film-thickness dependences of the diffraction-peak positions along the out-of-plane (L) and in-plane (H) directions. These positions are related to the reciprocal of the lattice spacing of GaN in each direction. In the conventional strain relaxation of crystals, the lattice spacing of the L-direction is varied in conjunction with that of the H-direction. That is, when a film with a larger lattice constant than the substrate is relaxed, the decrement in the lattice spacing along the L-direction is almost identical to the increment of that along H-direction; this is known as conventional elastic theory. However, Fig.5-47(c) shows that the variation in the H-direction is small compared with that in the L-direction. In order to understand this anomalous phenomenon, a new lattice-deformation model reflecting lattice expansion due to the incorporation of point defects (Ga anti-site defects) was considered and a good fitting result for experimental data was obtained, as shown by the calculation result of Fig.5-47(c). This suggests that depending on the growth condition, many more point defects than are expected in the general sense can be incorporated into the GaN film.

We have proposed a new lattice-deformation model of the GaN film based upon the results of real-time observation. Since this model is important for controlling the point-defect density in GaN, it is expected to optimize the growth condition for GaN films with high quality and low defect density in the future.

**Reference**

Sasaki, T. et al., Anomalous Lattice Deformation in GaN/SiC(0001) Measured by High-Speed *in situ* Synchrotron X-Ray Diffraction, Applied Physics Letters, vol.108, issue 1, 2016, p.012102-1-012102-5.

# Research and Development of HTGR, Hydrogen Production, and Heat Application Technologies

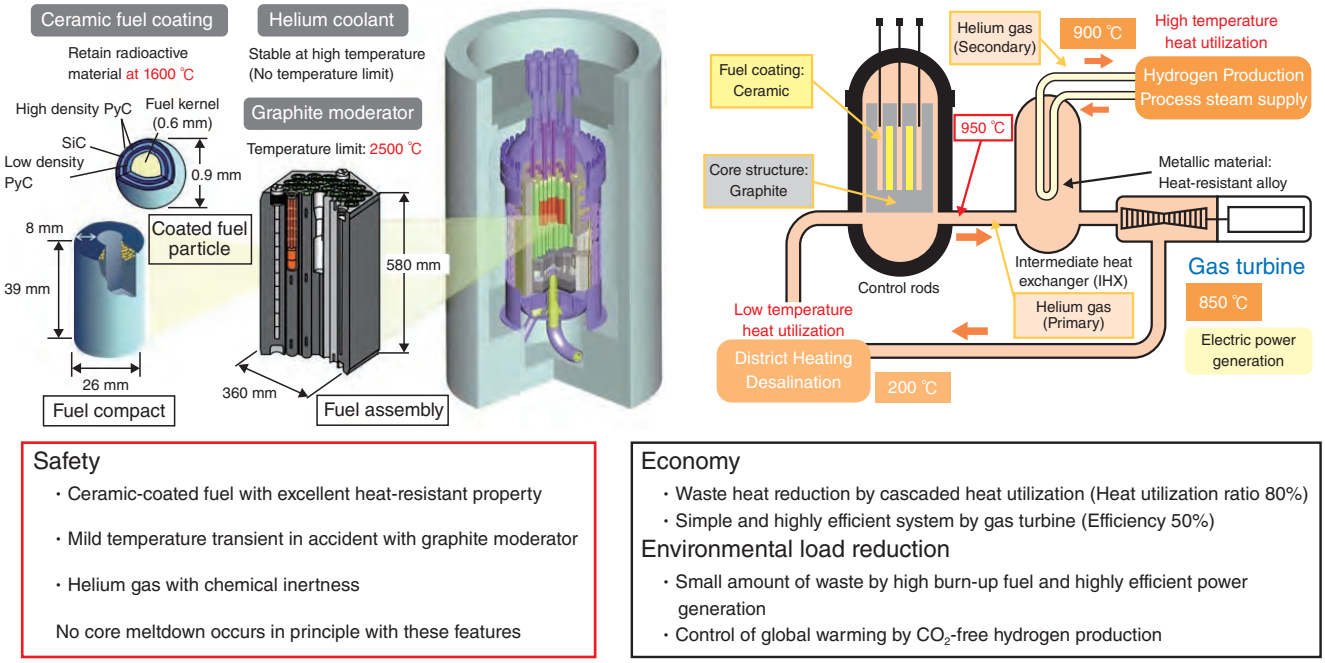


**Fig.6-1 Features of HTGR**
HTGR is a He gas-cooled and graphite-moderated thermal-neutron reactor that has excellent inherent safety features and can meet various heat application requirements such as hydrogen production and power generation. Its features are strongly expected to regain the public's trust in nuclear power.

To remedy the fragility of our country's energy supply-demand structure arising from excessive dependence on fossil fuel resources from abroad while simultaneously reducing greenhouse gas emissions in response to global warming, the basic philosophy of Japan is to advance nuclear-energy utilization on the premise of ensuring safety. We expect to use nuclear energy not only for power generation but also for various heat applications. The Strategic Energy Plan and the Japan Revitalization Strategy 2016, decided by the cabinet, list the promotion of research and development of a high-temperature gas-cooled reactor (HTGR) as a national policy because such reactors have excellent inherent safety and meet the energy demand for various industries. Reflecting on this social situation, the HTGR forum has been developing a strategy to commercialize HTGRs.

An HTGR can supply heat at a temperature of 950 °C using fuel particles coated with ceramics, graphite core material and inert helium, and can be designed as a meltdown-proof reactor in the case of any severe accident. The high-temperature engineering test reactor (HTTR) was constructed using the most advanced HTGR technologies developed in Japan such as coated-fuel-particle fabrication technology with excellent fission-product retaining performance and large-scale graphite-fabrication technology with high strength and irradiation resistance; it generated a temperature of 950 °C in 2004 for the first time in the world and demonstrated a stable supply of heat over a 50-day operation at 950 °C in 2010. We have demonstrated that even if the reactor cooling system shuts down and reactor scram fails, the reactor is naturally shutdown and kept in a stable condition.

HTGR has excellent safety features that allow it to respond to various industries, such as highly efficient power generation with a helium-gas turbine system, hydrogen production for fuel-cell vehicles and direct-reduction steel making, and seawater desalination using waste heat from a gas-turbine system (Fig.6-1).

We have promoted the establishment of safety standards for commercial HTGRs under international collaboration, taking advantage of the safety and economy features of HTGRs (Topic 6-1). We have also researched a fundamental advanced fuel technology to completely burn the Pu stored in Japan by HTGR (Topic 6-2) and developed oxidation-resistant graphite material to improve safety by preventing oxidation in any accidents (Topic 6-3).

As for the heat application research, the flowsheet around the Bunsen reaction, which is one of the key reactions of the Iodine-Sulfur process for producing hydrogen from water, was modified to improve hydrogen-production efficiency, and confirmation tests were conducted to confirm the applicability of the proposed technologies (Topic 6-4). Research and development of the demonstration test using the HTTR have been conducted to establish the hydrogen-electricity cogeneration system for enhancing the heat-utilization ratio (Topic 6-5). Moreover, the in-core graphite blocks in the HTTR, which stopped operation after the Great East Japan Earthquake (3.11 earthquake), were taken out from the core and visually inspected to confirm integrity in addition to the seismic evaluation (Topic 6-6).

We are preparing to resume operation of the HTTR by conducting the conformity review on new regulatory requirements issued by the NRA after the Great East Japan Earthquake.

# 6–1 Development of International Safety Standards for Commercial HTGRs

## — Safety Requirements for the Design of HTGRs Based on the Inherent Safety Features Demonstrated by HTTR —

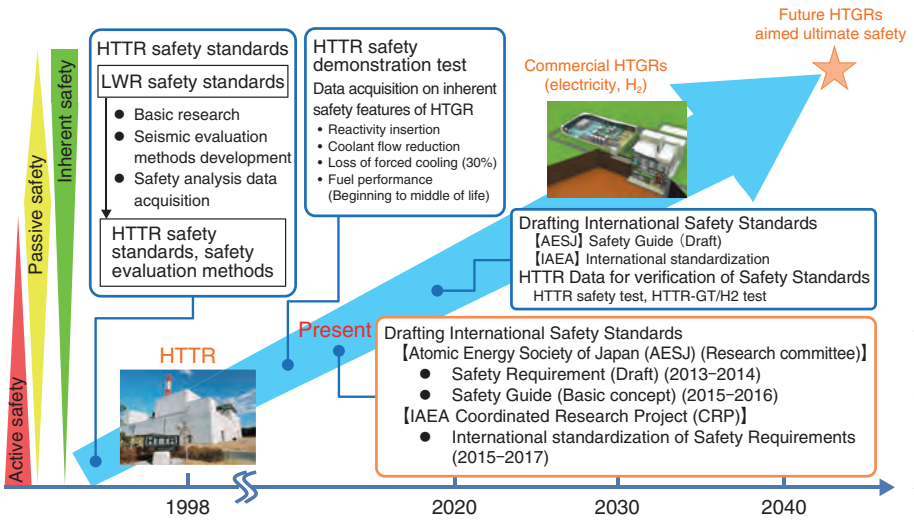


**Fig.6-2 Activities for developing international safety standards for HTGR**
We are drafting the safety standards for HTGRs as part a research committee of the Atomic Energy Society of Japan (AESJ) and the Coordinated Research Project (CRP) of the International Atomic Energy Agency (IAEA).

**Table 6-1 Safety requirements for HTGRs and light-water reactors**
Draft safety requirements are developed considering the safety features demonstrated by the HTTR and the HTGR-specific safety-design approach, which differs from that for light-water reactors.

| Safety requirements | | HTGRs | LWRs |
|---|---|---|---|
| Confinement of radioactive materials | Maintain integrity of fuel | In-operation states and in-accident conditions | In-operation states |
| | Containment vessel or confinement | Confinement (Moderated leak rate)<br>(Not required if fuel performance and design is good enough) | Containment Vessel (Leak-tight) |
| Reactor shutdown | | At least two diverse and independent means (Inherent design features is regarded as one of means) | At least two diverse and independent systems |
| Heat removal from core | | Passive cooling from the outside surface of reactor vessel (Passive cooling) | In shutdown states: Residual heat removal (Forced cooling)<br>In accident condition: Emergency core cooling (Forced cooling) |
| Emergency power | | To monitor plant parameters and radiological conditions (Emergency power supply is not required to mitigate the consequences of AOO and accidents) | To mitigate the consequences of AOO and accidents<br>To monitor plant parameters and radiological conditions |

We are developing safety standards for High-Temperature Gas-cooled Reactors (HTGRs) that incorporate the HTGR safety features demonstrated using the High Temperature Engineering Test Reactor (HTTR) to deploy Japanese HTGR technologies at global markets and also make an international contribution to the sophistication of nuclear-reactor safety (Fig.6-2). The specific safety requirements, which are high-level standards defining functional requirements, for the design of commercial HTGRs have been developed by research committee under the Atomic Energy Society of Japan (AESJ).

The safety design approach was developed on the basis that the safety (i.e., lack of core meltdowns or significant radionuclide release) should be assured not by active systems or by operator actions but by inherent and passive safety features, even in the event of major structural failures such as large pipe breaks of the reactor-coolant-pressure boundary. We devised eighty-two safety requirements using safety function analysis and an objective-provision-tree method to analyze the functional requirements.

The significant differences between the IAEA safety requirements for LWRs and the developed safety requirements for HTGRs are summarized in Table 6-1. For the confinement of radionuclides, coated fuel particles (CFPs) are required to maintain their confinement performance not only in operational states but also under accidental conditions. This is a significantly different approach from that taken toward LWRs because the confinement performance of the fuel is required only during normal operation and anticipated operational occurrences in LWRs. In contrast, HTGRs do not use a leak-tight containment vessel but a confinement structure with a moderated leak. The HTTR safety-demonstration test shows that when the core becomes subcritical, it takes several hours to achieve recriticality and the core residual heat, including decay heat, can be removed from the core via the external surface of the reactor-pressure vessel using natural convection and radiation during loss-of-force cooling events without scram. At least two diverse and independent means of reactor shutdown are required, but an inherent shutdown feature is regarding as such means based on the HTTR data. HTTR data also suggest that passive means are required to remove heat from the core in order to utilize the advantages of HTGRs.

We are participating in an IAEA CRP on HTGR Safety Design, of which the member states are USA, Germany, China, Kazakhstan, Indonesia, etc. We aim to achieve international standardization of the developed safety requirements. We lead CRP activities to contribute draft international HTGR-safety standards that incorporate the superior HTGR-safety features, as demonstrated by the HTTR.

**Reference**

Ohashi, H. et al., Safety Design Approach for the Development of Safety Requirements for Design of Commercial HTGR, Proceedings of 7th International Topical Meeting on High Temperature Reactor Technology (HTR 2014), Weihai, China, 2014, paper HTR2014-81150, 10p., in USB Flash Drive.

# 6–2 Toward Enhancing the Safety of Plutonium-Burner High Temperature Gas-Cooled Reactors
## — Prevention of Internal Gas-Pressure Failure of Fuel Particles Coated by Oxygen Getters —

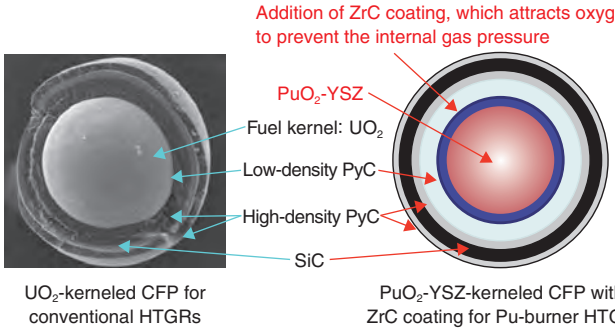


**Fig.6-3 CFPs for a conventional HTGR and a plutonium-burner HTGR**
Nuclear-proliferation resistance is enhanced by introducing YSZ as a fuel matrix, which is an inert chemical. Safety is also enhanced by using the ZrC coating layer as an oxygen getter on fuel kernels with diameters of approximately 1 mm to reduce the internal gas pressure of the CFPs.

**Fig.6-4 Schematic of the reactor core of a plutonium-burner HTGR**
The plutonium-burner HTGR is designed on the basis of the GTHTR300, whose conceptual design has already been conducted by JAEA. The GTHTR300 is a uranium-fueled HTGR with 600 MW of thermal power. The core height and equivalent core diameter are 8 m and 5.5 m, respectively. The fuel region of the plutonium-burner HTGR is larger than that of the GTHTR300 to increase criticality and incinerate as large an amount of plutonium as possible.

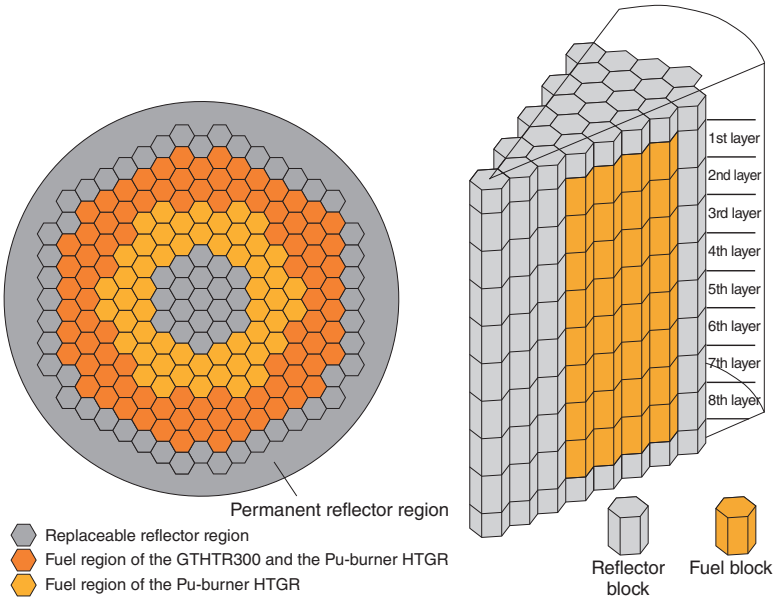


High-temperature gas-cooled reactors (HTGRs) have excellent safety features because their stopping, cooling, and fission-product-confinement behavior are ensured by physical phenomena, even if all electricity is stopped. Meanwhile, the establishment of plutonium-incineration technology is important from the viewpoint of nuclear security both internationally and domestically. Thus, we have proposed an HTGR system to incinerate Pu by fission.

For coated fuel particles (CFPs) in conventional HTGRs, an increase in the internal pressure, which is caused by the generation of carbon monoxide (CO) and fission product (FP) gases with burnup, is considered a major cause of the fuel failure occurring during operation. The CO gas is generated by the chemical reaction of the low-density pyrolytic carbon layer with the free-oxygen released from uranium dioxide ($UO_2$) or plutonium dioxide ($PuO_2$) by fission. Therefore, we have proposed a safety-enhanced Pu-burner HTGR by introducing CFPs with fuel kernels coated by zirconium carbide (ZrC), which acts as an oxygen getter (Fig.6-3).

A study on the safety-enhanced Pu-burner HTGR was started in FY2014 by the University of Tokyo, the Japan Atomic Energy Agency (JAEA), the Fuji Electric Co., Ltd., and the Nuclear Fuel Industries, Ltd. to establish the basic technologies necessary. The design studies of the fuel and the reactor core as well an experiment with ZrC coating will be completed in FY2017.

In the fuel-design study, an existing code for calculating the internal gas pressure in $UO_2$-kerneled CFP is being modified to analyze that in the $PuO_2$-kerneled one with consideration of the depression effect due to ZrC coating. In the design study of the reactor core, the input files have been prepared to perform nuclear burnup calculations for the reactor core illustrated in Fig.6-4. The nuclear burnup calculations with the whole core model and the fuel-temperature calculations will be performed. In addition, inspection and preparation for the ZrC-coating instrumentations were conducted. The ZrC-coating experiment will be conducted to obtain material properties such as stoichiometry, density, and microscopic structure of the ZrC, and then the optimization of the coating conditions such as temperature and gas-flow rate will be examined based on the obtained material-characteristic data.

The present study was partly sponsored by the Ministry of Education, Culture, Sports, Science and Technology of Japan (MEXT).

**Reference**

Goto, M. et al., Conceptual Study of a Plutonium Burner High Temperature Gas-Cooled Reactor with High Nuclear Proliferation Resistance, Proceedings of 21st International Conference & Exhibition; Nuclear Fuel Cycle for a Low-Carbon Future (GLOBAL 2015), Paris, France, 2015, paper 5426, p.507-513, in USB Flash Drive.

# 6–3 Development of Oxidation-Resistant Graphite Materials for High Temperature Gas-Cooled Reactor Cores — Collaborative Study with the Institute of Nuclear Physics in Kazakhstan —

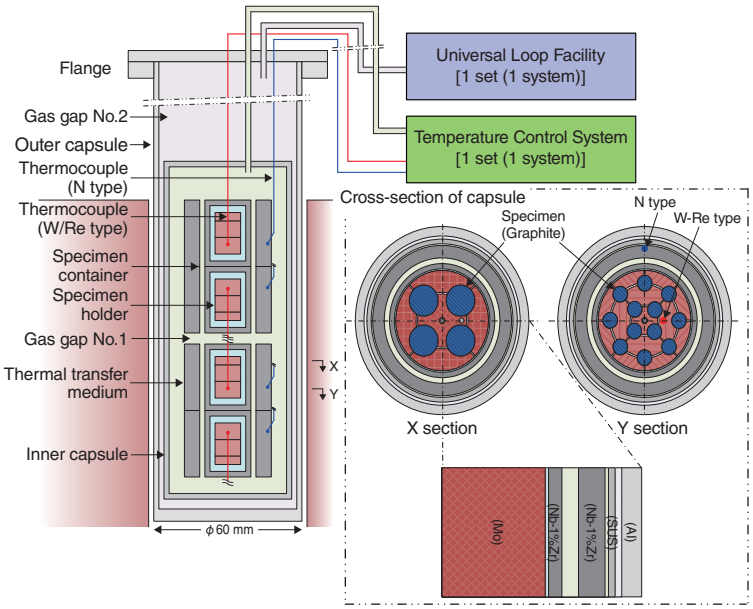


**Fig.6-5 Irradiation tests of oxidation-resistant graphite at the Institute of Nuclear Physics in Kazakhstan**
To understand irradiation behavior of oxidation-resistant graphite under high-temperature conditions, a neutron irradiation test was conducted with an irradiation capsule that could attain a maximum irradiation temperature of 1200 °C under $\gamma$-ray heat and vacuum control of helium gas.

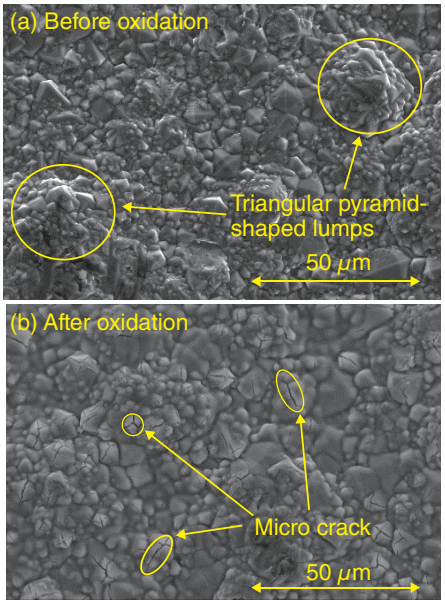


**Fig.6-6 Results of surface observation for oxidation-resistant graphite before and after a preliminary oxidation test**
Oxidation-resistant graphite specimens coated with SiC were oxidized under the condition (He+20%$O_2$, 1300 °C, 20 h) and surface observation was conducted using oxidized specimens. Many tiny cracks were generated during cooling of the specimens. However, it was confirmed that this coating was effective for preserving the material properties of graphite.

Fine-grained graphite materials are used as in-core components of high-temperature gas-cooled reactors (HTGRs). The fine-grained graphite material has a small number of pores, shows high density, has a small number of metal impurities (which act as oxidation catalysts), has high thermal conductivity for removing heat, and shows little release of burnable gas under heating. Therefore, a fine-grained graphite material does not burn with a flame and has excellent properties against air-ingress accidents.

To develop a graphite material that prevents oxidation of in-core components and improves the safety of the HTGR during any accidents, we and four graphite companies (the Toyo Tanso Co., Ltd., the Ibiden Co., Ltd., the Tokai Carbon Co., Ltd., and the Nippon Techno-Carbon Co., Ltd.) have been developing oxidation-resistant graphite coated with SiC.

Irradiation testing of the oxidation-resistant graphite manufactured by four graphite companies was conducted using the WWR-K reactor at Institute of Nuclear Physics in Kazakhstan, where the development of an HTGR is supported as a national policy. An irradiation capsule capable of attaining the maximum-irradiation temperature of 1200 °C under $\gamma$-ray heat and vacuum control of helium gas was fabricated to simulate the most severe condition of the reactor core (Fig.6-5). In contrast, prior to the irradiation test, a preliminary oxidation test was conducted under the un-irradiated condition to investigate the oxidation behavior of the oxidation-resistant graphite. A temperature of 1350 °C and a time of 20 h were set to saturate the value of the oxidation rate. Moreover, a mixed gas containing a 20% concentration of oxygen in helium with a flow rate of 100 ℓ/min was used to attain a condition that could sufficiently oxidize the graphite.

As a result of the oxidation test under an un-irradiated condition, it was confirmed that the weight of oxidation-resistant graphite increased with time. This shows that SiC coated on the surface of oxidation-resistant graphite was oxidized and that $SiO_2$ was formed. Moreover, the oxidation rate of graphite was evaluated according to the weight change between the conditions before and after oxidation, and it was confirmed that the oxidation rate decreased with time. The $SiO_2$ formed on the surface of oxidation-resistant graphite by oxidation worked as a protective film and prevented the graphite from being oxidized. According to surface observation, it is clear that there are numerous triangular pyramid-shaped lumps on the surface of the specimen and many cracks on top of the lumps generated in the cooling process, and that the surface of the specimen becomes smooth under oxidation. Since these changes do not degrade the material properties of oxidation-resistant graphite, it is confirmed that the SiC coating offered adequate oxidation resistance (Fig.6-6).

In the future, post-irradiation examinations, such as measurement of the dimensions, observation of the microstructure, and oxidation testing as well as analysis and evaluation of four types of oxidation-resistant graphite irradiated in the WWR-K reactor will be conducted. We are planning to clarify the oxidation resistance of this graphite irradiated under a neutron-irradiation environment.

**Reference**

Sumita, J. et al., Irradiation Test Plan of Oxidation-Resistant Graphite in WWR-K Research Reactor, Proceedings of 7th International Topical Meeting on High Temperature Reactor Technology (HTR 2014), Weihai, China, 2014, paper HTR2014-41236, 7p., in USB Flash Drive.

# 6–4 Investigation of the Process Conditions of Inhibition Reactions for Thermal-Efficiency Improvement — Effects of Impurity Contamination in an HI Concentrator —

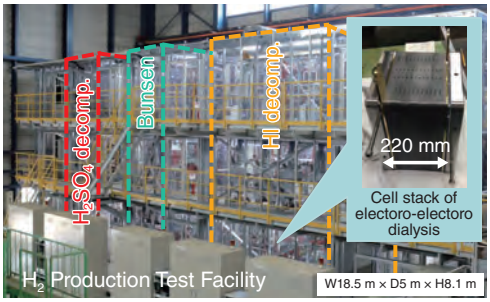


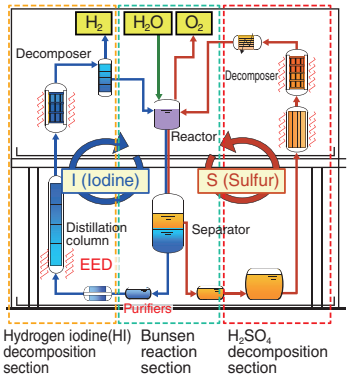


**Fig.6-7 External view of the hydrogen-production test facility**
We constructed a hydrogen-production test facility with all process components composed of industrial structural material in order to verify the integrity of the components and demonstrate continuous hydrogen-production ability. An electoro-electoro dialysis device (EED) was employed to concentrate the HI solution.

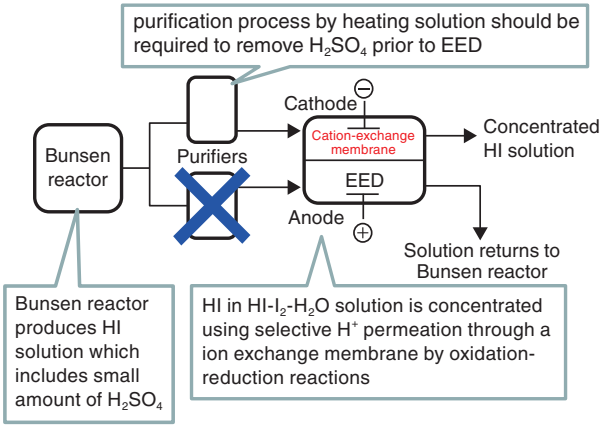


**Fig.6-8 Production and concentration of HI Solution**
The HI solution produced by the Bunsen reaction is purified to prevent harmful side reactions in HI concentration using the EED device. The purification process for the one-sided EED channel can be eliminated by adapting the proposed method.

Effect of sulfuric acid on electro-electro dialysis of HIx solution

| | Exp. conditions | Exp. results : transport number of protons | Visual inspection | |
|---|---|---|---|---|
| Case A (Purification of both sides) | Catholyte: no $H_2SO_4$<br>Anolyte: no $H_2SO_4$ | 1.0 |  | (No change) |
| Case B (Purification catholyte) | Catholyte: no $H_2SO_4$<br>Anolyte: with $H_2SO_4$ | 1.0 |  | (No change) |
| Case C (No purification) | Catholyte: with $H_2SO_4$<br>Anolyte: with $H_2SO_4$ | 0.7 | 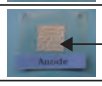 | Sulfur deposition |

**Fig.6-9 View of cation-exchange membrane after HI-concentration experiments using the EED device**
No contamination by $H_2SO_4$ in the bath sides (Case A); one-sided contamination by $H_2SO_4$ in anolyte (Case B); no sulfur is evidenced. Contamination by $H_2SO_4$ in catholyte; sulfur is produced (Case C).

We have pursued R&D on a thermochemical hydrogen-production iodine–sulfur process as a heat-utilization application for the high-temperature gas-cooled reactor. This chemical process uses chemical compounds of iodine and sulfur to split water to produce hydrogen by combining three chemical reactions. This process, which can harness heat for nuclear or renewable energy, is a promising next-generation hydrogen-production method that is independent of fossil fuels and that can provide energy security. One important task is to improve the thermal efficiency of hydrogen production.

Reduction of the heat for driving processes is an effective method of improving thermal efficiency. We focused on a purification operation for processing the Bunsen-reaction solution. Bunsen reaction, which is core chemical reaction in the iodine–sulfur process, produces two types of acids in HI- and $H_2SO_4$-rich solutions from $H_2O$, $I_2$, and $SO_2$; the two acids separate into upper and lower phases with a clear boundary set by the liquid–liquid phase-separation phenomenon. The lower phase, which is rich in HI and $I_2$, includes an impurity of $H_2SO_4$; this contamination probably causes HI concentration (an EED with a cation-exchange membrane, Fig.6-7) and HI distillation to occur as a harmful side reaction with the production of solid sulfur. Because of mutual solubility between the two phases, a certain amount of $H_2SO_4$ is solved into the lower phase; a purification process by heating of the solution is necessary to remove $H_2SO_4$. This purification causes an increase of heat input because of the heating requirement for solution vaporization.

While optimizations of the operating temperature for the purification process have been studied, we proposed a flow-rate-reduction method of the processed solution itself to reduce the required heat (Fig.6-8), based on the fact that $H_2SO_4$ turns into sulfur in the reduction environment. The solution after the purification should be concentrated by EED; the solution is fed to both channels of the EED device in the previous flowsheet; $H_2SO_4$ in the anolyte of the oxidation environment is therefore probably stable. If the method is workable, the required heat can be reduced by reducing the processing solution for the purification; moreover, the flowsheet can be simplified.

To validate the proposed method, we conducted concentration experiments of the HI solution including $H_2SO_4$ using an EED device. Results met our expectations; the sulfur was not produced in the anolyte; moreover, the contamination in the anolyte was not affected by the cell voltage or the membrane selectivity (Fig.6-9). We revealed that our proposal can save the input heat required for purification. An increase of the hydrogen-production thermal efficiency is approximately 10% of that of the previous method.

**Reference**

Tanaka, N., Kubo, S. et al., Effect of Sulfuric Acid on Electro-Electrodialysis of HIx Solution, International Journal of Hydrogen Energy, vol.39, issue 1, 2014, p.86-89.

# 6–5 Demonstration of Hydrogen-Cogeneration Technology using the HTTR

## — Designing the Helium Gas Turbine to Enable an Operability-Demonstration Test —

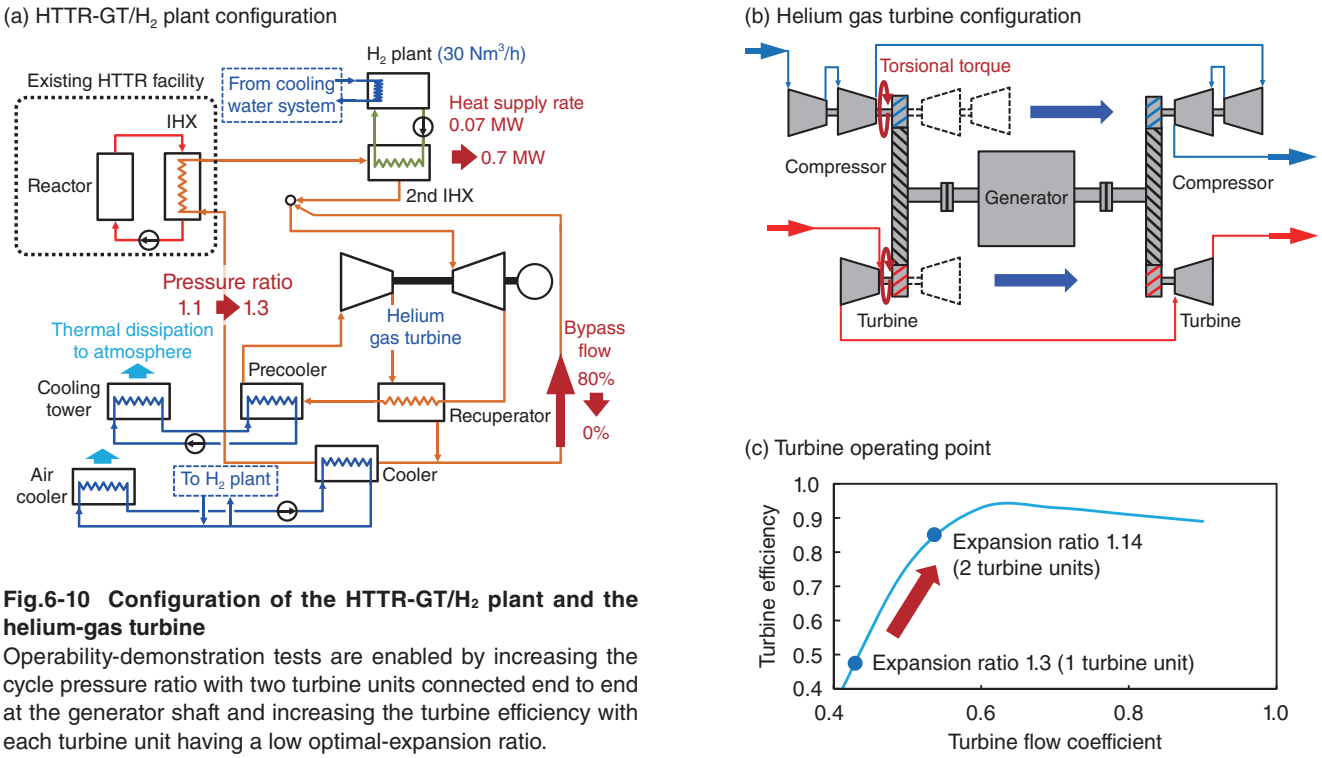


**Fig.6-10 Configuration of the HTTR-GT/$H_2$ plant and the helium-gas turbine**
Operability-demonstration tests are enabled by increasing the cycle pressure ratio with two turbine units connected end to end at the generator shaft and increasing the turbine efficiency with each turbine unit having a low optimal-expansion ratio.

We have been conducting research and development toward commercialization of highly efficient, $CO_2$-emission-free $H_2$ cogeneration by application of heat provided from a high-temperature gas-cooled reactor (HTGR) with inherently safe characteristics.

One of the key technologies for commercialization is a control method that considers the unique characteristics of HTGRs and closed-cycle helium gas turbines, namely (1) prevention of turbine overspeed by system-pressure control against loss of a generator load; (2) mitigation of turbine-inlet-temperature escalation by introducing low-temperature helium from the compressor outlet against upsets of the hydrogen-production plant ($H_2$ plant), and (3) start-up and shut-down operations by primary coolant-inventory control, which does not rely on a large external power supply. We are aiming to construct an HTTR gas turbine-cogeneration plant (HTTR-GT/$H_2$ plant) to perform demonstration tests for the control methods.

The requirements for the design of HTTR-GT/$H_2$ plant are to not only enable operability-demonstration tests but also minimize modification of the existing HTTR facility. In response, a heat-application system is devised as a secondary system and a second intermediate heat exchanger and a helium-gas turbine are installed in cascade to demonstrate the series operation of the $H_2$ plant and the helium-gas turbine in the commercial system (Fig.6-10(a)). In addition, design improvements for the helium-gas turbine are proposed to enable the observation of plant-dynamic behavior. First, two turbine units are connected to each end of a generator shaft to eliminate shaft vibration owing to torsional torque generation (Fig.6-10(b)). Second, two turbine units with a low optimal-expansion ratios are employed instead of one turbine unit with a high expansion ratio to operate at 90% efficiency while meeting the turbine-speed limit owing to structural integrity, and waste heat is utilized to maximize power-generation and $H_2$-production outputs (Figs.6-10(a) and (c)).

As a result of a heat-and-mass-balance evaluation and a manufacturability assessment by an equipment supplier for the HTTR-GT/$H_2$ plant design, it was confirmed that operability-demonstration tests such as loss of generator load, simulation of the upset of the $H_2$ plant, and start-up and shut-down operation tests can be performed in the HTTR-GT/$H_2$ plant with key achievements: $H_2$ cogeneration with a power output of 1 MW at a cycle pressure ratio above 1.3 and an $H_2$-production rate of 30 $Nm^3/h$, and elimination of bypass flow from the recuperator outlet to turbine inlet.

Further study will be made for component design and safety analysis of the HTTR-GT/$H_2$ plant. The external committee will review the results and make recommendations as to whether the project is ready to proceed to the construction phase.

**Reference**

Imai, Y., Sato, H. et al., Design Database of Helium Gas Turbine for High Temperature Gas-Cooled Reactor, JAEA-Data/Code 2016-007, 2016, 27p. (in Japanese).

# 6–6 Proving the Seismic Integrity of the High-Temperature Gas-Cooled Reactor

## — Integrity Confirmation of Graphite Components by Seismic Evaluation and Visual Inspection —

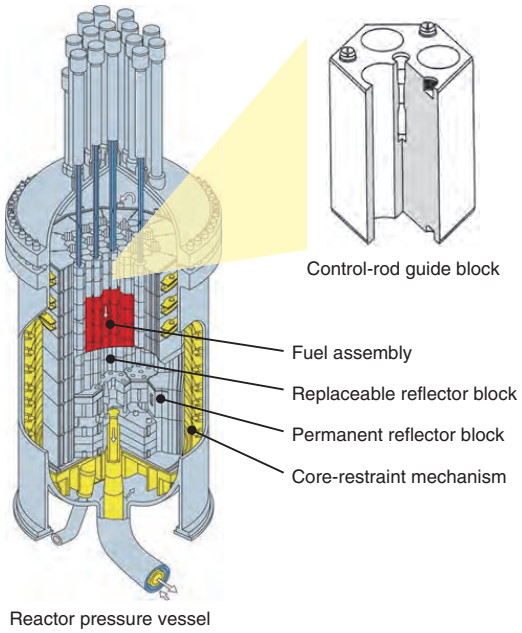


**Fig.6-11 Reactor pressure vessel and control-rod guide block of the High-Temperature Engineering Test Reactor (HTTR)**
This figure shows the control-rod guide block and a cutaway view of the reactor pressure vessel. The reactor components comprise graphite blocks such as control-rod guide blocks, fuel assemblies, permanent reflector blocks, and replaceable reflector blocks, all of which are installed in the reactor pressure vessel.

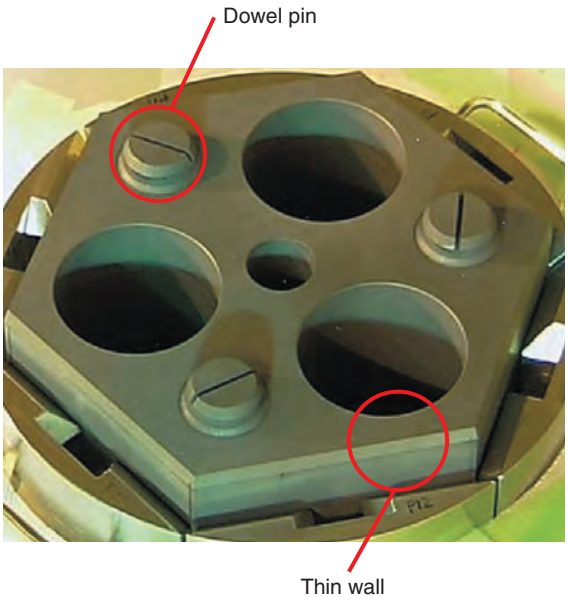


**Fig.6-12 Visual inspection of the control-rod guide block**
Control-rod guide blocks in the reactor pressure vessel were taken out in order to exchange neutron startup sources. An inspection of the control-rod guide block was conducted for the first time after the Great East Japan Earthquake. The integrity of the control-rod guide block was confirmed, and positive proof was acquired from the result of seismic analysis.

After the Great East Japan Earthquake (3.11 earthquake) on March 11, 2011, the seismic integrity of nuclear reactors became a primary concern. A visual inspection of reactor buildings, equipment, and instrumentation was conducted to confirm the seismic integrity of the High-Temperature Engineering Test Reactor (HTTR). However, it is very difficult to inspect components installed inside the reactor pressure vessel. Reactor components, which comprise graphite blocks, are circumferentially restrained by a core-restraint mechanism (Fig.6-11). However, because there are small gaps between the graphite components, these are considered likely to be damaged by collisions in seismic events on the scale of the 3.11 earthquake. Therefore, it is necessary to confirm the integrity of the graphite components by seismic analysis. Seismic acceleration imposed upon the graphite components should be calculated because seismic-observation systems cannot be installed inside the reactor pressure vessel. The seismic acceleration for the analysis was estimated from the relationship between the seismic acceleration observed inside and outside of the reactor building and from the frequency-transfer function of the foundation that supports the reactor building. The seismic-evaluation method for graphite components proceeded by calculations from outer to the inner components in the order of the reactor building, the reactor pressure vessel, and the graphite components, so as to evaluate the inner components using the seismic acceleration obtained by the evaluation of the outer components. For this seismic evaluation, the analytical model was validated through experiments using actual scaled-down equipment and its analysis. As a result of the evaluation, the seismic integrity of all graphite components was confirmed.

Neutron-startup sources were exchanged in HTTR in October 2015. The control-rod guide blocks, wherein the neutron startup sources were installed, were taken out from the reactor core and visually inspected subsequently, as shown in Fig.6-12. The reactor components were taken out for the first time since the 3.11 earthquake, providing a good opportunity to confirm the seismic integrity directly. As a result of the visual inspection, it was confirmed that there was no damage to the whole block surface, including the thin wall and the dowel pins where seismic force was concentrated upon the control-rod guide block.

For further investigation toward the restart of the HTTR, the seismic integrity of the graphite components as well as the other equipment and instrumentation will be confirmed by evaluation using a design-basis ground motion that will be established based on new knowledge by a safety review by the Nuclear Regulation Authority.

**Reference**

Ono, M. et al., Confirmation of Seismic Integrity of HTTR Against 2011 Great East Japan Earthquake, Proceedings of 24th International Conference on Nuclear Engineering (ICONE 24), Charlotte, North Carolina, USA, 2016, ICONE24-60571, 12p., in DVD-ROM.

# R&D of Fast Reactor Cycle Technology

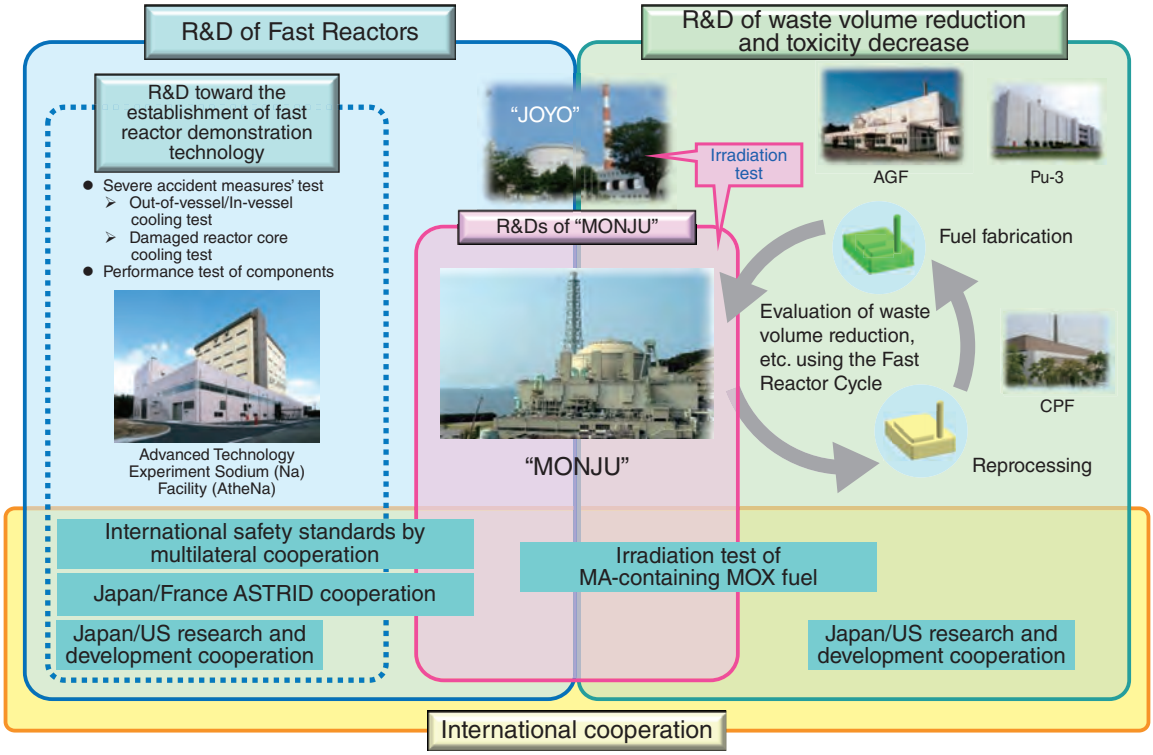


**Fig.7-1 Overview of research and development of fast reactor cycle technology**
In accordance with the 3rd Medium- and Long-term Goals established by government authorities in "the 4th Strategic Energy Plan", in 2015 we started conducting R&D on the subjects of waste-volume reduction and toxicity decrease, accumulation of a plant technology by utilizing "MONJU", and establishment of a fast-reactor-demonstration technology, with international cooperation.

Fast reactor cycle technology is essential for the establishment of a nuclear-fuel cycle appropriate to our nation's energy security and efforts to combat global warming, and "the 4th Strategic Energy Plan", which was approved by the Cabinet in April 2014, clearly stated that research and development (R&D) of this technology is a challenge that must be addressed. Based on the 3rd Medium- and Long-term Goals established in this plan, as of 2015, we are conducting R&D on waste volume-reduction and toxicity decrease, accumulation of a plant technology by utilizing "MONJU" prototype fast-breeder reactor, and establishment of a fast-reactor-demonstration technology with international cooperation (Fig.7-1).

"MONJU" is positioned to be an international research center for development of technologies such as those related to reducing the amount and toxicity level of radioactive waste; it will be focused on overcoming challenges such as responding to new regulatory requirements.

We are conducting the R&D necessary for the establishment of fast-reactor-demonstration technology using the results obtained by related studies on "MONJU", as well as participation in the international project for the demonstration phase of the French Advanced Sodium Technological Reactor for Industrial Demonstration (ASTRID).

To reduce the volume and toxicity of radioactive waste, we promote the development of a separation-and-recovery technology for minor actinides (MA) and performance evaluation of MA-containing fuel while leveraging international networks; these are major technological developmental challenges for nuclear transmutation using fast reactors to reduce the amount of radioactive waste and the long-term remaining toxicity level.

In this chapter, we will introduce our R&D achievements toward strengthening the safety of fast reactors, reducing the volume of radioactive waste, and decreasing toxicity, as well as our progress on "MONJU".

We are developing Safety Design Criteria and Safety Design Guidelines through international cooperation to establish international standards for next-generation sodium-cooled fast reactors (SFRs) (Topic 7-1).

We developed an MA-transmutation core for an SFR, wherein core safety and nuclear transmutation performance are enhanced simultaneously, and predicted a remarkable improvement in the MA transmutation amount—two times larger than that obtained in a conventional fast reactor (Topic 7-2).

We revealed by an experimental study that the installation of a duct in a fuel subassembly is effective in achieving a rapid discharge of molten fuel from the core, thereby eliminating the cause of rapid power increases in cases of core-disruptive accidents (Topic 7-3).

With respect to sodium-water-reaction phenomena that might occur when a heat-transfer tube fails in a steam generator, we elucidated the effects of factors influencing the corrosion behavior of heat-transfer tubes by means of experiments (Topic 7-4).

We also experimentally evaluated the relationship between oxygen potential and oxygen-to-metal ratio (O/M ratio), which significantly affected the sintering and irradiation behavior of oxide fuel, and estimated the effect of the minor actinide Am upon the oxygen potential (Topic 7-5).

Regarding the crush zones distributed in and around "MONJU", we attempted to estimate the timing of the slip episodes using a fission-track dating method (Topic 7-6).

# 7–1 Leading the World in Safety with the Next-Generation Sodium-Cooled Fast Reactor
## — Development and Standardization of Safety Design Criteria and Safety Design Guidelines —

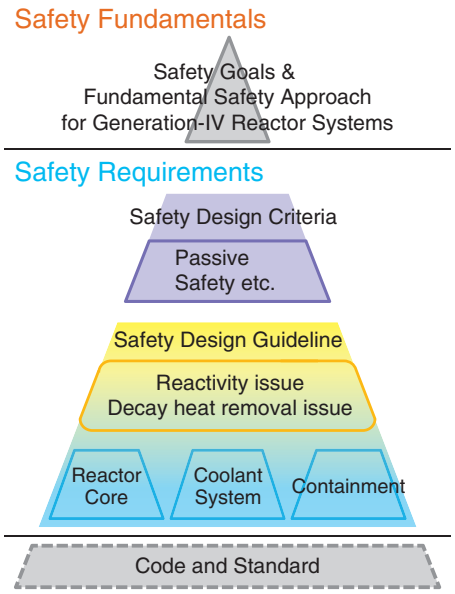


**Fig.7-2 Positions of SDC & SDG in the hierarchy of safety standards**
SDC provides approaches to designing SFR systems to realize a basic concept of the safety, whereas SDG shows recommendations on more specific items, including the functions and mechanisms of the SFR systems to prevent and/or mitigate accidents and how and when they should perform. These are the first international-safety standards ever established for Gen-IV reactors including SFRs.

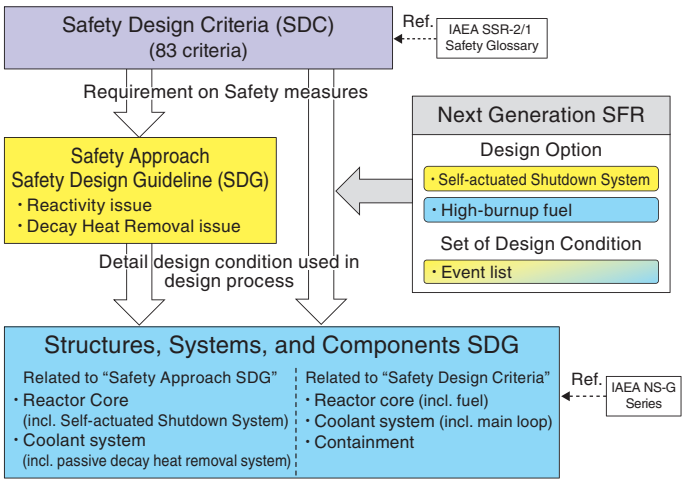


**Fig.7-3 Process of specification in SDG**
Safety Approach SDG summarizes design measures against issues of core reactivity and decay-heat removal, with design options and conditions for Gen-IV SFRs based on 83 criteria in SDC. SSC SDG describes the design measures of each SSC in detail.

The establishment of international standards for Generation IV (Gen-IV) sodium-cooled fast reactors (SFR), known as the Safety Design Criteria (SDC), started in 2010 under the Generation-IV International Forum (GIF). SDC was approved by the GIF in May 2013 and is currently being reviewed by international organizations and regulatory bodies of SFR-developing countries. Furthermore, a harmonious collaboration with the organizations in those countries is vigorously being promoted to develop Safety Design Guidelines (SDG) that show SFR designers how to apply the SDC to the actual design of an SFR. We have developed and proved various safety-related technologies in Gen-IV-fast-reactor programs in the past, and these technologies are incorporated into the SDC and SDG. These standardizations recognize that our safety technologies are widely accepted and take the initiative in SFR safety.

Fig.7-2 illustrates the positions of the SDC and SDG in the hierarchy of safety standards, placing them in the middle between upper-level fundamentals and lower-level codes and standards. In order to realize a basic safety concept, the SDC provide systematic and comprehensive approaches to the appropriate design of the structure, system, and components (SSC), which are manufactured according to the codes and standards. In contrast, the SDG show recommendations on more specific items, e.g., the functions and mechanisms of the SFR systems in preventing and/or mitigate accidents and how and when (under what conditions) they should perform, with examples. SDC and SDG are the first international safety standards ever, for not only SFRs but also Gen-IV reactors.

The SDG, established based on the SDC, explain the SSC in detail to ensure the safety of the reactor, even under more severe conditions than those of the design-basis accident in the light of lessons learned from the accident at the TEPCO's Fukushima Daiichi NPS. Fig.7-3 shows the relationship between the SDG and SDC and the specification process. The Safety Approach SDG puts special emphasis on design measures against accidents related to core reactivity and decay-heat removal. The design measures are comprehensively summarized with examples because they are important to safety and can affect the condition of the whole reactor. SDG on Safety Approach has been approved by GIF and is currently being reviewed by international organizations. In addition, we are drafting an SSC SDG document that clarifies design concepts related to achieving a higher degree of safety, focusing on each SSC. The SSC SDG established in Japan will be standardized internationally together with the collaboration framework for the GIF in the near future.

**Reference**

Okano, Y. et al., Research & Development of Safety Approach and Safety Assessment for the Next Generation SFR, Proceedings of Probabilistic Safety Assessment and Management Topical Conference; In Light of the Fukushima Dai-Ichi Accident (PSAM 2013), Tokyo, Japan, 2013, PSAM2013-1028, 6p., in USB Flash Drive.

# 7–2 Fast-Reactor-Core Design for Enhanced Radioactive-Waste Reduction
## — Harmonizing Safety and Nuclear Transmutation —

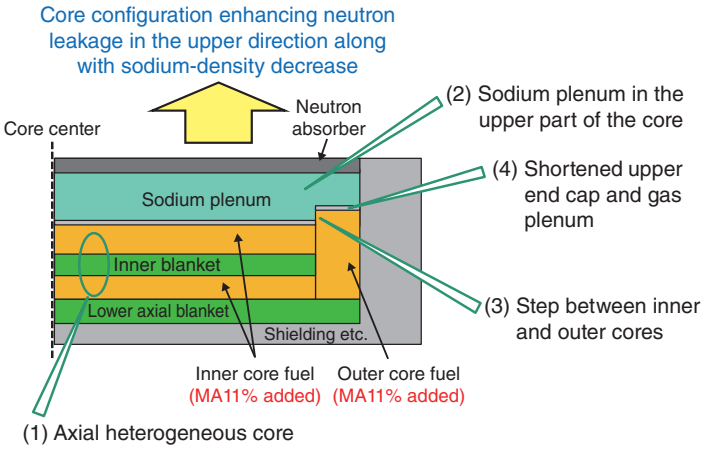


**Fig.7-4 MA-transmutation core with low-sodium void reactivity**
Design measures (1) to (4) were introduced to reduce safety-related sodium-void reactivity. Along with sodium-density decrease due to temperature increase, neutron leakage in the upper direction increases, thereby deactivating the reactor.

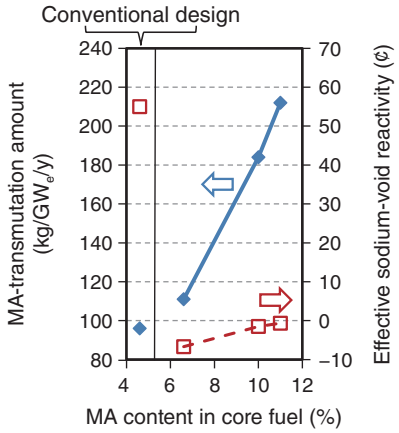


**Fig.7-5 Achievement of a large MA-transmutation amount**
The MA content was increased up to 11% under the conditions where the effective sodium-void reactivity was kept negative, resulting in a large MA-transmutation amount two times larger than that obtained in conventional fast reactors. The ¢ (cent) is a unit of reactivity. A reactivity of more than 100 ¢ leads to a rapid power increase.

High-level radioactive waste generated by reprocessing of spent fuel from nuclear-power plants includes minor actinides (MAs): neptunium, americium, curium, and the like. MAs exhibit long-term radiotoxicity and heat. Partitioning of MA from high-level waste and transmuting it in reactors is expected to contribute to the reduction in long-term underground radiotoxicity as well as to the reduction of waste-disposal area.

Fast reactors possess excellent neutronic characteristics that allow for recycling of MAs as a nuclear fuel and burning them to generate electricity. In the framework of a subsidized study led by the University of Fukui, the MA-transmutation core for a 750-$MW_e$ sodium-cooled fast reactor, which harmonizes core safety and nuclear-transmutation performance, was developed in cooperation with Hitachi-GE Nuclear Energy.

In order to increase the MA-transmutation amount, it is necessary to increase the MA content in core fuel. Since there is a trade-off between MA content and safety-related sodium-void reactivity, the reduction in this reactivity has been a major design challenge. Sodium-void reactivity, caused by sodium-density decrease due to temperature rise, has a positive value in conventional fast reactors, which can activate nuclear reactions in the core.

We invented a design index for the effective sodium-void reactivity (ESVR) by assuming the axial sodium-density distributions for a hypothetical accident in this study. In order to make the accident sluggish, a design condition that kept the ESVR negative was introduced. In the core design, the following measures were employed, as shown in Fig.7-4: (1) an axial heterogeneous core, (2) a sodium plenum in the upper part of the core, (3) a step between the inner and outer cores, and (4) a shortened upper-end cap and gas plenum. Then, the neutron leakage in the upper direction was enhanced, along with a decrease in the sodium density, such that the ESVR significantly decreased with the generation of a margin on the negative-value side (see red plots in Fig.7-5). This margin was consumed by maximizing the MA content; consequently, the MA content was increased up to 11% in the core-fuel heavy metal, as compared with a value of 5% for conventional fast reactors. We predict a remarkable improvement in the MA-transmutation amount, namely double that which is presently obtained in conventional fast reactors (see blue plots in Fig.7-5).

Since the condition where the MA content exceeds 5% rarely occurs in a breeding scenario in which light-water reactors are replaced with fast reactors, the conventional fast reactors have sufficient nuclear-transmutation capability. Nevertheless, the MA-transmutation core developed in this study offers great flexibility in MA management. For instance, concentrative MA burning becomes possible with the introduction of a small number of fast reactors; as does localized MA treatment at a minimal part of the fuel cycle in the case where many fast reactors are introduced in combination with conventional ones.

This study includes some results related to the Study of minor actinide transmutation using Monju data in FY2014, which was entrusted to the University of Fukui by the Ministry of Education, Culture, Sports, Science and Technology of Japan (MEXT).

**Reference**

Fujimura, K., Ohki, S. et al., Development of a Fast Reactor for Minor Actinides Transmutation (2) − Study on the MA Transmutation Core Concepts −, Proceedings of 21st International Conference & Exhibition; Nuclear Fuel Cycle for a Low-Carbon Future (GLOBAL 2015), Paris, France, 2015, paper 5105, p.592-598, in USB Flash Drive.

# 7–3 Improving Fast Reactor Safety

## — Experimental Confirmation of Fuel-Subassembly Melt and Discharge Behavior —

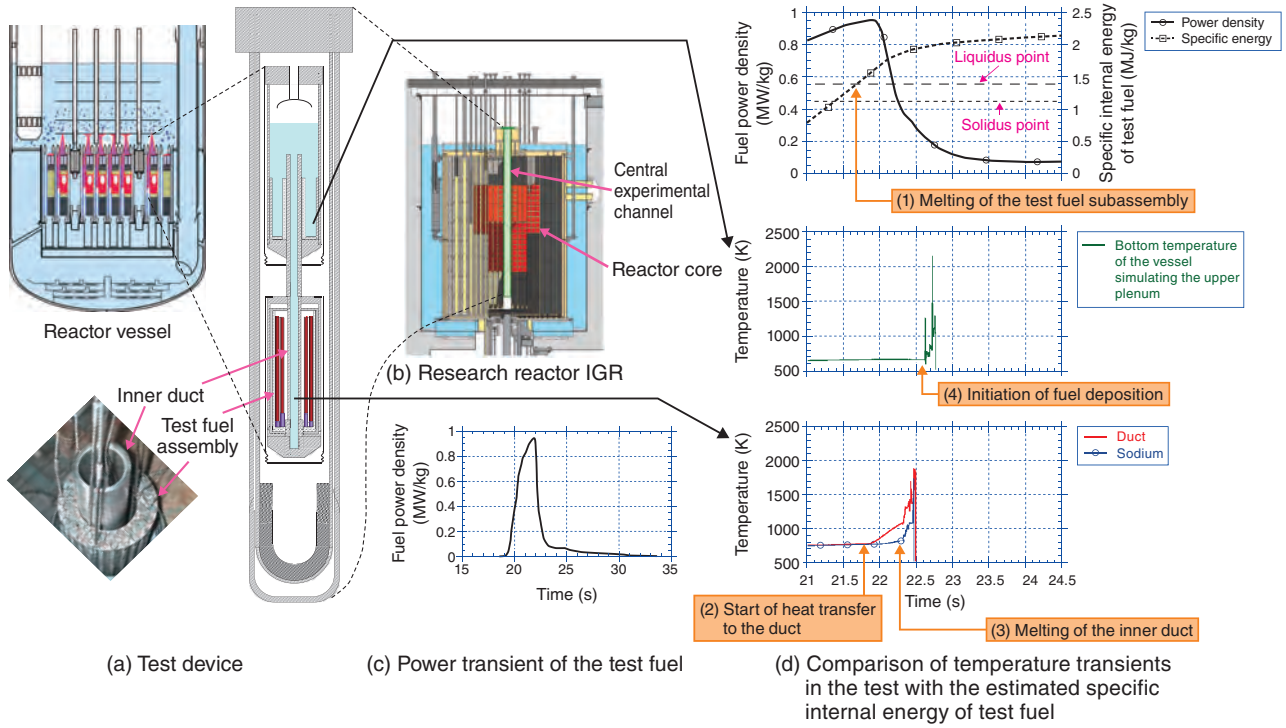


**Fig.7-6 Experiment for upward discharge of molten fuel from a fuel subassembly with an inner-duct structure (FAIDUS)**
Under a joint-research program with the National Nuclear Center of the Republic of Kazakhstan (NNC/RK), data on the upward discharge behavior of molten fuel through an inner duct was successfully obtained by simulating an accident condition in which an experimental fuel subassembly was molten and heated by nuclear heating up to approximately 3000 °C using the NNC's research reactor IGR (Impulse Graphite Reactor).

To ensure the safety of sodium-cooled fast reactors (SFRs), it is essential to protect the reactor vessel against failure in case of accident that causes fuel failure and resulting core disruption (core-disruptive accident). The failure of the reactor vessel under core-disruptive accident can occur when a large amount of molten fuel remaining in the core is rapidly compacted, resulting in a rapid power increase. In conventional SFR design, the integrity of the reactor vessel was ensured in case of such conditions; however, for next-generation SFRs, the aim is to further improve safety by eliminating the cause of a rapid power increase in case of a core-disruptive accident. Specifically, a dedicated duct is installed in the fuel subassembly to immediately discharge molten fuel from the core (i.e., the fuel subassembly with an inner-duct structure (FAIDUS)). Presently, from the perspective of the cooling of discharged fuel, the concept of discharging molten fuel toward the upper plenum by placing an inner duct with an opening at the upper end is examined with attention to the increase of the core pressure during fuel melting.

In this experimental study, a fuel subassembly was actually melted to confirm the upward discharge of molten fuel. The test device is shown in Fig.7-6(a). A test device partially simulating the FAIDUS was manufactured and installed in the central experimental channel of the NNC's research reactor IGR, as shown in Fig.7-6(b). The test fuel was heated by neutron irradiation to the test device by operating the IGR to simulate a core melt condition in the device, as shown in Fig.7-6(c). Fig.7-6(d) shows the main measured results compared with the estimated specific internal energy of the test fuel, leading to the following conclusions: (1) the estimated specific internal energy of the test fuel suggests that the test fuel subassembly melted completely at approximately 21.7 s; (2) the temperature of the inner duct started to rise due to heat transfer from the molten fuel at approximately 21.8 s; (3) the discontinuous temperature change found at approximately 22.3 s suggests the melting of the inner duct and the start of fuel discharge; and (4) the rapid temperature increase in the bottom of the vessel for simulating the upper plenum found at approximately 22.6 s suggests the start of deposition of the fuel discharged upward. The weight measurement of the deposit confirmed that the majority of the molten fuel in the core was discharged upward.

This study revealed that installation of a duct in a fuel subassembly is effective in achieving rapid discharge of molten fuel out of the core during a core-disruptive accident, and that upward discharge is also applicable.

**Reference**

Kamiyama, K. et al., Experimental Studies on the Upward Fuel Discharge for Elimination of Severe Recriticality during Core-Disruptive Accidents in Sodium-Cooled Fast Reactors, Journal of Nuclear Science and Technology, vol.51, issue 9, 2014, p.1114-1124.

# 7–4 Clarification of the Wastage Phenomena of the Heat-Transfer Tubes of a Steam Generator in a Sodium-Cooled Fast Reactor — Evaluation on Corrosion Behavior with High-Temperature Sodium Hydroxide Flow —

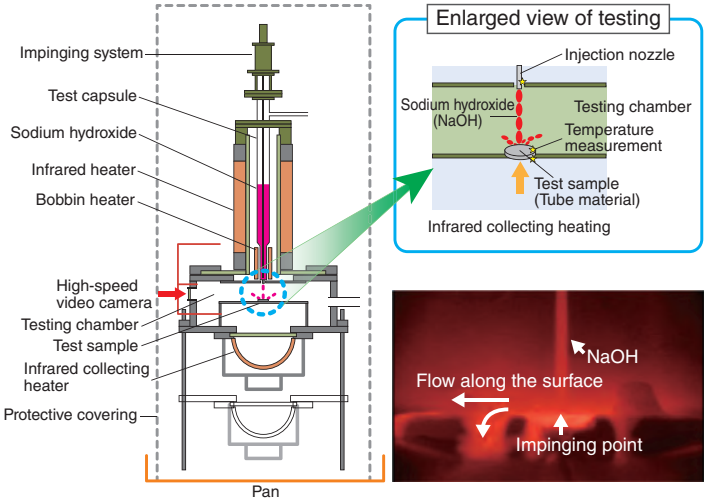


**Fig.7-7 Experimental apparatus and situation**
New experimental apparatuses and techniques were developed to investigate the separation effect of the factors influencing wastage phenomena and understand how the corrosion rate would be enhanced under sodium hydroxide flow caused by sodium-water reaction at high temperatures.

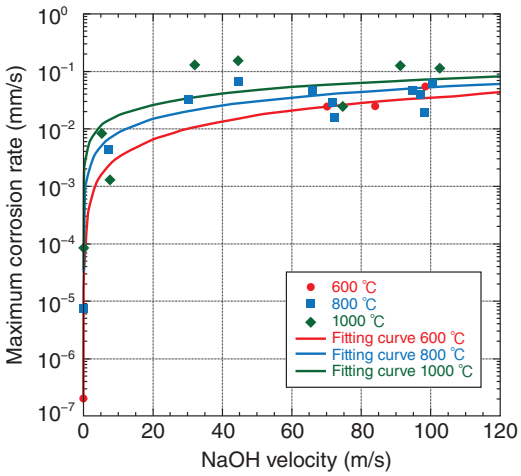


**Fig.7-8 The corrosion rate in a high-temperature sodium hydroxide environment**
In a high-temperature sodium hydroxide flow, the maximum corrosion rate moderately increased with the rise of the flow velocity and temperature of the sodium hydroxide.

A steam generator (SG) is a heat exchanger between sodium and water/water vapor in a sodium-cooled fast reactor (SFR). When the high-pressure water/water vapor leaks into sodium through a perforation breach of the tube, a high-temperature and highly caustic specific environment (reaction jet) may be formed. This reaction jet locally causes wear upon the neighboring tubes; this failure propagation may potentially reduce the structural integrity.

The wastage rate has thus far been evaluated on the basis of the data obtained in previous sodium-water-reaction experiments, which simulated the structure and operational conditions of existing SFR SGs. This approach is not a versatile option for design of future systems with high-temperature and high-pressure operation and is inadequate for optimization purposes. Therefore, a mechanistic sodium-water reaction-analysis system has been developed for the reasonable and socially-receptive design.

The authors proposed that wastage occurs as a combination of liquid droplet impingement erosion under the high-velocity reaction jet and corrosion induced by the sodium hydroxide (NaOH) and sodium monoxide ($Na_2O$) flow mainly produced by the sodium-water chemical reaction. The experimental apparatus shown in the Fig.7-7 was developed to elucidate the separation effect of the factors influencing wastage behavior. This experimental apparatus primarily consists of a testing capsule to enclose the reagents such as NaOH and $Na_2O$, an infrared heater to heat the testing capsule, a test sample manufactured of the same material as the candidate tube, an infrared-collecting heater to heat-test samples, and ancillary devices such as a data-acquisition system. The quartz-glass pipe was mounted between the infrared heater and the test capsule to sustain the argon-gas atmosphere in the experimental system. Experimental parameters include the temperatures of the reagent and the test sample (up to 1000 °C), the reagent-injection velocity (up to 100 m/s), and the reagent-mixture fraction. High-temperature liquid reagent impacted with the column at the predetermined position, as shown on the right side of Fig.7-7. The corrosion rate was measured by the reduced thickness of the test sample and the injection time.

Fig.7-8 indicates the maximum corrosion rate of the test sample in a NaOH environment. This rate tends to increase with the rise of reagent temperature, test-sample temperature, and reagent-impinging velocity. It was confirmed that the reagent-impinging velocity did not strongly affect the maximum-corrosion rate above approximately 30 m/s. This corrosion depression effect implies that the mass-transfer coefficients of iron and chromium, which are the reactants of the surface oxide, are much smaller within the material than those from the outer surface of the test sample to the outside fluid flow.

The results of this research will be utilized in the verification and validation of the mechanistic sodium-water reaction-analysis system.

The present study includes results obtained for the Ministry of Education, Culture, Sports, Science and Technology of Japan (MEXT).

**Reference**

Kurihara, A. et al., Study on Target Wastage for Sodium-Water Reaction Environment Formed on Periphery of Adjacent Tube in Steam Generator of Sodium-Cooled Fast Reactor; Composite Oxidation-Type Corrosion with Flow Experiment using High-Temperature Sodium Hydroxide, Nippon Genshiryoku Gakkai Wabun Ronbunshi (Transactions of the Atomic Energy Society of Japan), vol.14, no.4, 2015, p.235-248 (in Japanese).

# 7–5 The Effect of Am upon the Themophysical Properties of MA-MOX Fuel

## — The Relationship between Oxygen Potential and the O/M Ratio of $(Pu_{0.928}Am_{0.072})O_{2-x}$ —

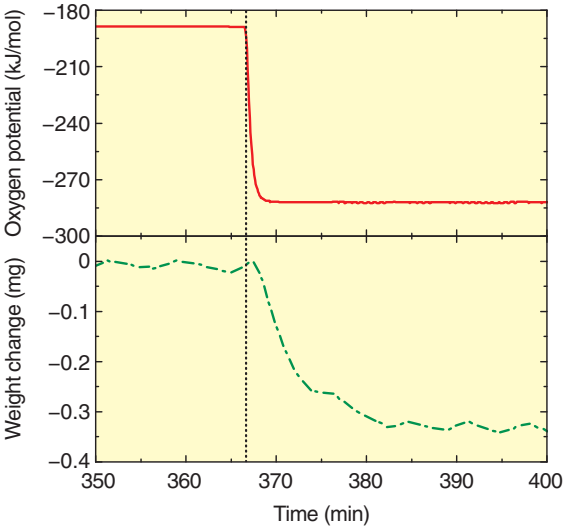


**Fig.7-9 The change of oxygen potential and specimen weight**
The upper and lower figures show the change in the oxygen potential and specimen weight, respectively. The specimen weight decreased with decrease in the oxygen potential, indicating that the specimen was reduced.

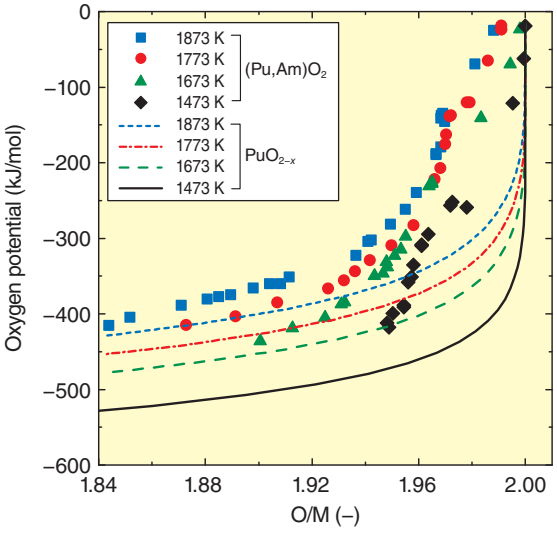


**Fig.7-10 Oxygen potentials of $(Pu_{0.928}Am_{0.072})O_{2-x}$ and $PuO_{2-x}$**
It was observed that the oxygen potential of $(Pu_{0.928}Am_{0.072})O_{2-x}$ was approximately 200 kJ/mol higher than that of $PuO_2$ in the near-stoichiometric region.

The spent nuclear fuels discharged from nuclear power plants contain minor actinides (MAs) such as americium (Am) and neptunium (Np). Since these MAs have high and long-term radiotoxicity, it is better to transmute MAs into stable or less-radiotoxic nuclides by leveraging fast reactors (FRs). MA-bearing oxide fuel is a major fuel candidate for FRs and is therefore required to measure various physical properties of the oxide fuel. Among MAs, Am significantly influences oxygen potential ($\Delta GO_2$), which is an important physical property. $\Delta GO_2$ has a direct effect upon the oxidation or reduction of oxide fuel. The change in $\Delta GO_2$ causes a change in the oxygen-to-metal (U, Pu, MAs) ratio (O/M ratio) in oxide fuel. It is well known that such a change significantly affects the sintering and irradiation behavior of oxide fuels.

In this study, we evaluate the relationship between $\Delta GO_2$ and the O/M ratio in Am-bearing $PuO_2$ ($(Pu,Am)O_2$) using thermogravimetry and estimate the effect of Am content upon $\Delta GO_2$. The oxygen is released into the atmosphere from a specimen or absorbed into the specimen from the atmosphere as the $\Delta GO_2$ value of the atmosphere changes. Weight change by release or absorption was measured using thermogravimetry (Fig.7-9). By means of measuring the change in the specimen weight under various atmospheres and temperatures, the relationship between $\Delta GO_2$ and the O/M ratio was evaluated.

The measured $\Delta GO_2$ data are plotted against the O/M ratio, together with the literature data for $PuO_{2-x}$ (Fig.7-10). $\Delta GO_2$ increased along with the increase in temperature. In particular, the $\Delta GO_2$ value of $(Pu_{0.928}Am_{0.072})O_{2-x}$ markedly increased in the near-stoichiometriy (O/M = 2.00) region compared with that in $PuO_2$ at the same temperature. Am is known to be more reductive than Pu; therefore, the increase in $\Delta GO_2$ of $(Pu,Am)O_2$ in the near-stoichiometry region is considered to be caused by preferential reduction of Am.

We are going to conduct a test using Am-bearing MOX fuel to clarify the detailed mechanism by which Am affects $\Delta GO_2$.

**Reference**

Matsumoto, T. et al., Oxygen Potential Measurement of $(Pu_{0.928}Am_{0.072})O_{2-x}$ at High Temperatures, Journal of Nuclear Science and Technology, vol.52, issue 10, 2015, p.1296-1302.

# 7–6 Dating of Crush-Zone Slip Episodes under a Subsurface High-Temperature Condition

## — Insights from Thermal-History Analyses Based on the Fission-Track Dating Method —

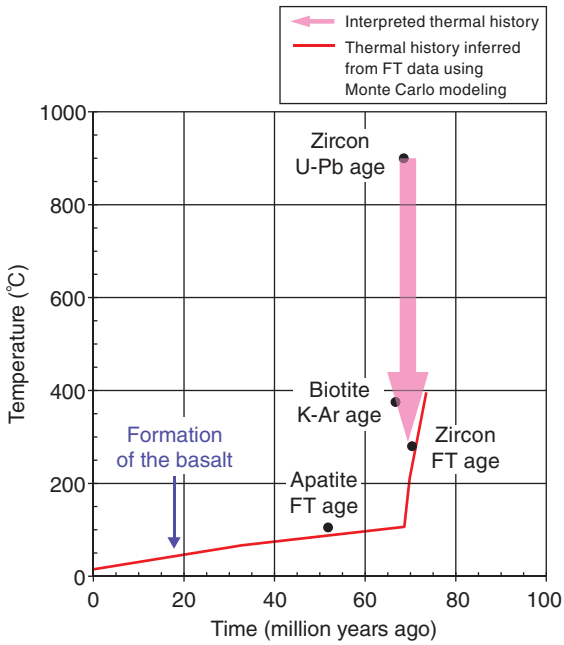


**Fig.7-11 Thermal history of granite in the Tsuruga region**
Radiometric ages are reset at a temperature higher than a characteristic value. This temperature depends upon the adopted dating method and target mineral. The thermal histories of rock samples can therefore be reconstructed using multiple dating methods and target minerals.

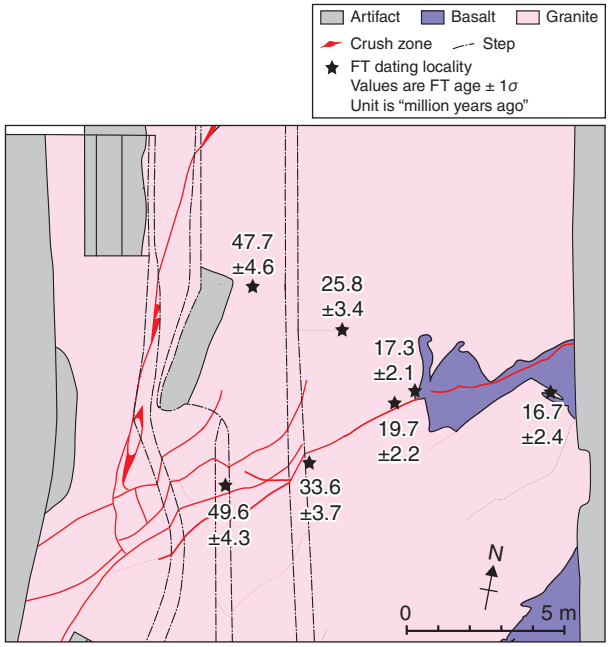


**Fig.7-12 FT ages around crush zones of the "MONJU" site**
A sketch of the crush zones at the "MONJU" site is shown. Although granite from this region generally produces an apatite FT age of ~50 million years, significantly younger ages were obtained around the crush zones. This observation can be explained by a thermal effect of the magmatic activity that formed the basalt 19 million years ago.

We have investigated the activity of crush zones distributed in and around the "MONJU"-prototype fast-breeder reactor site by following the guidelines and instructions of the Nuclear Regulation Authority (NRA), in order to assess the site's seismic safety. We here introduce an attempt to constrain the timing of slip episodes along the crush zones.

In general, the timing of slip episodes along crush zones is constrained by identifying deformation/displacement of the strata covering these zones and estimating the deposition ages of the strata. If the strata have been deformed/displaced in the last 120000–130000 years, the crush zones are regarded as active according to the guidelines of the NRA. This approach is, however, difficult to apply to areas where few strata are preserved owing to deposition and/or erosion conditions – in fact, this approach was not applicable to the "MONJU" site because the covering layers had been removed during construction.

In contrast, other informative structures were observed around the crush zones at the "MONJU" site – minerals called biotite occurring in granite were deformed plastically, indicating that the crush zones slipped at a high temperature of 200 °C or higher. Therefore, we attempted to constrain the timing of the slip episodes using a fission-track (FT) dating method. This method uses geochronometry based on counting of FTs, namely linear defects in mineral crystals formed by spontaneous fission of uranium-238. FTs are shortened and finally terminated by heating, resulting in apparently young FT ages. Theoretical models based on heating experiments and natural samples indicate that FTs shorten and cease more quickly when heated for a longer time and/or at a higher temperature. Then, time–temperature relationships, i.e., the thermal history of a rock sample, can be reconstructed by measuring the FT age and the lengths of the FTs.

The thermal history of granite from the Tsuruga region is shown in Fig.7-11. Granite of this region was formed 68 million years ago as a result of magma cooling. Fig.7-12 illustrates the spatial distribution of the apatite FT ages around the crush zones of the "MONJU" site. Although basalt formed 19 million years ago is distributed there, younger FT ages around the crush zones suggest a local reheating related to the magma activity that formed the basalt. Because the crush zones slipped at > 200 °C, they must have slipped 50–68 million years ago (before the granite cooled below 200 °C) and/or 19 million years ago (when the basalt was formed from magma). Consequently, these crush zones are interpreted as not being active.

We are conducting continuous investigations based on various methodologies and viewpoints to acquire a higher reliability and safety.

**Reference**

Sueoka, S., Shimada, K. et al., Cooling and Denudation History of the Tsuruga Body of Kōjaku Granite, Southwest Japan, Constrained from Multi-System Thermochronology, Chigaku Zasshi (Journal of Geography), vol.125, no.2, 2016, p.201-219 (in Japanese).

# 8 Research and Development Related to the Backend of the Nuclear Fuel Cycle and the Reprocessing of Spent Nuclear Fuel

## Progress in the Decommissioning of Nuclear Facilities and the Treatment and Disposal of Radioactive Waste

Safe and efficient decommissioning of our nuclear facilities and treatment and disposal of radioactive waste are important issues to consider in our research and development (R&D) activities. We are currently setting up systems to accomplish these goals and developing the related technologies (Fig.8-1). We will be responsible for disposing of radioactive waste generated not only from our research facilities but also from universities, industrial facilities, and other sites. We have also worked on the development of an automatic analysis system for Strontium-90 in environmental samples as a contribution to the decommissioning and radioactive-waste management of the TEPCO's Fukushima Daiichi NPS (1F). This research has already been related in Chapter 1, Topic 1-17.

### R&D for the Treatment and Disposal of Radioactive Waste

Storage drums of radioactive waste should record the origin of the waste (e.g., a "natural uranium system" or "recovered uranium"). It is necessary for us to identify the records to properly treat and dispose of radioactive waste with drums. On the contrary, the Ningyo-toge Environmental Engineering Center has developed a method for measuring the $\gamma$-ray spectrum over a short time, and using the characteristic $\gamma$-ray spectrum to identify the drums at the external surface (Topic 8-1).

It is important to "predict how nitrate ion leaches from solidified asphalt bodies" and to "prepare for processing technologies not to affect the disposal environment". Therefore, we researched the behavior of nitrate ions leaching from solidified asphalt bodies, and developed technology for removing these ions (Topic 8-2).

### Approach to the Disposal of Radioactive Waste

For disposal, radioactive waste must be prepared in accordance with certain technical standards. These standards aim to prevent scattering, ensure a homogenous radioactive-waste mortar, and avoid harmful voids in the drum. Therefore, a filling test was conducted focusing on the fluidity of the mortar (Topic 8-3).

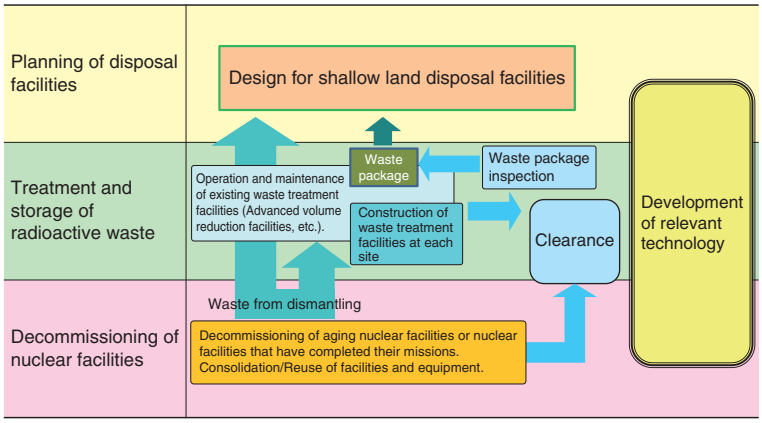


**Fig.8-1 Outline of measures toward the decommissioning of nuclear facilities and the treatment and disposal of radioactive waste**
We are establishing systems to decommission nuclear facilities and manage radioactive waste. In addition, we are developing related technologies (e.g., decommissioning, treatment, and disposal) and constructing radioactive-waste-treatment and -disposal facilities.

## R&D to Improve the Technology and Reliability of Geological Disposal in Japan

Geological disposal is an option for long-term isolation of high-level radioactive waste (HLW) produced during nuclear-power generation from human environments. This is a critical issue with which the present generation must sensibly deal, and it will remain crucial irrespective of any revision to national nuclear-energy policy. In Japan, spent fuel from power reactors is reprocessed to extract reusable uranium and plutonium for power generation. The liquids separated from the spent fuel during chemical reprocessing are solidified into a stable glass form. Under the Japanese disposal concept, vitrified wastes are then encapsulated in a thick steel overpack surrounded by highly compacted bentonite and placed in a stable geological environment at a depth of more than 300 m below the surface (Fig.8-2). Implementing geological disposal of HLW is a long-term project that will last over 100 years. The project begins with site selection and continues to repository construction and operation, which will be followed by backfill for repository closure. It is thus of great importance to proceed efficiently with the project as a national responsibility by continuously improving its sound technical basis and applying these attitudes to implementation, regulatory activities, and most importantly, enhancement of public confidence. To this end, we have made, and will continue to make, steady progress in R&D in various fields such as geoscience, repository engineering, and safety assessment to improve the technologies used for reliable geological disposal in Japan.

At present, our R&D focuses particularly on projects at two underground research laboratories (URLs)—one at

Mizunami, which researches crystalline rocks, and the other at Horonobe, which researches sedimentary formations (Fig.8-3). Multidisciplinary investigations are ongoing because the reliability of various investigative techniques should be tested and verified before the site-characterization program begins (Topics 8-4, 8-5, 8-6, and 8-7). In addition, studies on tectonics, volcanic and faulting activities, and the like are in progress to evaluate the long-term stability of geological environments in Japan (Topic 8-8).

The Toki Research Institute of Isotope Geology and Geochronology (TRIGGER) was established in November 2014 for the development of dating techniques using advanced equipment for isotope geology and geochronology. In parallel with such geoscientific efforts, we are conducting an extensive study to assess the performances of the disposal system, engineered barrier systems, and long-term chemistry and migration of radionuclides at Tokai to expand our knowledge base for geological disposal (Topics 8-9 and 8-10). These studies exploit data and information about geological environments that were obtained through geoscientific research at both URLs. The prototype knowledge-management system that was developed in 2010 is being improved to systematically provide and transfer multiple associated R&D results to both implementers and regulators and to ensure their safety. Furthermore, the results of the R&D activities have been summarized as an unconventional web-based report (CoolRep), which has been available on the Japan Atomic Energy Agency (JAEA)'s public website.

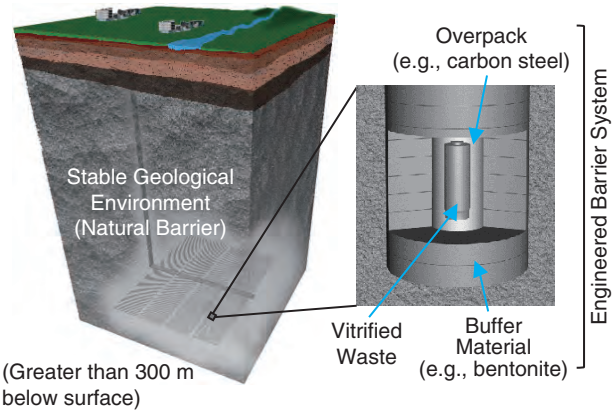


**Fig.8-2 Schematic view of the basic concept for the geological disposal of high-level radioactive waste in Japan**

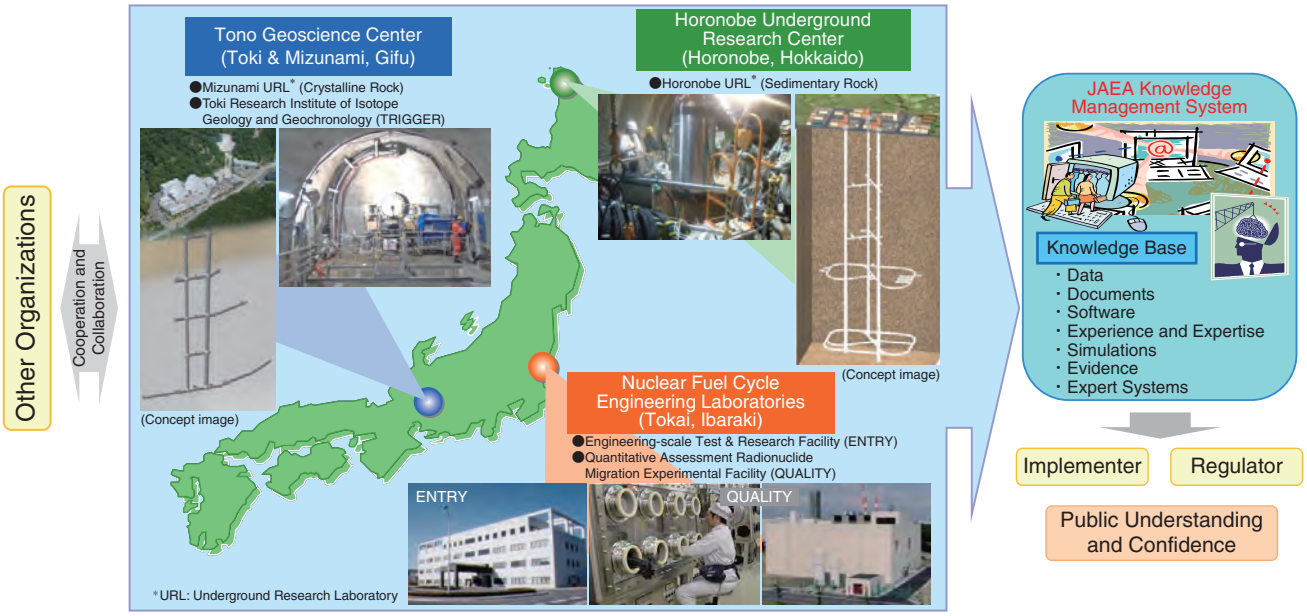


**Fig.8-3 System for implementing JAEA R&D activities**

## Implementing Safety Measures at the TRP and Enhancing Reprocessing Technologies

After the Great East Japan Earthquake and the accident at 1F, various emergency-safety measures were implemented at the Tokai Reprocessing Plant (TRP). To reduce the probability of hazards at the TRP, efforts have been focused on solidifying and stabilizing the highly active liquid waste (HALW) at the Tokai Vitrification Facility and the plutonium solution at the Plutonium Conversion Development Facility as soon as possible.

Vitrification of all the stored HALW is estimated to require two decades. Thus, an advanced glass melter is under development to make steady progress on the solidification and stabilization of HALW.

For low-level radioactive effluents, a cement-based solidification method accompanying a nitrate-ion decomposition process has been developed to reduce the environmental impact.

As an approach to the advancement of nuclear-fuel reprocessing technology, we measured the heating efficiency during the microwave-heating direct-denitration method, by which a microwave heats a mixture of uranyl nitrate and plutonium nitrate solution to form oxide powder for use in MOX fuel pellets. In this conversion process, the heating efficiency is very important for shortening processing time and improving energy-saving performance reducing power consumption. However, since there have not been reported cases about heating efficiency of MH method for detail, we have investigated the heating efficiencies were measured at the changing the kind of specimen and the specimen height. As a result, important knowledges to be used for new MH devise improvement in the future could be obtained (Topic 8-11).

# 8–1 The Rapid and Precise Large-Scale Classification of Waste Drums

## — Feasibility Study on the Application of Machine Learning to Large Datasets for Rapid Classification —

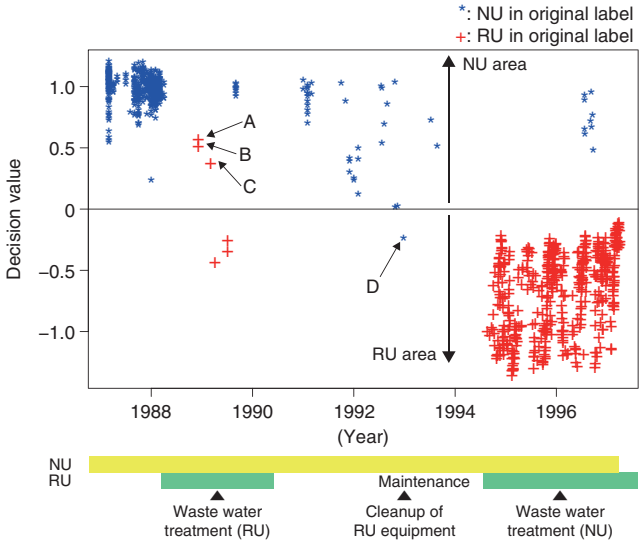


**Fig.8-4 Comparison between original labels and machine-learning-classification results**
The data in the upper and lower areas were classified as NU and RU, respectively. The classification results of data A–D were different from the original labels. The generated drums were depending on the operational periods.

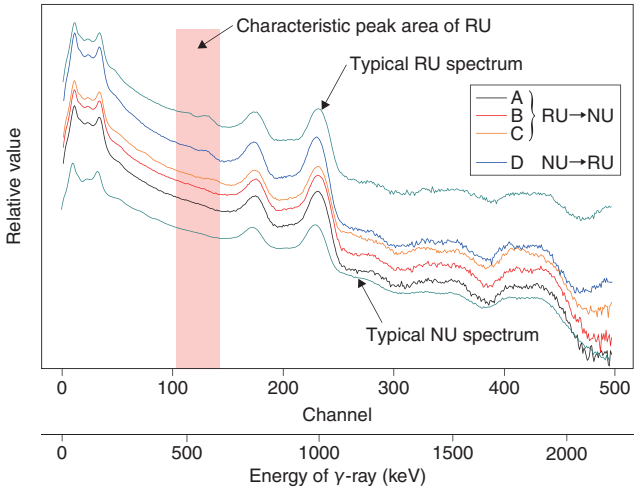


**Fig.8-5 Comparison of the typical γ-ray spectra for NU and RU with those of the four data classified differently from their original labels**
The spectra of A, B, and C have no characteristic peaks of RU, while that of D has characteristic peaks of RU. The original label of D was estimated to be incorrect.

Machine learning algorithms automatically extract and interpret the features of datasets to predict other datasets based on learning results. Pattern recognition, one of the machine-learning methods, chooses a class to which data should belong from classes ready beforehand. A feasibility study on the support vector machine (SVM) pattern-recognition method was performed to classify various waste drums based on low-resolution $\gamma$-ray spectral datasets that were obtained by non-destructive measurements.

The waste drums in the Ningyo-toge Environmental Engineering Center have been classified into two types according to their origins, namely natural uranium (NU) and reprocessed uranium (RU). Their compositions of radioactive nuclides differ depending on this origin. The $\gamma$-ray spectra of both NU and RU have energy peaks of 1001 keV and 766 keV caused by $^{238}$U progeny. In addition, those of RU have characteristic energy peaks of 238, 510, and 583 keV caused by $^{236}$U and $^{232}$U progeny.

In this study, the $\gamma$-ray spectra obtained from 967 drums with NaI scintillation detectors were investigated. The drums contain precipitation generated by wastewater treatment in the refining and conversion process to produce uranium hexafluoride ($UF_6$) from uranium ore or yellowcake. Their generation dates and origins, namely NU or RU, were traceable by the labels attached. 12 data from the dataset were chosen for "learning" about the correlation between the spectra and the labels. Another 955 drums were used for examination to classify into NU or RU by $\gamma$-ray spectra, and the examination itself took less than 1 sec. The results showed that 4 out of 955 data were different from their original labels. In Fig.8-4, a smaller decision value exhibited clearer the characteristic peaks of RU in the spectra, while a larger value showed vaguer characteristic peaks of RU. Considering the operation history, it was estimated that one of the named four data was mislabeled, whereas the others were misclassified by SVM (Fig.8-5).

These findings show that SVM is feasible for rapid classification of drums according to their uranium origin to an accuracy above 99%. It is a great advantage that SVM provides numerical indicators even in the boundary area of the classification. SVM is an effective method for supporting the classification of drums. Its application of classification to other classes should be studied further.

**Reference**

Hata, H., Ishimori, Y. et al., Application of Support Vector Machine to Rapid Classification of Uranium Waste Drums using Low-Resolution $\gamma$-Ray Spectra, Applied Radiation and Isotopes, vol.104, 2015, p.143-146.

# 8–2 Removal of Nitrate Salts from Bituminized Waste Products

## — Development of a Technology to Reduce the Impact of Nitrate Salts upon the Disposal Environment —

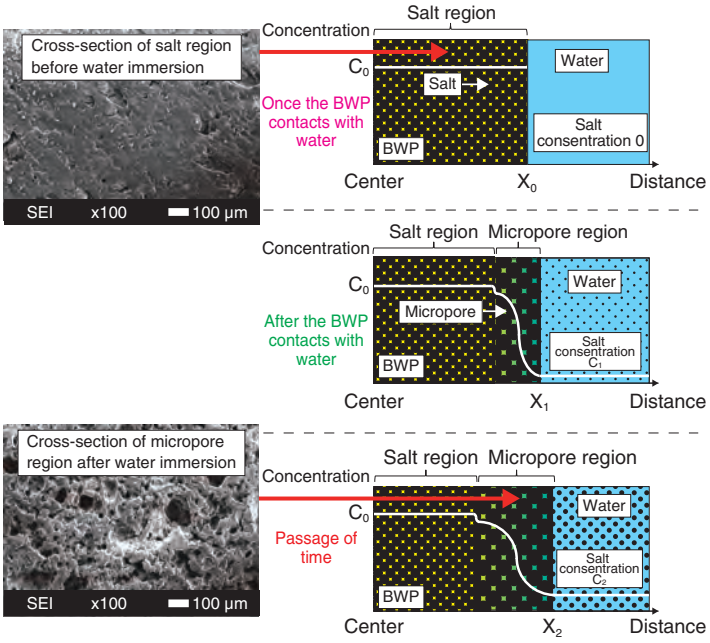


**Fig.8-6 Schematic images of the deformation and diffusion of a component in the BWP**
($C_i$, i = 0, 1, 2: salt concentration, $C_0 > C_2 > C_1 > 0$; $X_i$, i = 0, 1, 2: distance from the center of the BWP to the interface between the BWP and water in one direction, $X_2 > X_1 > X_0$).

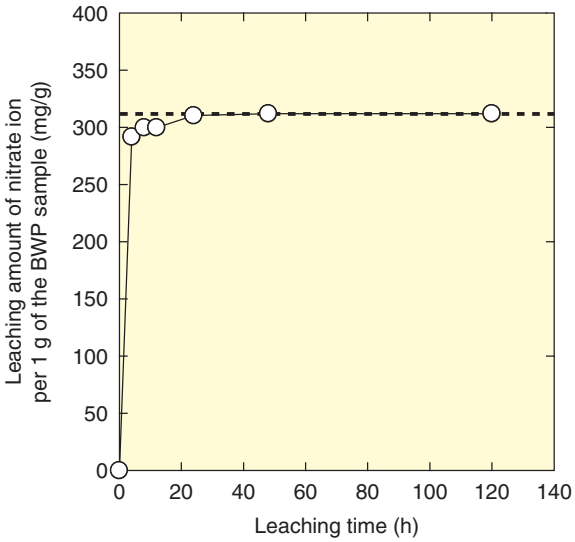


**Fig.8-7 Leaching behavior of nitrate ions**
We succeeded in removing approximately 100% (dotted line) of the nitrate ions from the fine-grinding BWP.

Low-level radioactive concentrate generated by the reprocessing of spent nuclear fuels was solidified as bituminized waste product (BWP) at the Tokai reprocessing plant from 1982 to 1997. Some of the Tokai BWPs were categorized as TRU wastes involving nitrate salts and will be co-disposed alongside high-level radioactive wastes (HLW) as low-level radioactive wastes suitable for geological disposal. If the BWP comes in contact with ground water after disposal, the reductive environment would change into an oxidative one through nitrate ion leaching from the BWP. This change is expected to result in corrosion of box-shaped waste containers for the BWP and of overpacking of co-disposed HLW. Hence, before disposal of the BWP, it is important to predict how nitrate ions will leach from the BWP and to prepare processing technologies to minimize their influence upon the disposal environment. We investigated the leaching behavior of nitrate ions in the BWP and developed a technique to remove them.

When the BWP comes into contact with water, water penetrates into it, dissolving soluble salts. Owing to this penetration, nitrate, nitrite, and sodium ions are leached out at the same rate. Thus, it was found that the BWP swelled by the water uptake and that micropores appeared by dissolution of the salts. This indicates that nitrate ions leached out according to diffusion in the BWP, swelling and forming micropores. Since the swelling of the BWP leads to make it longer for a distance from the center to the interface between the BWP and water, it can be predicted that the leaching rate of nitrate ions is delayed (Fig.8-6). In addition, under a restraint condition such as a disposal environment in which the BWP cannot expand, the swelling compresses the micropores near the surface of the BWP. It can also be predicted that the leaching rate of nitrate ions can be delayed by the compressing effect of the micropores.

As an application of this study, we synthesized bituminized waste samples involving nitrate salts and developed a technique to remove these salts from finely ground BWP samples (1–2 mm size) by water immersion (i.e., a water-leaching method). Our results showed that we could remove approximately 100% of the nitrate ions (310 mg/g) within 24 h (Fig.8-7). This technique can be used to convert BWP with 45wt% salt into de-nitrated BWP with 5wt% insoluble salt. Furthermore, if we apply compressing treatment to the de-nitrated BWPs, 16–20vol% of the BWP can be reduced on behalf of the volume of the nitrate salts occupied. Nitrate solution removed by this technique can be disposed of as a cementitious waste product after nitrate decomposition by a catalyzer.

On the basis of the above results, we expect that the developed technique may lead to a reduction in the disposal-environmental impact by nitrate salts.

**References**

Irisawa, K. et al., Effects of Salt Content on Leaching Properties of Synthetic Bituminized Wastes, Journal of Nuclear Science and Technology, vol.51, issue 3, 2014, p.323-331.

Irisawa, K. et al., Development of Denitration Technique for MA-Type Bituminized Waste Product by Aqueous Leaching Method, JAEA-Technology 2015-008, 2015, 28p. (in Japanese).

# 8–3 Toward Radioactive-Waste Conditioning Suitable for Near-Surface Disposal
## — Study on Standards Concerning a Solidification Method by using Mortar —

(a) Composition

| Kind of shape | Kind of waste | Weight ratio |
|---|---|---|
| Waste which is easily filled with mortar | Metal plate | 20% |
| | Metal piece | 20% |
| | Cable | 4% |
| Waste which is difficult to fill with mortar | Pipe | 45% |
| | Valve | 10% |
| | Meter | 1% |

(b) The voidage ratio after solidification

| P-funnel test time | Top voids | Inner voids (solidified) | Inner voids (drum) |
|---|---|---|---|
| 20 s | 19.6% | 3% | 23% |
| 30 s | 19.3% | 4% | 24% |
| 40 s | 19.8% | 4% | 24% |
| 50 s | 19.8% | 2% | 22% |


**Fig.8-8 Composition of Simulated waste, (a) as filled with mortar and the voidage ratio after solidification (b)**
The simulated wastes were placed in a 200-ℓ drum, which was then filled with mortar. The voidage ratio in this drum was then evaluated after solidification.


**Fig.8-9 A vertical cross-sectional view of the simulated waste**
The vertical cross-section of the waste sample was investigated by visual inspection.

We are planning for the disposal of radioactive wastes generated from research, industrial, and medical facilities. Before the radioactive waste is disposed of, it should be conditioned so as to meet technical standards. One technical standard is that radioactive waste should be solidified and stored in a container in which no harmful voids remain after filling. This is intended to prevent scattering of radioactive waste and the collapse of disposal facilities after backfilling with soil.

Solidification methods that ensure that wastes are immobilized in 200-ℓ drums within cementitious matrices and no harmful voids after filling are studied. Our aim is to confirm the adequacy of our solidification methods for conservative “simulated wastes” containing more valves and pipes (which are difficult to fill and likely to be left with voids) than actual waste.

The fluidity of mortar is important. Mortar’s viscosity decreases significantly in proportion to its water content, increasing the likelihood that the voids between wastes in the 200-ℓ drum will be filled. However, the effect of such inviscid mortar may cause faults after curing. In contrast, a strength gain readily occurs when the amount of water contained is small but the voids between wastes become difficult to fill with mortar.

The indicator of the fluidity is the test result of the P-type funnel method, expressed as the time at which a given mixture flows down under the funnel. Four types of fluid cement–water mixtures with fluidities of 20, 30, 40, and 50 s are prepared. The mix loses fluidity with increasing time.

Simulated waste packages were produced by placing the waste materials in 200-ℓ drums, which were then filled with mortar of the mix proportions at a general injection speed of 30 ℓ/min, followed by curing. The void ratios within these waste packages were less than the limit of 30vol% (Fig.8-8), equivalent to the assumed average void ratios in the installation ground of our disposal facilities. For this reason, it is considered not to be harmful.

The vertical cross-sectional view of the waste packages demonstrated that the wastes and mortar were in close contact with the inner walls of the 200-ℓ drums, as shown in Fig.8-9. For this reason, wastes are considered to be immobilized within a cementitious matrix and to exist in an un-scattered state.

From these results, an appropriate solidification method corresponding to the technical standards of waste-disposal confirmation were demonstrated under the condition that waste materials were placed in a 200-ℓ drum and filled with mortar in a controlled manner regarding the injection speed and fluidity described above.

On the basis of this result, this solidification method serves as a reference when manufacturing waste packages from research, industrial, and medical facilities.

**Reference**

Nakata, H. et al., Waste Acceptance Criteria for Waste Packages Destined for Near Surface Disposal Containing Radioactive Waste from Research, Industrial and Medical Facilities, JAEA-Technology 2016-001, 2016, 112p. (in Japanese).

# 8–4 Influence of Distant Earthquakes upon Groundwater Flow
## — A Case Study in the Tono Area —

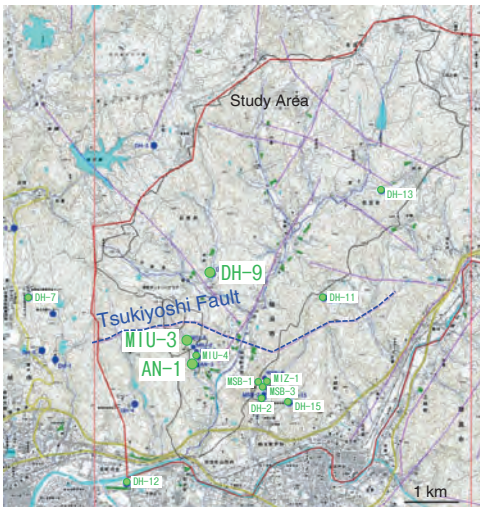


1:25000 digital map (Geographical Survey Institute September 1, 2000 publication) made by “Mitake”, “Takenami”, “Toki”, and “Mizunami”

**Fig.8-10 Locations of the study area and monitoring boreholes**
Groundwater-pressure monitoring has been conducted in boreholes with depths ranging from several meters to approximately 1000 m in the study area. This study uses monitoring data from the DH-9, MIU-3, and AN-1 Boreholes.

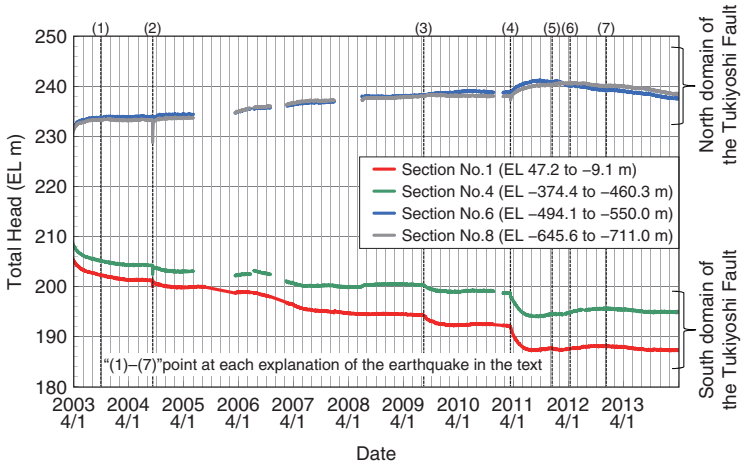


**Fig.8-11 Example of groundwater-pressure change by an Earthquake (MIU-3 borehole)**
This figure shows the monitoring results in the MIU-3 Borehole. The borehole intersects the Tsukiyoshi Fault at a depth of 700 m. Groundwater pressure in the southern part of the fault is monitored in sections No.1 and No.4. Groundwater pressure in the northern part of the fault is monitored in sections No.6 and No.8. At the south of the fault, the groundwater pressure decreased after earthquakes. In contrast, at the north of the fault, the groundwater pressure increased following earthquakes.

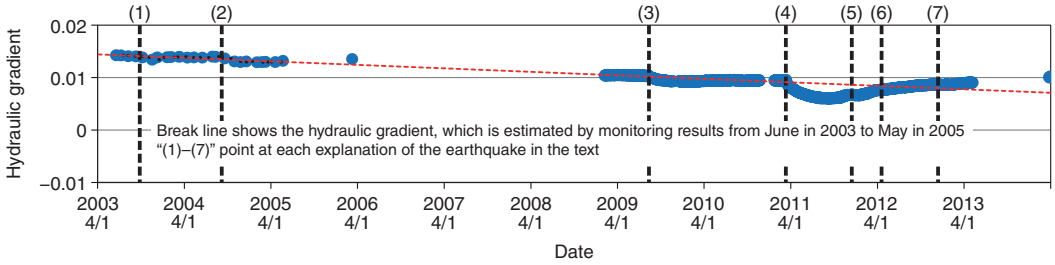


**Fig.8-12 Example of hydraulic-gradient change by an earthquake (between the DH-9 and MIU-3 Boreholes)**
This figure shows the change in the hydraulic gradient after earthquakes. After earthquakes with magnitudes of 7 to 8 (shown as (1) – (3) in the figure), the hydraulic gradient temporarily changed and was then restored with time before the earthquake. On the other hand, after the magnitude-9 earthquake (4), the hydraulic gradient changed but was not restored before the earthquake. The change in the hydraulic gradient during earthquake (5), whose epicenter is close to the study area, did not recover before the earthquake, too.

For geological disposal for high-level radioactive waste, evaluating the groundwater-flow condition is important. Therefore, evaluating the groundwater-pressure change is necessary because this distribution and its change help to control groundwater flow. Long-term groundwater-pressure monitoring has been conducted in our field of study (Fig.8-10), and it was found that groundwater-pressure changes as a result of earthquakes. The earthquakes that changed pressure include (1) the Tokachi-oki earthquake of 2003, (2) the earthquake off the coast of Kii Peninsula in 2004, (3) the Suruga Bay earthquake in 2009, (4) the 2011 earthquake off the Pacific coast of Tohoku, (5) the earthquake in the east of Mino in 2011, (6) the earthquake on the west coast of northern Sumatra in 2012, and (7) the earthquake off the Sanriku coast in 2012. Groundwater-pressure changes after each earthquake differed in each monitoring section. However, the changes all occurred in the same direction (increase or decrease) over the same monitoring section (Fig.8-11).

The change in hydraulic gradient differs depending on the magnitude or the distance between the epicenter and the monitoring point for each earthquake (Fig.8-12). Therefore, we will continue long-term groundwater-pressure monitoring to confirm changes in the hydraulic gradient.

These results show that it is important to focus on not only the change in groundwater pressure but also that in the hydraulic gradient in evaluating the long-term stability of the groundwater-flow condition.

**Reference**

Takeuchi, R. et al., Influence on Groundwater Flow Conditions by Groundwater Pressure Change Induced by Earthquakes: Case Study of Tono Area, Genshiryoku Bakkuendo Kenkyu (Journal of Nuclear Fuel Cycle and Environment), vol.22, no.2, 2015, p.37-52 (in Japanese).

# 8–5 Estimation of Underground Density Structure

## — Development of a Technique to Estimate Underground Density Structure using Cosmic-Ray Muons —

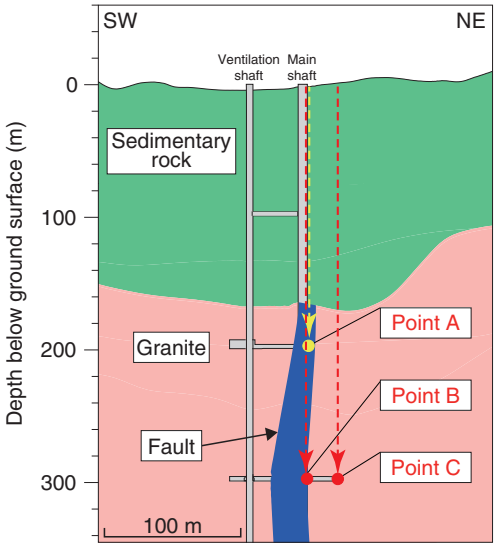


**Fig.8-13 Geological model (cross-section) showing the distribution of rock units and geological structures in the Mizunami Underground Research Laboratory with measurement points for cosmic-ray muons**
We measured upwards-directed cosmic-ray muons at each measurement point.


**Fig.8-14 Photograph of the experimental-muon telescope**
The telescope is equipped with two plastic scintillators 35 cm in diameter and 3 cm thick to detect simultaneous transmission of muons.

**Table 8-1 Measurement results at points A, B, and C**
Surface density indicates the weight per unit area. The densities of sedimentary rock, granite, and fault are based on the calculated surface densities and transmission distances of muons in each geological unit, which in turn coincide with the thicknesses of sedimentary rock, granite, and fault, respectively.

| Point | Location | Target rock | Measurement period | Muon count | Surface density (hg/cm$^2$) | Average density (g/cm$^3$) |
|---|---|---|---|---|---|---|
| A | G.L. –200 m | Sedimentary rock & fault | 55 | 1485 | 430.95 | 2.15 |
| B | G.L. –300 m | Sedimentary rock & fault | 173 | 1281 | 720.42 | 2.4 |
| C | G.L. –300 m | Sedimentary rock & granite | 135 | 773 | 788.05 | 2.63 |

Muons are elementary particles; although they are highly transmittable through materials, the number of transmittable muons decreases in proportion to material density and transmission distance. Thus, muons have been widely utilized to estimate internal structures such as those of active volcanos and the TEPCO's Fukushima Daiichi NPS.

To assess the safety of geological disposal of highly radioactive waste, the distribution of major geological structures such as fault needs to be confirmed. Three rock units—granite, fault, and sedimentary rock—are distributed in the Mizunami Underground Research Laboratory (Fig.8-13). We examined whether we could estimate the densities of these three rock units by means of muon measurements.

Muons were measured at three points, considering the fault distribution (Fig.8-13) with a muon telescope shown in Fig.8-14. The telescope was equipped with two plastic scintillators. We counted the simultaneous transmission of muons with two scintillators (Table 8-1) and calculated the surface densities from the muon counts and transmission distances of each measurement point based on an equation obtained from previous literature (Table 8-1).

The surface density indicates weight per unit area. The weight is the sum of the products of the density and thickness of each rock unit (for example, the weight at measurement point A is sum of the product of density and thickness of the sedimentary rock and fault). Because the thickness of each rock unit was are already known (Fig.8-13), the densities of these units can be calculated by the surface densities of the three measurement points. Consequently, we obtained densities of 3.38 g/cm$^3$ for granite, 2.88 g/cm$^3$ for fault, and 1.99 g/cm$^3$ for sedimentary rock, respectively.

The obtained densities are much higher than the previously measured values. The estimated density of granite obtained by muon observation is approximately 30% larger than the previously measured density (c. 2.6 g/cm$^3$). If the density of granite is assumed to be 2.6 g/cm$^3$, then the re-calculated densities of fault and sedimentary rock are 2.2 and 1.5 g/cm$^3$, respectively. The calculated densities accord with the previously measured densities.

We concluded that cosmic-ray muons have a high potential for detecting geological structures with different densities by confirming the ratio of the densities amongst the three rock units, although it is not clear why the density values obtained were obviously higher than previously obtained values. We expect muons to be applicable to the investigation of geological structures such as fault in the future.

**Reference**

Sasao, E. et al., Geological Investigations using Cosmic Ray Muons: A Trial to Detect Fault at the Mizunami Underground Research Laboratory, Proceedings of 12th SEGJ International Symposium, Tokyo, Japan, 2015, 4p., in USB Flash Drive.

# 8–6 Time History of Hydraulic Diffusivity Related to URL Excavation

## — A Poroelastic Analysis of Groundwater-Pressure Response to Atmospheric Loading —

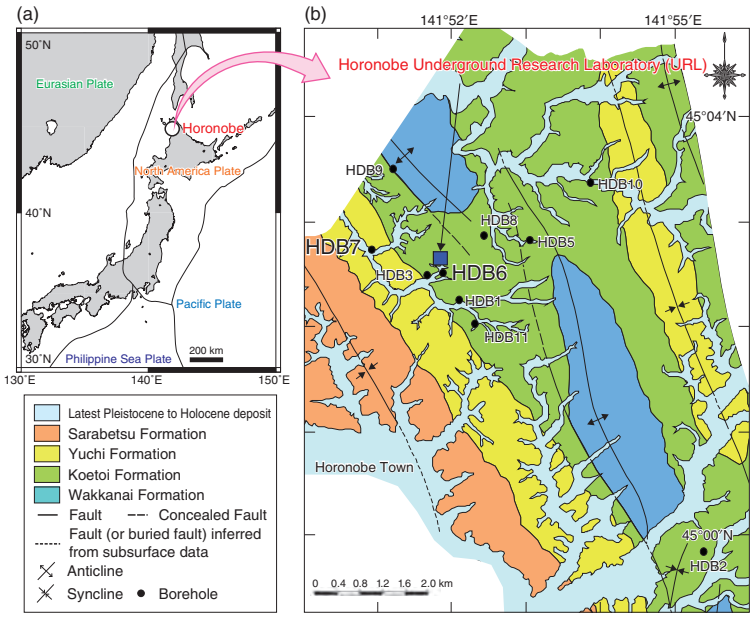


**Fig.8-15 Maps showing the location of the Horonobe URL site and boreholes (a) location map and (b) geological map**

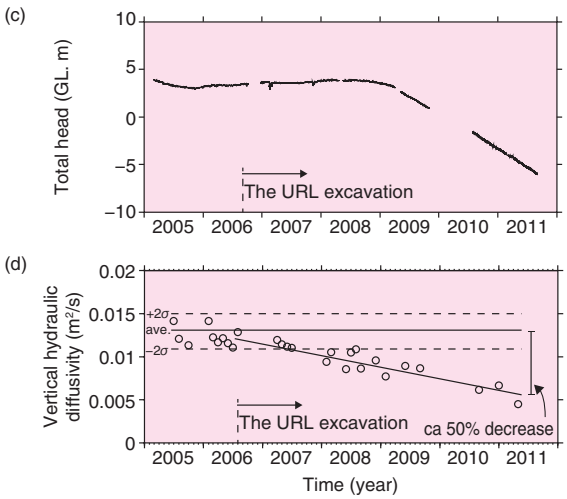


**Fig.8-16 (c) Total head and (d) time history of vertical hydraulic diffusivity**

(c) Total head = (pore pressure × density of groundwater/gravity acceleration) + sensor depth. (d) The horizontal solid line and broken lines indicate averages and two standard deviations of the vertical hydraulic diffusivity obtained before August 2006 (before the URL excavation).

In the development of an underground research laboratory (URL), significant groundwater drain induced by excavation leads to decreases in groundwater pressure at the URL site. A possible reduction in the porosity of sedimentary rock owing to groundwater drainage is predicted during the excavation and operation of the URL, leading to permeability reduction. Although these changes are reversible processes, the observation of a porosity reduction has not yet been reported. In assessing the safety of geological disposal of HLW, rock permeability is an important factor when considering the migration of nuclides from the waste with groundwater flow. Research on permeability change and recovery will be helpful for future operations. In this report, a groundwater-pressure record observed at a point approximately 130 m distant from a URL was analyzed and a permeability-change history was obtained.

The Horonobe URL is located in northern Hokkaido (Fig.8-15(a)) in an area covered by thick sedimentary formations (Sarabetsu, Yuchi, Koetoi, and Wakkanai formations in Fig.8-15(b)). Among the groundwater-pressure records at several boreholes (HDB1 to HDB11), the permeability-change history of HDB6 is presented in this report.

The groundwater level in a confined well generally falls in response to an increase of the atmospheric pressure, and vice versa. The responses of groundwater (whether quick or slow and large or small) are related to the hydraulic properties of formations, which can be handled mathematically using a poroelastic theory that assumes that rock comprises porous and elastic material such as hard rubber with numerous openings filled with groundwater. Rock permeability can be obtained by analyzing the atmospheric response of groundwater pressure with the poroelastic theory.

In the analysis, monitoring records observed during the seven-year period from 2005 to 2011 (Fig.8-16(c)) were used. Long-term data obtained through continual observations for three months were used for the calculation as a single set, which provides the permeability-change history.

The results are shown in Fig.8-16(d). Hydraulic diffusivity, which is one of the parameters of rock permeability and proportional to the propagation rate of groundwater-pressure change in a rock mass, was approximately $(1.2 \pm 0.2) \times 10^{-2}$ m²/s before URL excavation (before August 2006), whereas it decreased gradually from 2007–2008. Finally, it dropped to approximately $(0.6 \pm 0.2) \times 10^{-2}$ m²/s in May 2011.

According to a published study, the permeability in mudstone generally fluctuates by more than two orders of magnitude. The reason for this fluctuation is that conventional hydraulic testing is affected by local fractures whose occurrences differ by location even in the same rock. The small decrease of approximately 50% is significant because it was obtained continuously at the same point, a situation that is different from that of a conventional hydraulic test.

This study revealed that the groundwater flow was reduced by the pressure decrease associated with URL excavation, although this influence is limited. Because the operational period of the HLW geological-disposal site will be several decades in the future, this investigation yields important suggestions for considering long-term groundwater flow.

**Reference**

Miyakawa, K. et al., Seven-Year History of Vertical Hydraulic Diffusivity Related to Excavation around an Underground Facility, International Journal of Rock Mechanics and Mining Sciences, vol.70, 2014, p.332-342.

# 8–7 Technology for Long-Term Monitoring of Damage around a Shaft
## — Monitoring the Excavation-Damaged Zone using Optical-Fiber Sensors —

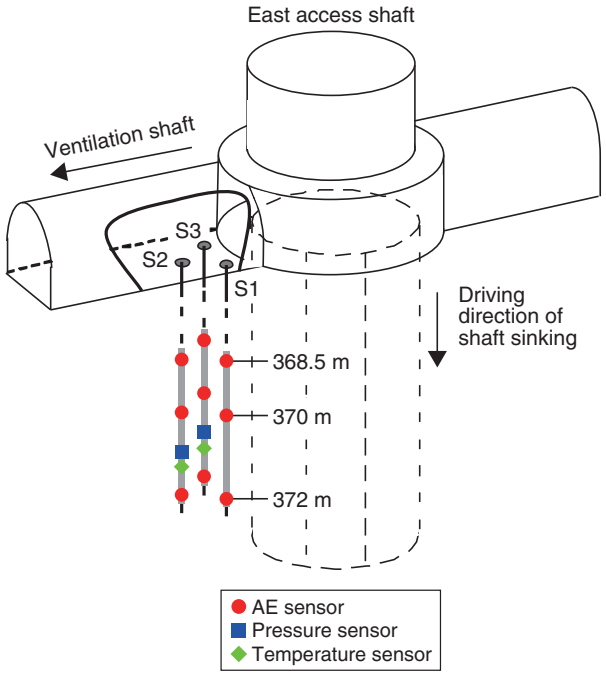


**Fig.8-17 Layout of the sensors**
The layout of the sensors installed around the wall of the east access shaft at a depth of approximately 370 m is indicated in this figure. S1 to S3 in the figure indicate the boreholes for installation of the optical-fiber sensors. AE stands for acoustic emission, which is the micro seismicity emitted when a crack is induced in a rock mass.

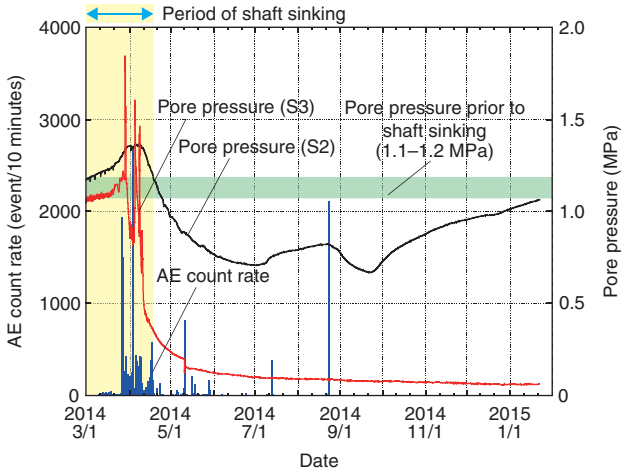


**Fig.8-18 AE count rate and pore pressure with elapsed time**
The yellow hatched zone in the graph indicates the period of shaft sinking, and the green hatched zone indicates the range of pore pressure prior to shaft sinking.

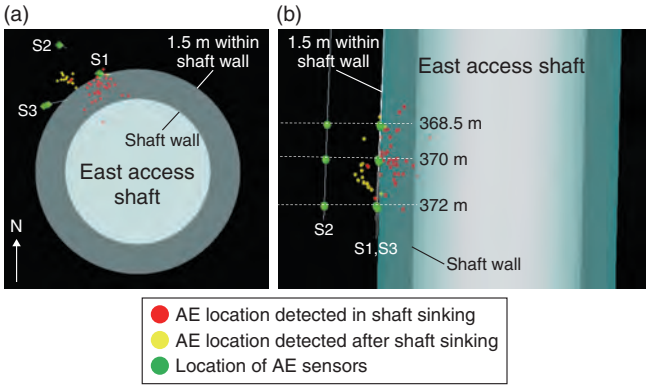


**Fig.8-19 Three-dimensional distribution of AE sources**
(a) shows a horizontal view of the shaft, and (b) shows a vertical view.

In the geological disposal of high-level radioactive waste, shafts, and spiral tunnels will be constructed as access galleries. During excavation, fractures will be induced around the wall of the gallery, owing to stress redistribution and the impact of excavation. This damage can act as a migration pathway for radionuclides to the surface. Therefore, we should investigate the characteristics of the damage around a shaft wall. However, this subject has yet to be studied in detail.

In the Horonobe URL, we developed optical sensors capable of detecting acoustic emission (AE), pore pressure, and temperature; we then inserted them into the boreholes excavated around the east access shaft (Fig.8-17).

Fig.8-18 indicates the AE count rate over 10 min and the pore pressure as functions of elapsed time. In the period of shaft sinking, AE events are drastically increased. The pore pressure in the borehole S3, which was drilled 1.5 m from the shaft wall, both increased and decreased drastically during the shaft sinking. After the sinking, a small AE count rate was observed. The pore pressure of borehole S3 decreased to almost 0 MPa; in contrast, the pore pressure of borehole S2, which was drilled 4.0 m from the shaft wall, decreased to 0.7 MPa, before increasing to its pre-excavation value (1.1 to 1.2 MPa), as indicated in the green hatched zone in Fig.8-18. Fig.8-19 shows the three-dimensional distribution of the AE sources. AE sources are concentrated within 1.5 m of the shaft wall during the period of shaft sinking, and then the distribution spreads out.

In the future, we will construct a long-term conceptual model of the excavation-damaged zone on the basis of long-term monitoring of AE and pore pressure.

**Reference**

Hata, K., Aoyagi, K. et al., Evaluation of EDZ (Excavated Damage Zone) by Multi-Optical Measurement Probe in Horonobe Underground Research Center, Proceedings of 44th Symposium on Rock Mechanics, Fukuoka, Japan, 2016, p.319-324 (in Japanese), in CD-ROM.

# 8–8 Powerful Tools for Dating of Sediments

## — Development of High-Accuracy Analysis for Volcanic Glass Shards —

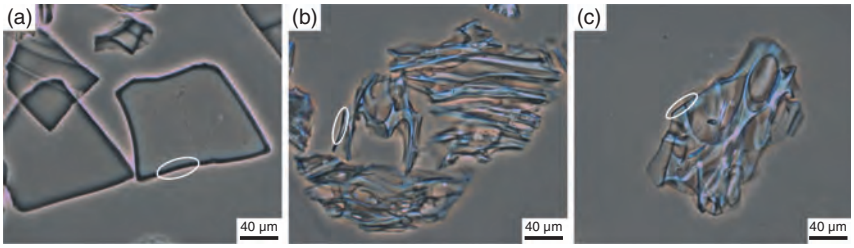


**Fig.8-20 Photomicrographs of volcanic glass shards**
(a) Glass shards from the Kikai Caldera eruption (7300 years ago), (b) glass shards from the Bunmei eruption (1471–1476 AD) of the Sakurajima volcano, (c) glass shards from pumice deposits in the Miyazaki Plain. The thickness of the hydration layer (the dark gray layer along the margin of the glass shard, shown by hollow circles) is greater in (a) than in (b) and (c). The shape of the glass shard and the thickness of the hydration layer is similar between (b) and (c).

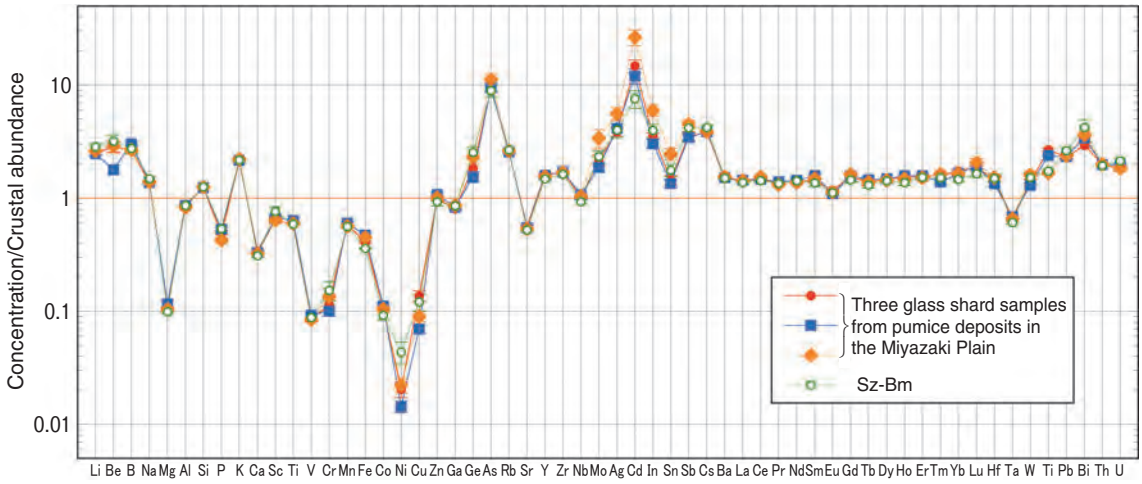


**Fig.8-21 Average values of elemental concentrations of volcanic glass shards normalized by crustal abundance**
Most elemental concentrations are similar between the three glass-shard samples obtained from the pumice deposits in the Miyazaki Plain and the Bunmei-eruption origin near the Sakurajima volcano (Sz-Bm).

Dating of sediments is often essential for determining the ages of events such as earthquakes and volcanic eruptions. One method for dating of sediments is based upon determining the origin of tephra (volcanic products such as glass shards and pumices) in sediments. In Japan, age determination using tephra is a powerful tool for dating of sediments because the Japanese Islands have many volcanos and the ages of the eruptions with widespread depositions of tephra several hundred thousand years ago or more recently are mostly well known.

In general, the origin of tephra can be determined based on the mineral composition and shape, refractive index, and chemical composition of the volcanic glass shards. However, discrimination of tephra from eruptions with different ages but from the same volcano is difficult using only conventional analytical methods.

We succeeded in discrimination of tephra from eruptions during the Bunmei, Anei, and Taisho Periods from the Sakurajima volcano, Kagoshima Prefecture, using highly developed measurements of refractive index and chemical compositions for volcanic glass shards. The methods developed in this study are applicable for identification of the unknown tephra found in an area far away from Sakurajima volcano.

The refractive index of a volcanic glass shard has a unique range value depending on its volcano of origin and its age of eruption. However, the range value differs even between hydrated and non-hydrated parts of the same glass shard. In this study, the refractive indices of hydrated and non-hydrated parts within each individual glass shard were measured separately. The thickness of the hydrated part increased along with elapsed time after the deposition (Fig.8-20). Thus, the depositional age of volcanic glass shards can be estimated from the thickness of their hydration layers. These in-depth analyses contribute to improving the accuracy of glass shard identification based on refractive indices.

In addition, multielemental simultaneous analysis of the chemical composition of volcanic glass shards was done using a femtosecond-laser-ablation inductively-coupled-plasma mass-spectrometry technique (Fig.8-21). Elemental concentrations of volcanic glass shards also had unique range values for different volcanos and different ages of eruption. We built a methodology to apply statistical analysis to the multiple elemental-concentration values for determination of the origin of tephra.

These advanced analyses for the refractive indices and chemical compositions of volcanic glass shards were applied to pumice deposits on the Miyazaki Plain. We also performed radiocarbon dating of the coaly materials in the deposits using accelerator mass spectrometry at the Toki Research Institute of Isotope Geology and Geochronology. On the basis of these analyses, we revealed that the pumice was derived from the Bunmei eruption of the Sakurajima volcano.

**Reference**

Ikuta, M., Niwa, M. et al., Identification of Pumice Derived from Historic Eruption in the Same Volcano: Case Study for the Sakurajima-Bunmei Tephra in the Miyazaki Plain, Chishitsugaku Zasshi (Journal of the Geological Society of Japan), vol.122, no.3, 2016, p.89-107 (in Japanese).

# 8–9 Assessment of the Effect of Geological Disposal upon Human Beings

## — Development of a Modeling Method for Biosphere Assessment Corresponding to Surface-Environmental Condition —

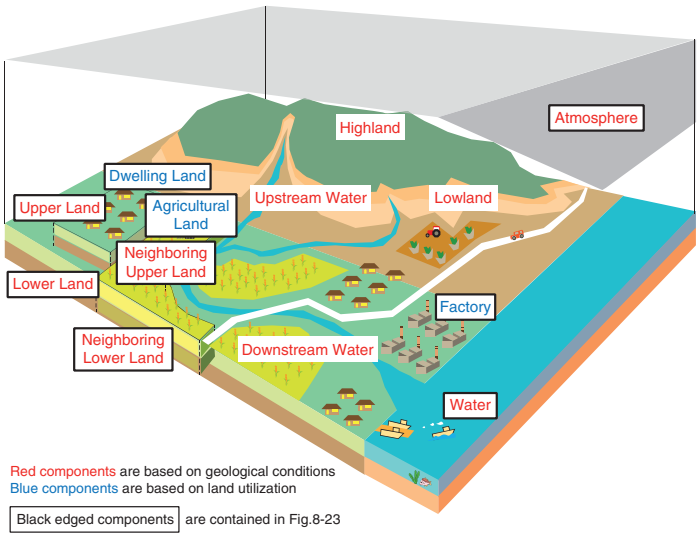


**Fig.8-22 An example of the components of the surface environment**
For biosphere assessment, components of the surface environment, mass-transport processes between those components, and exposure pathways from those components are modeled to assess the effect on human beings. The components are primarily set corresponding to geographical conditions and land utilization by human activities.

(a)

| | A | B | C | D |
|---|---|---|---|---|
| 1 | Upper Land | Infiltration and Recharge Bioturbation Diffusion Deposition | Movement of Soil Movement of Surface Water Diffusion Bioturbation | |
| 2 | Erosion and Weathering Diffusion Capillary Rise Bioturbation | Lower Land | | Diffusion Bioturbation Movement of Underground Water |
| 3 | Movement of Soil Movement of Surface Water Diffusion Bioturbation | | Neighboring Upper Land | Infiltration and Recharge Bioturbation Diffusion Deposition |
| 4 | | Diffusion Bioturbation Movement of Underground Water | Erosion and Weathering Diffusion Capillary Rise Bioturbation | Neighboring Lower Land |

(b)

| | A | B | C | D | E | F |
|---|---|---|---|---|---|---|
| 1 | Other Matrix | - | Shipping (Agricultural Chemicals, Fertilizer) | - | - | - |
| 2 | - | Atomosphere | - | - | - | - |
| 3 | Shipping (Thinning Wood) | Volatilization (From Submerged Paddy Field, etc.) | Agricultural Land | Shipping (Crops) | Outflow (Excessive Fertilizer) | Shipping (Crops) |
| 4 | Shipping (Fertilizer, Fodder) | - | Shipping (Fertilizer) | Factory | - | Shipping (Food, Oil, Laxuary Grocery Items, Paper, Clothes, etc.) |
| 5 | - | - | Water Intake (Irrigation) | - | Water | - |
| 6 | - | - | Shipping (Fertilizer) | - | - | Dwelling Land |

**Fig.8-23 Examples of the arrangement of mass-transport processes between components in the form of a "basic matrix"**
A basic matrix presents the components of the surface environment as diagonal elements and mass-transport processes between the components as non-diagonal elements. The upper matrix is an example of a "basic matrix" showing mass-transport processes by natural phenomena (a), and the lower matrix is an example of a basic matrix showing mass-transport processes by human activities (b).

In assessing the safety of geological disposal of radioactive wastes, exposure doses in the surface environment where humans live (known as the biosphere) are modeled and assessed. For this purpose, the transport processes of radionuclides derived from the repository as well as human-exposure processes in the surface environment are set based on the targeted surface-environmental conditions.

The surface-environmental conditions to be targeted have not yet been decided in Japan; thus, it is important to prepare a modeling method for biosphere assessment that can respond to disposal-site candidates flexibly when these are realized in the future. For this purpose, a modeling method that can be applied to various surface-environmental conditions is developed in this study.

A special feature of the modeling method proposed in this study is that mass-transport processes (e.g., movement of water or soil, and transport of radionuclides from the repository accompanying those movements) and exposure processes (e.g., drinking water containing radionuclides) are compiled widely for various surface-environmental conditions in a matrix-form (this is called a basic matrix). This makes it possible to construct biosphere-assessment models easily by simply abstracting transport and exposure processes from existing basic matrices, which are related to the surface-environmental conditions to be assessed. In compiling the basic matrix, first, generic components of various surface environments (e.g., upper land, water, and agricultural land shown in Fig.8-22) and their positional relations (e.g., horizontal, vertical, etc.) are identified. Then, transport processes between those components owing to natural phenomena in response to geographical conditions are compiled in 17 basic matrices (Fig.8-23(a) shows an example of this type of basic matrix) and transport processes between components owing to human activities in response to land utilization are compiled into 8 basic matrices (Fig.8-23(b) shows an example of this type of basic matrix). The exposure processes from those components are also compiled, with consideration of human activities in each component.

This method may help to construct an effective biosphere-assessment model and make it easy to check the consistency (or lack thereof) among the components and processes being considered. This method could also reduce the dependency of the modelling sufficiency based on the modelers' knowledge and experience by commonly using basic matrices. Another advantage of this method is the traceability of modeling processes (just record the results of abstraction of components and processes from existing basic matrices and note those reasons); therefore, past biosphere-assessment models can be efficiently reviewed and/or reassessed in the future.

The applicability of this method will be examined under various surface-environmental conditions and, if needed, further improvements will be made.

**Reference**

Nagao, F. et al., Development of the Method of Biosphere Modeling According to Surface Environmental Conditions, JAEA-Research 2016-003, 2016, 80p. (in Japanese).

# 8–10 Various Parameter Settings upon Radionuclide Release

## — Review of the Release Behavior of Radionuclides for Spent-Fuel Disposal —

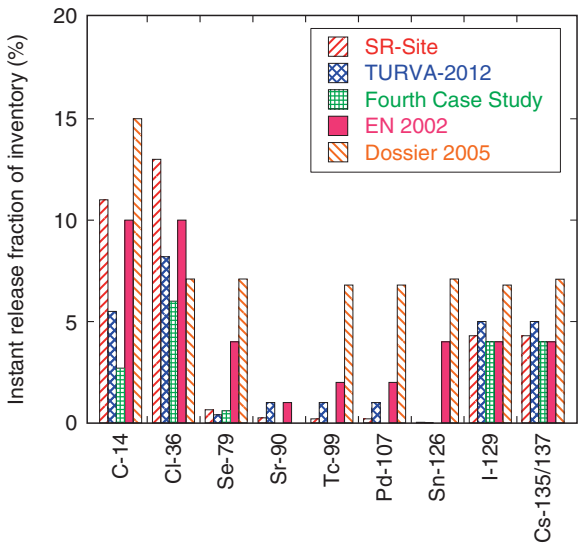


**Fig.8-24 Example of the instant-release fraction (IRF) of inventory for PWR-$UO_2$ fuels in various safety-assessment reports**

IRF denotes the ratio between instantly released inventories and total inventories. There is a consensus as to the selection of radionuclides (RNs) that are instantly released but the selected IRF values vary among safety-assessment reports. This is owing to various properties of spent nuclear fuel such as reactor type, fuel type, and burnup.

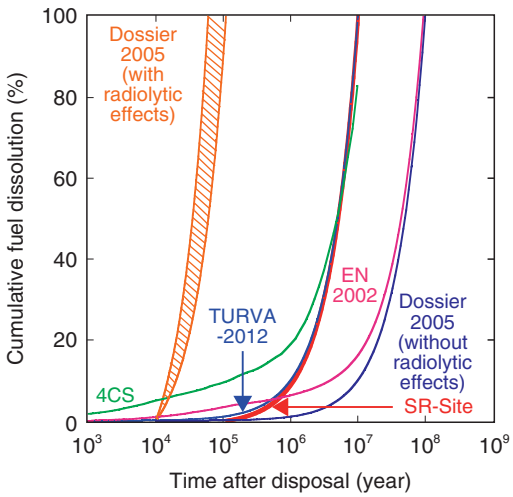


**Fig.8-25 Cumulative fuel dissolution as a function of time after disposal calculated with the fuel-dissolution rate selected in safety-assessment reports (reprint of Kitamura et al. (2016) with permission of the Atomic Energy Society of Japan)**

Spent fuel dissolves early when the dissolution rate is large. It is observed that curves using the latest values (selected from the SR-Site, TURVA-2012, and 4CS) are relatively similar to each other while other curves are scattered.

We have conducted research and development on the disposal of spent nuclear fuel (SF) in deep geological strata (hereafter “direct disposal of SF”) as an alternative management option to reprocessing followed by vitrification and geological disposal of high-level radioactive waste (HLW). Evaluation of the release behavior of radionuclides (RNs) for direct disposal of SF is very important because the RN release behavior from SF is completely different from that of vitrified HLW owing to different waste matrices and inclusion of gaseous and semi-volatile RNs. There have, however, been only a few studies in Japan on direct disposal of SF owing to the Japanese strategy being that all SF should be reprocessed.

Therefore, we collected and compared source-term parameters on RN release from SF in deep geological repositories for selection of the parameters applied to the performance assessment of the Japanese SF disposal system. We picked up the parameters from several foreign safety-assessment reports, e.g., the Swedish SR-Site, the Finnish TURVA-2012, the Swiss EN 2002, the French Dossier 2005, and the Canadian Fourth Case Study (4CS).

There are two types of RN-release behaviors from SF; one is relatively faster release of gaseous and semi-volatile RNs and is parameterized as instant-release fractions (IRFs) of inventory. The other is long-term release that is congruent with dissolution of the $UO_2$ matrix and other construction materials parameterized as “dissolution rates”. Examples of IRF and cumulative fuel dissolution as a function of time after disposal selected in the foreign safety assessment reports are shown in Figs.8-24 and 8-25, respectively. It was found that various IRF values were selected owing to a variety of SF properties (e.g., reactor types, fuel types, burnups) and handling of the most pessimistic case. A mechanistic understanding of RN-release behavior from SF has been drastically promoted since 2000; therefore, the selected parameters that apply those findings are similar to each other (SR-Site, TURVA-2012, and 4CS shown in Fig.8-25).

This study was a part of the “Project on the Research and Development of Spent Fuel Direct Disposal as an Alternative Disposal Option,” funded by the Ministry of Economy, Trade and Industry of Japan (METI) in FY 2015.

**References**

Nagata, M., Kitamura, A. et al., Evaluation of Source Term Parameters for Spent Fuel Disposal in Foreign Countries – (1) Instant Release Fraction from Spent Fuel Matrices and Composition Materials for Fuel Assemblies, Genshiryoku Bakkuendo Kenkyu (Journal of Nuclear Fuel Cycle and Environment), vol.23, no.1, 2016, p.31-54 (in Japanese).

Kitamura, A. et al., Evaluation of Source Term Parameters for Spent Fuel Disposal in Foreign Countries – (2) Dissolution Rates of Spent Fuel Matrices and Construction Materials for Fuel Assemblies, Genshiryoku Bakkuendo Kenkyu (Journal of Nuclear Fuel Cycle and Environment), vol.23, no.1, 2016, p.55-72 (in Japanese).

# 8–11 In Microwave Ovens, the Height of the Heating Specimen Changes the Ease of Warming
## — Heating Efficiency of the Nitric Acid by the Microwave —

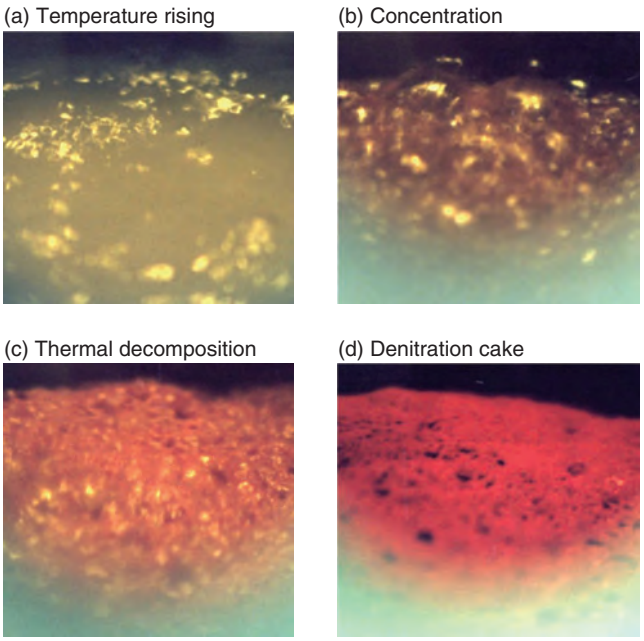


**Fig.8-26 Process of the microwave-denitration reaction**
In the microwave-heating direct-denitration method, a microwave-heated mixture of uranyl nitrate and plutonium nitrate is converted to oxide powder by a thermal-decomposition reaction.

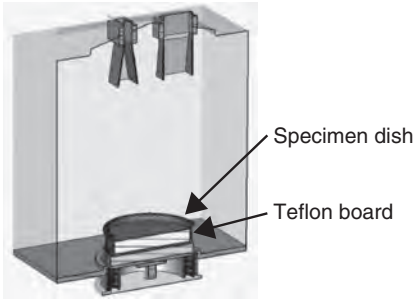


**Fig.8-27 Structure of the microwave oven**
The thickness of the Teflon board laid out under the specimen dish was changed along with the specimen height.

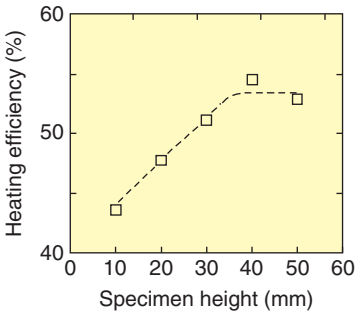


**Fig.8-28 Heating efficiency of the vaporized nitric acid**
The examination showed that heating efficiency increased as heights increased from 10 to 30 mm but became constant above 30 mm.

In Japan, where the fundamental law strictly confines the use of nuclear energy to peaceful applications, the microwave-heating (MH) direct-denitration method was developed as a preparation route to prevent nuclear materials from being diverted to military use.

Using this method, a mixture of uranyl nitrate and plutonium nitrate solution (Pu/U nitrate solution) is heated by a microwave. The temperature increases under heating, the concentration and thermal-decomposition-reaction form, and Pu/U nitrate solution is changed to oxide, as shown in Fig.8-26. The heating efficiency is very important for improving the energy-saving performance in this conversion process. Microwave-heating efficiency in the reheating of the food ranges from 60%–80%, but there have been very few reports on the heating efficiency of denitration.

Therefore, we used water, nitric acid, and Pu/U nitrate solution as heating specimens and examined the temperature rise and concentration of each of them as well as the thermal decomposition in the examination. Experimental results showed that the heating efficiency of the temperature rise and concentration was approximately 60%, about the same as that of food reheating.

However, the heating efficiency under nitric-acid evaporation and denitrification of the Pu/U nitrate solution was approximately 50% and decreased only a little. Then, the specimen height was changed from 10 mm to 50 mm, as shown in Fig.8-27 at the time of the experiment causing the nitric acid to evaporate, and the influence on heating efficiency was investigated.

Heating efficiency increased along with height from 10 mm to 30 mm but ceased to increase at larger specimen heights (Fig.8-28).

We examined the change in the efficiency with the heating condition through electromagnetic-field analysis. It was found that disorder of the electric field distribution in the oven decreased at the specimen heights above 30 mm, and that heating became easy. When the specimen height was increased beyond 30 mm, it was found that disorder of electric-field distribution ceased to change. These analysis results matched the experimental results well.

From these results, the heating efficiency of the MH method was found to be the same as that of reheating food during heating and evaporation of water but the efficiency decreased by approximately 10% during nitrate evaporation and denitration. In addition, the heating efficiency decreased if the specimen's height was low.

This information is important knowledge that should be considered during development of future equipment.

**Reference**

Kato, Y., Heating Efficiency of Microwave Heating Direct Denitration of a Mixture of Uranyl Nitrate and Plutonium Nitrate, Nippon Genshiryoku Gakkai Wabun Ronbunshi (Transactions of the Atomic Energy Society of Japan), vol.13, no.2, 2014, p.62-73 (in Japanese).

# Toward Practical Use of Fusion Energy

Crucial research and development (R&D) on fusion plasma and fusion engineering is being pursued through intensive international cooperation toward the practical use of fusion energy. For example, the International Thermonuclear Experimental Reactor (ITER) project, Broader Approach (BA) activities, and other collaborations (Fig.9-1), aiming for the early realization of a fusion DEMO reactor, are underway. Fusion plasma research is mainly being advanced at the Naka Fusion Institute, whereas fusion engineering research is mainly being advanced at the Rokkasho Fusion Institute.

## ITER Project

The ITER project is an international cooperative project aimed at demonstrating the scientific and technological feasibility of fusion energy through the construction and operation of an experimental reactor. The ITER agreement came into force in October 2007, and the Japan Atomic Energy Agency (JAEA) was designated as the domestic agency for the implementation of the ITER project in Japan. JAEA proceeded with preparing the equipment that Japan agreed to provide and achieved various results in terms of technological development (Topic 9-1). In particular, JAEA completed development of 1MV HV power supply components for plasma heating in December 2015.

## BA Activities

The BA activities are joint projects between Japan and the European Union to conduct supporting research for ITER and R&D for a DEMO reactor (which is the next step of ITER), aiming for early realization of fusion energy. The BA agreement came into force in June 2007, and JAEA was designated as the implementing agency of the BA activities in Japan.

These activities can be grouped into three categories: projects at the International Fusion Energy Research Center (IFERC), those related to the International Fusion Materials Irradiation Facility/Engineering Validation and Engineering Design Activities (IFMIF/EVEDA), and the Satellite Tokamak Program (STP).

## Fusion Plasma Research

As part of the STP, the construction activities on JT-60SA have progressed well. Topics 9-2, 9-3, and 9-4 are results contributing to JT-60SA. The analysis of JT-60 experimental data was promoted, and inter-machine experiments were conducted to achieve high economic efficiency for the fusion reactor by attaining a high plasma pressure.

## Fusion Engineering Research

Various R&D activities are being executed by the Rokkasho Fusion Institute, aiming at the construction of a technological basis for the DEMO reactor. Topics 9-5 and 9-6 are results that will assist in securing the safety of the fusion reactor. Topic 9-7 is a result that enables examination of fusion materials. Topic 9-8 is a result contributing to the decrease of radioactive waste, aiming at improving the social acceptability of the fusion reactor. Topic 9-9 is a result that is indispensable for the breeding blanket to function.

Nuclear fusion research development was taken over to the National Institutes for Quantum and Radiological Science and Technology (QST) established in April 2016.

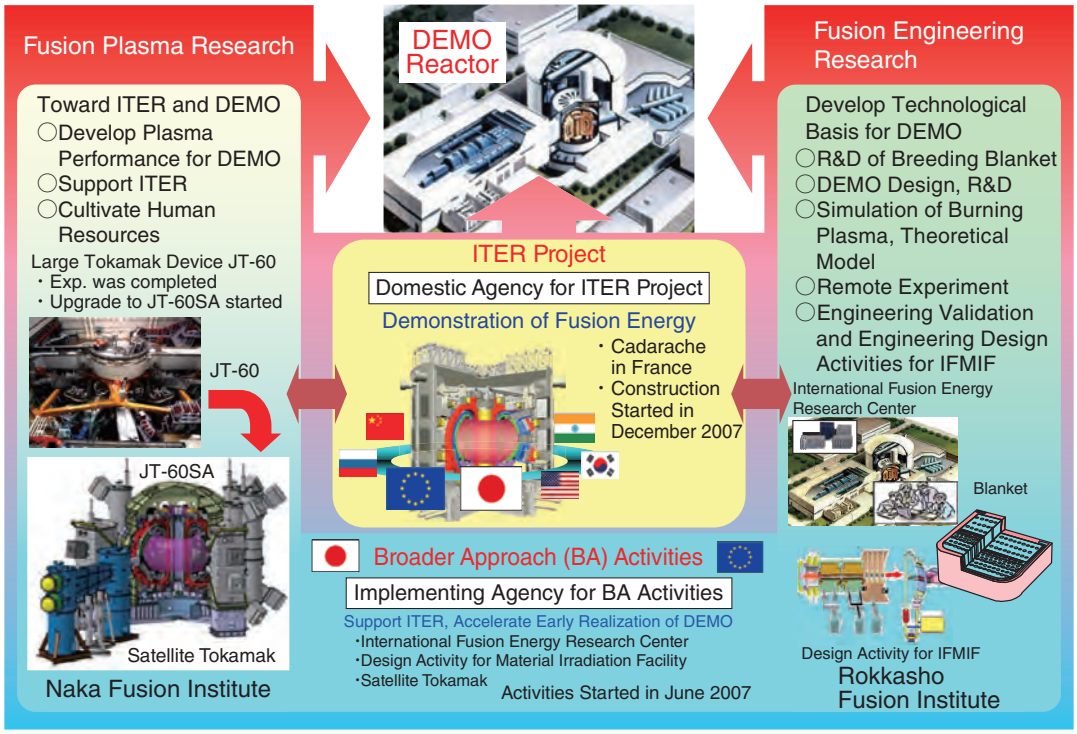


**Fig.9-1 Steps involved in the development of the fusion DEMO reactor**
Fusion plasma research and fusion engineering research are being pursued to develop a DEMO reactor. Furthermore, we are promoting international cooperation toward the development of the International Thermonuclear Experimental Reactor (ITER) project and the Broader Approach (BA) activities, aiming at the early realization of fusion energy.

# 9–1 Controlling Robots in a Radiation Environment

## — Using a Robot Vision-Based System to Position a Manipulator in a Fusion Reactor —

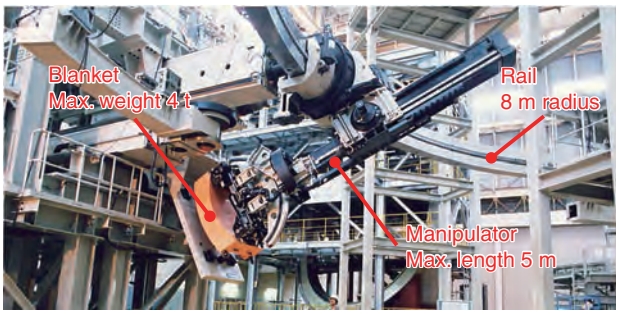


**Fig.9-2 Prototype of the ITER remote-handling robot**
A manipulator that can extend up to 5 m in length travels on a rail 8 m in radius and grasps, carries, and exchanges blanket modules weighing up to 4 t during remote maintenance of ITER.

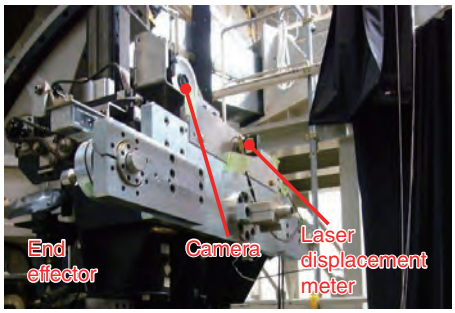


**Fig.9-3 Camera(s) used for robot vision**
Camera(s) are installed at the end of the manipulator (end effector), allowing the manipulator to be positioned automatically using robot vision. Positioning accuracy is measured using a laser-displacement meter.

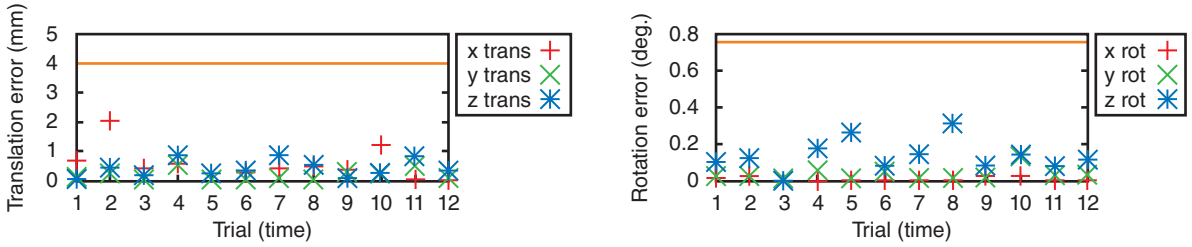


**Fig.9-4 Robot vision positioning errors**
We confirmed that the robot vision-based system satisfies the positioning accuracy requirements for the manipulator (less than 4 mm in translation, 0.76° in rotation, as indicated by the orange lines in the graphs).

A component called a “blanket” is installed in fusion reactors to prevent damage to the vacuum vessel caused by heat or radiation. The blanket in ITER is divided into 440 modules, some weighing up to 4 t. The blanket must be replaced, but as the radiation level inside the vacuum vessel will be 250 Gy/h (owing to $\gamma$-rays), the only way the blanket modules can be exchanged is by using remote-handling equipment. We have been developing a robot for this purpose. The robot uses a large manipulator that travels along a rail and was designed to be able to reach all areas of the vacuum vessel (Fig.9-2). The manipulator must be positioned in front of the blanket module to within 4 mm in translation error and 0.76° in rotation error in order to grasp the blanket modules. Positioning must be performed through a non-contact method, so as not to damage the surface of the blanket. The conventional method using laser-displacement meters cannot be applied here as these meters contain semiconductors that are susceptible to radiation. That is why we developed and tested a positioning method based on image processing with imaging-tube analog cameras having a radioresistance of approximately 2 MGy. This control method is called robot vision.

Our method uses camera(s) that are installed at the end of the manipulator (the end effector) (Fig.9-3). By processing the images of the blanket obtained with this camera, we can calculate the position of the manipulator relative to the blanket. The manipulator is then positioned based on this calculation. Since the resolution of the imaging tube is low, approximately 500 scanning lines, the images were grainy and caused an issue with positioning accuracy. To resolve this, we used two cameras and compared the image data from each to perform our calculations, improving accuracy.

Tests were performed to evaluate errors in positioning of the manipulator using the methods we developed. The positioning errors were measured using a laser-displacement meter installed at the end effector (Fig.9-3). The biggest errors were 2.0 mm in translation and 0.31° in rotation, confirming that there is sufficient positioning accuracy to grasp the blanket modules (Fig.9-4).

We confirmed that robot vision is a suitable method for positioning the manipulator in radioactive environments. We intend to develop a control method that not only automatically positions the manipulator with respect to the blanket but also grasps the blanket module automatically by combining robot vision with force sensors or the like.

**Reference**

Maruyama, T. et al., Robot Vision System R&D for ITER Blanket Remote-Handling System, Fusion Engineering and Design, vol.89, issues 9-10, 2014, p.2404-2408.

# 9–2 Manufacturing Superconducting Coils with High Accuracy

## — Establishing a Manufacturing Method for High-Circularity Superconducting Coils to Reduce the Error Magnetic Field —

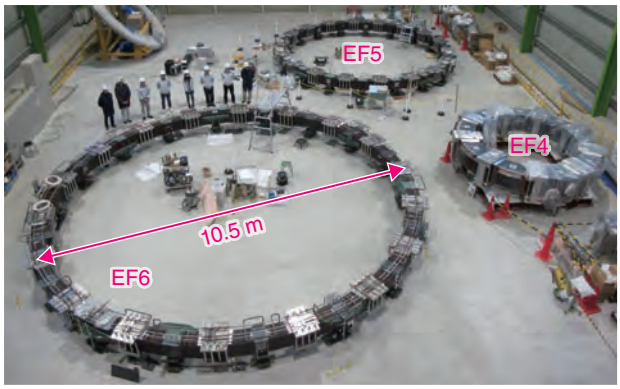


**Fig.9-5 Three completed equilibrium field coils**
These coils are ready to be installed in JT-60SA, together with cooling pipes and support structure.

**Table 9-1 Circularity of the equilibrium field coils (deviation from an exact circle)**
Much better circularity than the required value is achieved (the right figure shows definition of circularity).

| | Circularity (Achieved) | Circularity (Required) | Diameter |
|---|---|---|---|
| EF4 | 0.6 mm | ≤6 mm | 4.4 m |
| EF5 | 0.6 mm | ≤6 mm | 8.2 m |
| EF6 | 1.3 mm | ≤8 mm | 10.5 m |

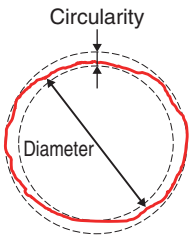


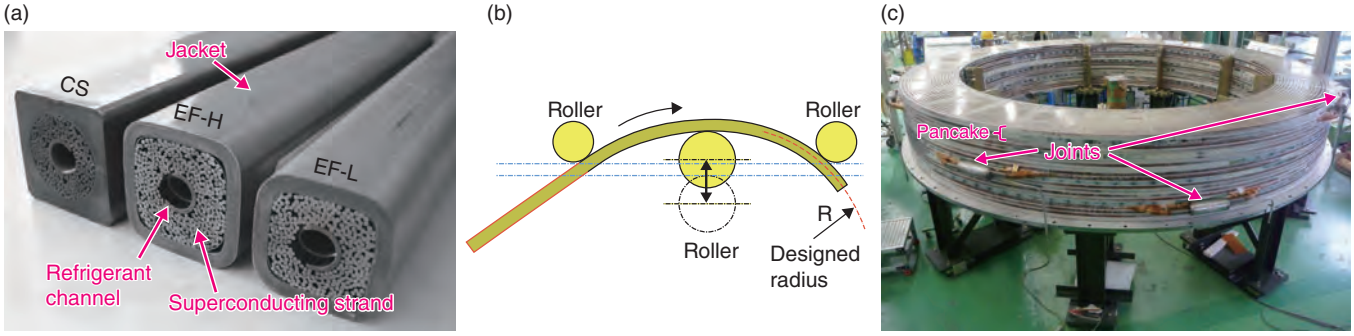


**Fig.9-6 Process of superconducting-coil manufacturing**
(a) Superconductors are fabricated by inserting the superconducting strand into the stainless jacket. (b) The conductor is bent by an advanced bending machine with the design radius to form a pancake layer. (c) The pancakes are stacked such that the error in the average current-center circularity is minimized about the stacking axis. In order to achieve this, the position of each pancake is tuned based on its measured current center.

The JT-60SA is an advanced tokamak device that supports the ITER mission and addresses key physics issues for DEMO with high mobility. One of its requirements is the ability to produce a high-precision magnetic field that stably confines fusion plasma of several hundred million °C in the air while controlling its shape and position. Manufacturing error of the superconducting coils should be minimized down to an permissible level.

Fig.9-5 shows completed circular coils, referred to as equilibrium field coils. The required circularity for the large coil EF6 (10.5 m in diameter) was estimated to be less than 8 mm (i.e., approximately 0.1% of the coil's diameter) based on the allowable error field. As a result of the establishment of the manufacturing method for the superconducting coils described below, a high circularity of 1.3 mm was achieved (Table 9-1).

(1) Accurate bending of the superconductor

The superconductor is manufactured by containing a superconducting cable in a stainless jacket (Fig.9-6(a)). Then, the straight conductor is bent according to the designed radius of curvature by pushing rollers to the jacket (Fig.9-6(b)). Since non-uniform bending stiffness exists owing to the welding part between each jacket of unit length, a high-precision bending machine was developed, resulting in accurate and stable bending work.

(2) Distribution of the connection parts

A coil comprises layers of approximately 10 pancake coils, with each pancake is connected electrically (Fig.9-6(c)). The position of the pancake joints and inlets (joggle parts), which deteriorates circularity, was distributed in the toroidal direction to avoid cumulation of the non-circularity.

(3) Tuning of the relative position of each pancake

In the stacking process, the position of each pancake was tuned based on its measured current center such that the average error in the current-center circularity was minimized about the stacking axis (Fig.9-6(c)).

**Reference**

Koide, Y. et al., JT-60SA Superconducting Magnet System, Nuclear Fusion, vol.55, no.8, 2015, p.086001-1-086001-7.

# 9–3 Measurement of Magnetic Fluctuation of Fusion Plasmas
## — Development of Simple, High-Performance Magnetic Sensors —

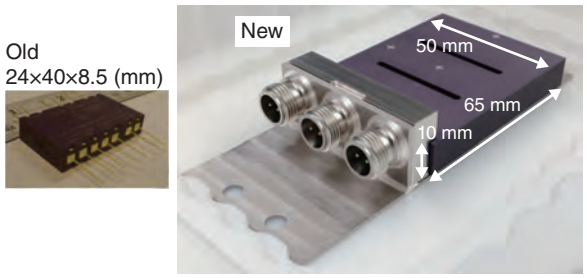


**Fig.9-7 Comparison between new and old magnetic-coil sensors**
These sensors are made with only metals and ceramic. The new ones combine one coil for position/shape control and two types of coils for measurement of instabilities. Enlargement of the new type of coil causes its sensitivity to be ten times higher than that of old one.

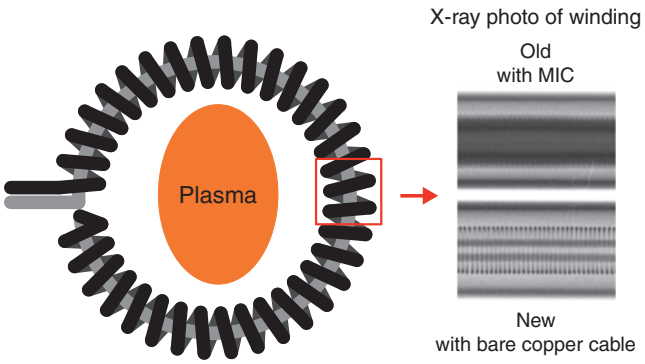


**Fig.9-8 Comparison between new and old Rogowski-coil sensors**
The X-ray photo of the old one is unclear because MIC is wound densely, whereas it can be seen that copper cable lines up perfectly.

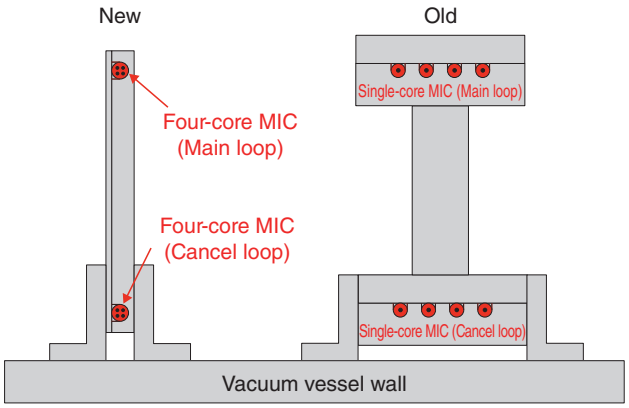


**Fig.9-9 Comparison between the cross-sections of new and old diamagnetic-coil sensors**
The use of a four-core MIC rather than a single-core one enables the diamagnetic loop to have a simple structure.

Fusion plasmas are confined within a magnetic field. Measurement of the magnetic field enables us to know various important characteristics of the plasmas because the field is induced by not only magnetic coils but also the current flowing in these plasmas. Therefore, magnetic sensors are the most important measuring equipment for fusion plasmas. Magnetic sensors are made with coil windings and measure the magnetic field inside these coils. They have to be made with metals and non-organic materials so as not to exhaust the gas in ultra-high vacuum because they are installed in the vicinity of the plasma within the vacuum vessel surrounding it.

The shape and position of the plasma are measured with a magnetic sensor. Instabilities are also identified. For this purpose, we developed a magnetic-probe type of sensor, which combines a coil for position/shape control and two types of coils for measurement of instabilities (Fig.9-7). It has a large sensitivity for its size because it comprises ceramic plates metalized with dense tungsten circuits. Moreover, enlargement of the coil leads to its sensitivity being ten times higher than that of a previous one. A mineral-insulated cable (MIC), which consists of a conductor insulated with a ceramic powder inside a stainless sleeve, is employed as the signal wire of the sensor. We developed a new connector for connection between the MIC and the sensor in order to allow the sensor to be easily changed in the event of a fault.

Plasma current is measured with a Rogowski type of sensor, which consists of a helical cable centered around a return conductor. We developed a new type of non-MIC-based Rogowski coil; whereas the previous coil consisted of a $\phi$ = 0.5-mm MIC winding with a diameter of 5 mm and a length of approximately 9 m (Fig.9-8). New one consists bare-wire-based helical winding with same diameter insulated with ceramic powder. It is brake-proof due to the thickness of the $\phi$ = 0.2-mm wire, whereas that of MIC is $\phi$ = 0.1 mm, and can measure the fast transition of the current. We successfully made coils with lengths 16 m.

Moreover, we can measure the plasma's stored energy with a diamagnetic-loop type of sensor, which comprises a pair of loops surrounding the plasma. This is the most important value for knowing the performance of the fusion plasma. We developed new type of diamagnetic loop consisting of only one turn of a four-core MIC for each loop, whereas previous types of coils consist of four and three turns single-core MICs. A diamagnetic loop has to be installed with absolute accuracy because it has to measure the magnetic field with to a precision on the order of ten-thousandths of signal amplitude. However, such a very simple structure (Fig.9-9) enables it to be installed with high accuracy.

**Reference**

Takechi, M. et al., Development of Magnetic Sensors for JT-60SA, Fusion Engineering and Design, vols.96-97, 2015, p.985-988.

# 9–4 Improving the Estimation Accuracy of Plasma Shape

## — Optimizing the Predictive Accuracy of the Plasma-Shape-Estimation System —

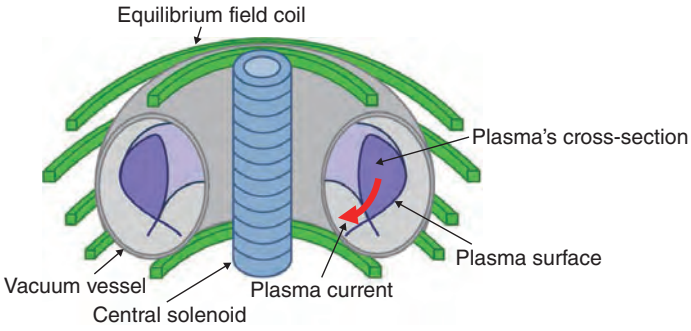


**Fig.9-10 Schematic of tokamak plasma (donut-shaped)**
Donut-shaped plasma is formed in the donut-shaped VV. The shape of the plasma's cross-section is controlled by operating the currents for the central solenoid and equilibrium field coils.

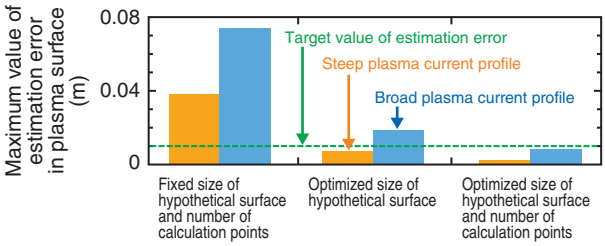


**Fig.9-12 Estimation errors by optimizing the size of the hypothetical surface and the number of calculation points**
The estimation errors in the plasma surface are kept within targets by optimizing the size of the hypothetical surface and the number of calculation points.

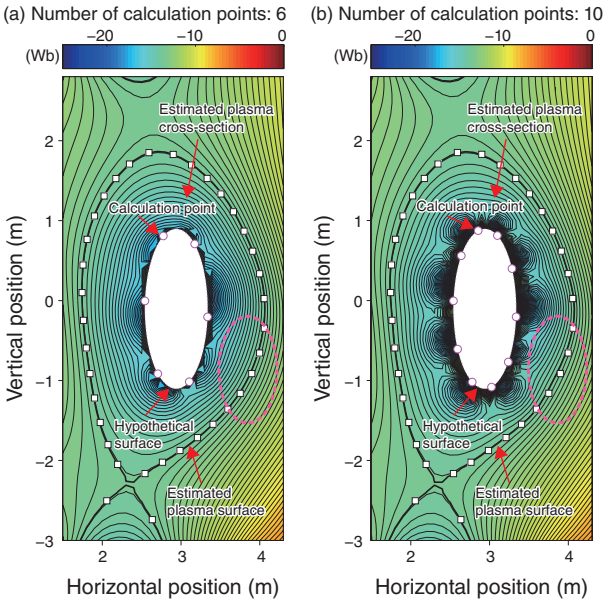


**Fig.9-11 Plasma-cross-section shape estimated by the plasma-shape-estimation system**
The difference between the locations of the plasma surface produced by the calculation code (□) and estimated by the plasma-shape-estimation system increases if the number of calculation points (○) arranged along a hypothetical surface increases from (a) 6 to (b) 10.

In order to maintain steady high-performance tokamak plasma and to prevent it from contacting structures such as the vacuum vessel (VV) and the like, it is necessary to control the plasma's cross-sectional shape accurately (Fig.9-10). Since this shape is determined by the interrelation between the magnetic field generated by current flowing in the plasma (plasma current) and current sources other than plasma, it can be controlled by operating the currents for the central solenoid and equilibrium field coils used for controlling the plasma current and cross-sectional shape. However, it is necessary to estimate an accurate cross-sectional shape from the signals for the measurements arranged outside the plasma using a plasma-shape-estimation system to control the cross-sectional shape accurately. The plasma-shape-estimation system based on the Cauchy-condition surface (CCS) method was used for the JT-60U plasma cross-sectional-shape control. A hypothetical surface that plays the same role as the current flowing in the plasma is placed well inside the plasma, and the plasma surface can be estimated speedily and with high accuracy by calculating conditions on the hypothetical surface from the coil currents and by measurement signals. In order to apply the plasma-shape-estimation system based on the CCS method to the JT-60SA plasma-cross-section shape control, it is necessary to predict the estimation accuracy of the plasma surface in JT-60SA.

The accuracy of the plasma surface estimated by the plasma-shape-estimation system has been assessed by preparing the coil currents and measurement signals in reference to the plasma information simulated by the calculation code. The plasma surface estimated by the plasma-shape-estimation system is compared with the standard one produced by the calculation code. Although various plasma shapes are easily exhibited again if the number of calculation points arranged along the hypothetical surface increases, the estimation error in the plasma shape becomes large (Fig.9-11). In contrast, this quantity decreases if the size of the hypothetical surface increases because the hypothetical surface and the plasma surface are brought close together.

By assessing the estimation error in the plasma surface on various shapes and profiles of the plasma while changing the size of the hypothetical surface and number of calculation points, the relation expression between the size of the hypothetical surface and number of calculation points for minimizing the estimation error is determined. The estimation errors for the plasma having a broad current profile are larger than those for the plasma having a steep current profile, but they remain within the target value of 1 cm according to the relation expression (Fig.9-12). It is shown that the estimation accuracy is largely improved by optimizing the size of the hypothetical surface and the number of calculation points in JT-60SA and future fusion reactors on with a high elongation and triangularity of the plasma shape. This is an important result for achieving stable plasma-cross-sectional shape control in JT-60SA and future fusion reactors.

**Reference**

Miyata, Y. et al., Assessment of the Accuracy of Plasma Shape Reconstruction by the Cauchy Condition Surface Method in JT-60SA, Review of Scientific Instruments, vol.86, issue 7, 2015, p.073511-1-073511-13.

# 9–5 Toward Safe Operation of Nuclear Fusion Reactors

## — Discovery of a New Magnetohydromagnetic Instability that Causes Disruptive Events in Fusion Plasmas —

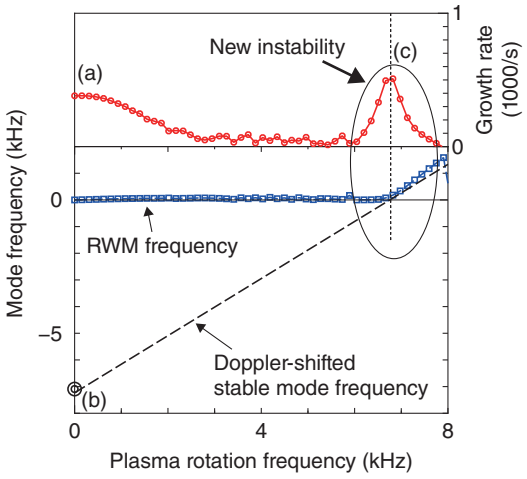


**Fig.9-13 Dependence of growth rate and mode frequency upon plasma-rotation frequency**
RWM (a) and stable eigenmode (b) have a finite-growth rate and frequency in a static plasma, respectively. When a plasma rotates, the eigenmode frequency is Doppler shifted to zero and the mode starts interacting with RWM. This interaction excites a new instability (c).

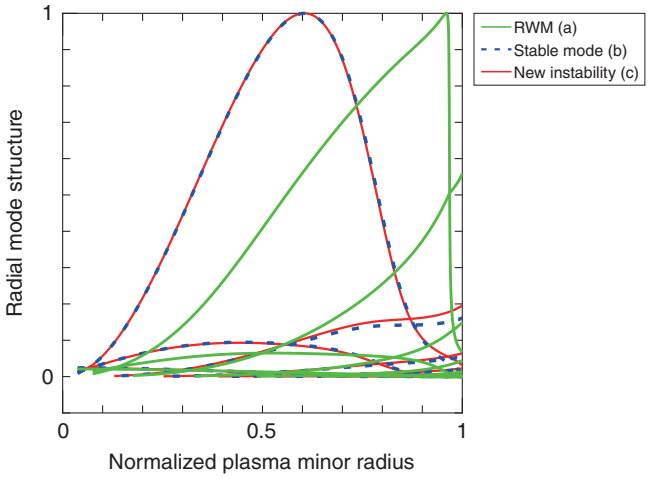


**Fig.9-14 Radial structures of the Poloidal Fourier harmonics of RWM (a), the stable eigenmode (b), and the new instability (c)**
The eigenfuction of the new instability (c) is almost the same as that of the stable eigenmode (b) but is clearly different from that of RWM (a). This result suggests that the stable eigenmode (b) is responsible for exciting the new instability (c).

To realize tokamak-type fusion reactors, achieving a steady-state burning plasma with high plasma pressure is necessary. Such high pressure is required to improve power-generation efficiency but sometimes triggers magnetohydrodynamic (MHD) instabilities that cause disruptive events. Hence, it is important to stabilize MHD instabilities by understanding the physics of their destabilization mechanism. Resistive wall modes (RWMs) are disruptive MHD instabilities that are destabilized owing to the finite resistivity at the vacuum chamber (wall) surrounding the plasma. The RWM has been confirmed to be stabilized by rotating the plasma in many experiments, but an MHD instability sometimes terminates the discharge disruptively, even though plasma rotation is kept sufficiently fast to stabilize the RWM. Hence, identifying the trigger of the MHD instability in a rotating plasma and determining how to avoid this instability are indispensable for realizing safe operation of a fusion reactor.

In this study, we analyzed the stability of MHD modes, including RWM, in rotating tokamak plasmas and discovered a new MHD instability. This instability is destabilized owing to the interaction between RWM stabilized by rotation and a stable MHD eigenmode (Fig.9-13). When a stable MHD eigenmode exists in a plasma, its eigenmode frequency can be modulated by rotation (Doppler shift). Conversely, since the RWM is excited by finite-wall resistivity, all RWM behavior is restricted by the wall. This means that the RWM frequency is always almost zero, even when a plasma rotates, because the mode is locked to the immobile wall. Hence, when the Doppler-shifted mode frequency of the stable mode approaches zero, this mode interacts with the RWM, exciting a new MHD instability. The radial-mode structure of this new MHD instability is almost the same as that of the stable MHD eigenmode, but is clearly different from that of RWM (Fig.9-14).

The newly discovered instability appears only when the frequency of the stable MHD eigenmode approaches zero owing to rotation. This mode frequency is determined by the magnetic configuration of the tokamak reactor, and the variation of the mode frequency is smaller than the maximum rotation frequency. Hence, it is possible to avoid this new MHD instability by adjusting the magnetic configuration to keep the eigenmode frequency higher than the plasma-rotation frequency.

The discovery of a new MHD instability owing to interaction between the MHD modes in plasmas is of importance from the physics point of view. In addition, a guideline on avoiding instabilities causing disruptive events is shown, as is required for designing tokamak fusion reactors safely and with high power-generation efficiency.

This work was supported by the Japan Society for the Promotion of Science (JSPS) KAKENHI Grant-in-Aid for Young Scientists (B) (No.24760712).

**Reference**

Aiba, N. et al., Excitation of Flow-Stabilized Resistive Wall Mode by Coupling with Stable Eigenmodes in Tokamaks, Physical Review Letters, vol.114, issue 6, 2015, p.065001-1-065001-5.

# 9–6 Confining Tritium in a Fusion Facility

## — A Catalytic-Reactor Design that Ensures Tritium Oxidation under All Possible Conditions —

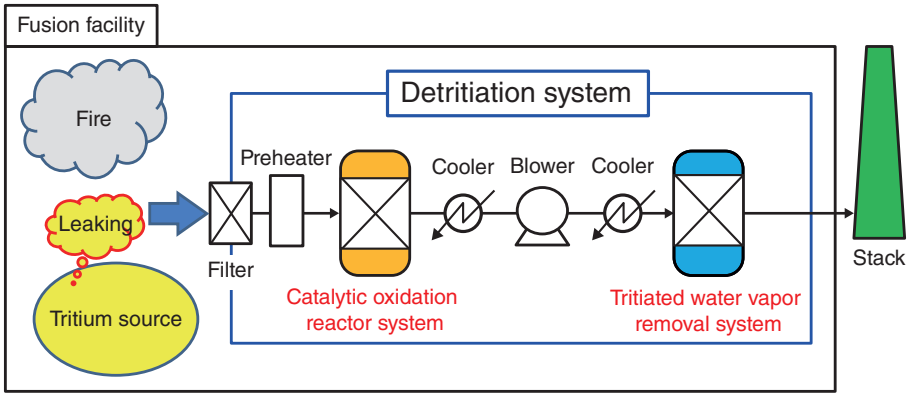


**Fig.9-15 A schematic diagram of a detritiation system**
Gaseous tritium leaked in a facility is oxidized by the catalytic-oxidation-reactor system and converted into tritiated water vapor. After that, the tritiated water vapor is removed by an appropriate system.

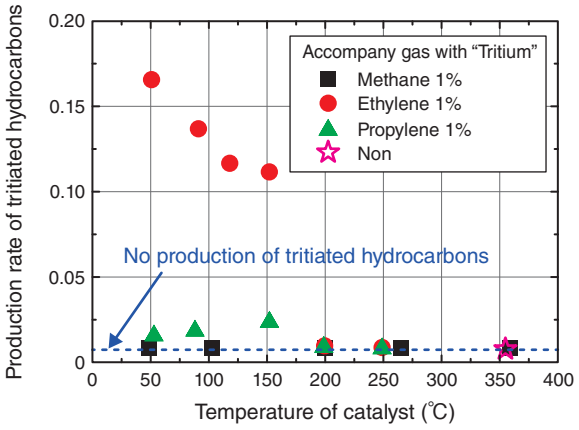


**Fig.9-16 Production rates of tritiated hydrocarbons in the case where tritium with hydrocarbons is introduced into the catalytic reactor**
Above the broken line in the figure, it is apparent that tritiated ethylene (or ethane) is produced by the reaction between tritium and ethylene only. The production rate of tritiated ethylene decreases with an increase in temperature of the catalyst since the tritium-oxidation reaction is promoted by temperature increase. Tritiated ethylene is not produced at 200 °C, since it completely combusts above this temperature.

A large amount of tritium is used as a fuel in nuclear-fusion facilities. Since tritium is a radioactive isotope of hydrogen, a detritiation system (DS) is installed in fusion facilities to prevent tritium release into the environment. The DS must ensure the detritiation efficiency under all possible extraordinary events. We have investigated the effects of the events upon the detritiation efficiency through experiments and analysis to design a DS that can work efficiently under all extraordinary events.

The DS comprises a catalytic-oxidation-reactor system and a water-vapor-removal system (Fig.9-15). The catalytic-oxidation-reactor system must ensure the tritium-oxidation efficiency in the case where various types of gases with tritium are fed into the system under extraordinary events. Assuming a fire event, hydrocarbons such as methane and ethylene are produced by combustion of flammable organic matter. Issues with the catalytic-reactor system include ensuring the tritium-oxidation efficiency, even when tritiated hydrocarbons are produced, and controlling excessive temperature increase owing to hydrocarbon-combustion reactions, which induce risks of excessive tritium permeation and explosion and so on.

We have clarified that a tritiated-hydrocarbon-production reaction only occurs to a notable extent for ethylene (Fig.9-16). This indicates that the isotopic-exchange reaction between tritium and hydrogen is very slow and that the hydrogenation reaction is the dominant producer of tritiated hydrocarbon. It is found that tritiated methane, which is combusted at a high temperature, is produced only by isotopic-exchange reactions, and also that tritiated hydrocarbons are combusted by the catalytic reactor, whose temperature is sufficient to combust ethylene completely. Therefore, these results suggest that a catalytic reactor at a comparative low temperature of 200 °C ensures both the tritium-oxidation efficiency and the excessive temperature rise by heat of reaction in the catalytic-reactor system.

The Japan domestic agency is in charge of procurement of DS for ITER construction in the south of France within the ITER organization. We are conducting qualification tests of DS and proceeding R&D for safety of a nuclear-fusion facility.

**Reference**

Edao, Y. et al., Effect of Hydrocarbons on the Efficiency of Catalytic Reactor of Detritiation System in an Event of Fire, Journal of Nuclear Science and Technology, vol.53, issue 11, 2016, p.1831-1838.

# 9–7 Achievement of a Prototype-Accelerator-Performance Goal for the International Fusion Material Irradiation Facility (IFMIF)
## — Successful Injector-Beam Acceleration of the High-Current Deuterium Accelerator —

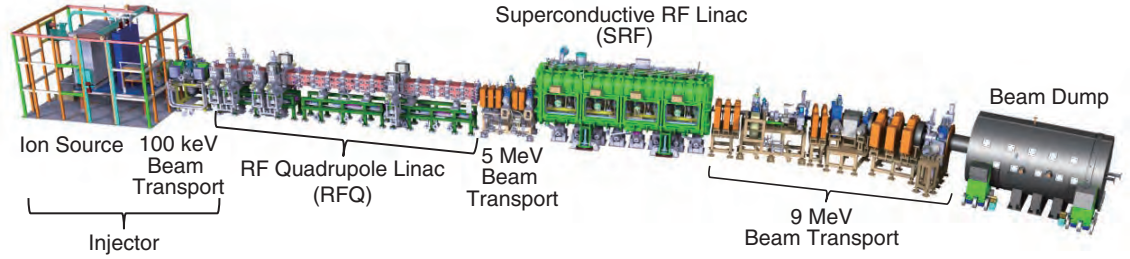


**Fig.9-17 Overview of the IFMIF/EVEDA prototype accelerator**

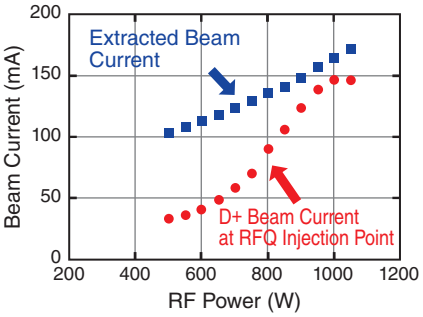


**Fig.9-18 Input RF power vs beam current**
The extracted beam current is linear to the input RF power. Since the input RF power changes the plasma density, inlet deuterium-gas flow rate has to be adjusted.

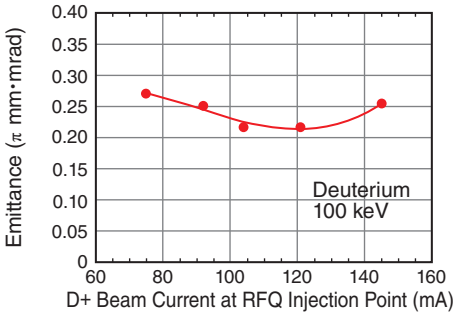


**Fig.9-19 Beam current vs emittance at the RFQ injection point**
After beam-orbit adjustment, we obtained an emittance of approximately 0.25 π mm·mrad at a 145-mA beam current that exceeds the goal value, with a low duty cycle.

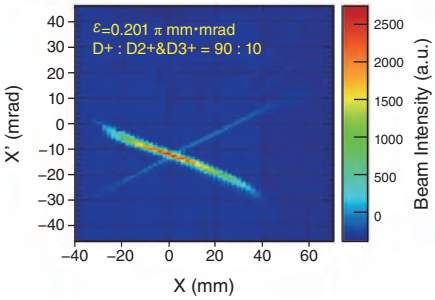


**Fig.9-20 Phase-space distribution of extracted beam-ion species**
These distributions were obtained after forcusing magnetic field. The D+ beam is distributed from upper-left to lower-right corners (converging), while the D2+ and D3+ molecular beams are distributed from upper-right to lower-left corners (diverging). Emittance can be derived based on each distribution area.

In the development of the DEMO reactor aimed at demonstrating fusion energy as a viable power source, it is a critical issue to understand the damage to the future reactor structural material owing to fast neutrons. It is essential that these reactor materials are evaluated under equivalent spectrum-neutron fluxes to those expected in a fusion reactor. Since 2007, the Engineering Validation and Engineering Design Activities (EVEDA) phase of the International Fusion Materials Irradiation Facility (IFMIF) established under the Broader Approach (BA) activities has been ongoing. A 40-MeV deuterium linear accelerator, the core component in the IFMIF, is characterized by its large current (two 125-mA accelerators) and continuous-wave (CW) output. We are installing and testing a prototype accelerator for engineering validation of the IFMIF accelerator at the Rokkasho site in a stepwise manner, as shown in Fig.9-17, with three main accelerating stages: an injector (100 keV), a radio frequency quadrupole (RFQ: 5 MeV), and a superconductive RF linac (SRF: 9 MeV).

At the injector, due to the high beam current (140 mA or more) with the lowest energy in this accelerator, the strong and nonlinear space charge effect tends to defocus the beam and increase the emittance (the figure of merit to express the beam spread, defined as the beam volume in phase space). It potentially causes undesired beam losses that might result in excessive activation and/or damage of accelerator equipments. Therefore, controlling both the space charge effect and the emittance (<0.25 π mm·mrad is specified as the nominal performance at the entrance of the RFQ) is the mission of the injector-beam-acceleration test.

Since impurity gas deposition on the ion source surface changes the plasma state, we have promoted the degassing by adjusted the deuterium gas flow rate, RF power, and microwave matching condition. And by optimizing parameters such as the magnetic field distribution (along the ion source chamber and the beam extraction system), we have established a stable beam operation condition to suppress discharge between electrodes and plasma instability, with satisfying the target performance.

By beam transport adjustment, as shown in Fig.9-18, we achieved the targeted 140 mA D+ current in the total beam current. As shown in Fig.9-19, we reached an emittance of approximately 0.25 π mm·mrad but only at the low duty cycle. As shown in Fig.9-20, we can calculate the beam-ion fraction based on each ion's area in the phase space. We achieved a D+ fraction of 90%, thereby meeting requirements.

The neutron source based on a high current deuterium accelerator that is realized by this project is a promising technology for providing not only high fast-neutron flux but also high facility availability and reliability for widespread applications. We will conduct the commissioning of the downstream parts of the accelerator and continue engineering-validation activitiy for the IFMIF.

**Reference**

Okumura, Y., Ichimiya, R. et al., Operation and Commissioning of IFMIF (International Fusion Materials Irradiation Facility) LIPAc Injector, Review of Scientific Instruments, vol.87, issue 2, 2016, p.02A739-1-02A739-3.

# 9–8 Management Scenario for Radioactive Wastes with Consideration of Public Acceptance of a Fusion Reactor — Study on Volume Reduction of Radioactive Wastes for a Fusion Reactor —

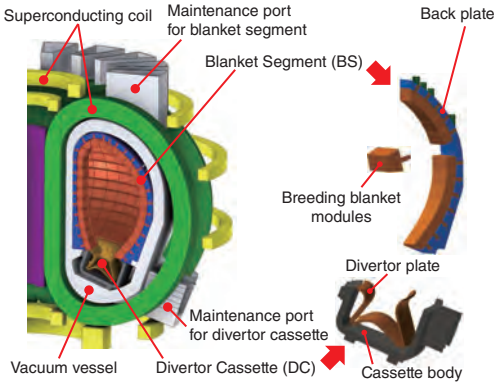


**Fig.9-21 Configuration of the DEMO reactor**
Superconducting coil, Vacuum vessel with maintenance port, Blanket segment, and Divertor cassette.

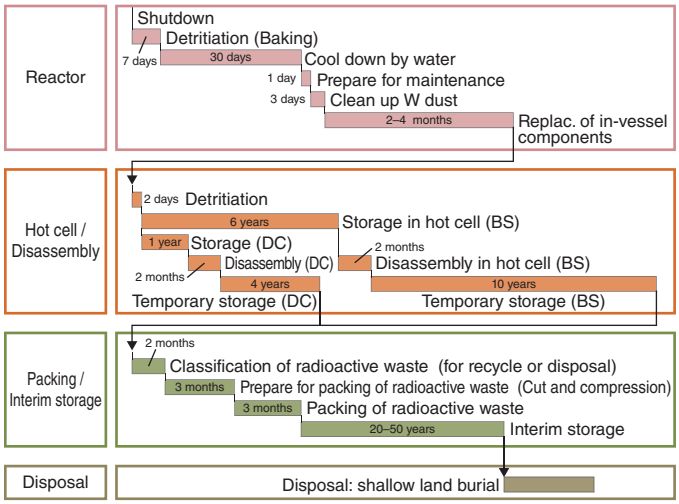


**Fig.9-22 Radioactive waste-management scenarios for regular maintenance of a fusion DEMO reactor**
We developed a waste management scenario for the DEMO based on the residual heat and dose rate of the used in-vessel components, including the blanket segment and the divertor cassette.

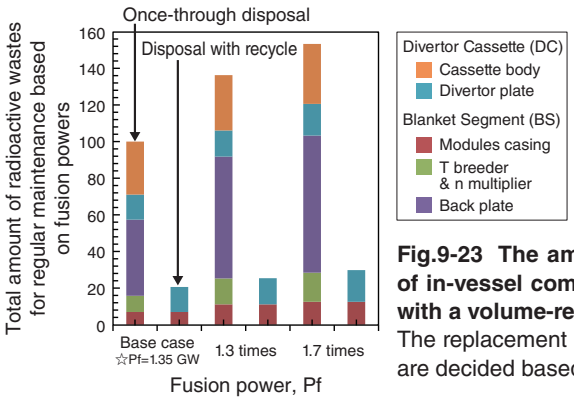


**Fig.9-23 The amount of the radioactive wastes generated by replacement of in-vessel components in the normal-operation cycle has been evaluated with a volume-reduction method**
The replacement periods of in-vessel components such as blankets and divertors are decided based on neutron damage.

There is a concern regarding fusion reactors that the replacements of in-vessel components such as blanket segments (BS) and divertor cassettes (DC), as shown in Fig.9-21, may generate a considerable amount of radioactive waste and represent a serious environmental burden. In this study, we have considered a strategy for reducing the waste generated by replacement of the components. Thus far, studies on the recycling of fusion-activated materials have focused on reducing the amount of waste that requires final disposal. Due to the necessity of replacing the components, waste management is required during the operation of a fusion reactor. Therefore, an appropriate waste-management scenario should be developed from the conceptual-design stage.

We have developed a waste-management scenario for a fusion DEMO reactor based on the residual heat and dose rate of the used the components, as shown in Fig.9-22. The management scenario for the replacement of radioactive components has an impact upon the cooling time for residual heat reduction before the removal of components from the reactor, the design of the hot cell, and waste storage. The components are moved to a hot cell through a maintenance corridor after a cooling time in the vacuum vessel of approximately one month. In order to maintain the health of the removal components, the residual heat must be removed using active cooling to keep the temperature below 550 °C for a structural strength of F82H. In the hot cell, the used components are handled as follows: blanket modules are removed from a back plate by remote-handling equipment after cooling for 6 years. The radiation environment in the hot cell is estimated to be 100 Gy/hr. Next, the neutron multiplier and tritium breeder are recovered from each blanket module for recycling at a disassembling facility. After that, the empty blanket modules and divertor plates are cut into small pieces and stored in a container. The radiation environment in the facility is estimated to be 10 Gy/hr and storage will last for 10 years. After waste classification in accordance with radioactivity, the waste is packed and stored in interim storage for disposal.

We considered a strategy for reducing the radioactive waste generated when the components are replaced in the DEMO. We evaluated the amount of waste generated by replacing the components during the normal operation cycle. In Fig.9-23, we suggest that the amount of waste can be reduced to 20% by reusing the back plate and cassette body and by recycling the breeding and multiplying materials. This result suggests the necessity of implementing waste-reduction programs. However, reusing the back-plate and cassette body in the assembly operation may be difficult with the existing RAMI program. The volume reduction of waste is very important for commercial fusion plants. Therefore, R&D efforts toward the development of an assembly operation for the BS and the DC should be initiated in the DEMO. The study of waste management should continue to reduce the amount of radioactive waste produced and to generate greater public acceptance of the construction and operation of future fusion reactors.

**Reference**

Someya, Y. et al., Management Strategy for Radioactive Waste in the Fusion DEMO Reactor, Fusion Science and Technology, vol.68, no.2, 2015, p.423-427.

# 9–9 Development of Highly Efficient Neutron-Multiplier Materials for Early Realization of a DEMO Reactor — Research on Ternary Advanced Neutron Multipliers —

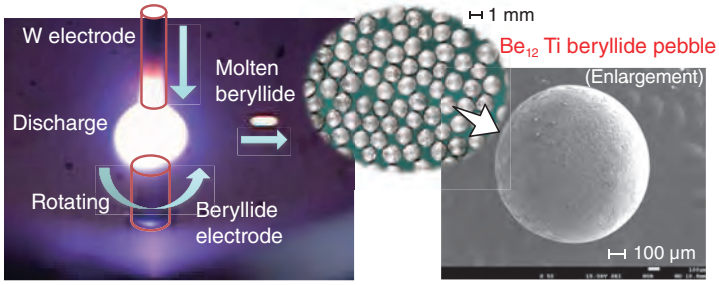


**Fig.9-24 Establishment of a granulation process for beryllide pebbles using a rotating-electrode method**
Pebbles with 1-mm diameters were successfully fabricated by the rotating-electrode method with a plasma-sintered electrode.

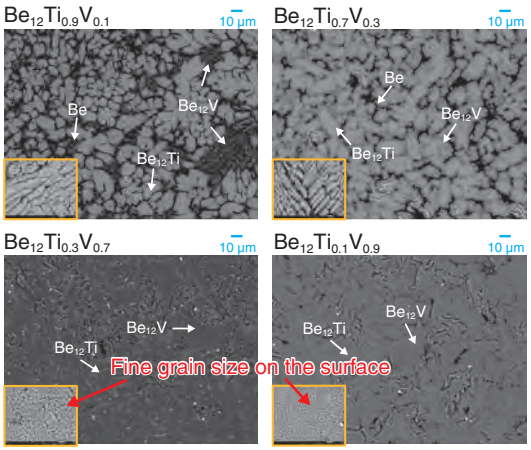


**Fig.9-25 Successful granulation of ternary beryllide pebbles**
Fabrication of ternary beryllide pebbles was conducted under increase in the vanadium (V) content in the chemical composition of $Be_{12}Ti_{1-x}V_x$.

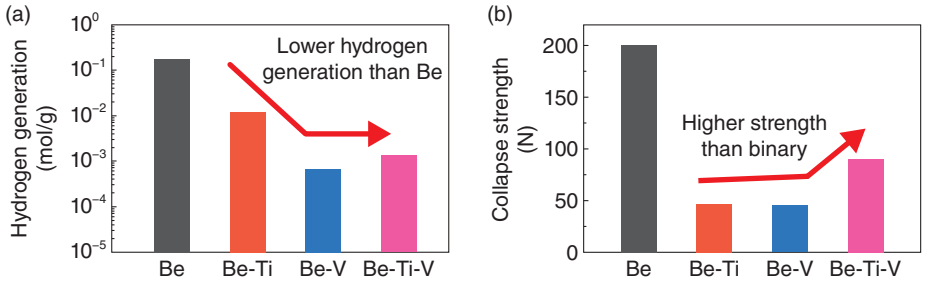


**Fig.9-26 Comparison of properties**
Hydrogen-generation amount (a) by reaction with water vapor at 1000 °C and collapse strength (b) were given.

Tritium as a fuel for a fusion reactor is produced by reacting neutrons generated from a fusion reaction with lithium (Li) as a breeder. At this time, to produce tritium with high efficiency, a neutron-multiplier material (so called because it multiplies the neutron number) is indispensably needed. Research and development of beryllium (Be) intermetallic compounds (beryllides) as candidate multiplier materials, which are more stable for high-temperature applications, have been carried out within the framework of broader approach (BA) activities because critical issues, such as the production of hydrogen gas generated by a reaction between Be and water vapor accidently leaked from the coolant, are anticipated.

Owing to the highly oxidant nature of Be, most beryllides fabricated by commercial powder metallurgy have been brittle and difficult to machine. However, using an optimized plasma-sintering method consisting of plasma activation by a pulse current and sintering by a direct current, a rod-shaped beryllide with good machinability and high thermal-shock resistance has been successfully fabricated as a granulation-starting material. Furthermore, beryllide pebbles 1 mm in diameter have been successfully fabricated using the rod material, and a fundamental technique for the granulation of beryllide has been established (Fig.9-24). Since beryllides have higher melting points and are more stable than Be, some results have shown them to have considerable potential as neutron-multiplying materials.

However, one issue has arisen, namely, that additional homogenization treatment is necessary owing to variation in the phase composition and existence of the Be phase after the granulation, although beryllide pebbles with a chemical composition of $Be_{12}Ti$ were fabricated at the first step. After consideration of the optimized chemical composition with no phase variation, single-phase $Be_{12}V$ pebbles were successfully fabricated by direct granulation.

Since the neutron multipliers with large amounts are loaded in the blanket, pebbles with high strength are required; however, the $Be_{12}V$ pebble indicated a relatively low collapse strength. To solve this issue, extensive research and development of ternary Be-Ti-V beryllide pebbles has been commenced and ternary pebbles with strengths higher than those of $Be_{12}V$ pebbles have been successfully fabricated. It was obvious from experiments that in cases of chemical composition with $Be_{12}Ti_{0.3}V_{0.7}$ and $Be_{12}Ti_{0.1}V_{0.9}$, ternary beryllide pebbles with very fine grains (Fig.9-25), which consisted of dual phases ($Be_{12}Ti$ and $Be_{12}V$) without a Be phase corresponding to no homogenization treatment, were successfully fabricated while the Be phase undesirably increased with an increase in titanium (Ti) amount in the ternary system. Moreover, results of hydrogen generation and collapse strength suggested that the ternary beryllide pebbles indicated relatively low hydrogen generation (Fig.9-26(a)) and higher strength (Fig.9-26(b)) than $Be_{12}V$ pebbles. Accordingly, we have successfully fabricated the world' first ternary pebbles with excellent properties.

**Reference**

Kim, J. et al., Synthesis and Characteristics of Ternary Be-Ti-V Beryllide Pebbles as Advanced Neutron Multipliers, Fusion Engineering and Design, vols.109-111, part B, 2016, p.1764-1768.

# Computational Science for Nuclear Research and Development

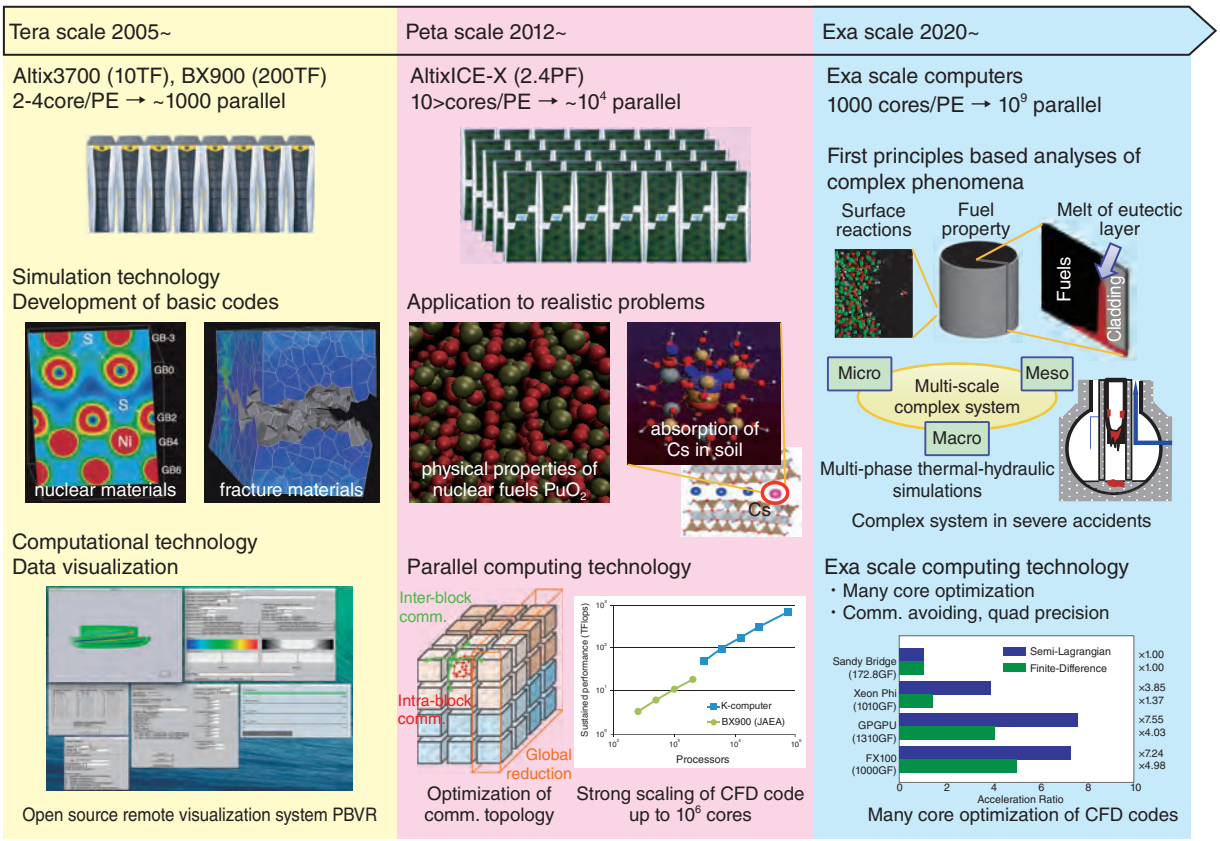


**Fig.10-1 Computer science research at the Center for Computational Science and e-Systems**
To analyze complex systems in nuclear research and development, exascale simulations are being developed by advancing the simulation and computational technologies that were devised for tera/petascale simulations.

Simulation techniques for analyzing complex phenomena comprising various physics effects are essential for resolving issues created by the accident at the TEPCO's Fukushima Daiichi NPS, such as the environmental dynamics of radioactive substances, the volume reduction of polluted soil, and the study of severe accidents. They are also required for research and development of future nuclear systems. For example, severe-accident analyses require not only macroscale thermal-hydraulic simulations for the melt-relocation behavior of nuclear fuels and structural materials but also mesoscale simulations for evaluating complicated interface formation owing to mixing of molten debris and fracture events such as crack growth, and microscale quantum simulations for estimating diffusion, chemical reactions, and phase transitions in extreme environments at high temperature and pressure. In addition to these new simulation techniques, computational technologies that support high-performance computing for simulating such complex phenomena are required.

Thus far, we have developed simulation techniques such as structural analysis, quantum simulations, and fluid simulations, which form the basis for analyzing complex phenomena, as well as computational technologies such as numerical algorithms and visualization systems. We further advance these techniques and perform new analyses of complex phenomena by actively addressing various results from observations and experiments (Fig.10-1). Such simulation techniques for complex phenomena will become a common foundation for general nuclear research and development.

In FY2015, as a computer-science contribution to the reconstruction and revitalization of Fukushima Prefecture, we established a method to evaluate air-dose rates from radioactive cesium in soil and then applied this method to different remediation strategies for contaminated soil (Chapter 1, Topic 1-10). In contrast, toward analyses of complex phenomena, the following simulation techniques were improved.

(1) Seismic analysis of the High-Temperature Engineering Test Reactor (HTTR) using a three-dimensional vibration simulator and its validation against the observation obtained during the Great East Japan Earthquake (Topic 10-1).
(2) Estimation of the specific heat of $PuO_2$ based on first-principles calculations and study of its mechanism at high temperature (Topic 10-2).
(3) First-principles-based study on the cross-slip mechanism of dislocations, which dictates the ductility of hexagonal close-packed metals such as magnesium and zirconium (Topic 10-3).
(4) Development of an electron model that enables multi-time-scale simulations of electron turbulence in fusion plasmas (Topic 10-4).

We steadily promote research of simulation and computational techniques, which are a common foundation for nuclear research and development, and provide them to the community.

# 10–1 Advancement of Seismic-Response-Simulation Techniques for Nuclear Facilities

## — Vibration Simulation of a Nuclear Facility Building using a Three-Dimensional Vibration Simulator —

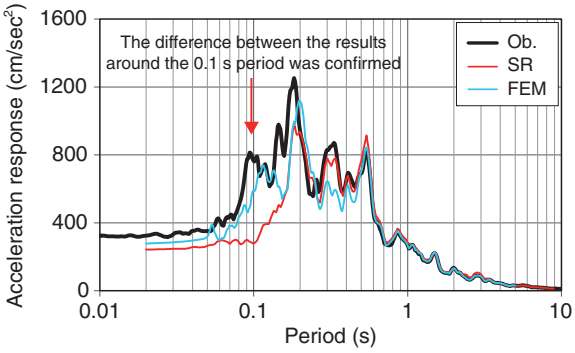


**Fig.10-2 Comparison between observed data and analytical results obtained using the SR and detailed 3D models (acceleration-response spectrum, EW direction, 2nd floor)**
The 3D FE model reproduces the response at a dominant period of approximately 0.1 s, although the peak period is marginally shifted toward the long-period region. Moreover, this mode cannot be confirmed from the results obtained using the SR model.

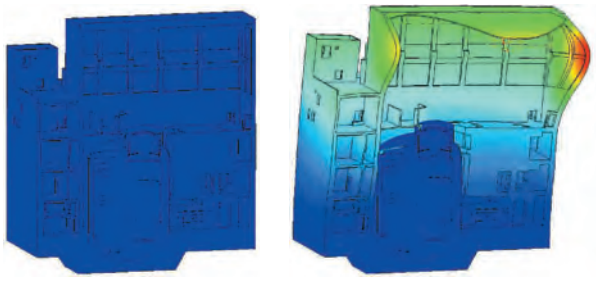


*EW direction, the color represents deformation value (blue and red denote small and large deformations, respectively)

**Fig.10-3 An example of vibrational mode of the detailed three-dimensional model of the HTTR building**
In the vibration-characteristics analysis of a detailed three-dimensional model, the vibration mode of the coupling deformation in the vertical and horizontal directions at periods of approximately 0.1 s has been confirmed. Moreover, the existence of similar vibration modes has been confirmed by analytical results of the seismic-observation record (the deformation is illustrated by a magnified view for visualization purposes).

We have constructed a framework called three-dimensional vibration simulator for seismic-response simulation using a detailed three-dimensional model (3D-FE model) of large, complicated structures such as nuclear power plants. In order to verify the applicability of this three-dimensional vibration simulator to actual problems, we compared the analytical results obtained with the SR model (which is a model meant for design) and with the 3D-FE model using acceleration records observed at the HTTR building at JAEA's Oarai site (Fig.10-2).

First, we compared the analytical results obtained using the SR model and the acceleration response of seismic-observation records. The results enabled us to confirm the difference between the analytical results and seismic-observation records in a short period range of approximately 0.1 s. To identify the cause, we analyzed the vibration of 0.1 s period based on seismic-observation records. We then confirmed the vibrational mode of the coupled deformations in the horizontal and vertical directions, which it is impossible to represent using the SR model. Next, we created a detailed three-dimensional model of the HTTR building to reproduce the vibrational mode and conducted similar seismic-response analysis using a three-dimensional vibration simulator. This confirmed the consistency between the analytical results and observational records of the acceleration-response spectrum; it also confirmed the existence of a coupled vibrational mode in the horizontal and vertical directions (Fig.10-3).

In the SR and detailed three-dimensional models employed in this study, the major modes of the vibrational effect upon the seismic response (approximately 0.2–0.4 s) are largely identical. Because the confirmed coupled vibrational mode has a relatively short period of approximately 0.1 s, the contribution to acceleration response is marginal and the effect on the maximum acceleration to be employed in the seismic evaluation was insignificant. However, as can be observed in Fig.10-3, because vibrational modes affect local responses, especially of the upper walls of the building and the roof, it is necessary to consider the vibrational mode in the stress evaluation of such components.

Since the Great East Japan Earthquake, seismic evaluation of nuclear facilities has required seismic-margin assessment beyond the design value for a variety of ground motions. For this purpose, a more reasonable response evaluation is necessary. An SR model is a model with an adequate margin; however, for highly accurate response evaluation, it is important to construct a model capable of reproducing the actual phenomena. In this research, we will continue the analysis of various seismic-observation records and conduct research and development toward the advancement of a seismic-evaluation method for nuclear facilities.

**Reference**

Nishida, A. et al., Seismic Response Simulation of High-Temperature Engineering Test Reactor Building Against 2011 Tohoku Earthquake, Proceedings of 23rd International Conference on Nuclear Engineering (ICONE 23), Chiba, Japan, 2015, ICONE23-1574, 7p., in DVD-ROM.

# 10–2 Determination of the Thermal Properties of Nuclear Fuels through Numerical Simulation
## — First-Principles Calculations of the Heat Capacity of Plutonium Dioxide —

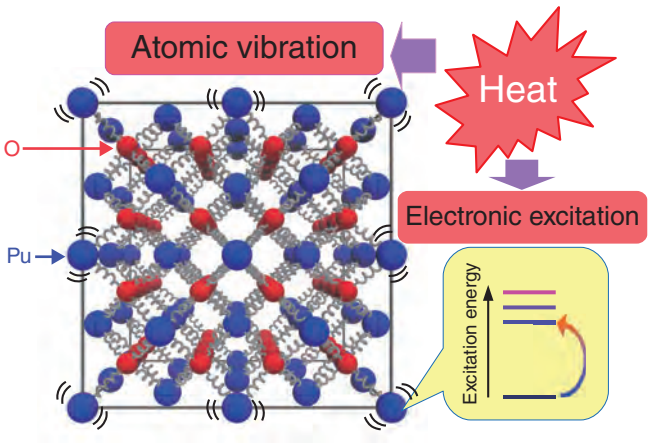


**Fig.10-4 Origins of heat capacity of plutonium dioxide**
The left panel shows the crystal structure of plutonium dioxide, where blue and red spheres denote plutonium and oxygen atoms, respectively. The distribution of electronic excitation energies is shown in the bottom-right panel. Heat capacity results from conversion of external heat into atomic-vibrational (lattice-vibrational) and electronic-excitation energies.

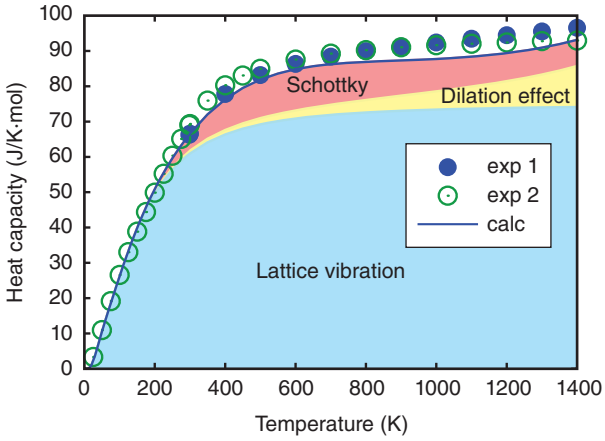


**Fig.10-5 Calculated heat capacity of plutonium dioxide**
Solid curves represent the calculated results of the heat capacity of $PuO_2$, and circles correspond to experimental data. The calculated lattice heat capacity, dilation effects, and Schottky heat capacity are illustrated separately. The calculated result agrees well with the experimental data.

To improve safety, it is important to have adequate knowledge of the thermal properties of nuclear fuel. However, it is difficult to accurately measure these properties at high temperature in experiments. Thus, numerical simulations are expected to compensate for insufficient experimental data. In nuclear-fuel development, one important thermal property is heat capacity, which corresponds to the heat needed to raise the temperature of the material a unit of temperature. So far, numerous theoretical and experimental studies have been conducted on precise measurements of the heat capacity of nuclear fuel and on understanding the mechanism giving rise to this capacity. One of the problems found in these studies is that the theoretically predicted heat capacity does not agree with measurements in the case of plutonium dioxide ($PuO_2$), which is one of main ingredients of nuclear fuel.

To solve this problem, we aimed to reproduce the heat capacity of $PuO_2$ using numerical simulation based on first-principles calculation, which is a reliable method for calculating the properties of materials based purely on interactions between nuclei and electrons, without the requirement for any empirical parameters. First, we evaluated the lattice heat capacity (Fig.10-4) as lattice vibration was expected to be the main source of the heat capacity in this material. The calculated lattice heat capacity was, however, not sufficient to reproduce the observed total heat capacity. Second, we tried to evaluate so-called Schottky heat capacity owing to electronic excitations. In $PuO_2$, some electrons bound in Pu atoms jump up to high-energy excited states at high temperatures; thus, the electronic excitation affects the heat capacity. So far, Schottky heat capacity has been evaluated with simple models considering only a few excited states, but these results have not agreed with experimental data. In contrast, we adopted more than 100 excited states obtained by first-principles calculations and recalculated the Schottky heat capacity. We then succeeded in reproducing the total heat capacity, as shown in Fig.10-5. This precise evaluation could not have been attained without first-principles calculations.

In this study, we succeeded in accurately evaluating the heat capacities of nuclear fuel materials by numerical simulation based on first-principles calculation. However, other thermal properties such as thermal conductivity are required to develop safer fuels. Thus, we will challenge accurate predictions of other nuclear-fuel properties by first-principles simulations and would like to contribute to the development of secure nuclear fuels.

**Reference**

Nakamura, H. et al., First-Principles Calculation of Phonon and Schottky Heat Capacities of Plutonium Dioxide, Journal of the Physical Society of Japan, vol.84, no.5, 2015, p.053602-1-053602-5.

# 10–3 Quest for Light Metals with Good Formability

## — A Novel Deformation Mechanism in Hexagonal Metals Revealed by Quantum Calculations —

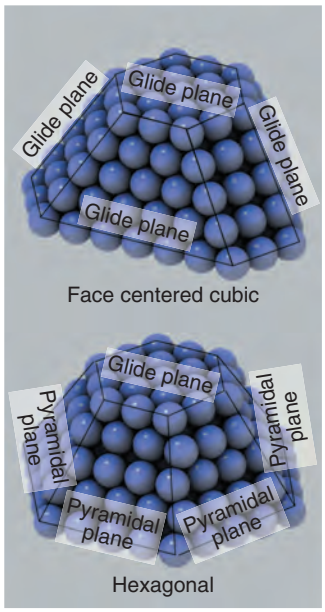


**Fig.10-6 Two typical atomistic structures of metals**
Two atomistic structures of metals are shown. The face-centered cubic structure has four distinct planes where atoms align in triangles, whereas the hexagonal structure has only one such plane and six other planes on the side comprising alternating triangles and squares.

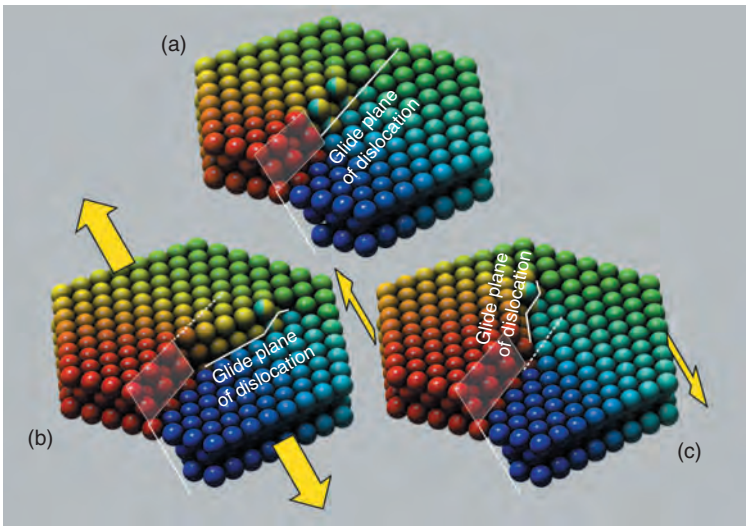


**Fig.10-7 Motion of a dislocation in a hexagonal structure**
(a) The atomistic structure around a dislocation in a hexagonal metal is shown. The semi-transparent plane and white lines are the glide plane of the dislocation. The color of each atom indicates the amount of displacement along the glide direction. (b)(c) Atomistic configurations when a force is applied in the direction indicated by the yellow arrows. One can see that the glide plane changes depending upon the direction of the force.

The structures of metallic elements are classified into three types, namely, face-centered cubic (FCC), body-centered cubic, and hexagonal. Hexagonal metals such as magnesium and zirconium are difficult to deform, and formation of these metals requires elevated temperature. Typical examples are the manufacturing of nuclear fuel claddings composed of zirconium alloy and the magnesium housing of notebook PCs. Recently, it has been observed that the addition of alloying elements into hexagonal metal lowers the temperature required for the forming process. To further lower the temperature and enable room-temperature forming, much effort is now being invested in elucidating the relevant mechanism and finding the optimal composition of the alloy. The success of these studies will enable several industrial breakthroughs, such as tougher fuel claddings and lighter automobiles. For this purpose, it is necessary to study the forming process at an atomistic scale.

Fig.10-6 shows atomistic planes in FCC and hexagonal structures. Planes with triangular alignment easily glide. Since the FCC structure has four such planes, glides can occur in various directions and formation of the material is easy. In contrast, the hexagonal structure has only one such plane and the six pyramidal planes on the side comprise alternating triangular and square alignments that make gliding more difficult.

To improve the formability of hexagonal metals, we need to identify the gliding mechanism of the pyramidal planes. We studied magnesium for this purpose. The glide of atomistic planes is induced by the motions of "dislocation lines," just like that one can glide a large carpet by moving a ruck on it. Typically, a dislocation line is confined to a specific plane, but in magnesium, it has been observed that the dislocation line changes its glide plane via some unknown mechanism. We closely investigated the glide process using first-principles calculation and elucidated the responsible mechanism.

In FCC metals, the change in the glide plane requires extensive rearrangement of nearby atoms and high activation energy; however, in hexagonal metals, we found a way to do it with only modest rearrangement. We also confirmed that the glide plane actually changes easily when a force is applied, as shown in Fig.10-7. Such behavior has not been known, until our close examination of the dislocation in hexagonal metal.

We will continue investigating the effect of alloying elements upon the glide process and elucidating the mechanism of formability improvement.

**Reference**

Itakura, M. et al., Novel Cross-Slip Mechanism of Pyramidal Screw Dislocations in Magnesium, Physical Review Letters, vol.116, issue 22, 2016, p.225501-1-225501-5.

# 10–4 Simulation Technology for Long-Time-Scale Analyses of Fusion Plasmas
## — Progress Toward Multi-Time-Scale Analyses —

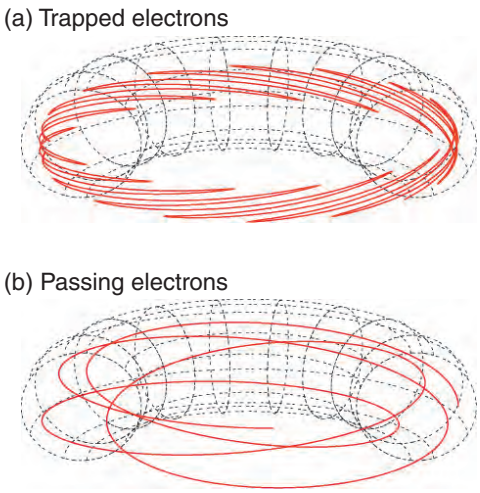


**Fig.10-8 Electron orbits in fusion plasmas**
(a) Trapped electrons are distributed in the outer torus region with weak magnetic fields and exhibit slow precession drifts (~100 kHz), which excite plasma turbulence by a resonant interaction. (b) Passing electrons show fast passing motion in torus plasmas (~6 Mhz), generating high-frequency noise.

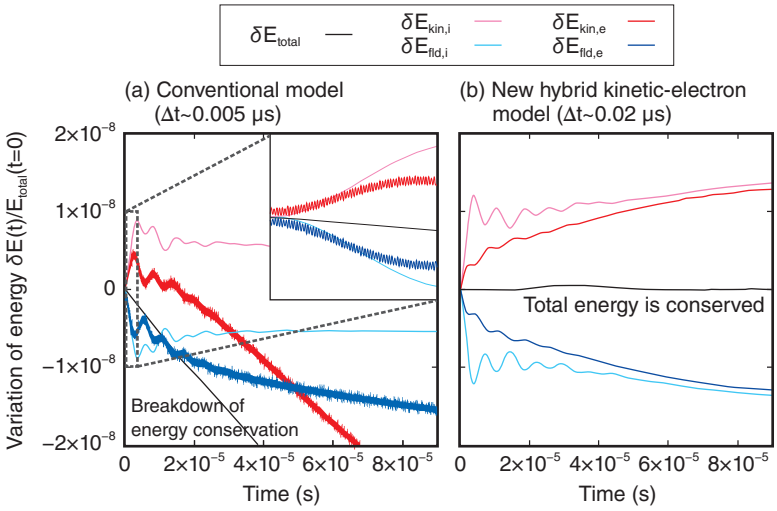


**Fig.10-9 Energy conservation in decaying turbulence simulations**
The time evolutions of the kinetic ($\delta E_{kin,i}$,$\delta E_{kin,e}$) and field ($\delta E_{fld,i}$,$\delta E_{fld,e}$) energies of ions and electrons as well as the total energy ($\delta E_{total}$) in decaying turbulence simulations, where given initial turbulent fields decay. (a) In the conventional model for computing passing electrons (Δt~0.005 μs), the accumulation of errors in the electron energy owing to high-frequency noise violates energy conservation, whereas (b) in the new hybrid kinetic-electron model (Δt~0.02 μs), the time-step width is extended (lower computational cost) and the accuracy of energy conservation is improved by eliminating high-frequency noise.

Long-time-scale simulations of electron turbulence are essential for estimating turbulent transport of fuel particles and energy, which dictates the performance of fusion reactors. However, such a simulation is difficult because of fast electron motion. We have resolved this issue by developing a new electron model.

Fusion plasmas involve multi-time-scale phenomena such as gyro motion of charged particles along confinement magnetic fields (electron~140 GHz, ion~40 MHz), passing motion of charged particles in torus plasmas (electron~6 MHz, ion~100 kHz), slow precession drifts of trapped electrons (~100 kHz), plasma turbulence (~100 kHz), collisions between charged particles (~1 kHz), and a time scale of temperature-profile variations (~1 s). The development of a first-principles model that analytically approximates gyro motion with higher frequency than plasma turbulence as well as advances in modern supercomputers have enabled simulations of ion turbulence covering time scales from those of plasma turbulence to those of temperature-profile variations. However, long-time-scale simulations of electron turbulence have been limited because the passing motion of electrons is two orders of magnitudes faster than plasma turbulence, and energy conservation cannot be maintained in the simulations.

To resolve this issue, we have developed a new electron model based on the properties of electron motion in fusion plasmas. Depending on the velocity, electron orbits are classified into trapped electrons, which are distributed in the outer torus region with weak magnetic fields and exhibit slow precessional drifts, and passing electrons, which exhibit fast passing motion in torus plasmas (Fig.10-8). The plasma turbulence is mainly excited by a resonant interaction with the former, while the latter generates high-frequency non-physical numerical noise. To enable low-cost and high-accuracy simulations by avoiding the high-frequency noise, in computing turbulent fields, the responses of passing electrons are approximated by an analytic solution for low-frequency fluctuations. Conversely, computation of collisions also requires strict treatments for passing electrons; thus, the same first-principles model is applied to both trapped and passing electrons. Such a hybrid electron model, in which different passing electron models are switched depending on physical processes, satisfies the reduction of computational cost and the improvement of energy conservation (Fig.10-9) and enables long-time-scale simulations of electron turbulence.

This work is supported by the Ministry of Education, Culture, Sports, Science and Technology of Japan (MEXT), Post-K Priority Issue 6, “Development of Innovative Clean Energy” (Core Design of Fusion Reactor).

**Reference**

Idomura, Y., A New Hybrid Kinetic Electron Model for Full-*f* Gyrokinetic Simulations, Journal of Computational Physics, vol.313, 2016, p.511-531.

# Development of Technology and Human Capacity Building in the Area of Nuclear Nonproliferation and Nuclear Security to Support Peaceful Use of Nuclear Energy

The Integrated Support Center for Nuclear Nonproliferation and Nuclear Security (ISCN) has been conducting the following technology and human capacity development activities related to nuclear nonproliferation and nuclear security, in cooperation with relevant domestic and overseas organizations (Fig.11-1).

## Technology Development for Japanese and International Applications

We have been developing the nondestructive assay technology to quantify nuclear materials in fuel debris by the accident at the TEPCO's Fukushima Daiichi NPS, and also examining the safeguards* technologies in case the spent fuel direct disposal is applied. In addition, we have been developing the nuclear detection technology by nuclear resonance fluorescence technique, the nondestructive assay technology using external pulse neutron source and the monitoring technology for plutonium solution containing fission products in order to enhance nuclear security and improve safeguards. Furthermore, we have been improving the technologies for the nuclear forensics. Topic 11-1 shows the summary of the international collaborative analysis comparison exercise for uranium age determination analysis which is one of nuclear forensics measures.

* Verification activity to ensure that nuclear materials are limited to peaceful uses and not diverted to nuclear weapons.

## Support for Government Policy Formulation Based on Our Technological Expertise

We conduct the research on synergy effects on Non-proliferation (Safeguards) and Nuclear Security measures at nuclear fuel cycle facilities. In order to enhance and promote both Safeguards and Nuclear Security (so called "2Ss"), international trend survey on synergy effects was proceeded as basic study, eyeing possibility of utilizing originally "1S"-purposed measurement and surveillance technologies, safeguards equipment and information for "2Ss" purposes in future nuclear fuel cycle facilities. We also examined applicability of the International Atomic Enagy Agency (IAEA) recommended measure for "2Ss" to MOX fuel fabrication and fuel storage facilities.

## Support for Human Capacity Development

Based on the commitments of the Japanese government made at the Nuclear Security Summit in April 2010, we have supported human capacity development, especially among Asian states, since April 2011 in order to strengthen nuclear security in these countries. In FY 2015, approximately 530 (approximately 300 from Asian states) participants benefitted from our seminars and training courses on nuclear security and safeguards held within and outside of Japan.

## International Contributions Based on Our Expertise and Experience

To establish the global verification regime for nuclear tests, we have been operating provisionally facilities of the international monitoring system of the Comprehensive Nuclear-Test-Ban Treaty (CTBT) and a national data center (NDC). For the 4th nuclear test conducted by North Korea in January 2016, JAEA reported the analysis and evaluation results of data observed at the CTBT radionuclide monitoring stations to the national government etc. in a timely manner and thereby contributed to the evaluation by the national government based on the CTBT operation system in Japan.

## Support to JAEA's Transportation and Duties of Research Reactor Fuels

We support to nuclear transportation carrying out by our research and development centers, we have coordinated the procurement of fresh fuels and disposal measures of spent fuels for our research reactors. Through these activities, we contribute to Global Threat Reduction Initiative (GTRI), which has been strengthening global nuclear security, by promoting the systematic return of high enriched uranium to USA.


**Fig.11-1 JAEA activities in the development of science and technology for nuclear nonproliferation and nuclear security**
We have been playing an active role in international organizations, such as IAEA, technology development in each country and ensuring transparency. And we continue human capacity development support project which contributes the capacity building in Asian countries.

# 11–1 Estimating the Production Date of Nuclear Material
## — Round-Robin Uranium-Age Dating for Nuclear Forensics —

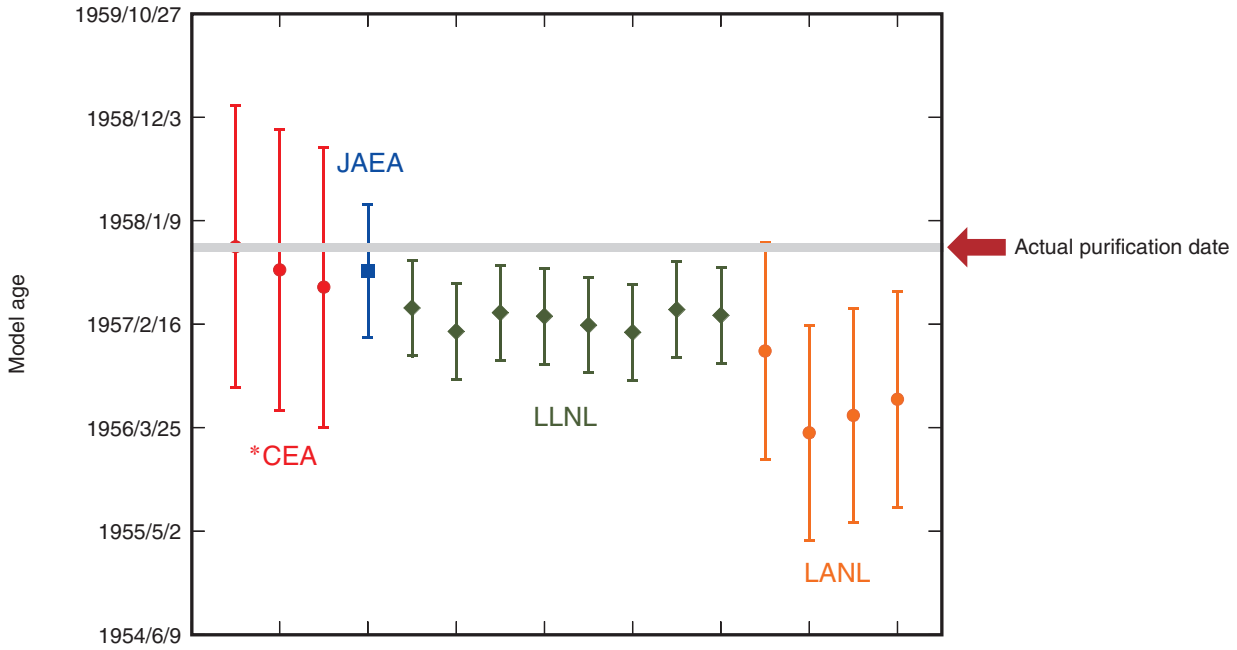


**Fig.11-2 The result of uranium-age dating using uranium standard material (U-050)**
As a result of round-robin analysis, we confirmed that each laboratory could estimate accurate production date of uranium material within a definite error. JAEA showed a good capability of nuclear forensics analysis comparable with other laboratories (*CEA: The French Alternative Energies and Atomic Energy Commission).

In order to prevent terrorist attacks using radioactive and nuclear (RN) materials, the International Atomic Energy Agency (IAEA) has positioned nuclear forensics as an important foundation of nuclear security that should be provided by each state. Nuclear forensics is technical measurement for analyzing and assaying the origin, history, route of transportation, and objective of RN materials seized by law-enforcement authorities.

Uranium-age dating in nuclear forensics is a technical measure for estimating the production date of nuclear materials, which is considered to be an effective way to determine their origin. The principle of uranium-age dating can be described as follows: in uranium (U)-production processes, other elements are eliminated, and the produced uranium material does not contain its daughter nuclide of thorium (Th). As time progresses, Th is produced again at a constant rate in purified U materials. Consequently, we can estimate the production date to measure the ratio of U and Th in materials.

We collaborated with the Lawrence Livermore National Laboratory (LLNL) and the Los Alamos National Laboratory (LANL) to conduct information exchange and round-robin analysis (comparing the analytical results obtained using the same material with some analyzers) on uranium-age dating. We adopted the isotope-dilution mass spectrometry method to measure $^{234}$U and $^{230}$Th in the uranium material. In this method, in order to measure the small amount of $^{230}$Th to high accuracy, we need to effectively eliminate the measured component of U. For this purpose, we prepared a homemade narrow separation column and successfully controlled this column's flow rate. Using this column, we achieved a high elimination factor ($10^{-8}$ = U in the Th fraction / primary U). Furthermore, because of the small column volume of 0.3 m$\ell$, we could reduce the volume of sample solution and the procedure time of separation and heating. The result of the round-robin analysis using the uranium standard U-050 agreed well between each laboratory (Fig.11-2). We could confirm that our analytical technique was comparable with that of top-level laboratories and applicable to practice for nuclear-forensics events.

**Reference**

Gaffney, A. M., Okubo, A. et al., Round-Robin $^{230}$Th-$^{234}$U Age Dating of Bulk Uranium for Nuclear Forensics, Journal of Radioanalytical and Nuclear Chemistry, vol.307, issue 3, 2016, p.2055-2060.

# Promotion of Collaboration

To make the technologies, patents and other research results, and facilities and equipment of the Japan Atomic Energy Agency (JAEA) widely available to society, we are promoting activities in three areas: “academia-industry collaboration”, “utilization of intellectual property”, and “facility usage”. We are also creating a database of patents and intellectual property information held by the JAEA. The following table is a list of intellectual property (patents in foreign countries) in the fiscal year 2015.

## Intellectual Property Held by JAEA
## Patent Information

| Title | Department | R&D Institutes and Centers | Publication Number | Date of Registration |
|---|---|---|---|---|
| 1 USA | | | | |
| Self-powered Gamma Detector | Oarai Research and Development Center, Sector of Nuclear Science Research | Oarai Research and Development Center | 9046611 | Jun. 2, 2015 |
| Packet Communication Method and Equipment Therefor | Safety and Nuclear Security Administration Department | Head Office | 9083616 | Jul. 14, 2015 |
| Continuous Collection Method of Particle Component in Aqueous Solution and Apparatus Therefor | Nuclear Science and Engineering Center, Sector of Nuclear Science Research | Nuclear Science Research Institute | 9108124 | Aug. 18, 2015 |
| Compound for Forming Fluorescent Uranium Complex, Method for Synthesizing Thereof, Fluorescent Probe for Detecting Uranium and Method for Analyzing Uranium | Nuclear Science Research Institute, Sector of Nuclear Science Research | Nuclear Science Research Institute | 9110047 | Aug. 18, 2015 |
| Neutron Detector | J-PARC Center, Sector of Nuclear Science Research | Nuclear Science Research Institute | 9268045 | Feb. 23, 2016 |
| 2 France | | | | |
| Radiation Resistant Resin Composition and Radiation-proof Wire/Cable | J-PARC Center, Sector of Nuclear Science Research | Nuclear Science Research Institute | 2036946 | Jun. 17, 2015 |
| Visualizing Apparatus using Gamma Ray Source | Oarai Research and Development Center, Sector of Fast Reactor Research and Development | Oarai Research and Development Center | 604804 | Jan. 1, 2016 |
| Visualizing Apparatus using Ultraviolet Rays in Liquid Sodium | Tsuruga Head Office | Tsuruga Head Office | 1250174 | Feb. 5, 2016 |

*About the Design of the Cover*

*The cover is designed with white hexagons similar to the pattern in a tortoise shell, an ancient Japanese symbol of people's wish for longer lives. Coincidentally, this shape is the same as that of core fuel assemblies for both the prototype fast breeder reactor "MONJU" and the high-temperature engineering test reactor "HTTR".*

*The images on the cover show a contour map of the air dose rate of a mountainous forest catchment, which was contaminated by radiocesium released by the accident at the TEPCO's Fukushima Daiichi NPS (top left) and appearance of the Extreme Environment Single Crystal Neutron Diffractometer "SENJU" (bottom right).*

*The top left image shows the results of detailed and systematic measurements of the air dose rate in a forest with complex topography. This study showed that the spatial distribution of radiocesium deposition was strongly affected by the topographical features (Chapter 1, Topic 1-12, p.24).*

*The bottom right image shows the SENJU, one of neutron instruments at J-PARC, which enabled us to observe hydrogens and magnetic spin moments in a crystalline material with a small single crystal under extreme sample environment such as low temperature or magnetic field. This new instrument is a powerful tool for understanding the nature of many functional materials (Chapter 5, Topic 5-4, p.62).*

**JAEA R&D Review 2016-17**

**Published by**
Japan Atomic Energy Agency in January 2017



This publication is issued by Japan Atomic Energy Agency (JAEA) on a yearly basis.
Inquiries about availability and/or copyright of the contents in this publication should be addressed to Institutional Repository Section, Intellectual Resources Management and R&D Collaboration Department, Japan Atomic Energy Agency (JAEA).

**Address:** 2-4 Shirakata, Tokai-mura, Naka-gun, Ibaraki-ken 319-1195, Japan
**Phone:** +81-29-282-6387, **Facsimile:** +81-29-282-5920, **e-mail:** ird-seika_shi@jaea.go.jp